

**Non-equilibrium solidification of high-entropy alloys monitored  
*in situ* by X-ray diffraction and high-speed video**

Von der Fakultät Maschinenwesen der Technischen Universität Dresden  
zur Erlangung des akademischen Grades  
Doktoringenieur (Dr.-Ing.)  
angenommene

**DISSERTATION**

von

Angelo Fernandes Andreoli  
geboren am 16.06.1981 in Ibitiúva, Brasilien

*This page is intentionally left blank*

To my parents Samira and Claudinei, to my wife Marina, and my son Benício.

*This page is intentionally left blank*



## Contents

<b>Abstract</b> .....	I
<b>Kurzfassung</b> .....	IV
<b>Chapter 1: Motivation and Fundamentals</b> .....	1
1.1 Introduction.....	1
1.2 The high-entropy alloy (HEA) design concept.....	4
1.3 Empirical rules of phase formation for HEAs .....	6
1.4 Calculation of phase diagrams of HEAs.....	18
1.5 The core effects of HEAs.....	20
1.5.1 Lattice distortion.....	20
1.5.2 Sluggish diffusion.....	22
1.5.3 Cocktail effect.....	23
1.6 Mechanical properties .....	24
1.6.1 Lightweight high-entropy alloys .....	24
1.6.2 Overcoming the strength-ductility tradeoff.....	26
1.6.3 Cryogenic high-entropy alloys .....	28
1.6.4 Refractory high-entropy alloys.....	30
1.7 Functional properties .....	33
1.7.1 Soft magnetic properties.....	33
1.7.2 Magnetocaloric properties .....	35
1.7.3 Hydrogen storage.....	36
<b>Chapter 2: Experimental</b> .....	38
2.1 Sample preparation .....	38
2.2 Electromagnetic levitation .....	40
2.3 <i>In situ</i> X-ray diffraction .....	43
2.4 Microstructural and structural analysis.....	44
2.5 Thermal analysis .....	45

2.6	Dilatometry.....	45
2.7	Magnetic moment.....	46
2.8	Heat treatment.....	46
<b>Chapter 3: <i>In situ</i> study of non-equilibrium solidification of CoCrFeNi high-entropy alloy and CrFeNi and CoCrNi ternary suballoys.....</b>		
3.1	Introduction .....	47
3.2	Results .....	48
3.2.1	<i>In situ</i> synchrotron X-ray diffraction .....	48
3.2.2	High-speed video imaging .....	52
3.2.3	Microstructure of the solidified samples.....	62
3.3	Discussion.....	64
3.3.1	<i>bcc-fcc</i> nucleation and growth competition .....	64
3.3.2.	Crystal growth kinetics.....	68
3.3.3.	Microstructural evolution.....	70
<b>Chapter 4: The effect of Al addition to the CoCrFeNi alloy on the non-equilibrium solidification behaviour.....</b>		
4.1	Introduction .....	72
4.2	Results and Discussion .....	73
<b>Chapter 5: Non-equilibrium solidification of the NbTiVZr refractory high-entropy alloy.....</b>		
5.1	Introduction .....	84
5.2	Results .....	85
5.2.1	<i>In situ</i> synchrotron X-ray diffraction .....	85
5.2.2	Room temperature synchrotron X-ray diffraction.....	88
5.2.3	High-speed video imaging .....	89
5.2.4	Microstructure and structure analysis .....	91
5.3	Discussion.....	94
5.3.1	Phase formation upon solidification.....	94

5.3.2	Crystal growth kinetics.....	98
5.3.3	Structural and microstructural features.....	99
<b>Chapter 6: Solid-state thermophysical properties of CrFeNi, CoCrNi, and CoCrFeNi medium- and high-entropy alloys .....</b>		<b>101</b>
6.1	Introduction.....	101
6.2	Results.....	102
6.3	Discussion.....	106
6.3.1	Thermophysical properties .....	106
6.3.2	Short-range order in medium- and high-entropy alloys .....	109
<b>Chapter 7: Summary.....</b>		<b>111</b>
7.1	Empirical rule of phase formation of complex concentrated alloys .....	111
7.2	Non-equilibrium solidification of medium- and high-entropy alloys.....	111
7.3	Thermophysical properties of the medium- and high-entropy alloys.....	113
<b>Chapter 8: Outlook.....</b>		<b>115</b>
<b>Appendix 1 .....</b>		<b>117</b>
<b>Appendix 2 .....</b>		<b>123</b>
<b>Appendix 3 .....</b>		<b>133</b>
<b>Appendix 4 .....</b>		<b>134</b>
<b>References.....</b>		<b>140</b>
<b>Acknowledgments.....</b>		<b>164</b>
<b>List of publications .....</b>		<b>166</b>
<b>Erklärung.....</b>		<b>167</b>

*This page is intentionally left blank*

## Abstract

High-entropy alloys (HEAs) have attracted significant interest in the materials science community over the last 15 years. At the first moment, what caught the attention was the fact that these alloys tend to form solid solutions at room temperature, despite being composed of multiple elements in equiatomic or near-equiatomic concentrations. It was initially concluded that the configurational entropy plays a key role in the stabilization of the solid solutions. Later studies revealed the importance of lattice strain enthalpies, enthalpies of mixing, structural mismatch of constituents, and kinetics in phase formation/stability.

The study presented in this thesis was branched into three major parts, all related to understanding phase formation, stability, or metastability in this class of alloys. The first part deals with developing an empirical method to predict single-phase solid solution formation in multi-principal element alloys. The second, which makes the core of this thesis, are non-equilibrium solidification studies of CrFeNi and CoCrNi medium-entropy alloys, and CoCrFeNi, Al<sub>0.3</sub>CoCrFeNi, and NbTiVZr high-entropy alloys. The last part is devoted to understanding the thermophysical properties of CrFeNi, CoCrNi, and CoCrFeNi medium- and high-entropy alloys.

An empirical approach, based on the theoretical elastic-strain energy, has been developed to predict the phase formation and its stability for complex concentrated alloys. The conclusiveness of this approach is compared with the traditional empirical rules based on the atomic-size mismatch, enthalpy of mixing, and valence-electron concentration for a database of 235 alloys. The proposed “*elastic-strain energy vs. valence-electron concentration*” criterion shows an improved ability to distinguish between single-phase solid solutions, mixtures of solid solutions, and intermetallic phases when compared to the available empirical rules used to date. The criterion is especially strong for alloys that precipitate the  $\mu$  phase. The elastic-strain-energy parameter can be combined with other known parameters, such as those noted above, to establish new criteria which can help in designing novel complex concentrated alloys with the on-demand combination of mechanical properties.

The solidification behavior of the CoCrFeNi high-entropy alloy and the ternary CrFeNi and CoCrNi medium-entropy suballoys has been studied *in situ* using high-speed video-camera and synchrotron X-ray diffraction (XRD) on electromagnetically levitated samples at Leibniz Institute for Solid State and Materials Research Dresden (IFW Dresden)

and German Synchrotron DESY, Hamburg. In all alloys, the formation of a primary metastable body-centered cubic *bcc* phase was observed if the melt was sufficiently undercooled. The delay time for the onset of the nucleation of the stable face-centered cubic *fcc* phase, occurring within *bcc* crystals, is inversely proportional to the melt undercooling. The experimental findings agree with the stable and metastable phase equilibria for the (CoCrNi)-Fe section. Crystal-growth velocities for the CrFeNi, CoCrNi, and CoCrFeNi medium- and high-entropy alloys, extracted from the high-speed video sequences in the present study, are comparable to the literature data for Fe-rich Fe-Ni and Fe-Cr-Ni alloys, evidencing the same crystallization kinetics. The effect of melt undercooling on the microstructure of solidified samples is analyzed and discussed in the thesis.

To understand the effect of Al addition on the non-equilibrium solidification behavior of the equiatomic CoCrFeNi alloy, the Al<sub>0.3</sub>CoCrFeNi HEA has been studied. While the quaternary alloy melt could be significantly undercooled, this was not possible in the five-component alloy. Therefore, the investigations on phase formation, crystal growth, and microstructural evolution were confined to the low undercooling regime. *In situ* XRD measurements revealed that the liquid crystallized into a *fcc* single-phase solid solution at this undercooling level. However, *ex situ* XRD revealed the precipitation of the ordered L1<sub>2</sub> phase for a sample solidified with  $\Delta T = 30$  K. Crystal growth velocities are shown to be smaller than in the CoCrFeNi, CrFeNi, and CoCrNi alloys; nonetheless, they are in the same order of magnitude. Spontaneous grain refinement, without the formation of crystal twins, is observed at low undercooling of  $\Delta T = 70$  K, which could be explained by the dendrite tip radius dependence on melt undercooling.

*In situ* studies of the equiatomic NbTiVZr refractory high-entropy alloys revealed the effect of processing conditions on the high-temperature phase formation. When the melt was undercooled over 80 K, it crystallized as a *bcc* single-phase solid solution despite solute partitioning between the dendritic and interdendritic regions. When the sample was solidified from the semisolid state, it resulted in the formation of two additional *bcc* phases at the interdendritic regions. The crystal growth velocity, as estimated from the high-speed videos, showed pronounced sluggish kinetics: it is 1 to 2 orders of magnitude smaller compared to literature data of other medium and high-entropy alloys.

The study of the linear expansion coefficient  $\alpha$  and heat capacity at constant pressure  $C_p$  of the equiatomic CoCrFeNi and the medium-entropy CrFeNi and CoCrNi alloys revealed an anomalous behavior with S-shaped curves in the temperature range of 700 – 950 K. The anomalous behavior is shown to be reversible as it occurred during the first and

second heating. However, a minimum is only observed on the first heating, while in the second heating a sudden increase of both the  $\alpha$  and  $C_p$  occurs at the temperature of the onset of the minima in the first heating. Magnetic moment measurements as a function of temperature showed that the observed anomaly is not associated with the Curie temperature. Consideration of the structural and microstructural evaluation discards a first-order phase transformation or recrystallization as probable causes, at least for the CoCrFeNi and CoCrNi alloys. Based on literature evidence, the anomalies in the temperature dependences of the linear expansion coefficient and heat capacity are believed to be caused by a chemical short-range order transition known as the K-state effect. However, to reveal the exact nature of this phenomenon, further experimental and theoretical studies are required, which is outside the frame of the present work.

## Kurzfassung

Hochentropie-Legierungen (engl. high-entropy alloys, HEAs) haben in den letzten 15 Jahren großes Interesse in der Materialwissenschaft gefunden. Was im ersten Moment die Aufmerksamkeit auf sich zog, war die Tatsache, dass diese Legierungen zur Mischkristallbildung bei Raumtemperatur neigen, obwohl sie aus mehreren Elementen in äquiatomaren oder nahezu äquiatomaren Konzentrationen zusammengesetzt sind. Es wurde zunächst vermutet, dass die mehrkomponentigen Mischkristalle durch die Konfigurationsentropie stabilisiert werden. Spätere Studien haben jedoch gezeigt, dass die Gitterverzerrungsenthalpie, Mischungsenthalpie, strukturelle Fehlanpassungen der Legierungskomponenten sowie die Kinetik eine wichtige Rolle bei der Bildung bzw. Stabilisierung von Hochentropie Mischkristallen spielen.

Die vorliegende Arbeit besteht aus drei Hauptteilen, die zur Aufklärung der Phasenbildung, Stabilität bzw. Metastabilität in dieser Legierungsklasse beitragen sollen. Der erste Teil beschäftigt sich mit der Entwicklung eines empirischen Ansatzes zur Vorhersage der einphasigen Mischkristallbildung in Viel-Hauptelement-Legierungen. Der zweite Teil, der den Kern dieser Arbeit bildet, umfasst Untersuchungen zur Nichtgleichgewichtserstarrung von CrFeNi und CoCrNi Mittelentropie-Legierungen (engl. medium-entropy alloys, MEAs) und CoCrFeNi, Al<sub>0.3</sub>CoCrFeNi und NbTiVZr Hochentropie-Legierungen. Der dritte Teil widmet sich den Untersuchungen von thermophysikalischen Eigenschaften von CrFeNi, CoCrNi und CoCrFeNi Legierungen.

Ein empirischer Ansatz auf Basis der theoretischen elastischen Verzerrungsenergie wurde zur Vorhersage der Phasenbildung und -stabilität in komplexen konzentrierten Legierungen entwickelt. Die Aussagekraft dieses Ansatzes wurde im Vergleich zu traditionellen empirischen Regeln, welche die Atomgrößenfehlanpassungen, Mischungsenthalpie und Valenzelektronenkonzentration berücksichtigen, anhand einer Datenbank aus 235 Legierungen geprüft. Es hat sich gezeigt, dass das vorgeschlagene „*elastische Verzerrungsenergie* vs. *Valenzelektronenkonzentration*“ Kriterium ist für die Unterscheidung zwischen einphasigen Mischkristallen, Mischkristall-Mischungen und intermetallischen Phasen im Vergleich zu den bisherigen empirischen Regeln besser geeignet. Das Kriterium ist besonders stark für Legierungen, die die  $\mu$ -Phase ausscheiden. Darüber hinaus kann der Parameter der elastischen Verzerrungsenergie mit anderen bekannten Parametern, wie die oben erwähnten,



kombiniert werden, um neue Kriterien zu erstellen, die für das Design von neuartigen komplexen konzentrierten Legierungen mit maßgeschneiderten mechanischen Eigenschaften hilfreich sein können.

Das Erstarrungsverhalten von CoCrFeNi Hochentropie-Legierung und der ternären CrFeNi und CoCrNi Mittelentropie-Sublegierungen wurde *in situ* mittels Hochgeschwindigkeitskamera und Synchrotron Röntgenbeugung (XRD) an elektromagnetisch levitierten Proben im Leibniz Institut für Festkörper und Werkstofforschung Dresden (IFW Dresden) und Deutschen Synchrotron DESY Hamburg untersucht. Bei allen Legierungen wurde die Bildung einer primären metastabilen kubisch-raumzentrierten (*krz*) Phase beobachtet, wenn die Schmelze ausreichend unterkühlt wurde. Die zeitliche Verzögerung bis zum Einsetzen der Keimbildung der stabilen kubisch-flächenzentrierten (*kfz*) Phase, die in *krz*-Kristallen auftritt, ist umgekehrt proportional zur Schmelzeunterkühlung. Die experimentellen Ergebnisse stimmen mit den stabilen und metastabilen Phasen-Gleichgewichten für den (CoCrNi)-Fe Querschnitt überein. Die Kristallwachstumsgeschwindigkeiten für die CrFeNi, CoCrNi und CoCrFeNi Legierungen, ermittelt aus den Hochgeschwindigkeits-Videosequenzen, sind vergleichbar mit den Literaturdaten für Fe-reiche Fe-Ni und Fe-Cr-Ni-Legierungen, was auf die gleiche Kristallisationskinetik hinweist. Der Zusammenhang zwischen der Unterkühlung der Schmelze und das Erstarrungsgefüge ist in dem vorliegenden Dissertationschrift ebenfalls analysiert und diskutiert.

Der Einfluss von Al-Zusätze auf die Nichtgleichgewichtserstarrung der äquiatomaren CoCrFeNi Legierung wurde anhand der  $\text{Al}_{0.3}\text{CoCrFeNi}$  Hochentropielegierung untersucht. Während die quaternäre Metallschmelze deutlich unterkühlt werden konnte, wurde dies bei der fünfkomponentigen Legierung nicht möglich. Aus diesem Grund beschränkten sich die Untersuchungen zur Phasenbildung, Kristallwachstum und Gefügeentwicklung auf den Bereich geringer Unterkühlung. Die *in-situ* XRD Untersuchungen haben gezeigt, dass die Metallschmelze bei der Unterkühlung von 77 K zu einem *kfz*-Mischkristall erstarrt. *Ex-situ* XRD Messung wies jedoch die Ausscheidung einer geordneten  $L_{12}$ -Phase in einer erstarrten Probe nach der 30 K Unterkühlung. Die Geschwindigkeit des Kristallwachstums in der  $\text{Al}_{0.3}\text{CoCrFeNi}$  Legierung ist kleiner als bei CoCrFeNi, CrFeNi und CoCrNi Legierungen, liegt jedoch in der gleichen Größenordnung. Bei relativ geringer Unterkühlung von  $\Delta T = 70$  K wurde eine spontane Kornfeinung ohne Bildung von Kristallzwillingen beobachtet, was durch die Abhängigkeit des Dendritenspitzenradius von der Schmelzeunterkühlung erklärt werden könnte.

In den *in-situ* Untersuchungen der äquiatomaren NbTiVZr refraktär Hochentropie-Legierung wurde den Einfluss von Porzessierungsparametern auf die Hochtemperaturphasenbildung entschlüsselt. Bei Untertemperaturkühlung der Schmelze von mehr als 80 K kristallisierte sie trotz der Verteilung (engl. partitioning) der Legierungskomponenten zwischen dendritischen und interdendritischen Bereichen als einphasiger *krz*-Mischkristall. Die Erstarrung aus einem halbfesten (engl. semisolid) Zustand erfolgte mit der Bildung von zwei zusätzlichen *krz*-Phasen in den interdendritischen Bereichen. Die aus den Hochgeschwindigkeitsvideos ermittelten Kristallwachstumsgeschwindigkeiten sind im Vergleich zu Literaturdaten anderer Mittel- und Hochentropielegierungen um 1 bis 2 Größenordnungen kleiner, was auf eine ausgeprägt-träge Kristallisationskinetik hinweist.

Die Untersuchungen des Längenausdehnungskoeffizienten  $\alpha$  und Wärmekapazität bei konstantem Druck  $C_p$  der CoCrFeNi und CrFeNi und CoCrNi Legierungen haben ein anomales Verhalten mit S-förmigen Kurven im Temperaturbereich von 700 – 950 K gezeigt. Die beobachtete Nichtlinearität tritt sowohl bei der ersten als auch bei der zweiten Erwärmung auf. Ein Minimum wird jedoch nur beim ersten Aufheizen beobachtet. Beim zweiten Aufheizen tritt ein steiler Anstieg von  $\alpha$  und  $C_p$  bei der Temperatur des erwärmten Minimums auf. Messungen des magnetischen Moments als Funktion der Temperatur zeigten, dass diese Anomalie nicht mit der Curie-Temperatur zusammenhängt. Die strukturelle und mikrostrukturelle Betrachtungen schließen eine Phasenumwandlung erster Ordnung oder Rekristallisation als mögliche Ursachen aus, zumindest für die CoCrFeNi und CoCrNi Legierungen. Basierend auf Literaturangaben wird angenommen, dass die Anomalien auf der Temperaturabhängigkeiten für den Längenausdehnungskoeffizient und Wärmekapazität durch einen chemischen Nahordnungsübergang verursacht werden können, der als K-Zustandseffekt bekannt ist. Die Ermittlung der genauen Natur dieses Phänomens erfordert jedoch weitere experimentelle und theoretische Untersuchungen, die außerhalb des Rahmens dieser Arbeit liegen.

## Chapter 1: Motivation and Fundamentals

### 1.1 Introduction

Since the dawn of time, the relationship between mankind and materials was essential for the advancement of civilization. Therefore, some periods of human history are classified from the materials discovered and used as tools for feeding, transportation, and housing. We lived through the Stone Age, the Bronze, and Iron Ages. Today, it is agreed to name it the Silicon Era, about the great advances in the electronics industry. Metals and alloys continue to be of great importance for human development; "traditionally, the utilization of native metals and artificial alloys from extractive elements is almost entirely based on one principal element or compound" [1], such as steels, or aluminum alloys. In the 1980's an increased interest in the design of alloys formed by multicomponent elements begun, and those advancements in research led to the development of bulk metallic glasses (BMGs), and more recently, the discovery of high-entropy alloys (HEAs).

Over the almost two decades since the introduction of HEAs intensive research has been carried out worldwide. It is agreed in the community that the field is reaching its 'teenage' stage, where many early concepts and theories could be proven to be correct or disregarded. Although the initial development of equiatomic multicomponent alloys was independently carried out by Cantor [2] and Yeh [3], it was in the article 'Nanostructured high-entropy alloys with multi-principal elements – novel alloy design concepts and outcomes' [4] where Yeh *et al.* first defined the term *high-entropy alloys*. They believed that the configurational entropy ( $S_{\text{config}}^{\text{SS,ideal}}$ ) of these multi-principal element alloys would stabilize single-phase solid solutions (SPSS) instead of competing intermetallic phases. A more detailed discussion about this topic will be given in section 1.2.

The early stage of development was centered on discovering new SPSS compositions and understanding their underlying thermodynamic, physical, chemical, and mechanical properties. As the field became more mature extensive research showed that multi-phase HEAs, including multiple solid solutions and/or a mixture of solid solutions and intermetallic compounds, could lead to more desirable mechanical and/or functional properties [5–7]. Following these advancements in the field, a new definition of *complex concentrated alloys* (CCAs) was proposed by Miracle and Senkov [8]; they aimed at exploring the vast compositional space of multi-principal element alloys, and not being restricted to equiatomic alloys or SPSSs. Nonetheless, the initial designation was too 'catchy', and it is now used in

the broader sense to define multi-principal element alloys. In this thesis, the terms HEAs and CCAs will be used interchangeably to designate multi-principal element alloys. Though the term HEAs will be preferred in the case of SPSSs as it is well established in the literature.

High-entropy alloys have attracted high attention of fundamental and applied science over the last decade as can be seen in the recent reviews of Senkov and Miracle [8], and George, Raabe, and Ritchie [9]. On the one hand, the research is focused on the basic principles of SPSS formation in alloys with multi-principal elements often having different crystal structures. On the other hand, it aims at understanding and tailoring their mechanical and functional properties and in the development of new advanced materials for various applications. It is common knowledge in metallurgy that tailoring the microstructure can improve an alloy's performance. Microstructural engineering can be done by numerous methods and technologies: alloy design, e.g., precipitation of a hard phase in a soft matrix, thermomechanical processing, e.g., grain refinement, or non-equilibrium solidification by rapid quenching from the liquid state. Recently, there has been a debate on whether if not all HEAs should be in a metastable state and that the SPSS structure is formed through rapid solidification from the liquid. This idea is corroborated by long-time annealing treatments that have shown phase separation to occur in most HEAs, at intermediate temperatures.

Along these lines, the investigation of rapid solidification of these materials allows for a clearer understanding of their phase stability/metastability and microstructure development upon non-equilibrium solidification. The study of the effects of rapid solidification on medium- (MEAs) and high-entropy alloys has been carried out only by conventional methods so far, e.g., copper-mold casting, melt spinning method, or gas-spray atomization. These techniques solely permit investigating phase and microstructure formation *postmortem*. *In situ* investigations of the solidification process, specifically non-equilibrium and containerless processing, have not yet received consideration in the high-entropy alloys field. The goal of this study is to understand phase selection, crystal growth kinetics, and microstructural evolution of multi-principal element alloys during non-equilibrium solidification. For this purpose, selected compositions of MEAs and HEAs were chosen for investigation during containerless processing using a mobile electromagnetic levitation (EML) facility.

EML [10] is a suitable experimental technique for the investigation of the non-equilibrium solidification of metal alloys. Large samples (mm-sized) can be processed in a highly purified atmosphere while the sample is levitating. This opens the possibility for different *in situ* measurements such as pyrometry, video imaging, and synchrotron X-ray

diffraction (XRD) [11]. Since the sample is containerlessly processed heterogeneous nucleation can be avoided or delayed so that it is possible to achieve some degree of liquid undercooling before crystallization. The simultaneous use of different measurement techniques enables obtaining a comprehensive picture of the solidification as well as for the phase transformations upon heating/cooling of the solid sample. A detailed description of the EML technique is given in Chapter 2: Experimental.

From high-speed video imaging analysis, it is possible to determine with reasonable accuracy the crystallization kinetics. To date, there are only a few available data in the literature related to crystal growth velocity of HEAs, and the results presented in Chapters 3, 4, and 5 may collaborate for a better understanding of phase transformations in this class of materials. Besides the determination of crystal kinetics, video imaging allows studying different phase selection pathways that may occur in undercooled liquid metals. This topic will be discussed in Chapter 3.

*In situ* X-ray diffraction studies using levitation techniques allow to determine time- and temperature-dependent phase transformations which are difficult to predict theoretically, because of their compositional complexity, and experimentally challenging to access due to the high melting temperatures. In this sense, the study of high-temperature transformations, notably crystallization from the liquid state, is made feasible using EML combined with synchrotron radiation sources. To date, the main investigation route in the field of HEAs relies on structural/microstructural post-processing analysis. Though they can provide valuable information they are not suitable techniques to completely describe phase transformations that may occur during cooling from the liquid state to room temperature.

This study mainly focused on the non-equilibrium solidification of *fcc*- and *bcc*-structured HEAs and MEAs. As the *fcc*-structured representatives, the equiatomic CoCrFeNi alloy, and its suballoys CrFeNi and CoCrNi MEAs were selected. Also, to study the effect of Al addition on the rapid solidification behaviour of the quaternary alloy mentioned above, the quinary Al<sub>0.3</sub>CoCrFeNi was investigated. As the representative of *bcc*-structured alloys, the equiatomic NbTiVZr composition was chosen. The reasons for choosing these specific compositions will be addressed later in the Introduction sections 3.1, 4.1, and 5.1, of the corresponding Chapter related to each alloy.

There have been considerable studies on non-equilibrium solidification in binary and ternary (dilute) alloys, however, there is extraordinarily little information on phase selection, crystal growth kinetics, and microstructural evolution regarding metastable solidification of multi-principal elements alloys. This also motivates this Thesis.

## 1.2 The high-entropy alloy (HEA) design concept

Before the introduction of HEAs, the design strategy of crystalline alloys was almost entirely based on the concept of alloying a base element with minor quantities of elements targeting to improve specific properties. A classic example is stainless-steels, where chromium is added to an iron base to enhance the corrosion resistance, while nickel is added to achieve better mechanical performance. Aluminum alloys with minor additions of copper are known since the early 1900s, where solid-solution strengthening and/or the formation of precipitates play a vital role to increase its specific strength. The introduction of HEAs disturbed this foundation in classical metallurgy by introducing the concept of alloys formed by multi-principal elements, meaning there is no base element, and it is not possible to distinguish between solvent and solute elements in a solution. Figure 1.1 shows an atomic body-centered cubic *bcc*-structure model of a completely random five-element equiatomic alloy. The model was generated by Monte Carlo simulation using the principle of maximum entropy (MaxEnt) [12] and each color represents a different atomic species.

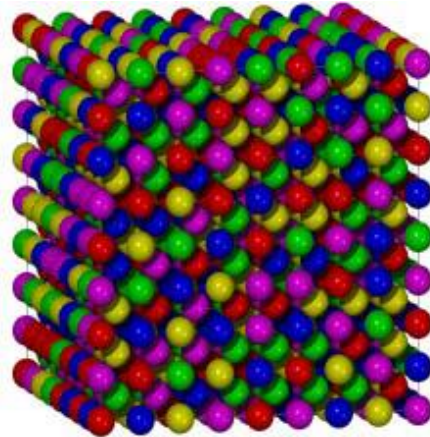


Figure 1.1. Atomic structure model of five-element *bcc* HEA phase by the MaxEnt method. Taken from [12].

As mentioned in section 1.1, HEAs were introduced by Yeh *et al.* [4] in 2004, they were defined as multicomponent alloys with (near)-equiatomic composition (5 - 35 at. %) containing at least 5 principal elements. The term “high-entropy” for these solid-solution-(ss)-type alloys refers to the configurational entropy for an ideal solution,  $S_{\text{config}}^{\text{SS,ideal}}$ , [13]:

$$S_{\text{config}}^{\text{SS,ideal}} = -nR \sum_{i=1}^N c_i \ln c_i \quad (\text{Eq. 1.1})$$

where  $R$  is the gas constant,  $8.31 \frac{J}{mol \cdot K}$ ,  $n$  is the amount of substance in moles,  $N$  is the number of components, and  $c_i$  is the molar fraction of component  $i$ . Because the  $S_{config}^{SS,ideal}$  generally increases with increasing  $N$  and is the highest for equiatomic compositions, it was initially suggested that the  $S_{config}^{SS,ideal}$  was the only thermodynamic property responsible for SPSS stability [4]. The contributions of vibrational, magnetic, and electronic entropies to the total entropy are regarded as negligible. Table 2.1 shows the calculated configurational entropies (Eq. 1.1) for some traditional alloys and also HEAs at their liquid state or complete random state [14]:

Table 1.1. Configurational entropies calculated for one mole of traditional alloys and high-entropy alloys at their liquid state or complete random state. Adapted from [14].

System	Alloy number, name, or composition in at. %	$S_{config}^{SS,ideal}$
Low-alloy steel	4340	$0.22 \cdot R$ low
Stainless steel	304	$0.96 \cdot R$ low
	316	$1.15 \cdot R$ medium
High-speed steel	M2	$0.73 \cdot R$ low
Mg alloy	AZ91D	$0.35 \cdot R$ low
Al alloy	2024	$0.29 \cdot R$ low
	7075	$0.43 \cdot R$ low
Cu alloy	7-3 brass	$0.61 \cdot R$ low
Ni-base superalloy	Hastelloy X	$1.31 \cdot R$ medium
	Inconel 718	$1.37 \cdot R$ medium
Co-base superalloy	Stellite 6	$1.13 \cdot R$ medium
Bulk metallic glass	$Cu_{47}Zr_{11}Ti_{134}Ni_{18}$	$1.17 \cdot R$ medium
	$Zr_{53}Ti_5Cu_{16}Ni_{10}Al_{16}$	$1.30 \cdot R$ medium
High-entropy alloy	$Co_{25}Cr_{25}Fe_{25}Ni_{25}$	$1.19 \cdot R$ medium
	$Co_{20}Cr_{20}Fe_{20}Ni_{20}Mn_{20}$	$1.61 \cdot R$ high

Yeh [14] suggested the value of  $1.5 \cdot R$  as the borderline between medium- and high-entropy alloys, and values lower than  $1 \cdot R$  for low-entropy alloys. He argued that a configurational entropy of  $1.5 \cdot R$  is large enough to compete with the mixing enthalpy, stabilizing solid solutions in these alloys. Today it is reasonable to consider 4 or more element alloys ([near]-

equiatomic) as HEAs and ternary alloys in equiatomic or near equiatomic compositions as MEAs [8].

Zhang *et al.* [15] contested that if the  $S_{\text{config}}^{\text{SS,ideal}}$  was the only parameter responsible for the phase stability in HEAs, then this would mean that: (i) the higher the number of elements in an alloy the greater the probability to form a SPSS is; (ii) alloys containing the same number of different elements would have the same probability to form a SPSS; (iii) the highest probability for equiatomic compositions to form a SPSS than non-equiatomic alloys with the same number of components.

Experimental results have shown that the simple stability rule based only on the  $S_{\text{config}}^{\text{SS,ideal}}$  is not enough to explain the phase formations in HEAs. For example, Otto *et al.* [16] prepared five equiatomic quinary alloys by replacing individual elements (Ti for Co, Mo or V for Cr, V for Fe, and Cu for Ni), one at a time, in the CoCrFeMnNi (Cantor) alloy, that was previously shown to have a SPSS structure at room temperature [2]. After three days of annealing at 1123 or 1273 K, all alloys except the Cantor alloy had a microstructure composed of multiple phases. This confirms that the above-mentioned statement (ii) of Zhang *et al.* [15] holds.

Just recently (2016), investigations of the effect of long-time annealing on the phase stability of HEAs begun. Pickering *et al.* [17] were the first to demonstrate phase separation to occur in the Cantor alloy, which up to that moment was considered a prototype of SPSS in the HEAs community. They observed decomposition of the solid solution into an *fcc* matrix and precipitates of the tetragonal Cr-rich sigma ( $\sigma$ ) phase, and  $M_{23}C_6$  carbides, after aging at 700 °C for 125, 250, 500, and 1000 hours followed by water quenching. Recently, Kube and Schroers [18] stated that the configurational entropy is “often insufficient to outweigh competing contributions such as lattice strain enthalpies, chemical mixing enthalpies ( $\Delta H_{\text{mix}}$ ), or structural mismatch of constituents all of which promote the formation of competing phases, in particular, intermetallics”. According to the authors, most SPSS HEAs, if not all, are metastable in nature and formed by quenching from elevated temperature phases. They proposed the critical cooling rate of SPSS formation  $R_C^{\text{SPSS}}$  as a universal parameter to quantitatively describe the degree of metastability of HEAs.

### 1.3 Empirical rules of phase formation for HEAs

Up to this point only the role of the  $S_{\text{config}}^{\text{SS,ideal}}$  in phase stability was discussed. Over the last ten years, many empirical rules were proposed that aimed at predicting SPSS



formation in multi-principal element alloys. A summary of the ability of some of these rules will be addressed below. Also, an empirical rule based on a theoretical elastic-strain energy criterion [19] proposed by the author of this thesis and contributors will be described in this section.

Senkov and Miracle [20] pointed out the importance of the enthalpy of mixing of the intermetallic (IM) phases,  $\Delta H_{mix}^{IM}$ , competing with the SPSS. The authors state that the conditions to suppress an IM phase and to obtain SPSS microstructures are given as:

$$k_1^{cr}(T) > \Delta H_{mix}^{IM} / \Delta H_{mix}^{SS} \quad (\text{Eq. 1.2})$$

where  $k_1^{cr}(T)$  is a critical value at a given temperature,  $T$ , computed as:

$$k_1^{cr}(T) = \frac{T\Delta S_{mix}}{|\Delta H_{mix}|(1-k_2)} + 1 \quad (\text{Eq. 1.3})$$

$$k_2 = \Delta S_{IM} / \Delta S_{mix} \quad (\text{Eq. 1.4})$$

where  $\Delta S_{IM}$  is the mixing entropy of the IM phase, and  $\Delta S_{mix}$  the mixing entropy of the ideal random SS phase. The  $\left[ k_1^{cr}(T) \text{ vs. } \frac{\Delta H_{IM}}{\Delta H_{mix}} \right]$  plot was used as a criterion to separate IMs and SPSS alloys. The criterion of Senkov and Miracle [20] works reasonably well despite that some IM-containing alloys overlap the region delimited as SPSS. Furthermore, they do not discuss which IM phases are being correctly predicted and for which ones the method fails to forecast.

Zhang *et al.* [21,22] studied the relationship between the enthalpy of mixing,  $\Delta H_{mix}$  (Eq. 1.5), and the atomic-size mismatch,  $\delta$  (Eq. 1.6), and concluded that SPSSs would form for  $-15 \leq \Delta H_{mix} \leq 5 \text{ kJ mol}^{-1}$  and  $1 \leq \delta \leq 6 \%$ . The mixing enthalpy of a solution of two elements can be estimated using Miedema's model, as in Ref. [23]. Then, the enthalpy of mixing for an  $N$ -component solid solution can be estimated as follows:

$$\Delta H_{mix} = \sum_{i,j \ i \neq j}^N c_i c_j \Omega_{ij} \quad (\text{Eq. 1.5})$$

where  $\Omega_{ij} = 4\Delta H_{mix}^{ij}$ ,  $c_i$  the atomic fraction of the element,  $i$ , and  $H_{mix}^{ij}$  is the mixing enthalpy of the binary liquid alloy. The atomic-size mismatch is calculated as follows:

$$\delta = 100 \sqrt{\sum_{i=1}^N c_i \left(1 - \frac{r_i}{\bar{r}}\right)^2}, \bar{r} = \sum_{i=1}^N c_i r_i \quad (\text{Eq. 1.6})$$

where  $c_i$  and  $r_i$  are the atomic fraction and atomic radius of the element  $i$ , respectively.

Following the Hume-Rothery theory for solid solutions, Guo *et al.* [24] proposed a criterion for the formation of *fcc* and *bcc* crystal structures based on the valence electron concentration (*VEC*);

$$VEC = \sum_{i=1}^N c_i (VEC) \quad (\text{Eq. 1.7})$$

according to this criterion, *fcc* crystal structures are formed when  $VEC \geq 8$ , and *bcc* structures are formed when  $VEC < 6.7$ .

According to López and Alonso [25], one of the contributions to the enthalpy of formation  $H$  of a substitutional metallic solid solution is the elastic energy due to the atomic-size mismatch between solutes and solvents. As stated in Ref [26], in systems where the atomic-size mismatch is considerable, the quasichemical model, which assumes that the volume of the elements are the same and do not change upon mixing, will underestimate the change in the internal energy on mixing because no account is taken of the elastic-strain fields, which introduce a strain energy term into  $\Delta H_{\text{mix}}$ . When the size difference is large enough this effect can prevail over the chemical term [26].

Toda-Caraballo and Rivera-Díaz-Del-Castillo [27] introduced two empirical parameters for predicting the phase formation of CCAs based on the lattice distortion: the interatomic spacing mismatch,  $s_m$ , and the bulk modulus mismatch,  $K_m$  (see Ref. [27] for equations). These parameters were plotted as functions of the  $\Delta H_{\text{mix}}, \chi, \Omega = \frac{TS_{\text{mix}}^{\text{ideal}}}{|H_{\text{mix}}|}$  [28], and  $\mu = \frac{T_m}{T_{\text{SC}}}$  [29], where  $T$ ,  $T_m$ , and  $T_{\text{SC}}$  are the absolute temperature, melting temperature, and spinodal-decomposition temperature, respectively.  $\chi$  is a criterion based on Pauling's electronegativity difference among constituent elements [30]. This method showed a good ability to separate SPSSs from duplex phase alloys (e.g., *bcc + fcc*), ss + IM phases, and bulk metallic glasses (BMGs) from SPSSs, although a complex methodology was used to achieve the results.

Ye *et al.* [31] developed a general self-contained geometrical model to compute the intrinsically-residual strains due to different atomic-size elements in CCAs, which takes into account the atomic size, atomic fraction, and packing efficiency. They showed that a

transition from *SPSS* to multi-phase microstructures occurs when the root mean square (RMS) of the residual strain approaches  $\sim 5\%$ . However, this methodology is not as straightforward, compared to the approach proposed in the present thesis.

Melnick and Soolshenk [32] argued that the lattice elastic-strain energy ( $\Delta H_{el}$ ) derived from the atomic-size mismatch, inherent to CCAs, should be considered to calculate the Gibbs free energy,  $G$ , see Eqs. (1.8 – 1.10):

$$G = \Delta H_{mix} + \Delta H_{el} - TS \quad (\text{Eq. 1.8})$$

$$\Delta H_{el} = \sum_1^N c_i B_i \frac{(V_i - V)^2}{2V_i} \quad (\text{Eq. 1.9})$$

$$V = \frac{\sum_{i=1}^N c_i B_i V_i}{\sum_{i=1}^N c_i B_i} \quad (\text{Eq. 1.10})$$

here,  $B_i$  is the bulk modulus of the element  $i$ ,  $V_i$  is the atomic volume of the element  $i$ .

Melnick and Soolshenk [32] have not investigated the effect of the  $\Delta H_{el}$  itself on phase stability. Therefore, the effect of the lattice elastic-strain energy on the phase stability of CCAs was studied at the beginning of the present Ph.D. work. The results have been published in Ref. [19]. The  $\Delta H_{el}$  is calculated with Eq. 1.9 for 235 different alloys of the 3d-transition metal CCAs family, refractory CCAs family, and bulk metallic glasses (BMGs) (some are regarded as amorphous CCAs) and are given in Table A1 in Appendix 1. The local atomic volumes and bulk moduli for solid solutions are considered equal to the values for one-component systems. The elastic-strain energies are calculated for room temperature  $T_0$  since all phases described in the references are at room temperature. The values of atomic radii are taken from Ref. [8],  $B_i$  are taken from Ref. [33]. References [27,34] are used as databases for the calculated values of  $\delta$ ,  $\Delta H_{mix}$ , and  $VEC$ . Then, plots for  $\Delta H_{el}$  vs.  $\Delta H_{mix}$ ,  $\Delta H_{el}$  vs.  $VEC$ ,  $\delta$  vs.  $VEC$ , are produced to evaluate their abilities to correctly forecast the resulting microstructures of 235 known CCAs from the literature. The *SPSS* regions in these plots are defined as tangent lines to the outermost *SPSS* alloys confined in these areas.

The  $\Delta H_{el}$  vs.  $\Delta H_{mix}$  plot is exhibited in Figure 1.2. An *fcc* *SPSS* populated region lies in the range of  $0 < \Delta H_{el} \leq 6.89 \text{ kJ mol}^{-1}$  and  $-10.7 \leq \Delta H_{mix} \leq 3.9 \text{ kJ mol}^{-1}$ ; the latter condition for the *fcc* *SPSS*s formation was already reported by Zhang and Zhou [21]. The *bcc* *SPSS*s, unlike the *fcc* *SPSS*s, are spread in a broader range of  $\Delta H_{el}$  and  $\delta$ , and they

overlap with the duplex alloys, IMs, *fcc* + *bcc* + IMs, *bcc* + IMs, and *fcc* + IMs microstructures. Six crystalline alloys (5 single-phase IMs and one alloy with a mixture of ss and IM phases) lie in the BMGs region.

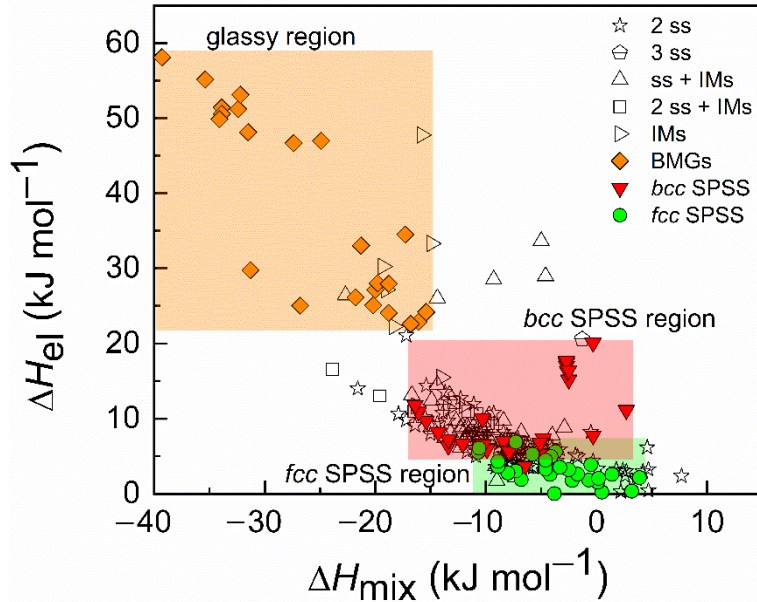


Figure 1.2. The  $\Delta H_{el}$  vs.  $\Delta H_{mix}$  criterion for the 235 complex concentrated alloys and bulk metallic glasses given in Table A1 in Appendix 1 (SPSS – single-phase solid solution, ss – solid solution, IMs – intermetallics).

The  $\Delta H_{el}$  vs.  $\Delta H_{mix}$  criterion may work reasonably well to distinguish the *fcc* SPSSs within different microstructures, but it clearly cannot separate the *bcc* ones. The  $\Delta H_{mix}$  of the *bcc* SPSSs studied ranges from  $-16.4$  to  $2.7$   $\text{kJ mol}^{-1}$  (Table A1 in Appendix 1) which overlaps with the enthalpy of formation for other phases, including IMs and BMGs. The criterion may work reasonably well to distinguish the *fcc* SPSS region especially for the compositions that tend to ideal solid solutions for the range of  $-5 \leq \Delta H_{mix} \leq 5$   $\text{kJ mol}^{-1}$ .

From the 22 alloys with the duplex microstructures (e.g., *fcc* + *bcc*, or *fcc* + *fcc*) that share the common region with the *fcc* SPSS alloys (Fig. 1.2), 13 have positive values of  $\Delta H_{mix}$  and all 22 have Cu as a constituent element. Copper is known to have a high positive  $\Delta H_{mix}$  with some transition metals in binary solutions. This leads to the atoms organizing in A-A and B-B rather than A-B arrangements and will mostly result in segregation and phase separation. This can explain why these alloys have low values of  $\Delta H_{el}$  but phase separation occurs. As shown by Otto *et al.* [16], the phase formation in higher-order multicomponent alloys is consistent with a minimization of the total Gibbs free energy, with contributions of

both enthalpy and entropy. They suggest that the binary  $\Delta H_{mix}$  of the constituent elements will also play a key role in the formation of SPSS or a compound in CCAs.

The *bcc* SPSS populated region is clearly defined in Fig. 1.3, unlike in Fig. 1.2, in the range of  $3.59 \leq \Delta H_{el} \leq 20.08 \text{ kJ mol}^{-1}$  and  $4.40 \leq VEC \leq 6.2$ . From the 28 CCAs with the *bcc* SPSS microstructure in Table A1 in Appendix 1, 16 (57.1 %) lie in this region. In the *bcc* SPSS region, 1 alloy containing an IM phase stands, representing 1.3% for these alloys, without any duplex alloys overlap. The remaining *bcc* SPSS alloys overlap with other microstructures in the range of  $6.5 \leq VEC \leq 7.5$ . Considering all 56 SS alloys, including both *fcc* and *bcc* alloys, 44 of them fit the limits of  $\Delta H_{el}$  vs. *VEC* for the *bcc* and *fcc* SPSS microstructures. This trend means that 78.6 % of all the SPSS alloys belong to the SPSS regions highlighted in Fig. 1.3. Twenty-two *fcc* + *bcc*, or *fcc* + *fcc* (80 alloys from Table A1 in Appendix 1) duplex microstructures and six alloys containing IM phases (74 in total) overlap with the *fcc* SPSS region, yielding 27.5 % and 8.1 %, respectively. When all microstructures, except the SPSS (179 alloys in Table A1 in Appendix 1), are considered then 16.2 % of all these alloys overlap with the SPSS regions (delimited in Fig. 1.3). When only the IM-phase-containing alloys are considered then 9.5 % overlap with the SPSS regions is found.

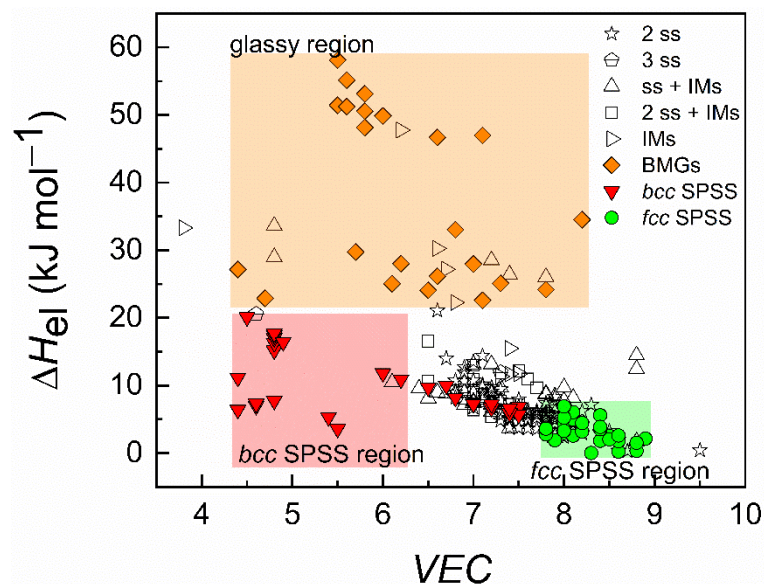


Figure 1.3. The  $\Delta H_{el}$  vs. *VEC* criterion for the 235 complex concentrated alloys and bulk metallic glasses in Table A1 in Appendix 1 (SPSS – single-phase solid solution, ss – solid solution, IMs – intermetallics).

Following what Guo *et al.* [24] proposed, the *VEC* criterion can separate *fcc* and *bcc* SPSS alloys for CCAs. All the evaluated *bcc* SPSS alloys have *VEC* lower than 7.5, while all the *fcc* SPSS alloys have *VEC* higher than 7.8. From the 28 alloys with the *fcc* SPSS microstructure listed in Table A1 in Appendix 1, 86 % of them obey the range proposed by Guo *et al.* [24]. For the *bcc* SPSS alloys, 79% of them follow the range proposed. The  $\Delta H_{el}$  vs. *VEC* criterion (Fig. 1.3) shows a plausible ability to distinguish SPSS alloys from all different microstructures described in the literature for CCAs.

It should also be noted that the *bcc* SPSS may also form for low values of  $\Delta H_{el}$ , for example, the MoNbTaW and MoNbTaVW alloys have  $\Delta H_{el} = 3.59 \text{ kJ mol}^{-1}$  and  $5.31 \text{ kJ mol}^{-1}$ , respectively. These values are comparable with those for the *fcc* SPSS. All the constituent elements of the MoNbTaW and MoNbTaVW alloys have the *bcc* A2 structure at  $T_m$  and  $T_0$ . Therefore, it is not surprising that these CCAs precipitate with the same crystal structure characteristic of the constituent elements, in what Miracle and Senkov [8] defined as the “structure in – structure out” correlations (SISO). The SISO analysis takes into account the crystal structure of the element being used to design an alloy, and it develops the Hume-Rothery concept of the link between the crystal structure of an extended SPSS and the crystal structures of the constituent elements. Therefore, the SISO correlations should also be considered in the CCAs design.

Two SPSS regions are distinguishable in Fig. 1.4 in agreement with the  $\Delta H_{el}$  vs. *VEC* criterion (Fig. 1.3). In total, 18 alloys with duplex microstructures and 10 IM-containing alloys overlap with the *fcc* SPSS region, which yields 22.5 % and 11.5 % of these microstructures, respectively. The criterion can correctly predict 40 % less in the number of alloys with IM phases than the  $\Delta H_{el}$  vs. *VEC* criterion (Fig. 1.3). When the *bcc* SPSS region is investigated, 1 alloy with a mixture of ss and IM phases and none of the duplex alloys are found. The comparison of the two criteria for the prediction of the *fcc* SPSS region is shown for the  $\delta$  vs. *VEC* criterion in Fig. 1.5a and the  $\Delta H_{el}$  vs. *VEC* criterion in Fig. 1.5b. A clear shift can be seen for some IM-containing alloys to the outside of the *fcc* SPSS region in Fig. 1.5b.

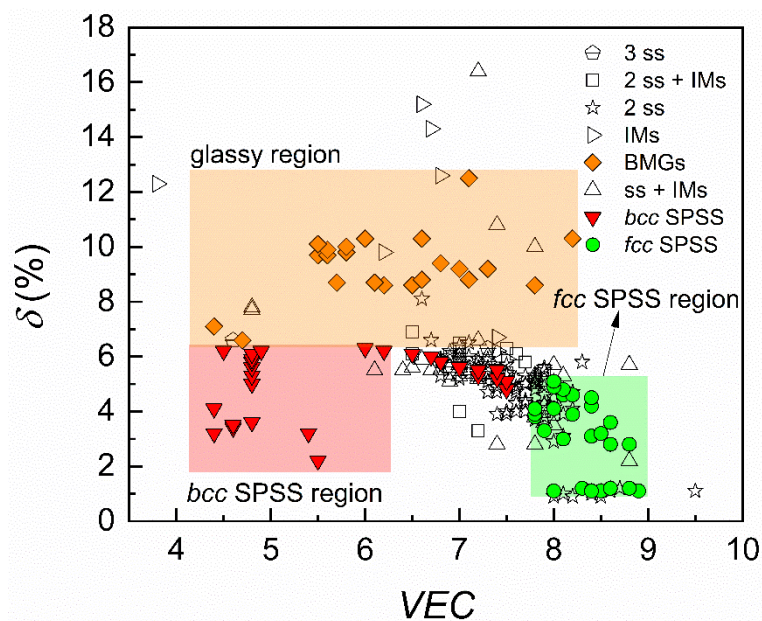


Fig. 1.4. The  $\delta$  vs. VEC criterion for the 235 complex concentrated alloys and bulk metallic glasses given in Table A1 in Appendix 1 (SPSS –single–phase solid solution, ss –solid solution, IMs – intermetallics).

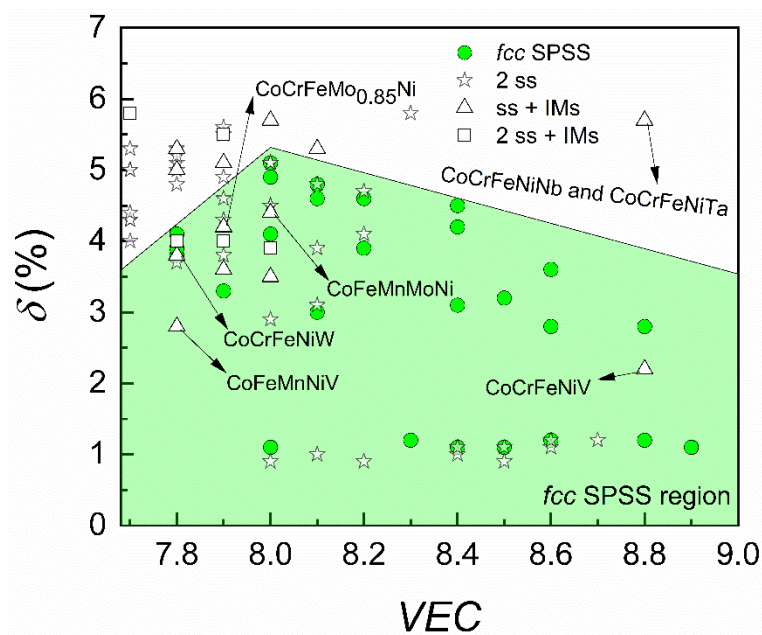


Fig. 1.5a. The ability of two criteria (a)  $\delta$  vs. VEC and (b)  $\Delta H_{el}$  vs. VEC to correctly predict the phase formation of some intermetallic alloys that overlap with the *fcc* single-phase solid-solution regions in Figs. 1.3 and 1.4, respectively.



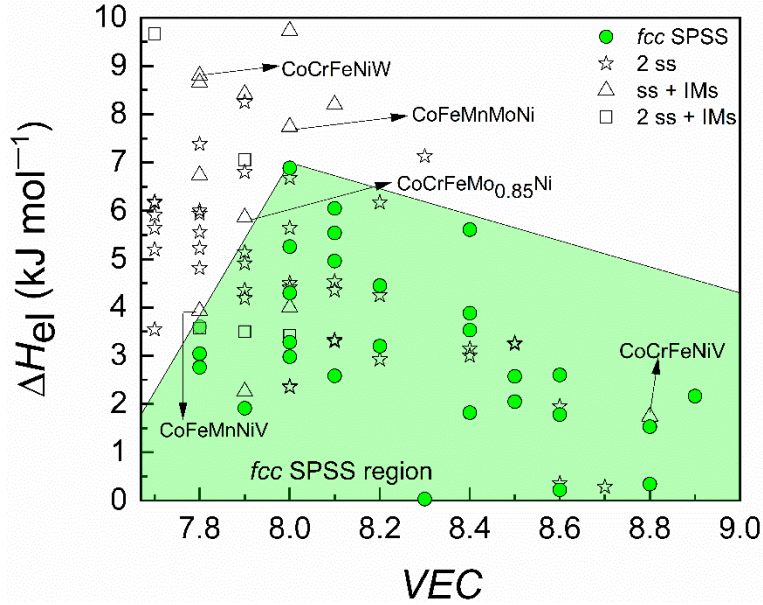


Fig. 1.5b. The ability of two criteria (a)  $\delta$  vs.  $VEC$  and (b)  $\langle \Delta H_{el} \rangle$  vs.  $VEC$  to correctly predict the phase formation of some intermetallic alloys that overlap with the  $fcc$  single-phase solid-solution regions in Figs. 1.3 and 1.4, respectively.

At this point, let us explore the prediction capability of the  $\Delta H_{el}$  parameter by considering the 6 alloys with a mixture of ss and IM phases that overlap with the  $fcc$  SPSS region delimited in Fig. 1.3. Of these 6 alloys, 5 of them exhibit a mixture of a ss phase, and the sigma phase,  $\sigma$ , usually found in low volume fractions in interdendritic regions and grain boundaries [16]. These 5 alloys are CoCrFeNiV, CoCrFeMo<sub>0.5</sub>Ni, Al<sub>0.5</sub>CoCrCuFeNiV, Al<sub>0.5</sub>CoCrCuFeNi<sub>0.6</sub>, and Al<sub>0.5</sub>CoCrCuFeNiV<sub>0.8</sub>. Four of these alloys contain V, 2 alloys have V as a minor addition, and 2 alloys contain the equimolar concentration. Vanadium is known to extend the  $\sigma$  phase stability in alloys containing Co, Mn, and Fe, and it is the only element to form the  $\sigma$  phase when combined with Ni. "Among the intermetallic phases, it is probably the phase having the broadest range of existence among the different systems" [35]. This seems reasonable to explain why the  $\sigma$  phase forms in these alloys. However, it does not give any insight into how to correctly predict and avoid the precipitation of the  $\sigma$  phase. The remaining Al<sub>0.3</sub>CoCrFeNi alloy shows a different intermetallic phase and the microstructure is composed of  $fcc$  ss and L1<sub>2</sub> phase [36].

Table A1 in Appendix 1 contains 34 alloys with the  $\sigma$  phase. Regarding the elements that are prone to form this phase, 32 alloys contain Cr, 5 alloys contain Ti, 6 alloys contain V, and 23 alloys have Mo. Molybdenum is one of the alloying elements exhibiting the  $\sigma$  phase formation for the largest number of binary systems [35]. Tsai *et al.* [37] proposed an empirical method using the  $VEC$  alone to predict the formation range of the  $\sigma$  phase in CCAs.



They suggested that alloys were prone to the precipitation of the  $\sigma$  phase when  $VEC$  is between 6.88 and 7.84, and the method works well for Cr- and V-containing alloys. Eight of the alloys listed in Table A1 in Appendix 1 (24%), that form the  $\sigma$  phase, fall outside the range in  $VEC$ . All eight alloys contain Cr, 3 of them have V, and 5 contain Mo. This suggests that care must be taken when using this criterion to predict SPSS HEAs, which is demonstrated in Table 1.2 (the table shows the outcome of different criteria to predict the phase formation for the IM alloys overlapping with the SS regions) and Fig. 1.5. From the 6 alloys that contain V and form the  $\sigma$  phase, 5 alloys are incorrectly predicted with the  $\delta$  vs.  $VEC$  criterion (Fig. 1.5a and Table 1.2), and 4 alloys are wrongly predicted with the  $\Delta H_{el}$  vs.  $VEC$  criterion (Fig. 1.5b and Table 1.2).

Table 1.2. The compositions (in molar fraction), microstructures, and the prediction outcomes using 5 different criteria:  $\delta$  vs.  $\Delta H_{mix}$ ;  $\Delta H_{mix}$  vs.  $VEC$ ;  $\Delta H_{el}$  vs.  $\Delta H_{mix}$ ;  $\delta$  vs.  $VEC$ ; and  $\Delta H_{el}$  vs.  $VEC$  for the intermetallic alloys that overlap with the single-phase solid-solution regions for these criteria (L – Laves phase;  $\sigma$  – sigma phase;  $\mu$  – mu phase).

Composition	Phases	Ref.	$\delta$ vs. $\Delta H_{mix}$	$\Delta H_{mix}$ vs. $VEC$	$\Delta H_{el}$ vs. $\Delta H_{mix}$	$\delta$ vs. $VEC$	$\Delta H_{el}$ vs. $VEC$
Outcome							
Al <sub>0.5</sub> CoCrCuFeNiV	$fcc + bcc + \sigma$	[38]	Failed	Failed	Failed	Failed	Failed
Al <sub>0.3</sub> CoCrFeNi	$fcc + L$	[36]	Failed	Failed	Failed	Failed	Failed
Al <sub>0.5</sub> CoCrCuFeNiV <sub>0.8</sub>	$fcc + bcc + \sigma$	[38]	Failed	Failed	Failed	Failed	Failed
CoCrFeMo <sub>0.5</sub> Ni	$fcc + \sigma$	[39]	Failed	Failed	Failed	Failed	Failed
Al <sub>0.5</sub> CoCrCuFeNiV <sub>0.6</sub>	$fcc + bcc + \sigma$	[38]	Failed	Failed	Failed	Failed	Failed
CoCrFeNiV	$fcc + \sigma$	[34]	Failed	Failed	Failed	Failed	Failed
CoFeMnNiV	$fcc + \sigma$	[16]	Failed	Failed	Failed	Failed	Succeeded
CoCrFeMo <sub>0.85</sub> Ni	$fcc + \sigma + \mu$	[39]	Failed	Failed	Failed	Failed	Succeeded
CoCrFeNiW	$fcc + \mu$	[34]	Failed	Failed	Succeeded	Failed	Succeeded
CoFeMnMoNi	$fcc + \mu$	[16]	Failed	Failed	Succeeded	Failed	Succeeded
AlCoCrFe <sub>2</sub> Mo <sub>0.5</sub> Ni	$bcc + \sigma$	[40]	Failed	Succeeded	Failed	Succeeded	Succeeded
Al <sub>0.5</sub> CrFe <sub>1.5</sub> MnNi <sub>0.5</sub>	$bcc + fcc + B2$	[41]	Failed	Succeeded	Failed	Succeeded	Succeeded
Al <sub>0.3</sub> CrFe <sub>1.5</sub> MnNi <sub>0.5</sub>	$bcc + fcc + B2$	[41]	Failed	Succeeded	Failed	Succeeded	Succeeded
CoCrCuFeNiTi	$fcc + L$	[42]	Succeeded	Failed	Succeeded	Succeeded	Succeeded
CoCrCuFeNiTi <sub>0.8</sub>	$fcc + L$	[42]	Succeeded	Failed	Succeeded	Succeeded	Succeeded
Co <sub>1.5</sub> CrFeMo <sub>0.8</sub> Ni <sub>1.5</sub> Ti <sub>0.5</sub>	$fcc + \sigma$	[43]	Failed	Failed	Succeeded	Succeeded	Succeeded
AlCoCu <sub>0.33</sub> FeNi	$fcc + fcc + B2$	[44]	Succeeded	Failed	Failed	Succeeded	Succeeded
CoCrMnNiV	$fcc + \sigma$	[16]	Failed	Succeeded	Failed	Succeeded	Succeeded

It can be concluded that for CCAs of the 3d transition metals family, V and Mo may lead (depending on the alloying elements and the overall composition) to the formation of the  $\sigma$

phase and that the prediction of the  $\sigma$ -IM phase for V-containing alloys is somewhat difficult. The reasons for this are discussed in the following paragraphs.

Tsai *et al.* [34] examined the predicting quality for the phase formation using five different criteria available, with variable terms. The CoCrFeNiX (X = Y, Ti, Zr, Hf, V, Nb, Ta, Cr, Mo, and W) alloys were used as the master composition for the comparison. The empirical methods and the SPSS-forming conditions are summarized in Table 2.3. Inclusive of the common rules for  $\Delta H_{mix}$  (Eq. 1.5),  $\delta$  (Eq. 1.6), and  $\Omega_T$ , introduced previously, additional parameters are defined as: [45–47]:

$$\gamma = \frac{\omega_S}{\omega_L} \quad (\text{Eq. 1.11}) [45]$$

$$\omega_L = 1 - \sqrt{\frac{(r_{S+\bar{r}})^2 - \bar{r}^2}{(r_{S+\bar{r}})^2}} \quad (\text{Eq. 1.12}) [45]$$

$$\omega_S = 1 - \sqrt{\frac{(r_{L+\bar{r}})^2 - \bar{r}^2}{(r_{L+\bar{r}})^2}} \quad (\text{Eq. 1.13}) [45]$$

$$\Lambda = \frac{\Delta S_{mix}^{ss,ideal}}{\delta^2} \quad (\text{Eq. 1.14}) [46]$$

$$\phi = \frac{S_c - S_H}{S_E} \quad (\text{Eq. 1.15}) [47]$$

Here,  $r_S$  and  $r_L$  are the radii of the smallest and largest atoms in a multicomponent metallic mixture, respectively. The  $S_c$  denotes the configurational entropy of mixing for an ideal gas, and the  $S_E$  is the excess entropy of mixing which is the function of atomic packing and atom size. The  $S_H = |\Delta H_{mix}/T_m|$  is defined as complementary entropy. The results by Tsai *et al.* [34] revealed that 4 criteria, unlike the present work, consistently fail to correctly predict at least the phase formation for the alloys with X = V, Mo, and W; these form the *fcc* +  $\sigma$  phases for X = V and Mo and *fcc* +  $\mu$  phases for the X = W alloy (Table 1.3). All five methods are unable to correctly predict at least for the alloys with X = V and Mo (Table 1.3). In the present work, the results show that only for the alloy with X = V, it is not possible to separate the *fcc* SPSS region using the  $\Delta H_{el}$  vs. *VEC* criterion (Fig. 1.5b and Table 1.3). The  $\Delta H_{el}$  vs. *VEC* criterion has a greater ability to predict alloys with IM phases, compared with the 5 existing empirical models [34], in particular for alloys that form the  $\mu$  phase (Table 1.2). For the  $\sigma$  phase, when Mo is the element leading to its formation, it was also possible to correctly predict the phase formation (Table A1 in Appendix 1, alloys highlighted in blue).

Table 1.3. The single-phase solid-solution (SPSS) forming conditions and the prediction outcomes for five different approaches, summarized by Tsai *et al.* [34]. The SPSS-forming conditions applied to the  $\Delta H_{el}$  vs.  $VEC$  criterion and the prediction outcomes for the CoCrFeNiX (X = Y, Ti, Zr, Hf, V, Nb, Ta, Cr, Mo, and W) alloys.

Ref.	SPSS-forming conditions	Incorrect predictions
[48]	$-11.6 \leq \Delta H_{mix} \leq 3.2 \text{ kJ mol}^{-1}$ , $\delta < 6.6\%$	X = V, Mo, W
[45]	$-11.6 \leq \Delta H_{mix} \leq 3.2 \text{ kJ mol}^{-1}$ , $\gamma < 1.175$	X = V, Mo, W
[28]	$\Omega \geq 1.1$ , $\delta \leq 6.6\%$	X = V, Nb, Ta, Mo, W
[46]	$A > 0.96 \text{ J K} \cdot \text{mol}^{-1}$	X = V, Mo
[47]	$\Phi > 20$	X = V, Mo, W
This thesis	<i>fcc</i> SPSS: $0 \leq \Delta H_{el} \leq 6.8 \text{ kJ mol}^{-1}$ , $VEC \geq 8$	X = V
This thesis	<i>bcc</i> SPSS: $3.59 \leq \Delta H_{el} \leq 20.08 \text{ kJ mol}^{-1}$ , $4 \leq VEC \leq 6.2$	X = $\emptyset$

Tsai *et al.* [41] argued that the failure of the well-established methods to correctly predict the regions of the formation of SPSSs and IMs is because they consider SPSSs formation only when the  $\Delta H_{mix}$  is near zero and  $\delta$  of the constituent elements is small  $< 6.6\%$ . However, IM phases can also form with the near-zero mixing enthalpy and for the small atomic-size difference. This is the case of the  $\sigma$  and  $\mu$  phases. One may notice that only the CoCrFeNiV (*fcc* +  $\sigma$  phases) alloy overlaps with the *fcc* SPSS region in Fig. 1.5b, and 2 alloys overlap with the *fcc* SPSS region when the  $\delta$  criterion is considered in Fig. 1.5a. These are the CoCrFeNiV and CoCrFeNiW alloys with microstructures of *fcc* +  $\sigma$  phases and *fcc* +  $\mu$  phases, respectively. The  $\mu$  phase is topologically close-packed and has a rhombohedral lattice crystal structure. The phase has been reported for many Ni- and Co-based systems [49]. In Table A1 in Appendix 1, 3 alloys form the  $\mu$  phase. These are the CoCrFeMo<sub>0.85</sub>Ni [39], CoCrFeNiW [34], and CoFeMnMoNi [16] alloys (highlighted in green in Table A1 in Appendix 1). When the  $\delta$  vs.  $VEC$  criterion is applied, all the alloys are predicted to be *fcc* SPSSs which does not correspond to their real microstructures (Table 1.2 and Fig. 1.5a). On the other hand, when the  $\Delta H_{el}$  vs.  $VEC$  criterion is applied, all three alloys are shifted outside of the *fcc* SPSS region (Table 1.2 and Fig. 1.5b). It is tempted to assume that the  $\delta$  vs.  $VEC$  criterion could flawlessly predict the alloys that precipitate the  $\mu$  phase. However, there are not enough alloys published in the literature to date to fully verify it.

The reason that it is possible to correctly predict the formation of the  $\mu$  phase using the  $\Delta H_{el}$  parameter is that the bulk modulus of both Mo and W is typically much higher than for the other constituent elements in these alloys. Therefore, when computing the  $\Delta H_{el}$ , the

bulk modulus has a more pronounced effect contrary to  $\delta$ . The atomic radii of Mo and W do not differ greatly from the other elements in these alloys. The same applies when predicting alloys that form the  $\sigma$  phase by adding Mo. This can be seen for the highlighted alloys in blue in Table A1 in Appendix 1. However, when the V-containing alloys forming the  $\sigma$  phase are considered, neither the bulk modulus nor atomic radius of V differs greatly from the other elements. For this reason, both  $\delta$  vs.  $VEC$  and  $\Delta H_{el}$  vs.  $VEC$  criteria fail to correctly predict the microstructures despite that the  $\Delta H_{el}$  parameter has an overall better performance (Table 1.2).

#### 1.4 Calculation of phase diagrams of HEAs

The calculation of the phase diagrams method (CALPHAD) has had significant success in the design of new alloys, especially in binary and ternary systems, by predicting the phase equilibria and the thermodynamic properties. However, HEAs impose a challenge for the correct prediction of phase equilibria and optimization of CALPHAD databases due to their inherent compositional complexity.

Dedicated databases for HEAs (e.g., TCHEA1 [50]) rely on the extrapolation of binary and ternary descriptions (when available) to predict phase equilibria for ‘higher order’ alloys. It is assumed that the extrapolation is reliable because "the probability of the occurrence of quaternary or higher-order intermetallic phases is low and decreases rapidly with an increase in the number of components", according to Gorsse and Senkov [51]. The challenge relies on the fact that not all binary and ternary thermodynamic descriptions are complete even for the most advanced databases known today. For example, Ref. [51] reports that the TCHEA3 database, which includes 26 elements and can form 325 binary and 2600 ternary systems, lacks the complete description in the full composition and temperature range, for 31 binary and 2464 ternary systems.

Bracq *et al.* [52] have used an experimental and theoretical approach (CALPHAD) to investigate the *fcc* SPSS stability in the Co-Cr-Fe-Mn-Ni system. They constructed 10,626 phase diagrams using the TCHEA1 database and compared them to phase formation in 11 alloys, corresponding to 8 different compositions and 2 temperatures, which were cast and annealed at 1273 and/or 1373 K for 6 days. Among the 11 alloys, 5 were predicted to be a *fcc*-SPSS at the corresponding temperature by CALPHAD. From those 5 only 3 alloys were experimentally proven to be a *fcc* solid solution using XRD and SEM analysis. One alloy (in the Co-rich section) which was predicted to be a *fcc*-SPSS showed a dual-phase *fcc* and  $\epsilon$  hexagonal closed-packed (*hcp*) structure and was explained by an allotropic

transformation that occurs in Co. The authors stated that the martensitic-like transformation occurred during cooling and that at 1373 K the alloy should be a *fcc* SPSS, as predicted. For the other wrongfully predicted alloy (in the Mn-rich section) it was demonstrated to be a  $\beta$ -Mn SPSS while calculations predicted a *fcc*-SPSS, indicating that the *fcc* stability range is overestimated.

The other 6 alloys were correctly predicted to be dual-phase by CALPHAD, nonetheless, there were discrepancies between the phases experimentally determined and those predicted. For instance, the  $\text{Co}_{14.5}\text{Cr}_{42}\text{Fe}_{14.5}\text{Mn}_{14.5}\text{Ni}_{14.5}$  (at. %) alloy is predicted to form *fcc* + *bcc* phases below the solidus  $T_s$  and that the  $\sigma$  phase should precipitate below 814 K. The  $\sigma$  phase was identified in the alloy annealed at 1273 K. The authors concluded that the TCHEA1 database is accurate to describe the compositional space where the *fcc* solid solution is present for this system, however, the stability of the  $\sigma$  phase is underestimated, which results in a wrongful description of multi-phased HEAs.

Gorsse and Senkov [51] assessed the reliability of extrapolation of the binary and ternary data using the HEAs dedicated database TCHEA3 for quaternary systems. One of the investigated systems was Co-Cr-Fe-Ni. To achieve their goal, they started with a quaternary system that had a full description of all binary and ternary thermodynamic data (named FAT1) and considered this the case where the prediction was 100 % correct. Then they artificially excluded from the calculation all ternary interaction parameters (named FAT0) and compared the extent of the compositional range of each phase throughout the 3D composition space as a comparison metric (see Fig 1.6). In the latter case, FAT0, the results are exclusively obtained from the extrapolation of the 6 binary interactions. Their results showed that there is no significant difference (98 % match) between the phase equilibria and locations of the phase boundaries (solubility limits) delimiting the SPSS regions in both cases (Fig. 1.6). This suggests that the predictions of SPSS ranges, for this system, are not sensitive to the number of ternary interactions assessed. However, they pointed out that reliable prediction of miscibility gaps and/or intermetallic phases may require a more complete description of ternary interactions.

The quality of CALPHAD prediction mainly relies on the correct thermodynamic descriptions. This may limit the reliability of the predictions especially as the number of elements in an alloy increase, as the number of binary and ternary interactions also increase.

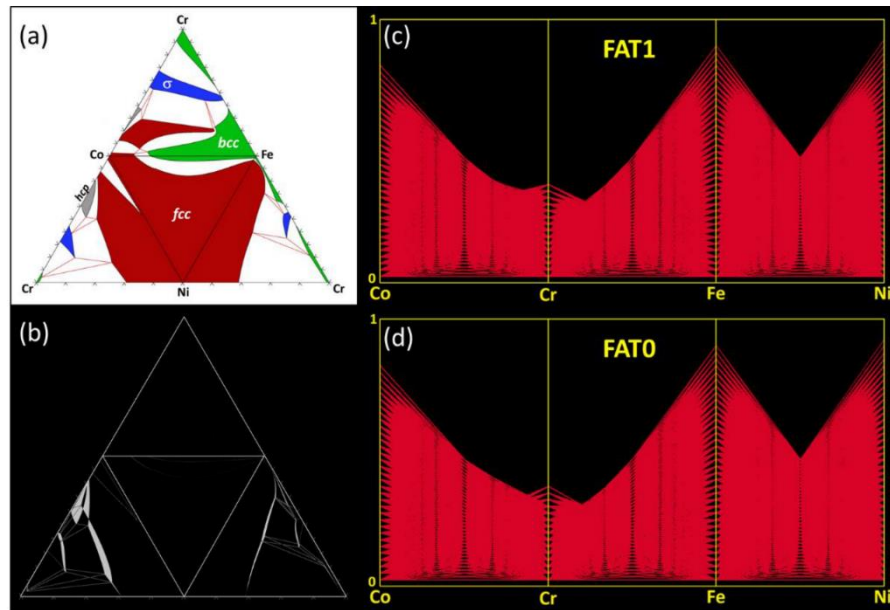


Figure 1.6. Co-Cr-Fe-Ni system: (a) Unfolded tetrahedral quaternary phase diagram showing the four isothermal sections of the ternary subsystems calculated at 800 °C for FAT = 1, highlighting the single-phase fields. (b) Difference (appearing in white) between the extent of the various phase fields calculated for FAT = 1 and FAT = 0. (c,d) Parallel coordinate plots showing the predicted range of existence (4D compositional coordinates) of the *fcc* phase in the quaternary Co-Cr-Fe-Ni phase diagram. Taken from Ref. [51].

## 1.5 The core effects of HEAs

In a review letter two years after the first publications on HEAs, Yeh [53] hypothesized four core effects that HEAs should exhibit. (i) the high-entropy effect, previously discussed in section 1.2; (ii) a local lattice distortion (LLD) effect, linked to atomic-size mismatch; (iii) sluggish diffusion, which would make these materials suitable for high-temperature operations; and finally (iiii) the cocktail effect. These core effects are addressed in the following paragraphs.

### 1.5.1 Lattice distortion

Based on the available data at the time, Yeh [53] suggested that solid solutions with multi-principal elements would lead to a high degree of lattice distortion and this would have the following effects; pronounced solid-solution strengthening [4], increased thermal and electrical resistivity [54], and a strong decrease in X-ray diffraction intensities [55]. To assess the hypothesis of lattice distortion, suggested by Yeh [53], Owen *et al.* [56] used neutron radiation total scattering measurements on gas atomized powders of Ni-33Cr (at. %)

and a homogenized equiatomic CoCrFeMnNi alloy. The samples were measured for 4 hours at room temperature. Pair distribution function (PDF) plots, which give information of the interatomic distances ( $r$ ) within the irradiated volume, were analyzed and compared to pure Ni, Ni-20Cr, Ni-25Cr, and ternary Ni-37.5Co-25Cr alloys. Their results showed that all alloys were *fcc* SPSS, statistically disordered, and with no preferential texture so any decrease in intensity should come from LLD, which was not observed. They concluded that the peaks full widths at half maximum of the HEA were in general larger compared to the other alloys analyzed, considering the first 6 coordination shells. In terms of a static displacement, this can be interpreted as that the HEAs lattices contain a higher degree of local strain. Nonetheless, they emphasized that the widths of these PDF peaks were not exceptionally greater than the binary and ternary alloys compared in their investigation.

Tong *et al.* [57] quantitatively described the degree of LLD for three homogenized SPSS *fcc* medium- and high-entropy alloys (CoCrNi, CoCrFeNi, and CoCrFeMnNi) using X-ray total scattering measurements in transmission mode. They calculated the degree of LLD by fitting first the lattice parameter in the  $r$ -range from 1.5 Å to 3 Å (first atomic shell) to obtain the local lattice constants,  $a_{1st}$ , and then extended to the whole measured PDF but with the fixed lattice parameter of  $a_{1st}$ . The LLD was quantitatively analyzed in terms of  $r$ -dependent lattice parameter ( $a_{var}$ ) extracted from the  $r$ -dependent refinement. A divergence between  $a_{1st}$  and  $a_{var}$  revealed that the local structure of CoCrNi and CoCrFeMnNi (at the low  $r$  region) disagrees with the average structure at the high  $r$  region and some degree of LLD exists in these two alloys, while for the CoCrFeNi it was insignificant. They discuss that the origin of the LLD for the former alloys is of different natures. For the CoCrFeMnNi alloy, all elements have remarkably similar atomic sizes, except for Mn (~ 8 % difference), and this difference was given by the authors as the explanation for its LLD. However, for the CoCrNi MEA all elements have similar atomic sizes, thus, could not explain the LLD. The reason for the local lattice strain in CoCrNi, according to Tong *et al.* [57], comes from chemical short-range order (CSRO), which has been investigated both theoretically and experimentally [58–61]. Short-range order in MEAs and HEAs will be more thoroughly addressed in Chapter 6.

Kube *et al.* [62] measured the crystal structure of 2478 alloys in the systems based on Al, Cr, Mn, Fe, Co, Ni, and Cu. Two subsets were arranged, one based on the Al-group and the other on the Mn-group. All possible quinary combinations from Al, Cr, Fe, Co, Ni, and Cu, and Cr, Mn, Fe, Co, Ni, and Cu were studied. It was shown the preference of HEAs with a large atomic-size mismatch,  $\delta$ , to crystallize with the loose-packed *bcc* structure. Tong

*et al.* [63], using X-ray total scattering analysis, showed that the first and second shells of the PDF of *bcc* refractory HEAs (RHEAs) containing hafnium and zirconium overlap, and pronounced damping of the structure features occurs at larger  $r$ . Contrary, other Hf- and Zr-free *bcc* RHEAs investigated had discernable first and second peaks. They concluded that for the former it is caused by a severe LLD due to the large atomic-size difference of Hf and Zr with the other refractory elements. These new findings are contradicting to the initial generalization of Yeh [53], that all HEAs should show severe lattice distortion. Perhaps with the improvement of experimental and theoretical techniques, and more available data on lattice distortion in HEAs, a more conclusive theory may be established.

### 1.5.2 Sluggish diffusion

The sluggish diffusion effect was stated as one of the core effects of HEAs from the beginning and it was presumed that these materials would have great advantages to be used as structural alloys in high-temperature services. Diffusion in HEAs requires the cooperative movement of different atom species. It was supposed in Ref. [1] that the vacancy concentration for substitutional diffusion is still limited in HEAs, as it is in less complex alloys because the formation of a lattice vacancy is associated with a positive enthalpy of formation and excess entropy. The competition between these two factors establishes an equilibrium vacancy concentration with minimum free energy at a given temperature. The vacancies in the multi-element matrix are surrounded by different atom species during diffusion establishing competition among them. "Either a vacancy or an atom would have a fluctuated diffusion path to migrate and have slower diffusion and higher activation energy" [1]. Additionally, the inherent lattice distortion proposed by Yeh [53] was thought to hamper atomic movement and limit the diffusion rate in HEAs. For the reasons given above, diffusional phase transformations in HEAs were believed to be universally sluggish [1]. Nonetheless, these allegations were made based on indirect evidence such as the formation of nanosized crystals and qualitative analysis of microstructural stability upon cooling.

The first study to determine the solid-state diffusion coefficients of HEAs was done on the CoCrFeMnNi alloy by Tsai *et al.* [64] in 2013. Diffusion couples were arranged as that only two of the five elements would have a concentration gradient across the interface. The couples were then annealed at four different temperatures: 1173, 1223, 1273, and 1323 K. The authors constructed Arrhenius plots and calculated the activation energies. They concluded that diffusion coefficients were smaller, and the activation energies were



significantly higher than traditional alloys and pure metals. The authors then stated that diffusion in high entropy alloys is sluggish.

From the point of view of data analysis, the quasi-binary approach used by Tsai *et al.* [64] was essential for the outcome of the results. The use of such an approach allows obtaining one interdiffusion coefficient, a characteristic for a given couple and common for both elements (the ones with gradients of concentration). Tsai *et al.* [64] assumed it would be possible to obtain two interdiffusion coefficients by analyzing separately the profiles of components 1 and 2. While for binary systems, it would make no difference, since the sum of molar fractions  $n_1 + n_2 = 1$ , in a quasi-binary system the presence of uphill effects of the other elements may modify the profiles for elements 1 and 2 [65]. The method adopted by Tsai *et al.* [64] was contested by experts in the field of diffusion [65–67] which have questioned the conclusions they arrived at.

Most studies on diffusion of high-entropy alloys, using both diffusion couples and the radio tracer methods [68–70], did not come to the same findings as Ref. [64]. For example, Vaidya *et al.* [70] investigated both bulk and grain boundary diffusion with the radio tracer method on polycrystalline CoCrFeNi and CoCrFeNiMn alloys. They concluded that the diffusion coefficients are only smaller, comparing to other *fcc* alloys if a homologous temperature scale is used for comparison. In the absolute temperature scale, the diffusion rates are of the same magnitude. Above a critical value, Co diffusivity was shown to be faster in CoCrFeNi than in CoCrFeMnNi alloy. This suggests that diffusion in HEAs does not necessarily become sluggish with increasing the number of elements. Dabrowa and Danielewski [65] stated in their review about diffusion in HEAs that: “looking at the described state-of-the-art of diffusion studies in HEAs, it can be said that there is completely no evidence of any diffusion sluggishness in the absolute temperature scale if the tracer diffusivities are considered”. However, they point out that all studies carried out so far have focused on *fcc*-structured alloys, and that although sluggish diffusion has not yet been proved to occur it may be the case for *bcc* HEAs.

### 1.5.3 Cocktail effect

From the four core hypotheses proposed the ‘cocktail’ effect is the only one that cannot be measured or quantified. It is invoked that the properties of HEAs result from unforeseen synergies between the multicomponent structure. That is, the properties of multi-principal element alloys do not obey the linear rule of mixtures, because at an atomic scale HEAs can be regarded as composites benefiting from the mutual interactions of different

elements in a lattice. The hypothesis may be true, but it is rather difficult to prove it scientifically.

## 1.6 Mechanical properties

It is possible to summarize four different lines of development for HEAs related to their mechanical properties. (i) lightweight materials with high specific strength which are reflected in the development of lightweight high-entropy alloys (LW-HEAs); (ii) overcome the long-lasting strength-ductility trade-off; (iii) alloys for cryogenic applications, specifically in the transition metal HEAs class (TM-HEAs); and finally, (iiii) materials for high-temperature applications that can exceed the existing limits of work temperature and resistance to softening. The latter class is designated as refractory high-entropy alloys (RHEAs).

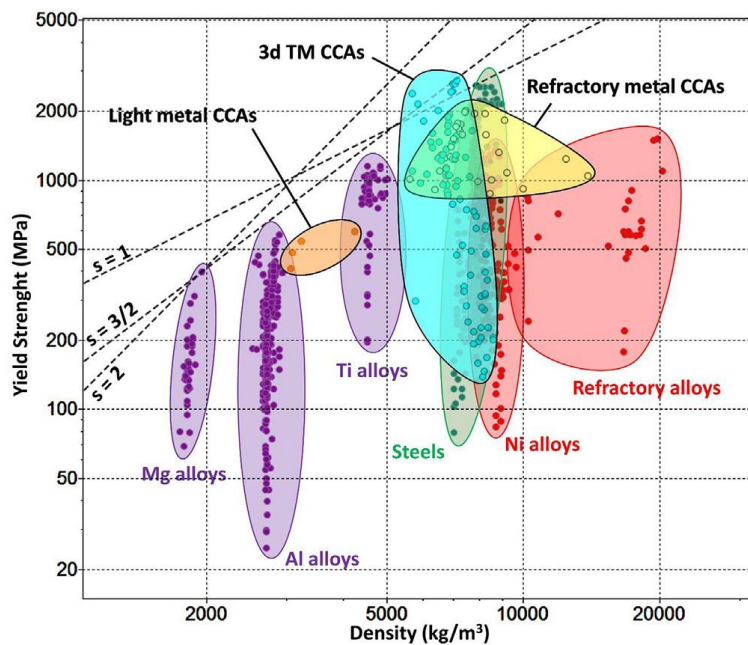


Figure 1.7. Materials property space for room temperature yield strength versus density of conventional metal alloys and CCAs. Taken from [71].

### 1.6.1 Lightweight high-entropy alloys

The development of LW-HEAs is generally based on alloying Al and Ti with other elements [72]. As can be seen in Figure 1.7 [71] there is an existent gap, in terms of density, between Al and Ti alloys. Because HEAs have a high degree of freedom regarding compositional space, this gap may be filled by LW-HEAs.

The LW-HEA with the lowest density produced was an equiatomic AlCaCuLiMg alloy ( $2.2 \text{ g/cm}^3$ ) consisting of a SPSS with a tetragonal crystal structure. The SPSS structure was analyzed by XRD and microstructural investigation with a scanning electron microscope (SEM). Room-temperature compression tests showed a fracture strength of 910 MPa, and thus, the specific strength of this alloy is about  $413 \text{ MPa/g/cm}^3$ .

Kang *et al.* [72] used the CALPHAD method for screening the binary phase diagrams of Al and Ti and other elements to develop new LW-HEAs with extended solid solubility for intermediate temperature services. They designed two equiatomic compositions which were *bcc* SPSS, AlCrMoTi, and AlCrMoTiV, and the other five compositions had a *bcc* matrix and minor B2 phase precipitates. Their Vickers' hardness, theoretical density, and specific hardness are summarized and compared with commercial alloys in Table 1.4. As can be seen, the HEAs' densities are higher than Ti-base and lower than Nickel-base alloys, and their specific hardness are superior to both. It is suggested in their work that the high hardness comes from the solid solution hardening effect due to atomic-size mismatches.

Table 1.4. Comparison of the specific hardness of the lightweight HEAs in Reference [72] with commercial alloys.

Alloys	Hardness (HV)	Theoretical density ( $\text{g/cm}^3$ )	Specific hardness ( $\text{HV/g/cm}^3$ )
AlCrMoTi	606	6.01	100.83
AlCrMoTiV	556	6.00	92.67
Ti-6Al-4V	346	4.43	78.10
Ti-6242	339	4.54	74.67
Inconel 718	335	8.18	43.40

Youssef *et al.* [73] produced a low-density ( $2.67 \text{ g/cm}^3$ ) non-equiatomic  $\text{Al}_{20}\text{Li}_{20}\text{Mg}_{10}\text{Sc}_{20}\text{Ti}_{30}$  nanocrystalline alloy by ball milling at low temperatures and subsequent hot pressing. They showed, by XRD and transmission electron microscopy (TEM), that the as-prepared alloy was a *fcc* SPSS and after annealing at  $500 \text{ }^\circ\text{C}$  for 1 hour the sample transformed into a *hcp* SPSS structure. The hardness of the samples were 5.8 and 4.9 GPa for *fcc* and *hcp* structures, respectively, which are 2-3 times higher than nanocrystalline Al alloys. Interestingly, few samples that were contaminated during preparation and had prominent levels of N and O did not transform to *hcp* structure upon annealing and it was explained by the authors based on the octahedral site distance difference

between the *fcc* and *hcp* structures. To accommodate the impurities in octahedral sites the *fcc* structure, which has a larger octahedral site distance, was preferred in the samples with high impurity levels. The authors stated that the *hcp* structure is the stable phase for this alloy and that the low stacking fault energy of the *fcc* phase contributed to the high hardness.

According to Feng *et al.* [74], there is limited solubility of Al and Ti with late transition metals because of the difference in atomic sizes and electronegativity. This leads to the formation of very stable intermetallic compounds and very few SPSS can be found in the LW-HEAs class. It has also been reported the formation of quasicrystal phases [75], which had a strong negative effect on the ductility, and amorphization during prolonged ball milling of *hcp* exclusive element compositions, e.g., BeCoMgTi and BeCoMgTiZn [76].

LW-HEAs are the least explored among all other classes of HEAs. As can be seen from the discussion above, they have the potential to perform better than existing Al and Ti alloys in terms of specific strength. With careful design, it is also possible to seek project-targeted densities for special applications, which is unlikely to happen for Al- and Ti-base alloys since the density is determined by the major alloying element. One of the limitations for the development of new LW-HEAs is they mainly have relied on empirical and CALPHAD methods, and both approaches may have limited accuracy to predict SPSS or other desired microstructures. The improvement of thermodynamic databases and reliable experimental determination of temperature-dependent phase formation, in different systems, should push the field forward.

### 1.6.2 Overcoming the strength-ductility tradeoff

The strength-ductility tradeoff has been a longstanding dilemma in the development of structural alloys [77]. For example, *fcc*-structured solid solutions usually show particularly good plasticity but have low strength. Contrarily, *bcc*-structured solid solutions show higher strengths but limited plasticity at room temperature. Since generally ductility and strength are mutually exclusive a compromise between one and the other must be made. Several approaches have been developed in metallurgy to overcome the strength-ductility tradeoff and some of the same principles are applied in the HEAs field.

Twinning-induced plasticity (TWIP) or transformation-induced plasticity (TRIP) are two mechanisms described in the literature of HEAs as effective methods in overcoming the tradeoff. TWIP-alloys were first developed as austenitic steels with high manganese content which were designed to have low stacking fault energies (SFEs) [78], enabling the TWIP effect. The deformation-induced twinning is capable of enhancing the work hardening

which delays the formation of necking, in this way increasing simultaneously the tensile strength and ductility [78]. The plastic deformation of the *fcc* phase is mainly governed by the SFE. A transition from dislocation slip mode to deformation twinning (TWIP) is favored as the SFE is lowered, and for very low values of SFE, strain-induced *fcc*  $\rightarrow$  *hcp* martensitic transformation (TRIP) deformation mode occurs [79].

Wei *et al.* [80] studied theoretically and experimentally composition modifications on the equiatomic Cantor alloy and its influence on the SFE and the *fcc* phase stability. It was shown that the SFEs could be lowered by augmenting the Co and Cr concentration and decreasing Fe, Ni, and Mn content. Moreover, in addition to lowering the SFE, increasing the amount of Co, and especially Cr, decreased the stability of the *fcc* phase in favor of the *hcp* phase at 300 K. Based on the theoretical investigations they produced two non-equiatomic alloys;  $\text{Co}_{35}\text{Cr}_{20}\text{Fe}_{15}\text{Ni}_{15}\text{Mn}_{15}$ , and  $\text{Co}_{35}\text{Cr}_{25}\text{Fe}_{10}\text{Ni}_{15}\text{Mn}_{15}$  (at. %), besides the Cantor alloy. All alloys were *fcc* SPSSs before uniaxial tensile tests and had comparable grain sizes. After testing, XRD and EBSD analysis revealed that the  $\text{Co}_{35}\text{Cr}_{25}\text{Fe}_{10}\text{Ni}_{15}\text{Mn}_{15}$  formed *hcp* phase by martensitic transformation (TRIP) evidenced by the elongated strips inside the *fcc* grains. Furthermore, EBSD maps showed that twinning occurred during deformation (TWIP) in both non-equiatomic alloys. The tensile yield strengths were 199, 231, and 305 MPa for the Cantor,  $\text{Co}_{35}\text{Cr}_{20}\text{Fe}_{15}\text{Ni}_{15}\text{Mn}_{15}$ , and  $\text{Co}_{35}\text{Cr}_{25}\text{Fe}_{10}\text{Ni}_{15}\text{Mn}_{15}$  alloys, respectively. The total elongations until fracture were 74%, 96%, and 76%, respectively. Other publications [81–83] have demonstrated the effectiveness of designing *fcc* HEAs with low SFE and the possibility to overcome the strength-ductility tradeoff using TWIP and TRIP effects.

Liang and co-workers [84] were able to significantly increase the tensile strength of the CrFeNi MEA, which intrinsically has low strength, by first creating a nanostructured supersaturated *fcc* solid-solution via ball-milling and inducing the formation of Cr-rich nano precipitates and Cr-oxide nanoparticles via spark plasma sintering. The ultrafine-grained MEA showed a high yield strength of 640 MPa and fair tensile ductility of 26 %, a combination that makes it attractive among other MEAs and HEAs. The good mechanical properties were attributed to grain boundary and precipitation strengthening mechanisms.

Another method that has been applied for MEAs and HEAs is heterogeneous-structures-architecting [85–88]. This approach focus on achieving partially recrystallized microstructures by annealing at intermediate temperatures for shorter periods after preliminary cold-rolling, or via hot-rolling. Wu *et al.* [85] applied this strategy to the  $\text{Al}_{0.1}\text{CoCrFeNi}$  HEA cold worked and annealed at 873 K for 1 hour and were successful.

According to Wu *et al.*, the non-recrystallized grains contribute to high strength due to strain-hardening while the fully recrystallized grains can increase ductility. The microstructure was composed of three different types of grains at different length scales and dislocation densities. The tensile yield and ultimate strengths were  $711 \pm 40$  and  $928 \pm 35$  MPa, respectively. The uniform elongation reached  $30.3 \pm 3.7\%$ . These results reveal the advantages of the heterogenous microstructure on mechanical behavior. It is a very interesting combination of strength and ductility especially for *fcc*-structured alloys, which stands out from other HEAs and TWIP-TRIP steels.

### 1.6.3 Cryogenic high-entropy alloys

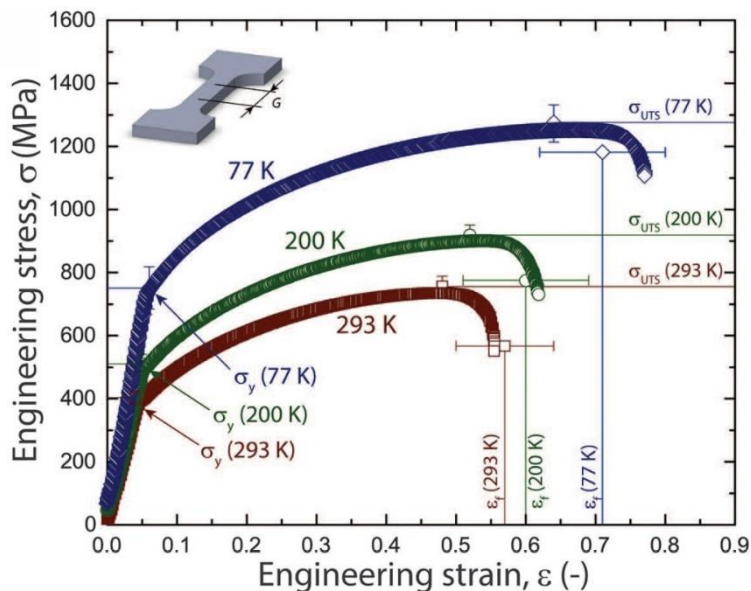


Figure 1.8. Yield strength  $\sigma_y$ , ultimate tensile strength  $\sigma_{UTS}$ , and ductility (strain to failure,  $\epsilon_f$ ) all increase with decreasing temperature for the CoCrFeMnNi alloy. (Taken from Ref. [89]).

It is normally expected that an increase of strength at lower temperatures is accompanied by a decrease in ductility [90]. MEAs and HEAs containing 3d-transition metals have consistently shown to deviate from this ideal concept. For example, Gludovatz *et al.* [89] revealed that the fracture energy of a five-component CoCrFeMnNi alloy increased by more than two-fold when the uniaxial stress-strain test temperature was decreased from 293 to 77 K. An increase of 85 % in yield strength occurred and simultaneously the tensile ductility increased by 25 %, as can be seen in Fig. 1.8. According to Gludovatz *et al.* [89], an increment in yield strength at cryogenic temperatures has been observed for some stainless and cryogenic steels, but contrasting with MEAs and HEAs their

fracture toughness, without exception, decreased with decreasing temperature. The Cantor alloy revealed a considerable fracture toughness which was shown to be independent of testing temperature. The measured crack initiation fracture toughness  $J_{Ic}$  was determined to be 250 kJ/m<sup>2</sup> at 293 K and 255 kJ/m<sup>2</sup> at 77 K. The simultaneous increase in yield strength and ductility at cryogenic temperatures were attributed to; (i) a steady high-degree of strain-hardening both at room temperature and 77 K; (ii) a transition from exclusively planar glide deformation mode at room temperature, to both planar dislocation slip and deformation-induced nano-twinning at lower temperatures.

Wu *et al.* [91] have investigated a series of Co-Cr-Fe-Mn-Ni containing alloys at temperatures ranging from 77 to 673 K. It was shown that CoCrNi, CoCrFeNi, and CoCrMnNi alloys, the two former ones studied in this thesis, exhibited significant strengthening as the temperature was decreased to 77 K, with a concurrent improvement of engineering plastic strain. Some of the conclusions drawn were that the solid-solution strengthening of HEAs may be much more related to the interaction of specific elements than to the number of elements in an alloy. This was backed up by revealing that the ternary CoCrNi and quaternary CoCrFeNi alloys exhibit higher yield strength at 293 K compared to the five-component CoCrFeMnNi alloy. The authors concluded, based on the different alloys investigated, that Cr should have the most powerful strengthening potential. Another conclusion was that the temperature dependence of the yield strength can be explained by the Peierls lattice friction barrier and that the magnitude of the barrier is determined by the dislocation's width, which is temperature-dependent.

One of the most crucial properties of structural materials is damage tolerance, e.g., a balance of high yield strength, ductility, and fracture toughness [90]. In this respect, the ternary CoCrNi MEA was described as one of the toughest materials in any materials class ever reported [92], and shows increasing damage tolerance at cryogenic temperatures. Again, the mechanisms that lead to superior yield strength and ductility at liquid nitrogen temperature were a continuous steady strain work hardening effect and nano-twins formed during plastic deformation.

The mechanical behavior of the CrFeNi alloy, which is also one of the alloys studied in this work, was investigated by Schneider and Laplanche [93] in the temperature range of 77 to 873 K. It was also demonstrated an inverse relation of both tensile and compression yield stresses at low temperatures. According to the authors, at the early stage of plastic deformation, the governing mechanism is the planar glide of dislocations which eventually pile up at the grain boundaries. At true strains between 1.9% and 4.5% at 77 K,



and 16.0% and 17.4% at 293 K, an additional mechanism of nano-twinning starts to act. At 77 K the nucleation of twins promotes a dynamic Hall-Petch effect, meaning that the dynamic reduction of grain size enhances the work hardening effect and postpones necking (localized plastic deformation), leading to increased ductility. On the other hand, at 273 K dislocations do not interact with nano-twins because dislocation cells are formed shortly before the nucleation of twins. Thus, the dislocation mean free path is determined by the cell sizes which are considerably smaller than twin spacings.

#### 1.6.4 Refractory high-entropy alloys

The following properties are desired for materials capable to work in high-temperature environments; (i) structural thermal stability, (ii) resistance to thermal softening, (iii) surface stability, and (iiii) adequate resistance against corrosion and oxidation. For the past 70 years, Ni- and Co-base superalloys have been used for high-temperature applications especially in the aerospace industry. Ni-base superalloys have the highest homologous work temperature ( $0.9 \cdot T_m$ ) between all alloys. While for intermediate strength applications solid-solution strengthened alloys (*fcc* matrix, e.g., Hastelloy X) are the choice, for the more demanding services (turbine blades) precipitation strengthened materials (*fcc* matrix + L1<sub>2</sub> coherent precipitates) are preferred. Ni-base alloys are limited to temperatures between 1160 and 1277 °C due to their melting points [94]. Therefore, the goal in the development of refractory high-entropy alloys is to overcome the work temperature limit.

RHEAs were first proposed by Senkov *et al.* [95] in 2010. The Nb<sub>25</sub>Mo<sub>25</sub>Ta<sub>25</sub>W<sub>25</sub> and V<sub>20</sub>Nb<sub>20</sub>Mo<sub>20</sub>Ta<sub>20</sub>W<sub>20</sub> (at. %) alloys were synthesized and their phase constitutions, thermal stability, and mechanical properties were investigated at room and elevated temperatures [96]. Neutron diffraction studies revealed that both alloys had a SPSS *bcc* structure and retained the single-phase character after annealing at 1400 °C for 19 hours. Their mechanical behavior was studied at room temperature and 600, 800, 1000, 1200, 1400, and 1600 °C by compression tests. Both alloys showed yield strengths above 1 GPa but extremely limited ductility at room temperature. As expected, their yield strength decreased, and ductility was substantially improved with an increase in testing temperatures.

Fig 1.9 shows a comparison of the yield strength vs. temperature for these alloys and two commercial Ni-base alloys (Inconel 718 and Haynes 230). Despite the Inconel 718 shows higher yield stress at 600 °C, its strength deteriorates rapidly above this temperature. On the other hand, the RHEAs were shown to have much less pronounced thermal softening



up to 1600 °C. These specific RHEAs have their densities, brittle nature at room temperature, and costs as disadvantages compared to Ni-base superalloys.

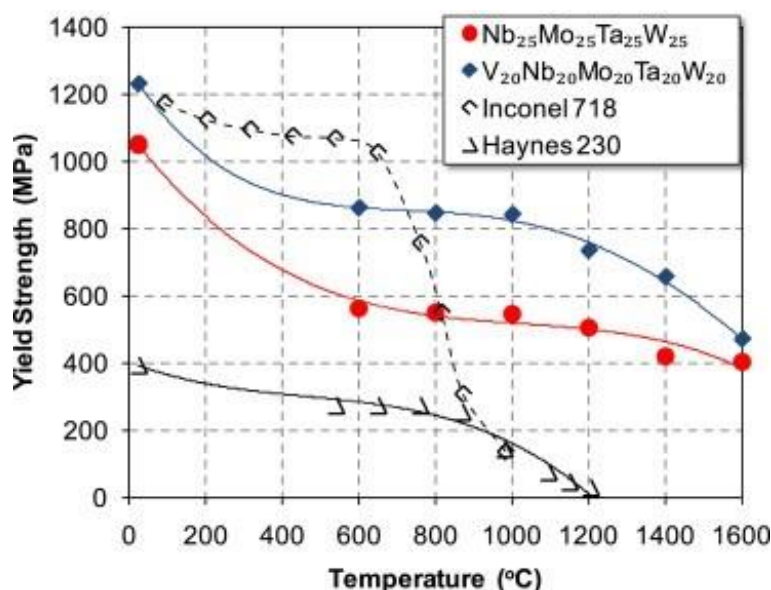


Figure 1.9. The temperature dependence of the yield stress of Nb<sub>25</sub>Mo<sub>25</sub>Ta<sub>25</sub>W<sub>25</sub> and V<sub>20</sub>Nb<sub>20</sub>Mo<sub>20</sub>Ta<sub>20</sub>W<sub>20</sub> RHEAs and two superalloys, Inconel 718 and Haynes 230. Taken from Ref. [96].

Most RHEAs designed to date use 9 elements with high melting points from the periodic table: Mo, Nb, Ta, V, W, Ti, Zr, Hf, and Cr, with sometimes additions of other non-refractory metals, mainly Al, Si, Co, or Ni. They crystallize with the *bcc* structure and may contain intermetallic compounds, namely B2 and/or Laves phases. Their densities lie in the range of 5.6 to 13.8 g/cm<sup>3</sup> [97].

Senkov *et al.* [98] investigated the effect of Al addition to previously reported RHEAs. AlMo<sub>0.5</sub>NbTa<sub>0.5</sub>TiZr and Al<sub>0.4</sub>Hf<sub>0.6</sub>NbTaTiZr (both in molar fractions) alloys had a substantial decrease in density compared to the Al-free RHEAs. Their densities were 7.40 and 9.05 g/cm<sup>3</sup>, respectively. The AlMo<sub>0.5</sub>NbTa<sub>0.5</sub>TiZr was shown to have two *bcc* phases after being hot isostatically pressed (HIPed) at 1400 °C and 207 MPa for 2 h and then annealed at 1400 °C for 24 hours. Its compression yield strength was 2 GPa and fracture strain of 10 % at room temperature. When tested at 1000 and 1200 °C (in vacuum), its yield strengths were 745 and 250 MPa, respectively, with fracture strains above 50 %. The compressive yield strength of ~750 MPa at 1000 °C exceeds the performance of any superalloy [99]. The Al<sub>0.4</sub>Hf<sub>0.6</sub>NbTaTiZr received the same treatment but the temperature, in this case, was 1200 °C for HIPed and annealing and formed a *bcc* SPSS. Its compression

yield strength at room temperature was 1.8 GPa and fracture strain of 10 %. At 1000 and 1200 °C respectively, its yield strengths were 298 and 89 MPa, and with fracture strains above 50 %.

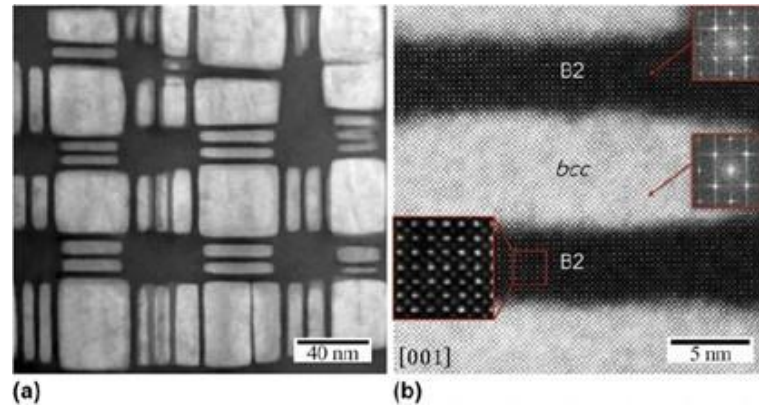


Figure 1.10. TEM images of the nano-phase structure present inside the grains of  $\text{AlMo}_{0.5}\text{NbTa}_{0.5}\text{TiZr}$ . (a) Cuboidal and plate-like precipitates of a disordered  $bcc$  phase are separated by continuous channels of an ordered B2 phase. (b) The fast Fourier transforms (shown inside the red squares) reveal an ordered B2 structure for the dark channels and a disordered  $bcc$  structure for the cuboidal precipitates. Taken from Ref. [100].

A subsequent publication [100] revealed that the outstanding mechanical performance of the  $\text{AlMo}_{0.5}\text{NbTa}_{0.5}\text{TiZr}$  at elevated temperatures is due to the fine nano-scale mixture of B2 and cuboidal or plate-like  $bcc$  phase (Fig. 1.10). This microstructure mimics the  $\gamma/\gamma'$  structure of Ni-base superalloys, therefore, the alloys having the B2/ $bcc$  ( $\beta'/\beta$ ) structure were designated as refractory high-entropy superalloys [101]. However, in Ni-base superalloys the soft  $\gamma$  is the continuous phase and the hard and brittle phase  $\gamma'$  is the discontinuous phase. In the alloys proposed by Ref. [100], this relation is inverted, thus, the alloys have limited ductility at room temperature. It was also shown that brittle hexagonal intermetallic particles precipitated at the grain boundaries and an attempt to avoid them was made by compositional modifications.

As other  $bcc$  metals and alloys RHEAs lack adequate ductility at room temperature. The majority of RHEAs, independently of crystal structure(s), show a brittle-to-ductile transition above room temperature [102]. An exception is the  $\text{HfNbTaTiZr}$  which revealed suitable plasticity under compression test at room temperature with engineering strain  $> 50$  %, with a yield stress of 929 MPa [103]. It also shows room temperature tensile ductility above 10 %. Solid-solution strengthening is regarded to play a significant role in the

mechanical properties of RHEAs at room temperature, while precipitation strengthening is described as the key contributor at elevated temperatures [103]. It is, therefore, crucial to be able to control the volume fraction, type, and distribution of coherent precipitates to achieve a balanced performance both at room and elevated temperatures.

Soni *et al.* [104] could reverse the B2/*bcc* microstructure by a sequence of heat treatments on the  $\text{Al}_{0.5}\text{NbTa}_{0.8}\text{Ti}_{1.5}\text{V}_{0.2}\text{Zr}$  alloy. The final microstructure revealed that the *bcc* was then the continuous matrix and the B2 phase the precipitates. This had a significant impact on the ductility of the alloy at room temperature (> 20 %). It was also shown that the alloy in this condition exhibits high compression yield strength at room temperature ~1345 MPa and 600 °C ~1423 MPa. The authors stated that the anomalous increase of strength at 600 °C needs further investigation.

In the review article published by Senkov *et al.* [102], they identified the need for high-temperature tensile tests as most published data for RHEAs were on compression tests. Not only that but most of the reported data on the mechanical properties of RHEAs are for room temperature, which does not permit an evaluation of their behavior at elevated temperatures. They also pointed to the fact that fatigue and creep resistance data was not available for RHEAs by early 2018.

## 1.7 Functional properties

The production costs of HEAs [105] are a drawback in their development as structural materials since their mechanical properties have not yet been shown to be remarkably superior to the available commercial alloys [106]. Another major challenge with the large-scale production of HEAs is that they are not competitive as a modern society focus on clean and green material sources. Recycling of HEAs has not, to the best of the author's knowledge, been the focus of any investigation so far. Naturally, it should be more complex as one compares it to one-element-base alloys. Therefore, the future of HEAs must not be focused exclusively on their development as structural materials but rather seek a combination of suitable mechanical and functional properties for special applications. Some studies have already disclosed the potential use of HEAs as functional materials with soft-magnetic, magnetocaloric, hydrogen storage, and superconducting properties.

### 1.7.1 Soft magnetic properties

Soft-magnetic alloys are crucial in electrical systems and can be used in power supply transformers, transmission, and as electromagnets. Conventional materials used for

this purpose, e.g., Fe-Al alloys, silicon steels, Fe-Co alloys, and soft ferrites may in some cases be brittle, have low strength, or have low magnetization [86]. Bulk metallic glasses used as soft magnetic materials are limited in dimension and are constrained to work temperatures below the glass transition [106]. HEAs have been shown to have adequate soft magnetic properties with the advantage of, in particular cases, high strength combined with excellent ductility, superior corrosion resistance, and flexible manufacturability [106].

The development of soft magnetic HEAs is usually based on the ferromagnetic elements Fe, Co, and Ni with additions of other elements to tune auxiliary properties [106]. Lu *et al.* [86] demonstrated that the microstructure of the  $\text{Al}_{0.25}\text{CoFeMn}_{0.25}\text{Ni}$  (molar fraction) HEA could be highly tuned by thermomechanical treatments. The heterogeneous structure (recrystallized *fcc* matrix + *bcc* precipitates) obtained after cold rolling and annealing the alloy at 850 °C for one hour resulted in an attractive combination of both mechanical and soft magnetic properties. The yield strength was 578.8 MPa with total uniform elongation of 22.6 %, while the magnetization saturation  $M_s$  was 112.4 emu/g and the coercivity 9.8 Oe.

Zuo *et al.* [107] investigated the magnetic properties of  $\text{CoFeMnNi}(X)$  ( $X = \text{Al, Cr, Ga, and Sn}$ ). It was shown that the SPSS *fcc*-structured  $\text{CoFeMnNi}$  had a  $M_s = 18$  emu/g. The addition of Al causes a dramatic change to an ordered B2 matrix with *bcc* nanoparticles. The  $\text{AlCoFeMnNi}$  had a maximum  $M_s = 148$  emu/g, however, its coercivity also increased from 119 to 629 A/m compared to the base alloy. The authors discussed that the addition of Al suppressed the original antiferromagnetic effect of Mn atoms in  $\text{CoFeMnNi}$  to favor ferromagnetism.

Rao *et al.* [108] explored a different route to investigate soft magnetic properties than the traditional HEAs community has aimed. They intentionally sought phase separation in the  $\text{Fe}_{15}\text{Co}_{15}\text{Ni}_{20}\text{Mn}_{20}\text{Cu}_{30}$  (at. %) by triggering bulk spinodal decomposition upon annealing treatments. They showed an increase of 48 % in the Curie temperature, from 201 to 303 K, and a 70 % increase in magnetization at room temperature for the samples annealed for 240 hours compared to the samples in the homogenized state (1000 °C). Density functional theory calculations revealed that the increment in magnetic properties was due to the formation of Fe-Co enriched regions caused by spinodal decomposition. According to the authors, the formation of Fe-Co regions alone could not describe such drastic change in the Curie temperature which was explained by volume dilatation due to coherency strains imposed by the matrix.

Though usually, HEAs have lower saturation magnetization than Fe-Co alloys and intrinsic coercivity higher than silicon steels [106] (see Fig. 1.11), their better mechanical performances and corrosion resistance, and higher electrical resistivity, make them an interesting option where high-strength and soft magnetic properties are needed to be combined.

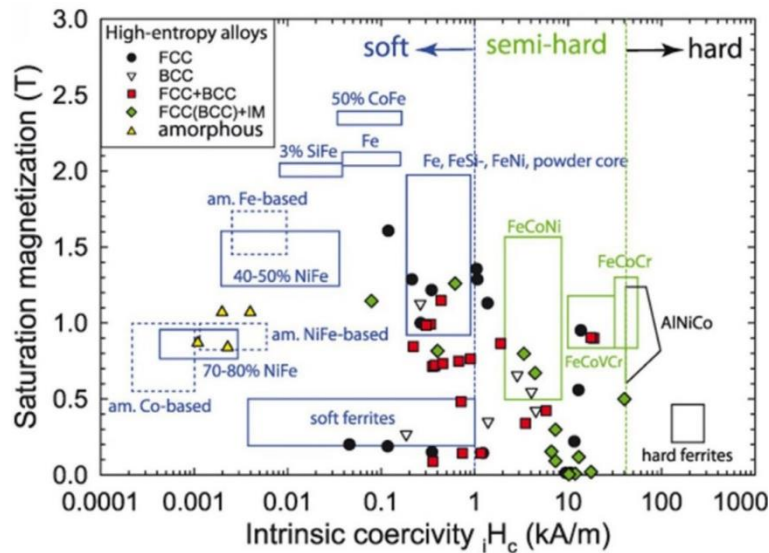


Fig. 1.11. The saturation magnetization (T) versus coercivity  $H_c$  (kA/m) of HEAs compared with major conventional soft and semi-hard magnetic Fe materials (taken from Ref. [106]). Original data for HEAs was published in Ref. [109]).

### 1.7.2 Magnetocaloric properties

Magnetocaloric materials are capable of heat generation under the effect of an applied magnetic field. The fundamental idea is that under an applied magnetic field a material tends to align its magnetic domains to that of the applied field, thus, decreasing the magnetic entropy  $\Delta S_m$ . At the same time, the vibrational entropy of the system increases while the total entropy change remains zero, which increases the temperature of the system [7]. If the reverse process is used, e.g., the magnetic field is removed the total entropy of the system remains constant but the magnetic entropy increases and, thus, the temperature of the system decreases. Magnetocaloric materials should have Curie temperature  $T_c$  close to room temperature and high variation in  $\Delta S_m$  and refrigeration capacity  $R_c$ . They have been developed as an alternative to gas refrigerants.

From the 22 HEAs reported in the literature with magnetocaloric effects by July 2020, 16 contain rare-earth elements and 6 are composed of transition metals and Al. Their phase constitutions are: 15 are amorphous, 5 are single-phase *fcc*, one is single-phase *hcp*,

and one is a dual-phase *fcc* + *bcc* (Table 1.5). On the one hand, the HEAs with rare-earth elements have  $T_c$  far below room temperature while almost all the rare-earth free alloys have  $T_c$  close or above room temperature. On the other hand, the rare-earth HEAs have higher changes in magnetic entropy and higher refrigeration capacity than HEAs without rare-earths (see Table 1.5).

Table 1.5. Reported HEAs with magnetocaloric effects. Adapted from [110].

Composition	Phases	$\Delta S_m$ (J/kg K) @ 5T	$R_c$ (J/Kg)	$T_c$ (K)	Ref
AlCoDyGd	amorphous	8.7	567	60	[111]
AlCoGdHo	amorphous	9.8	626	50	
AlCoGdTb	amorphous	8.9	577	73	
AlCoDyErGd	amorphous	9.1	619	43	[112]
AlCoDyErTb	amorphous	8.6	525	29	
AlCoDyErTm	amorphous	11.9	405	13	
AlCoDyErHo	amorphous	12.6	468	36	[113]
AlCoDyGdTb	amorphous	9.4	632	58	[114]
AlCoErGdHo	amorphous	11.2	627	40	[113]
AlCoErHoTm	amorphous	15	375	32	
AlDyFeGdTb	amorphous	5.9	691	112	[114]
AlDyGdNiTb	amorphous	7.3	507	45	
AlErFeGdHo	amorphous	5.1	446	55	[115]
AlErGdHoNi	amorphous	9.5	511	25	
DyErGdHoTb	<i>hcp</i>	8.6	627	186	[116]
AgAlCoDyEr	amorphous	10.6	532	24	[117]
AlCoCrFeNi	<i>fcc</i>	0.51*	242.6	380	[118]
AlCoCr <sub>0.5</sub> FeNi <sub>1.5</sub>	<i>fcc</i> + <i>bcc</i>	0.277*	275	2T	
CoCuFeMnNi	<i>fcc</i>	0.115**	127	395	[119]
CoCuFeMnNi	<i>fcc</i>	0.8	–	400	[120]
CoCu <sub>0.95</sub> FeMnNi <sub>1.05</sub>	<i>fcc</i>	0.46	~120	280	
CoCu <sub>0.9</sub> FeMnNi <sub>1.1</sub>	<i>fcc</i>	0.39	–	65	

\* @ 2T \*\* @ 0.55T.

### 1.7.3 Hydrogen storage

Hydrogen is a serious candidate to substitute fossil-base fuels in the future because it is one of the most abundant elements, it has a high-energy density, and the oxidation products are environmentally friendly [110]. Alloys designed for hydrogen storage should

be able to store and release appreciable quantities of hydrogen at moderate temperatures and pressures, and capable of resisting pulverization caused by structural changes due to the absorption of hydrogen [7].

One of the early studies on hydrogen storage of HEAs was done by Kao *et al.* [121] in 2010. The  $\text{CoFeMnTi}_x\text{V}_y\text{Zr}_z$  system was investigated. Among other alloys, the  $\text{CoFeMnTiVZr}_{2.3}$  alloy was synthesized. It crystallized into a single phase with a C-14 Laves crystal structure (MgZn<sub>2</sub>-type). The alloy was able to absorb hydrogen at room temperature to a maximum capacity of 1.7 wt. %. The authors concluded that the absorption capacity is linked to the affinity of hydrogen to the alloy's elements, thus, from the alloys designed the one with higher Zr content had higher hydrogen storage capacity. Furthermore, the study revealed the important role of the size of interstitial sites in the kinetic and thermodynamic properties.

Young *et al.* [122] produced the  $\text{Zr}_{21.5}\text{Ti}_{12}\text{V}_{10}\text{Cr}_{7.5}\text{Mn}_{8.1}\text{Co}_{8.1}\text{Ni}_{32.2}\text{Sn}_{0.3}\text{Al}_{0.4}$  and  $\text{Zr}_{25}\text{Ti}_{6.5}\text{V}_{3.9}\text{Mn}_{22.2}\text{Fe}_{3.8}\text{Ni}_{38}\text{La}_{0.3}$  alloys. The former forms mainly a C14 Laves phase while the latter precipitates in a C15 Laves phase (MgCu<sub>2</sub>-type). Reversible capacity at room temperature was determined to be 1.32 and 1.44 wt. %, respectively.

High-entropy alloys with a *bcc* structure have also been investigated. Strozi *et al.* [123] investigated the effect of the addition of non-hydride forming elements on the  $\text{NbTiV}(\text{Z}_x)$  system ( $Z = \text{Cr, Mn, Fe, Co, Ni}$ ). After thermodynamic calculations, Cr was chosen because it would favor *bcc* formation and for its corrosion resistance attributes. Alloys with varying amounts of Cr were synthesized ( $x = 15, 25, \text{ and } 35$  at. %). The alloys revealed a dual-phase *bcc*-matrix plus *fcc*-precipitates microstructure in the as-cast state. At room temperature and at a H<sub>2</sub> pressure of 2000 kPa the alloys could absorb H to a hydrogen-to-metal ratio of 2. After the first hydrogenation, the alloys experienced phase transformations. XRD patterns of the alloys with  $x = 15$  and 25 at. % revealed a *fcc* matrix and Ti-precipitates. The *fcc* matrix is associated with the dihydride phase (CaF<sub>2</sub>-type structure). According to the authors, this is the structure expected for the fully hydrogenated *bcc* phase.

*In situ* XRD experiments have shown that a two-step transformation pathway, as a function of temperature, occurred during hydrogen absorption in the TiZrNbHfTa alloy [124]. Initially, the *bcc* transforms into a body-centered tetragonal monohydride structure, and in sequence to a *fcc*-dihydride. The transformations were shown to be completely reversible as hydrogen was desorbed.

## Chapter 2: Experimental

In this Chapter, the materials and methods used for developing the experimental parts of the thesis are described. Also, a brief description of the EML technique and the physical phenomena involved in the levitation and heating processes are presented.

### 2.1 Sample preparation

All alloys, except the NbTiVZr, described in the experimental procedures in this thesis were fabricated in form of rods (4.5 mm in diameter,  $\approx 100$  mm in length) and prepared from high-purity elements ( $\geq 99.995$  %). The amounts of the constituting raw elements were weighed using a Sartorius laboratory balance with a device accuracy of  $\pm 0.01$  g. An arc-melting furnace (Edmund Bühler GmbH) equipped with a copper mold was used for casting. The furnace was evacuated to  $5 \cdot 10^{-5}$  mbar and backfilled with Ar up to a pressure of 600 mbar. Additionally, a Ti-getter was used to absorb residual oxygen in the furnace. The alloys were flipped and remelted at least four times to ensure chemical homogeneity before casting. The casting occurred by the natural flow by the gravity of the molten alloys into the Cu mold after a certain arc-melting time, without the need to trigger the suction-casting apparatus which is coupled to the furnace. The samples of a required mass or length, depending on compositions and/or experiments, were cut out from the rods using a precision-cutting device (Accutom 50, Struers).

The NbTiVZr samples were prepared as 0.55-1 g spherical-like samples from high-purity elements ( $\geq 99.8$  %) by arc-melting the raw materials mixture in the copper hearth of the same furnace and with the same experimental procedures described above. It was found during preparation that this alloy composition could not be cast into rods with the setup mentioned above because of its higher melting temperature. Before any of the experimental procedures described below, the samples were cleaned in an ultrasonic bath in acetone for 10 minutes. The compositions, in molar fraction and atomic percent, of the medium- and high-entropy alloys investigated are given in table 2.1.



Table 2.1. The composition of the alloys investigated given in molar fraction and atomic percent.

Molar fraction	Atomic %
CrFeNi	$\text{Cr}_{33.33}\text{Fe}_{33.33}\text{Ni}_{33.33}$
CoCrNi	$\text{Co}_{33.33}\text{Cr}_{33.33}\text{Ni}_{33.33}$
CoCrFeNi	$\text{Co}_{25}\text{Cr}_{25}\text{Fe}_{25}\text{Ni}_{25}$
$\text{Al}_{0.3}\text{CoCrFeNi}$	$\text{Al}_{6.96}\text{Co}_{23.26}\text{Cr}_{23.26}\text{Fe}_{23.26}\text{Ni}_{23.26}$
NbTiVZr	$\text{Nb}_{25}\text{Ti}_{25}\text{V}_{25}\text{Zr}_{25}$

The sum of the components in CrFeNi and CoCrNi do not equal 100 at. % because the values are a periodic continued fraction.

To verify the accuracy of alloy preparation, a chemical analysis of a set of as-cast CrFeNi, CoCrNi, CoCrFeNi,  $\text{Al}_{0.3}\text{CoCrFeNi}$ , and NbTiVZr alloys have been done by inductively coupled plasma optical emission spectrometry (ICP-OES) using an iCAP 6500 Duo View (Thermo Fischer Scientific GmbH) device. The chemical analysis was carried out by Mrs. Andrea Voß (IKM-IFW). The results obtained by averaging over three specimens for each composition are given in Table 2.2 and Table 2.3. The concentrations of alloy components deviated by 0.06 – 0.6 at. % from the nominal values. Since the alloy preparation was always kept at similar conditions, it can be assumed that the composition of the samples studied in this work was within these uncertainty limits. It was identified in the NbTiVZr alloy 0.3 % of Hafnium as an impurity element, see Table 2.3.

Table 2.2. Measured chemical composition of the CrFeNi, CoCrNi, CoCrFeNi, and  $\text{Al}_{0.3}\text{CoCrFeNi}$  as-cast alloys.

Alloy	Chemical composition (atomic %)				
	Al	Co	Cr	Fe	Ni
CrFeNi	-----	-----	$33.11 \pm 0.20$	$33.39 \pm 0.17$	$33.49 \pm 0.18$
CoCrNi	-----	$33.29 \pm 0.25$	$33.22 \pm 0.23$	-----	$33.49 \pm 0.26$
CoCrFeNi	-----	$25.02 \pm 0.19$	$24.90 \pm 0.16$	$24.99 \pm 0.18$	$25.09 \pm 0.18$
$\text{Al}_{0.3}\text{CoCrFeNi}$	$6.90 \pm 0.03$	$23.10 \pm 0.21$	$23.10 \pm 0.12$	$23.20 \pm 0.19$	$23.20 \pm 0.19$

The sum may not equal 100 % as they are average numbers over 3 measurements.

The origin of this impurity should be the raw Zr rod. Hf and Zr have the same crystal structure, comparable electronegativity, atomic radius, and similar physical properties [125], which leads to believe that the small amount of Hf will not influence the results of this study.

Table 2.3. Measured chemical composition of the NbTiVZr as-cast alloy.

Alloy	Chemical composition (atomic %)				
	Nb	Ti	V	Zr	Hf
NbTiVZr	24.80 ± 0.17	24.90 ± 0.10	24.80 ± 0.15	24.40 ± 0.45	0.3 ± 0.00

The sum may not equal 100 % as it is an average number from 3 measurements.

## 2.2 Electromagnetic levitation

Levitation is defined in the Cambridge dictionary as “to rise and float in the air without any physical support”. The first theoretical description of high-frequency EML was presented by Muck in 1923 [126]. The first experimental results by a levitation technique were reported by Okress, Wroughton, and Comenetz in 1952 [127]. Following their pioneering experiments, levitation techniques have been used for studies in different areas of metallurgy such as alloy preparation, metal purification, vapor plating, sintering, measurement of liquid-metal densities and emissivity, viscosity measurements, liquid undercooling, and alloy thermodynamics [128].

EML is the most suitable levitation technique for metallic materials. The levitation process occurs because of the induction of eddy currents in an electrically conducting material when the metal droplet experiences a time-dependent magnetic field  $B$  (Lenz rule) [10]:

$$\nabla \times E = \frac{\partial B}{\partial t} \quad (\text{Eq. 2.1})$$

where  $E$  is the electrostatic field. For a non-uniform magnetic field, the eddy currents induced in a sample create a magnetic dipole moment  $m$  that is opposite to the primary field  $B$ . This leads to a diamagnetic repulsion force  $F_r$  between the sample and the primary field as can be visualized in Fig. 2.1:

$$F_r = -\nabla(m \cdot B) \quad (\text{Eq. 2.2})$$

being the repulsion force equal and with opposite direction to the gravitational force,  $F_r = m_g \cdot g$ , where  $m_g$  and  $g$  represent the mass of the sample and the gravitational force, respectively. The levitation and heating processes are coupled in EML and the advantage is that there is no need for an external heating source, while the disadvantage is that control of

the heating process is limited to a narrow range.

The average force on an electrically conductive non-ferromagnetic sample is determined by:

$$F_{em} = -\frac{4\pi r}{3} \cdot \frac{B \cdot \nabla B}{2\mu_0} \cdot G(q) \quad (\text{Eq. 2.3})$$

where  $r$  represents the radius of the sphere and  $\mu_0$  the permeability of vacuum. The term  $G(q)$  is determined by:

$$G(q) = \frac{3}{4} \left( 1 - \frac{3 \sinh(2q) - \sin(2q)}{2q \sinh(2q) - \cos(2q)} \right) \quad (\text{Eq. 2.4})$$

$q$  is the ratio of the sample  $r$  and the skin depth  $\delta_{sd}$ :

$$q = \frac{r}{\delta_{sd}} \quad \text{with} \quad \delta_{sd} = \sqrt{\frac{2}{\mu\omega\sigma}} \quad (\text{Eqs. 2.5 and 2.6})$$

The skin depth represents the surface thickness of a conductive sample whose direct current DC resistance is equivalent to the total alternate current AC resistance. It is defined as the depth below the surface of a sample where the current density or magnetic field strength has decreased to  $e^{-1}$  (37% of its value at the surface) [129]. Being  $\omega$ ,  $\sigma$ , and  $\mu$  the angular frequency of the electrical current, the electrical conductivity, and the magnetic permeability of the sample, respectively. As can be seen from Eq. 2.3 the levitation force is proportional to the gradient of the magnetic field. For the levitation process it is essential a proper design of the levitation/induction coil geometry and to optimize the function  $G(q)$  (Eq. 2.4). The efficiency of electromagnetic levitation is adjusted by the parameters of the frequency of the alternating electromagnetic field, the sample size, and the electrical conductivity of the sample.

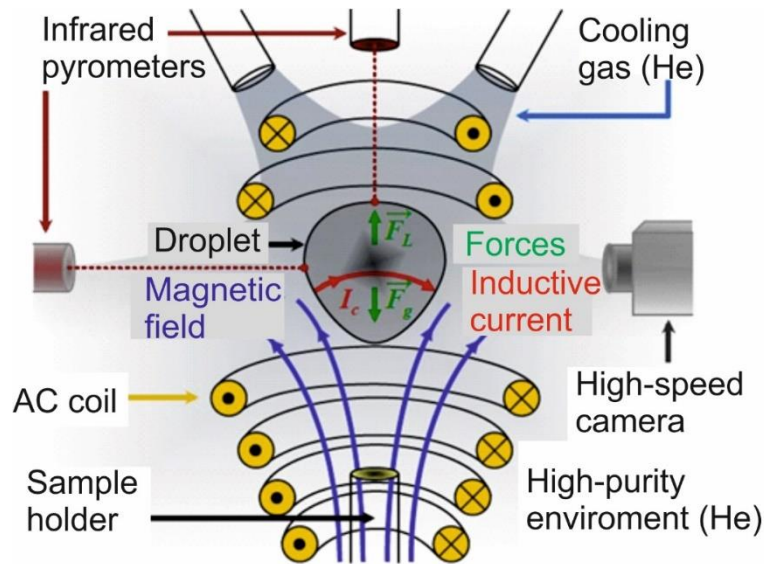


Figure 2.1. Schematic representation of electromagnetic levitation; the droplet is placed in a levitation coil consisting of four water-cooled windings and two counter windings at the top to stabilize the position of the levitated drop. The arrows give the geometry of the magnetic field inside the coil.  $F_L$  and  $F_g$  denote the levitation force and the gravitational force while  $I_c$  is the current induced in the droplet by the alternating electromagnetic field. Adapted from [10].

In EML, due to containerless processing in a high-purity inert-gas atmosphere, heterogeneous nucleation in a molten sample can essentially be suppressed, and undercooling up to several hundred Kelvin can be reached before solidification. Furthermore, simultaneous use of different *in situ* measurement techniques such as thermal analysis by pyrometer, high-speed video (HSC), and high-energy synchrotron XRD [130] enables obtaining a comprehensive picture of solidification as well as for the phase transformations upon heating/cooling of the solid sample.

Non-equilibrium solidification studies were carried out using a mobile EML facility. A schematic illustration of the device is given in Figure 2.2. Spherical- or cylindrical-like samples (4-7 mm in diameter or 6-9 mm in length,  $\approx 0.55$ -1 g in weight) were electromagnetically levitated and induction heated using a specially shaped water-cooled coil made of copper tube with an inner diameter of 1 mm and an outer diameter of 2 mm. A high-frequency generator TruHeat HF 3010 from Hüttinger Elektronik (10 kW) was operated at 280 kHz. The experimental chamber was evacuated to better than  $5 \cdot 10^{-6}$  mbar and backfilled with high purity He (6N) to 500-700 mbar. An active sample cooling was done by two He gas jets (6N purity) directed to the sample surface from opposite sides with a flow of up to  $28 \text{ l} \cdot \text{min}^{-1}$ . The samples were weighed before and after the experiments,

and the maximum mass loss was determined to be  $\leq 0.2$  wt. %.

The behavior of the levitated samples during EML processing was recorded with a high-speed camera FASTCAM SA5, model 775K-M3 from Photron, at speeds between 1000 and 50000 fps (frames per sec). The image size, in pixels, is dependent on the speed chosen and varied between  $1024 \times 1024$  and  $524 \times 218$ . Time-temperature profiles were acquired using a single-color pyrometer with a sampling rate of 20 ms. The sample emissivity was calibrated to reproduce the liquidus temperature ( $T_l$ ) of each alloy measured by differential scanning calorimetry (DSC).

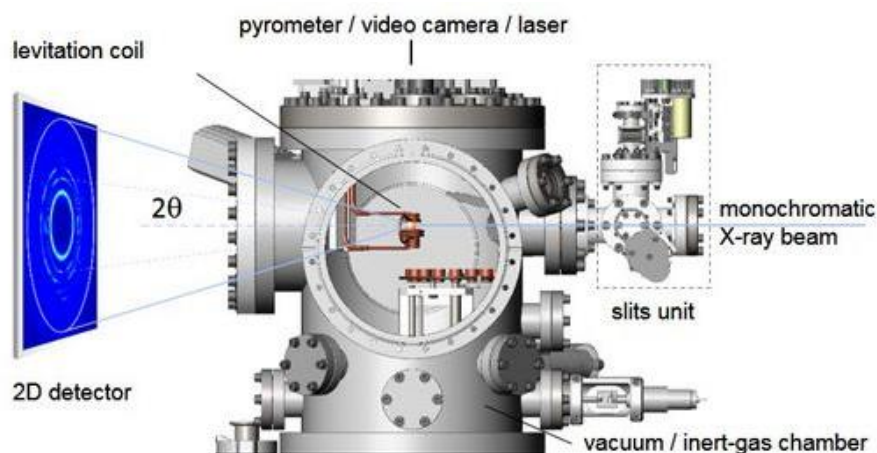


Figure 2.2. Schematic representation of the IFW-EML facility.

### 2.3 *In situ* X-ray diffraction

Temperature- and time-resolved high-energy XRD measurements have been performed on electromagnetically levitated samples at the beamline P21.1 (PETRA III, DESY Hamburg) using the IFW-EML facility. The EML processing parameters were the same as those for in-house experiments described in section 2.2. The diffraction experiments were carried out in transmission mode; the energy of photons and the beam size were 101.55 keV and  $1.1 \times 1.1$  mm<sup>2</sup>, respectively. Two-dimensional (2D) XRD patterns were taken by a hybrid pixel PILATUS3 X2M CdTe detector (DECTRIS) with sampling rates of 20, 250, or 500 Hz, depending on alloy composition and the processing conditions. Using the FIT2D software [131], the recorded 2D images were azimuthally integrated to obtain XRD intensities as functions of the diffraction vector  $Q = \frac{4\pi \sin \theta}{\lambda}$ , where  $2\theta$  is the diffraction angle and  $\lambda$  is the wavelength. Figure 2.3 shows the actual experimental setup for *in situ* X-ray diffraction studies that occurred at DESY in November 2019.

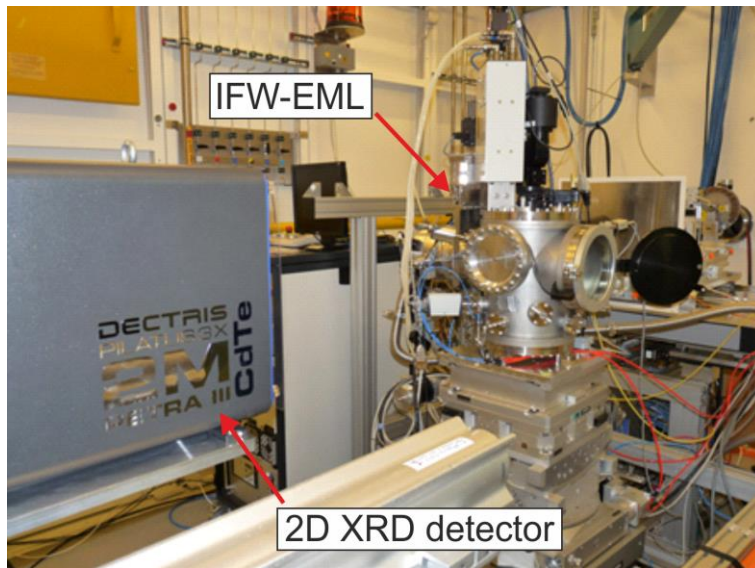


Figure 2.3. Experimental setup for *in situ* X-ray diffraction studies at DESY. In the image, one can see the mobile EML facility and the Pilatus detector.

## 2.4 Microstructural and structural analysis

The microstructure and phase constitution of the solidified samples were studied using a scanning electron microscope (SEM) and laboratory XRD. For this, the samples were cut using a cut-off device, and the specimens for microstructure analysis were prepared by a standard metallographic procedure using SiC grinding paper up to P4000 grit size, diamond polishing suspensions with 3, 1, and 0.25  $\mu\text{m}$  particle size, and 0.05  $\mu\text{m}$  colloidal silica final polishing. XRD measurements of cross-sectioned samples were done using a PANalytical X'Pert Pro diffractometer with a Co-anode (current: 40 mA, voltage: 40 kV,  $2\theta$ -range:  $20^\circ - 120^\circ$ ). The diffraction patterns were analyzed using the X'Pert HighScore Plus software [29].

Room temperature high-energy synchrotron XRD was measured on the cross-sectioned samples of the NbTiVZr RHEA at the P21.1 beamline at DESY (1 x 1 mm beam,  $\lambda = 0.122 \text{ \AA}$ ). The diffraction patterns were analyzed using the X'Pert HighScore Plus program [132] and the lattice constants were calculated with the UnitCell software [133].

A ZEISS Gemini field emission SEM device was always operated at 20 keV. SEM micrographs were recorded either in the secondary-electron (SE) or electron backscattered (BSE) modes. Electron backscatter diffraction (EBSD) patterns were recorded with a  $70^\circ$  tilt of the sample, at a detector distance of 16-18 mm, accelerating voltage of 20 keV, exposure time of 20-45 ms, and a step size of 0.5-1.5  $\mu\text{m}$ . The SEM device is coupled with an energy-dispersive X-ray spectroscopy (EDX) detector which has been used with the following

parameters: 10 mm working distance, a spot size of 60  $\mu\text{m}$ , and 20 keV accelerating voltage to create elemental maps.

Transmission electron microscopy (TEM) samples were prepared as follows. First, cross-sections of the sphere-like samples processed in the EML were thinned by grinding to 100  $\mu\text{m}$ . Next, thin cross-sections in the range of approximately 50-80 nm (electron-transparent) were obtained from these ground samples by ion beam milling using a focused ion beam (FIB) in the SEM, after which these thin cross-sections were fixed onto a TEM grid. The specimens were placed in a TEM single-tilt holder and measured using an FEI F30 TEM operating in a conventional mode at an acceleration voltage of 300 kV and a Thermo Fisher Scientific Talos F200X operating in conventional and scanning modes at an acceleration voltage of 200 kV. The TEM images were analyzed and processed using the FEI TEM Imaging and Analysis, Thermo Fisher Scientific Velox software, and Gatan Digital Micrograph package. The selected area electron diffraction (SAED) patterns collected in the TEM were indexed using the software ELDISCA C# [134]. The TEM analysis was performed in collaboration with Dr. Rafael G. Mendes (IFW-Dresden, Utrecht University).

## 2.5 Thermal analysis

The DSC measurements for determining the liquidus  $T_l$  and solidus  $T_s$  temperatures of the alloys investigated were carried out with samples of  $\sim 10$  mg using a Netzsch-DSC 404 C device. The scans were obtained during heating and cooling cycles at a rate of  $20 \text{ K} \cdot \text{min}^{-1}$  under Ar-flow after a preliminary evacuation of the experimental chamber to about  $10^{-4}$  mbar.

The DSC measurements for determining the specific heat capacity at constant pressure  $C_p$  of CoCrFeNi, CrFeNi, and CoCrNi alloys were performed on samples with  $\sim 40$  mg using a Netzsch-DSC 404 C device according to the sapphire method described by ASTM International [135]. The DSC scans were recorded during two, non-stop, heating and cooling cycles with a rate of  $10 \text{ K} \cdot \text{min}^{-1}$  from room temperature to 973 K. The  $C_p$  was calculated using the Netzsch Proteus<sup>®</sup> software according to the method described by Ref. [135].

## 2.6 Dilatometry

Thermal expansion measurements were carried out using a Netzsch Dil 402 C

dilatometer from room temperature to 1263 K at a  $10 \text{ K} \cdot \text{min}^{-1}$  heating and cooling rate. The measurements were done on 25 mm long rods, cast according to section 2.1, under an Ar atmosphere using a sample holder and a pushrod made of fused silica. The equipment was calibrated using fused silica standard specimens from Netzsch. The data analysis was performed using the Netzsch<sup>®</sup> Proteus software.

## 2.7 Magnetic moment

The temperature-dependent magnetic moment was measured on cast samples of CoCrFeNi, CrFeNi, and CoCrNi (1 mm length and 4.5 mm diameter) by heating-cooling cycles ( $5 \text{ K} \cdot \text{min}^{-1}$ ) in the temperature range of 10-900 K. Since it was not possible to measure the entire temperature range at once, two separate measurements were performed (10-350 K and 300-900K). Measurements were done with an applied magnetic field of 1000 Oe with the Vibrating Sample Magnetometer (VSM) option of a Quantum Design Physical Property Measurement System (PPMS).

## 2.8 Heat treatment

Based on the DSC curves of the CoCrFeNi, CrFeNi, and CoCrNi alloys, as-cast samples were thermally-treated as described: aged for 24 hours at 973 K under a continuous Ar flow (not sealed in quartz tube) and subsequently water-quenched. The heating rate was  $6.66 \text{ K} \cdot \text{min}^{-1}$ .



## Chapter 3: *In situ* study of non-equilibrium solidification of CoCrFeNi high-entropy alloy and CrFeNi and CoCrNi ternary suballoys

In this first results Chapter, non-equilibrium solidification of the equiatomic CoCrFeNi, CrFeNi, and CoCrNi alloys was studied. Special attention was given to describe phase selection, crystal growth kinetics, and microstructure formation under different liquid undercooling. The results of this Chapter have been published in Ref. [130].

### 3.1 Introduction

As discussed in Chapter 1, five-component CoCrFeMnNi [89], quaternary CoCrFeNi [91], and ternary CoCrNi [92] and CrFeNi [93] alloys exhibit a simultaneous increase of tensile strength and ductility upon decreasing temperature and are interesting for low-temperature applications. Besides the specific features of CoCrFeNi, CoCrNi, and CrFeNi alloys, these compositions make a base for a large class of HEAs (3d-transition metals) and have been therefore extensively studied so far.

It has been widely accepted that CoCrFeNi alloy forms a SPSS with a *fcc* structure when processed by different routes such as casting [136], quenching and subsequent annealing [137], recrystallization [138], selective laser melting [139], or sputtering [140]. However, there are also reports on the existence of at least two distinct phases in CoCrFeNi HEA and ternary, so-called medium-entropy alloys (MEAs).

Dahlborg *et al.* [141] studied as-cast and annealed CoCrFeNi samples (3 h annealing at 673 K, 973 K, or 1373 K) with high-energy X-ray diffraction (XRD) and concluded about the coexistence of two *fcc* phases with remarkably similar lattice constants after analysis of a diffraction peak asymmetry in the as-cast samples. Using transmission electron microscopy, He *et al.* [142] also observed two *fcc* phases with close lattice constants in CoCrFeNi annealed for 800 h at 1023 K. However, Christofidou *et al.* [143], who later observed the same lenticular features in an annealed CoCrFeNi alloy, argued that the features observed by He *et al.* [142] are more likely to be stacking faults due to their same composition to the matrix.

Minor *bcc* phase was identified at the grain boundaries of the *fcc* matrix in a recrystallized CrFeNi alloy (1 h annealing at 1173 K after preliminary homogenization and swaging) in the work of Laplanche *et al.* [144], whereas only *fcc* solid solution was found in CoCrNi and CoCrFeNi alloys processed in the same manner. Regarding the CoCrNi alloy,

there are no reports in the literature about the presence of a secondary phase upon liquid state processing.

Precipitates of a minor *bcc* phase in the *fcc* matrix were also reported for CoCrFeNi solidified after melt undercooling in the works of Li *et al.* [145], Wang *et al.* [146], and Zhang *et al.* [147], solidified using B<sub>2</sub>O<sub>3</sub> glass fluxing. Only a single *fcc* solid solution was observed in the ternary CoFeNi and binary CoNi alloys in Ref. [147].

As introduced in Chapter 1, it was initially supposed that a high configurational entropy plays a dominant role in the stabilization of SPSSs in HEAs [4], whereas later studies showed that this is essentially an overestimated assumption [16,19]. Kube and Schroers have suggested in a recent paper [18] that SPSS structure in most, if not all, HEAs is metastable and is formed through a polymorphic solidification upon rapid cooling.

Given the just mentioned, contradicting results, investigation of phase formation, temperature-dependent transformations, and microstructure development upon solidification of HEAs and MEAs, such as CoCrFeNi, CrFeNi, and CoCrNi, studied in the present thesis, are of high interest. A metastable solidification regime was achieved by using the electromagnetic levitation technique described in section 2.2. Extensive studies of undercooling and metastable solidification have been carried out for a variety of classical metallic alloys so far, e.g., see Ref. [128]. However, there are just a few reports on phase selection, crystal growth kinetics, and microstructural evolution in undercooled HEAs and MEAs, which additionally motivates the present study.

## 3.2 Results

### 3.2.1 *In situ* synchrotron X-ray diffraction

A typical 3D plot showing XRD intensities  $I(Q)$  measured from a levitated CoCrFeNi sample during a heating-cooling cycle is presented in Fig. 3.1. The XRD patterns were captured at the highest speed-mode (500 fps) of the PILATUS3 X 2M detector. The measurement over a 50 s time-interval, limited by the detector's memory at this frequency, started at about 625 K upon heating and finished at about 870 K upon cooling. There are patterns with decreasing height of the Bragg peaks measured from the solid sample during heating, patterns with broad diffuse maxima from the melt, and patterns with re-appearing and increasing reflections from crystalline phases taken upon solidification and cooling. The apparent increase of the intensity of crystalline reflexes observed during melting (approximately from 17th to 25th s) is due to the movement of the remaining solid phase to

the equator of the rotating semi-solid sample, i.e., into the X-ray beam. The crystalline reflexes decrease and disappear upon continuing to melt. It must be mentioned that the sample position is rather unstable during melting, which also contributes to the variations of the measured XRD intensity. The XRD data obtained with the same detector parameters for CrFeNi, CoCrNi, and CoCrFeNi alloys are shown as 2D time-intensity contour plots together with the correspondent thermograms in Figs. 3.2a – 2c. Such data presentation is more convenient for data analysis and comparison.

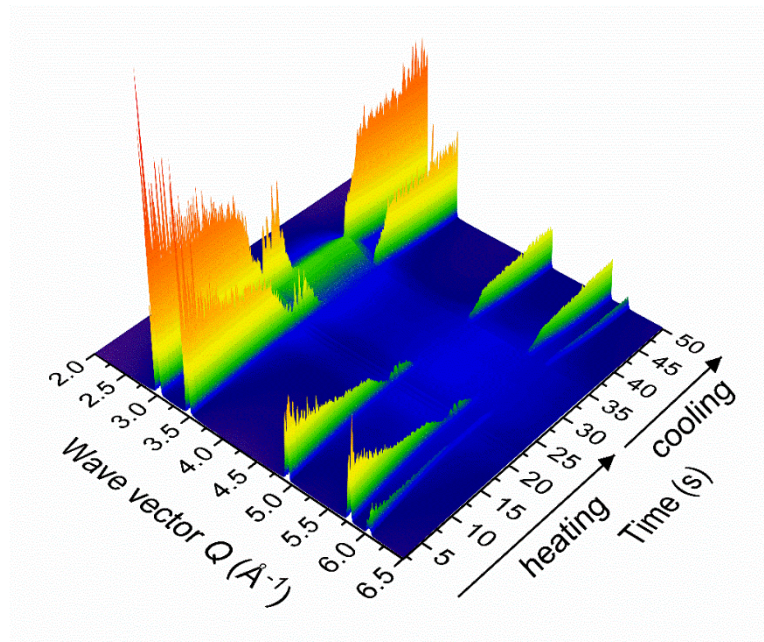


Figure 3.1. 3D plot showing XRD intensities  $I(Q)$  measured from an electromagnetically levitated CoCrFeNi sample during a heating-cooling cycle; the melt was undercooled by 135 K upon solidification as shown in Fig. 3.2c.

A distinct thermal arrest appearing on the  $T(t)$  curves (Figs. 3.2a – 3.2c) measured upon heating corresponds to the sample melting, occurring within a narrow temperature interval between the solidus and liquidus temperatures  $T_s$  and  $T_l$ . This event, correlated with the respective data obtained by DSC (Table 3.1), is used for the adjustment of the temperature measured by the pyrometer. The DSC scans are shown in Fig. 3.3.

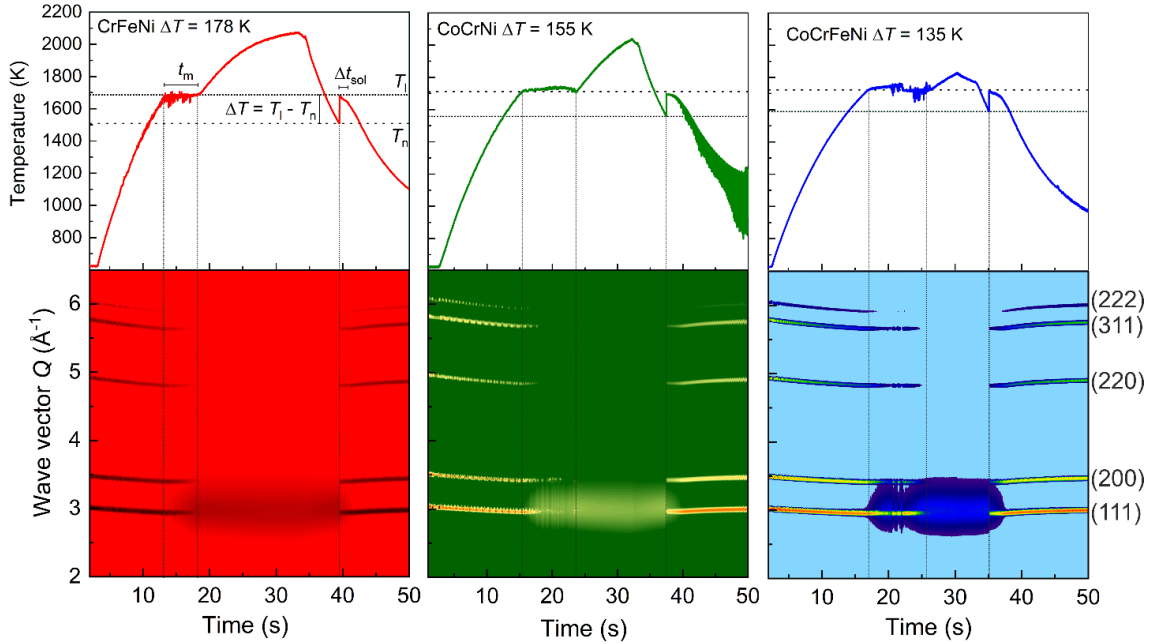


Figure 3.2. (a) - (c) Thermograms and corresponding XRD contour plots measured from levitated (a) CrFeNi, (b) CoCrNi, and (c) CoCrFeNi samples. Labels in panel (a):  $T_l$  – liquidus temperature,  $T_n$  – temperature of the melt at a maximum undercooling;  $\Delta t_m$  and  $\Delta t_{sol}$  – time intervals corresponding to the sample melting upon heating and solidification after recalescence upon cooling.

Once molten, the sample is further heated well above  $T_l$  and cooled at a rate of about  $80 - 130 \text{ K} \cdot \text{s}^{-1}$  by reducing the electric current in the induction coil and by applying the gas-jet cooling. Due to the containerless processing, high-purity elements used for sample preparation, and high-purity sample environment the levitating molten alloy is undercooled below the  $T_l$  without crystallization. Spontaneous nucleation occurring at a temperature  $T_n$  below the liquidus is accompanied by a steep temperature rise due to the fast, quasi-adiabatic latent heat release from the crystallizing sample, as observed on the cooling part of  $T(t)$  curves in Figs. 3.2a – 3.2c. In most experiments, the sample undercooling  $\Delta T = T_l - T_n$  was in a range of about 70 K to 170 K. The largest  $\Delta T$  value of 230 K was achieved in an experiment with the CoCrNi alloy.

After recalescence, the sample temperature decreases again: relatively slowly until the solidification of the remaining liquid is completed (the corresponding time interval  $\Delta t_{sol}$  is marked on the  $T(t)$  curve in Fig. 3.2a), and faster for the solid sample. The slope on  $T(t)$  in the solidification regime depends on the level of undercooling and therefore, on the fraction of the remaining liquid, as demonstrated for a CrFeNi sample in Fig. 3.4.

The measured XRD patterns follow the respective temperature-time curves (Figs. 3.2a – 3.2c). There are patterns with decreasing height of the Bragg peaks measured during

heating and melting, patterns with broad diffuse maxima from the melt, and patterns with re-appearing and increasing crystalline reflections taken upon sample solidification and cooling. For all three compositions studied, the measured crystalline reflections correspond to the *fcc* structure only; no other reflections could be found neither on the XRD plots shown in Figs. 3.1 and 3.2a – 3.2c, nor on those obtained in other runs. The positions of the Bragg peaks shift to smaller or larger  $Q$ -values due to the thermal expansion/contraction if the sample temperature changes.

Table 3.1. Solidus and liquidus temperature,  $T_s$  and  $T_l$ , for CoCrFeNi, CrFeNi, and CoCrNi alloys obtained from DSC scans measured during heating at  $20 \text{ K} \cdot \text{min}^{-1}$ .

	Composition		
	CrFeNi	CoCrNi	CoCrFeNi
$T_l$ (K)	1686	1712	1723
$T_s$ (K)	1671	1692	1704

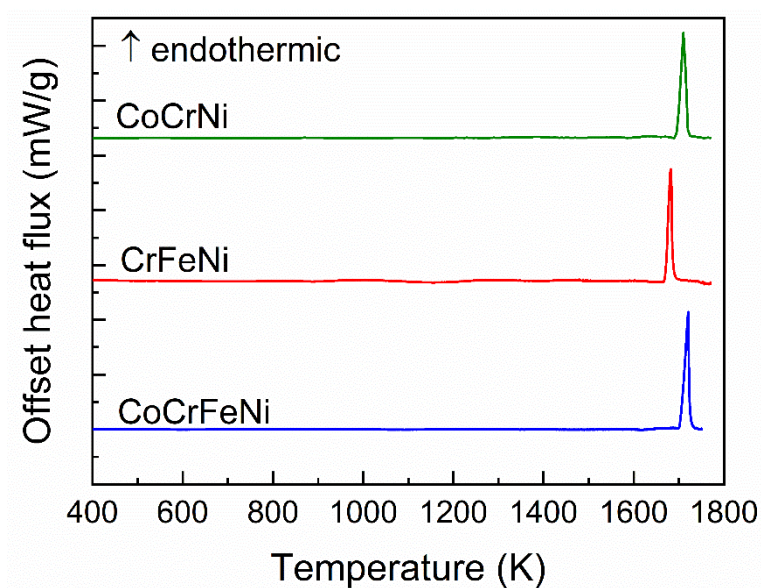


Figure 3.3. DSC scans measured on CoCrNi, CrFeNi, and CoCrFeNi alloys at a heating rate of  $20 \text{ K} \cdot \text{min}^{-1}$ .

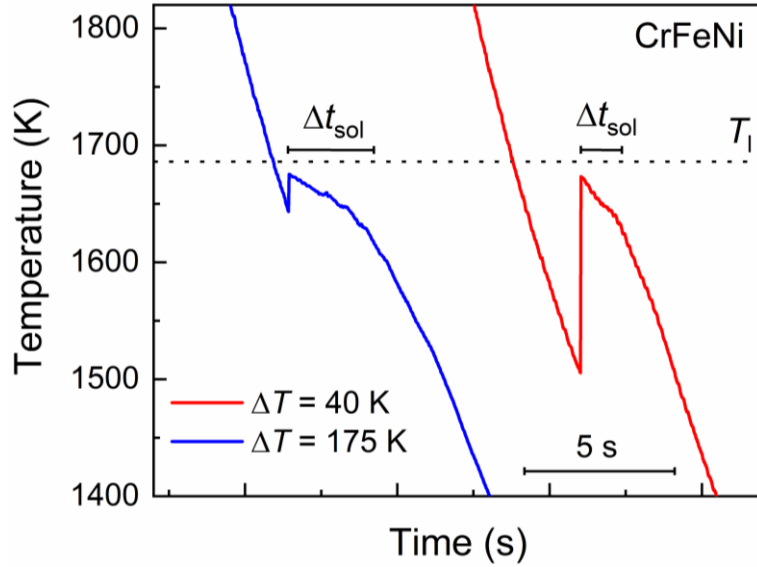


Figure 3.4. Recalescence and crystallization of CrFeNi melt at different undercooling  $\Delta T$ .  $\Delta t_{\text{sol}}$  – time required for the solidification of the residual liquid.  $\Delta t_{\text{sol}}$  is determined from the end of recalescence until a change of slope in the  $T(t)$  curves.

### 3.2.2 High-speed video imaging

#### *Phase selection*

Selected digital images representing the solidification of CrFeNi, CoCrNi, and CoCrFeNi melts at low and large undercooling are shown in Figs. 3.5a – 3.5f. Detailed image sequences are available in Appendix 2 (Video montages A2.1 – A2.6).

Each series in Fig. 3.5 begins with an image taken from a levitated molten sample shortly before crystallization. For convenience, the time scale was set to zero at this point. Due to the higher temperature of a crystallized phase (recalcescence), it appears as a brighter spot in the background of the darker liquid. At a lower undercooling (Figs. 3.5a, 3.5c, 3.5e, video montages A2.1, A2.3, and A2.5 in Appendix 2) only one solid phase nucleating and expanding over the sample surface with time is observed. At a larger undercooling (Figs. 3.5b, 3.5d, 3.5f, video montages A2.2, A2.4, and A2.6 in Appendix 2) another bright spot corresponding to a second crystalline phase comes out from the primary phase and quickly overtakes it, growing through the whole sample. This essentially differs from the results of *in situ* XRD measurements in which only one crystalline phase (*fcc*) could be identified for all compositions and undercooling investigated. Also, only one crystallization (recalcescence) event is observed on the thermograms measured by the pyrometer. The reason for 'unseeing' the two-step crystallization at a larger undercooling, neither by *in situ* XRD nor pyrometry, is the noticeably short lifetime ( $< 2$  ms) of the primary phase (see Figs. 3.5b, 3.5d, 3.5f, and

the corresponding video montages in Appendix 2). The time resolution of the XRD detector at the highest speed mode is 2 ms and the pyrometer is 20 ms.

Table 3.3. Statistics on the high-speed videos taken from the levitated samples and observed crystal phases. The values refer to the number of cases when one or another phase has been observed to nucleate primarily in the undercooled melt.

	CrFeNi	CoCrNi	CoCrFeNi
Videos analyzed	45	47	56
Nucleation observed	18	19	17
Primary <i>bcc</i>	14	9	13
Primary <i>fcc</i>	4	10	4
Double recalescence ( <i>bcc-fcc</i> ) (%)	78	47	76
Single recalescence ( <i>fcc</i> ) (%)	22	53	24

In total, 45 high-speed videos were recorded for CrFeNi composition, 47 videos for CoCrNi composition, and 56 videos for CoCrFeNi composition. Crystal nucleation could be detected on about one-third of the videos when it occurred on a sample side viewed by the camera. Detailed statistics are given in Table 3.3.

To estimate possible composition changes during the high-temperature processing in the EML facility, a dedicated study of the mass loss has been carried out. For this, the samples of the three alloys were weighed before and after each heating-cooling cycle. Six CrFeNi, five CoCrNi, and nine CoCrFeNi samples were studied in the case of a single cycle, and two to six samples for the higher number of cycles. The mean values of the mass loss were calculated based on the experiments carried out. The results presented in Table 3.4 show that the mass loss was < 0.05 % after two cycles, < 0.1 % after three cycles, and ≤ 0.2 % after four cycles, considering all alloys. As the densities of Co, Cr, Fe, and Ni are quite similar, it can be safely concluded that the sample composition changes are of the same order.

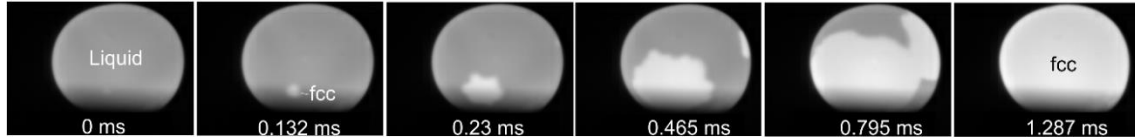
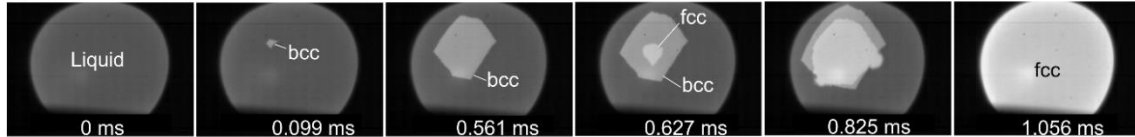
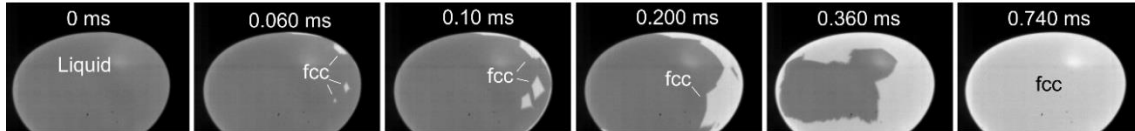
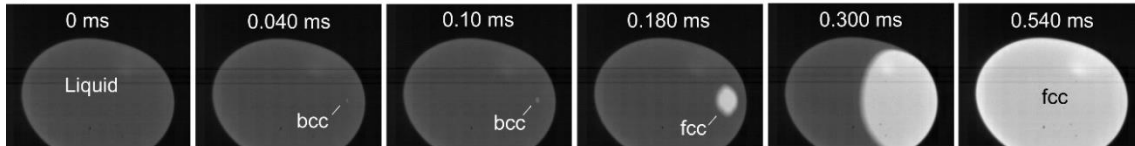
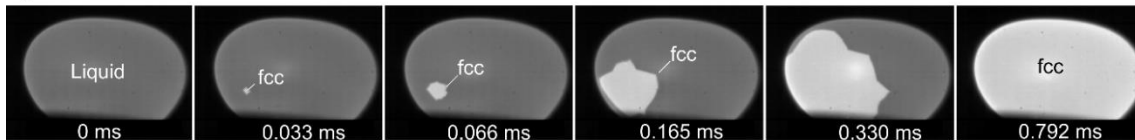
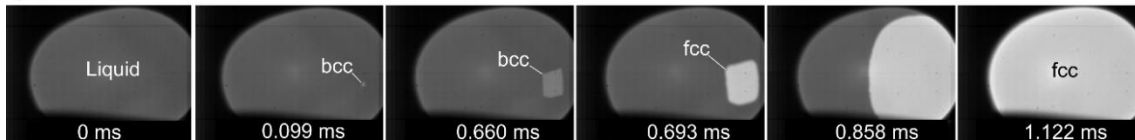
a) CrFeNi  $\Delta T = 70$  Kb) CrFeNi  $\Delta T = 138$  Kc) CoCrNi  $\Delta T = 84$  Kd) CoCrNi  $\Delta T = 155$  Ke) CoCrFeNi  $\Delta T = 120$  Kf) CoCrFeNi  $\Delta T = 150$  K

Figure 3.5. Digital images representing different solidification modes of CrFeNi (a, b), CoCrNi (c, d), and CoCrFeNi (e, f) melts at low (a, c, and e) and large undercooling (b, d, and f).  $\Delta T$  is the undercooling temperature. For each image series, the time scale was set to zero at a moment shortly before the crystallization onset.

Table 3.4. Relative changes of the sample mass after heating-cooling processing in EML facility: the mean values and the experimental standard deviations of the mean. The relative values are calculated with respect to the sample mass before the first heating.

Alloy	Relative mass change (%)				
	Number of heating-cooling cycles				
	1	2	3	4	5
CrFeNi	$-0.02 \pm 0.01$	$-0.02 \pm 0.01$	$-0.09 \pm 0.04$	$-0.20 \pm 0.03$	–
CoCrNi	$0.00 \pm 0.00$	$-0.02 \pm 0.01$	$0.00 \pm 0.00$	$-0.05 \pm 0.04$	$-0.02$
CoCrFeNi	$-0.02 \pm 0.01$	$-0.04 \pm 0.01$	$-0.04 \pm 0.02$	$-0.10 \pm 0.05$	$-0.14 \pm 0.05$



The temporal resolution of phase formation can be essentially increased by extracting the sample temperature from the grayscale level of the high-speed video data. The relationship between the gray value  $H$  of a pixel or selected area on a digital image and the temperature  $T$  on the sample surface can be written by Eq. 3.1 as shown by Wang *et al.* [148]:

$$H = A \cdot e^{-\frac{a}{T}}, \quad (\text{Eq. 3.1})$$

where  $A$  and  $a$  are constants. Thus, considering a linear correlation between  $\ln H$  and  $\frac{1}{T}$  and having the temperature of the melt just before and after the recalescence event measured by a pyrometer, the intermediate temperatures can be calculated with the same temporal resolution as that of the corresponding high-speed video data.

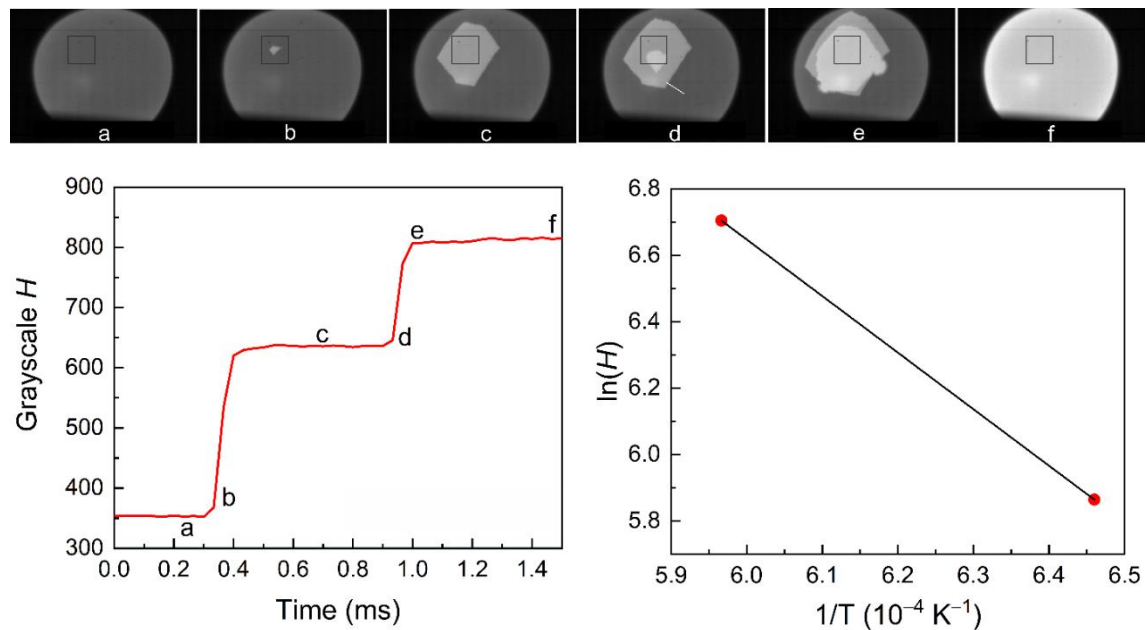


Figure 3.6. The determination of the sample temperature using a grayscale analysis of the digital images taken by a high-speed video camera during solidification of the CrFeNi alloy,  $\Delta T = 138$  K. *Upper panel* – selected area for grayscale analysis marked by a rectangle. *Bottom left panel* – grayscale values  $H$  extracted from the area marked in the upper panel. *Bottom right panel* – grayscale values corresponding to the temperature of the levitated sample just before and after the recalescence event measured by pyrometer (minimum and maximum temperature on  $T(t)$  curves) and linear interpolation of  $\ln H$  between the two temperatures on the inverse scale.

To account for all phases (liquid, solid one, and solid two), a pixel area of 10 x 10 pixels in the center of the primary crystalline phase has been selected and analyzed as shown in Fig. 3.6. The gray values of the selected pixel area were determined using the Fiji ImageJ program [149].

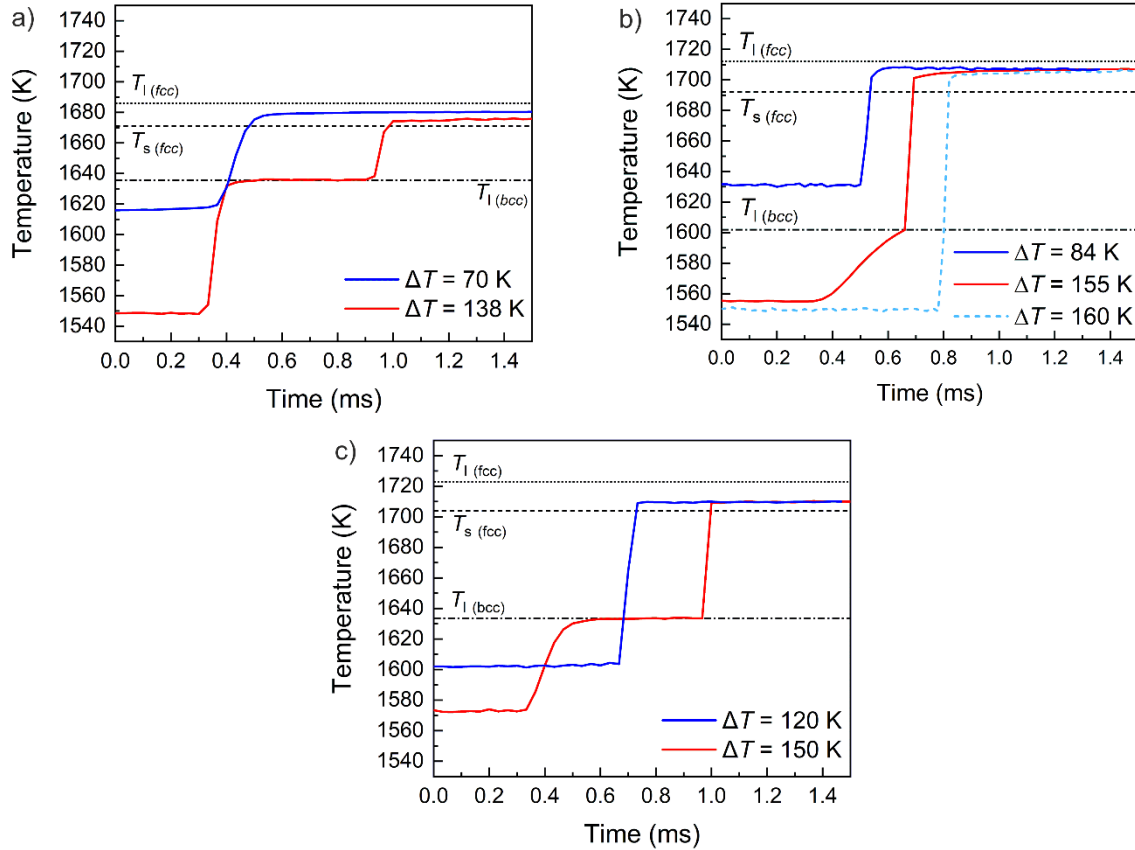


Figure 3.7. Time-temperature profiles derived from the grayscale analysis from high-speed digital video data taken during solidification of undercooled liquid alloys: a) CrFeNi; b) CoCrNi; c) CoCrFeNi.

The high-resolution time-temperature curves obtained by the gray level analysis of the video data for CrFeNi, CoCrNi, and CoCrFeNi melts (Video montages A2.1 – A2.7 in Appendix 2) are plotted in Fig. 3.7. The  $T(t)$  curves corresponding to the samples undercooled to smaller  $\Delta T$  are characterized by just one step temperature increase due to a single recalescence event. In contrast, the  $T(t)$  curves for the samples with larger undercooling exhibit a two-step temperature increase related to a sequence of two recalescence events. However, due to the stochastic nature of the nucleation process, a double recalescence has not always been observed at a large undercooling as it can be seen, for example, on the  $T(t)$  curves for CoCrNi solidifying at  $\Delta T$  of 155 K and 160 K (Fig.

3.7b). Above a critical undercooling the formation of both, stable *fcc* and metastable *bcc* phases, is thermodynamically possible. As a result, a single recalescence due to direct *fcc* formation has been detected at the undercooling where double recalescence is observed, but not vice versa (Fig. 3.8).

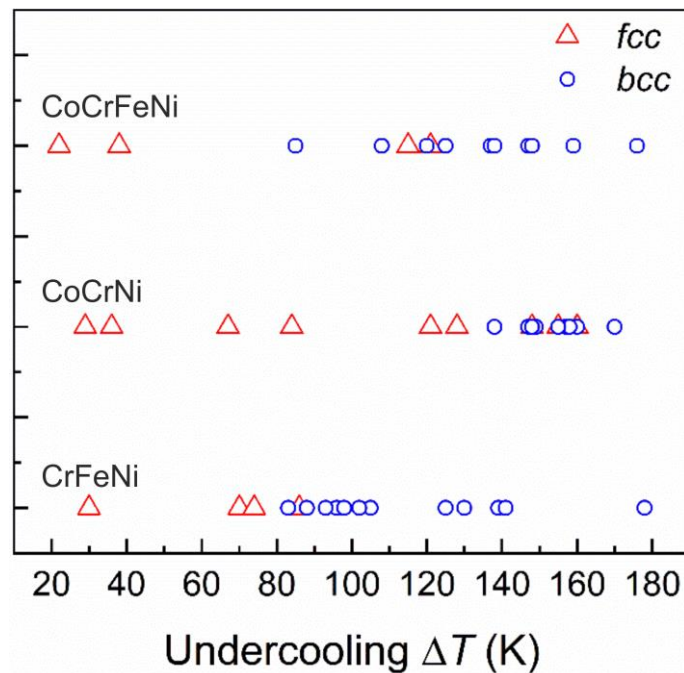


Figure 3.8. Formation of primary *bcc* or *fcc* phases in CrFeNi, CoCrNi, and CoCrFeNi melts depending on liquid undercooling.

A double recalescence occurring during solidification of deeply undercooled Fe-based melts has been observed earlier, e.g., in Fe-Co alloys by Rodriguez *et al.* [150] and Herman *et al.* [151], and in the Fe-Cr-Ni system by Koseki and Flemings [152], and Matson *et al.* [153]. Based on the thermodynamics considerations and microstructure analysis of the solidified samples it was concluded about a transient crystallization with the formation of a metastable *bcc* phase followed by a stable *fcc* phase. The *in situ* XRD diffraction studies of non-equilibrium solidification of a Fe<sub>72</sub>Cr<sub>16</sub>Ni<sub>12</sub> (wt. %) alloy [154] have unambiguously proven that it was a *bcc* phase formed under a large undercooling. It is worth noting that the morphology of the primary phase formed in deeply undercooled CrFeNi, CoCrNi, and CoCrFeNi melts is the same as that of the *bcc* phase in the Fe<sub>72</sub>Cr<sub>16</sub>Ni<sub>12</sub> undercooled melt, identified by *in situ* XRD. Compare, for example, Fig. 4 in Ref. [154] and Fig. 3.5 and corresponding Video montage sequences (A2.1 – A2.6) in Appendix 2.

It is, therefore, reasonable to conclude that the just described phase formation sequence ( $bcc \rightarrow fcc$  at a large undercooling; single  $fcc$  at a low undercooling) is valid for the CrFeNi, CoCrNi, and CoCrFeNi melts. The only difference is the significantly shorter lifetime of the metastable  $bcc$  phase in the equiatomic compositions. In the case of a single recalescence (*blue curves* in Fig. 3.7), the sample temperature increases to above the solidus of the  $fcc$  phase  $T_{s(fcc)}$ . In the case of a double recalescence, the sample temperature firstly grows to an intermediate value, being well below  $T_{s(fcc)}$ , and after some delay jumps to the semisolid range of the  $fcc$  phase (*red curves* in Fig. 3.7). A distinct plateau at the intermediate temperature observed on most  $T(t)$  curves with double recalescence suggests that this is the liquidus temperature of the  $bcc$  phase, denoted as  $T_{l(bcc)}$ .

### *Crystal growth velocity*

Crystal growth velocity  $v$  was calculated from the propagation of a recalescence front in a definite time interval recorded by the high-speed video camera as shown in the schematic representation in Fig. 3.9. The pixel size was determined using the digital images of a standard (steel-ball of known size) taken at the same video settings at the beginning of experiments. The image sequences were analyzed with the Fiji ImageJ software [149].

The crystal growth velocities for the stable ( $fcc$ ) and metastable ( $bcc$ ) phases nucleating and growing in the undercooled CrFeNi, CoCrNi, CoCrFeNi melts are shown in Fig. 3.10. For comparison, the published data for Fe-12Cr-16Ni (wt. %) by Matson [153] and Fe-15Cr-16Ni (at. %) by Volkman *et al.* [155] are also plotted. In both studies, the samples were processed using the EML technique; the crystal growth velocities were obtained from high-speed video in Ref. [153] and using a silicon photodiode in Ref. [155]. For a proper comparison of the growth velocity of the  $bcc$  phase in different alloys (CrFeNi and CoCrFeNi (this work), Fe-15Cr-16Ni [155], Fe-2Ni [156]), it is presented in Fig. 3.11 as a function of the undercooling concerning the corresponding liquidus temperature of the  $bcc$  phase  $T_{l(bcc)}$ .

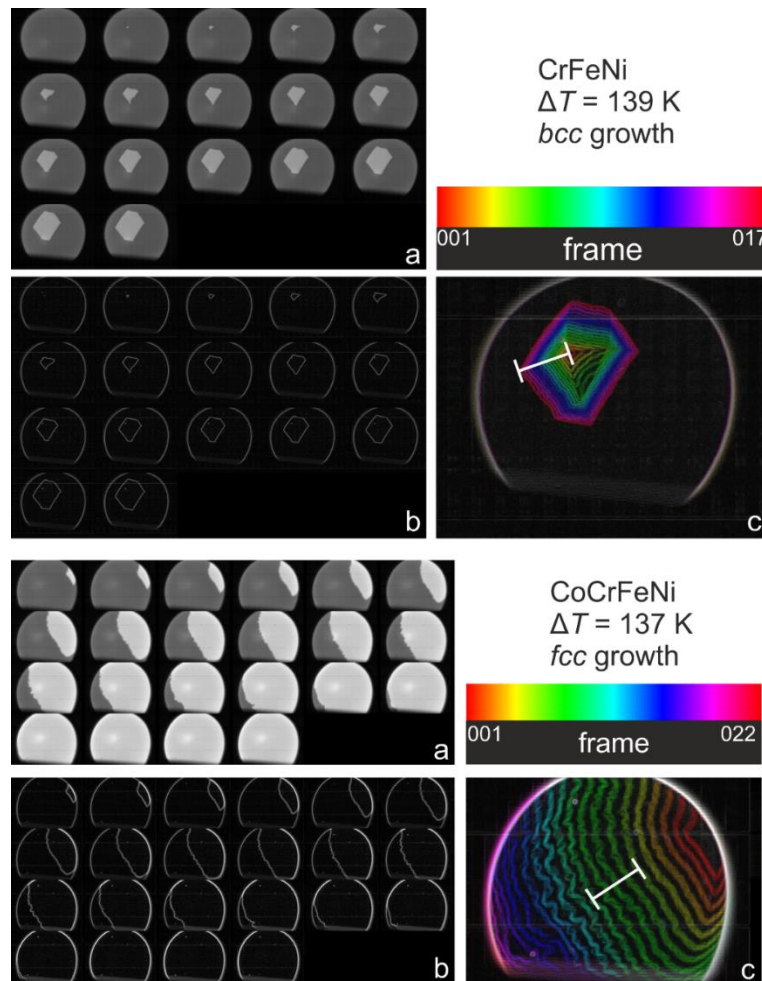


Figure 3.9. To the determination of the crystal growth velocity using high-speed videos taken during crystallization of the undercooled melts: (a) montage of video frames sequences of the crystallization event recorded with a high-speed camera during EML processing; (b) edge-contour montage of the sequence of frames shown in (a); (c) temporal-color code representation of the image sequence shown in (b). The inset scale represents the measured travel distance of the crystallization front in a definite time. *Upper panel* – *bcc* crystal growing in CrFeNi sample at  $\Delta T = 139$  K; *bottom panel* – *fcc* crystal growing in CoCrFeNi sample at  $\Delta T = 137$  K.

The observed scattering of the growth velocity values plotted in Figs. 3.10 and 3.11 can be explained by the experimental uncertainties and by uncertainties arising during the analysis of the digital images, both are hard to be estimated. Most problematic is a correct determination of the recalescence front travel distance if a growing crystal is situated close to an apparent drop edge as the images just give a projection of a curved surface. To estimate this effect, crystal growth was simulated by Y. Yang (University of Alberta, Canada) using stereographic projection modeling for three cases: *bcc* phase in CrFeNi and CoCrFeNi and *fcc* phase in *fcc*-CoCrNi. The *bcc* dendrites were simulated as regular octahedrons, while the

*fcc* dendrite was approximated by a sphere due to its rather smooth growth front. A model dendrite was placed into a sphere of the samples' size and moved to reproduce the contours of the real crystal in a reference image when viewed from the front (see Figs. A2.8 and A2.9 in Appendix 2). From the movement of the simulated dendrites, the dendrite tip velocity was calculated. It was found out that the velocity values obtained directly from the recalescence front propagation and using dendrite simulation were quite close if the crystals were nucleated and grown in a central part of the sample, as viewed by video. However, the growth velocity obtained from the recalescence front propagation was  $\approx 2.1$  times smaller than the dendrite tip velocity obtained in the simulations (see Fig. A2.8 in Appendix 2). This demonstrates that the uncertainties related to the curvature of the sample should not be neglected. To minimize the inaccuracy of velocity, the analysis was done for crystals nucleating and growing in a central part of the video frame to minimize errors due to surface curvature.

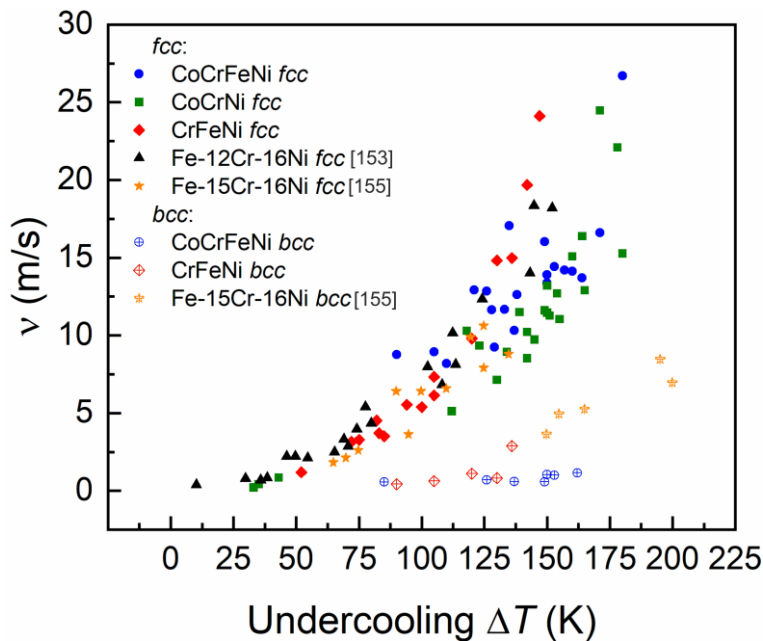


Figure 3.10. Crystal growth velocity as a function of melt undercooling for *fcc* and *bcc* phases in CoCrFeNi, CoCrNi, and CrFeNi alloys measured by a high-speed camera. The reference temperature for  $\Delta T$  is the  $T_{l(fcc)}$  of the respective alloys.

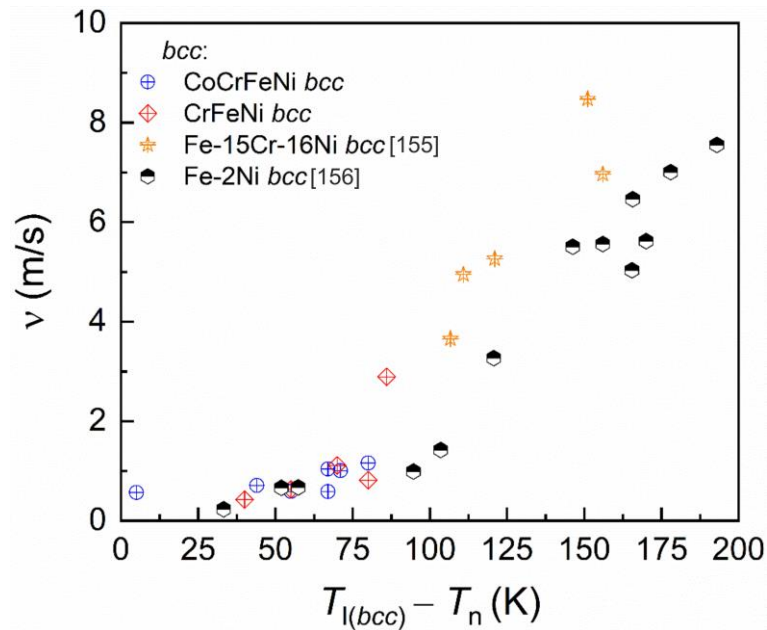


Figure 3.11. Crystal growth velocity as a function of melt undercooling for the metastable *bcc* phase in CoCrFeNi and CrFeNi alloys measured by a high-speed camera. The reference temperature for  $\Delta T$  is the  $T_{l(bcc)}$  of the respective alloys. Also included in the plot are the results for Fe-15Cr-16Ni (at. %) [155], and Fe-2Ni (at. %) [156].

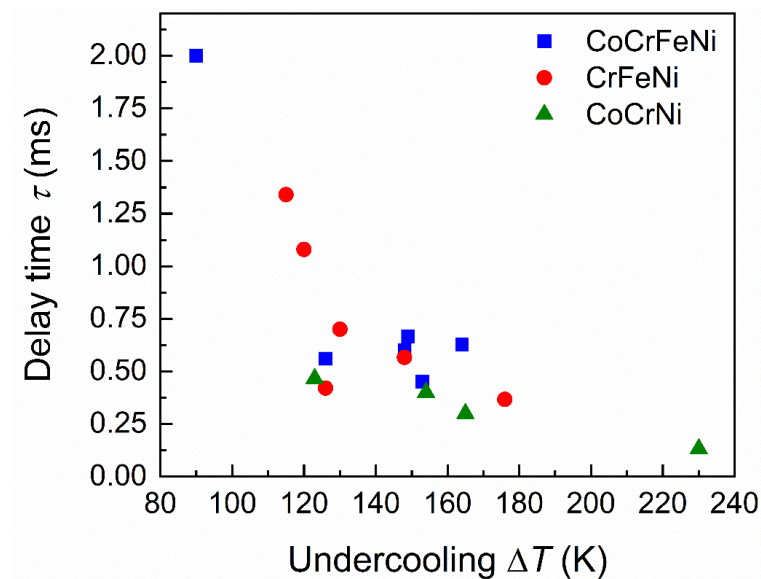


Figure 3.12. Delay time  $\tau$  for nucleation of *fcc* phase within preexisting metastable *bcc* phase as a function of melt undercooling for CrFeNi, CoCrNi, and CoCrFeNi alloys.

A time interval between the nucleation of *bcc* and *fcc* phases, so-called delay time,  $\tau$ , determined from analysis of the high-speed videos is shown in Fig. 3.12. The delay time quickly drops with increasing  $\Delta T$  from  $\sim 90$  K to  $\sim 140$  K (decrease from  $\sim 2$  ms to about 0.4 – 0.7 ms) and exhibits rather a weak variation upon further increase of  $\Delta T$ .



### 3.2.3 Microstructure of the solidified samples

XRD patterns measured from the cross-sectioned CoCrFeNi samples after solidification at different undercooling (Fig. 3.13) show peaks of a *fcc* phase only, without indication of any other crystalline phase(s) including the metastable *bcc* observed as a primary phase under larger undercooling.

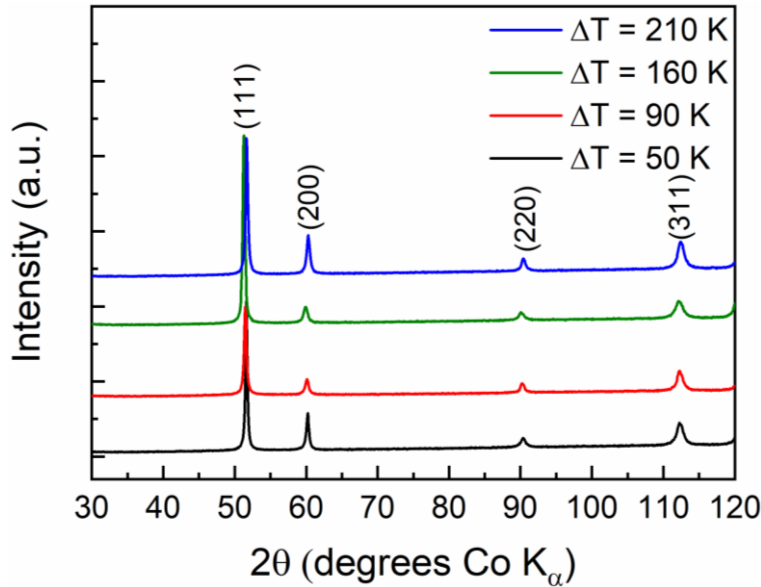


Figure 3.13. X-ray diffraction patterns of *postmortem* samples of the CoCrFeNi alloy with different undercooling.

The microstructure of CoCrFeNi samples solidified at a small, medium, and large undercooling ( $\Delta T$  (38 K, 150 K, and 212 K, respectively) is presented by SEM images and EBSD maps in Fig. 3.14. The panels a'', b'', and c'' in Fig. 3.14 show the distribution of grain boundary misorientation angle (GBMA) for the three samples. The values presented in the histogram were calculated as fractions of pixels corresponding to a specific misorientation angle relative to the total number of pixels along all grain boundaries within the analyzed area.

#### *Low undercooling*

Figure 3.14a shows an SEM image from the cross-section of a sample solidified at low undercooling ( $\Delta T = 38$  K). Coarse grains with a solidification direction from the surface to the center of the spherical sample are seen. In the right-top region of the image, a solidification void is shown. For the CoCrFeNi alloy and the ternary suballoys processed with the EML, this occurred for samples with low and medium undercooling, while samples



that solidified with an undercooling  $\geq 160$  K did not show the presence of a void. In Fig. 3.14a', the orientation map overlapped with the SEM image, clearly shows well-developed primary trunk dendrites, with coarse secondary arms, covering several hundred micrometers in length. The GBMA distribution (Fig. 3.14a'') shows preferred distributions of high-angle grain boundaries with peaks at about  $22^\circ$  and  $45^\circ$  and a small fraction of low-angle boundaries.

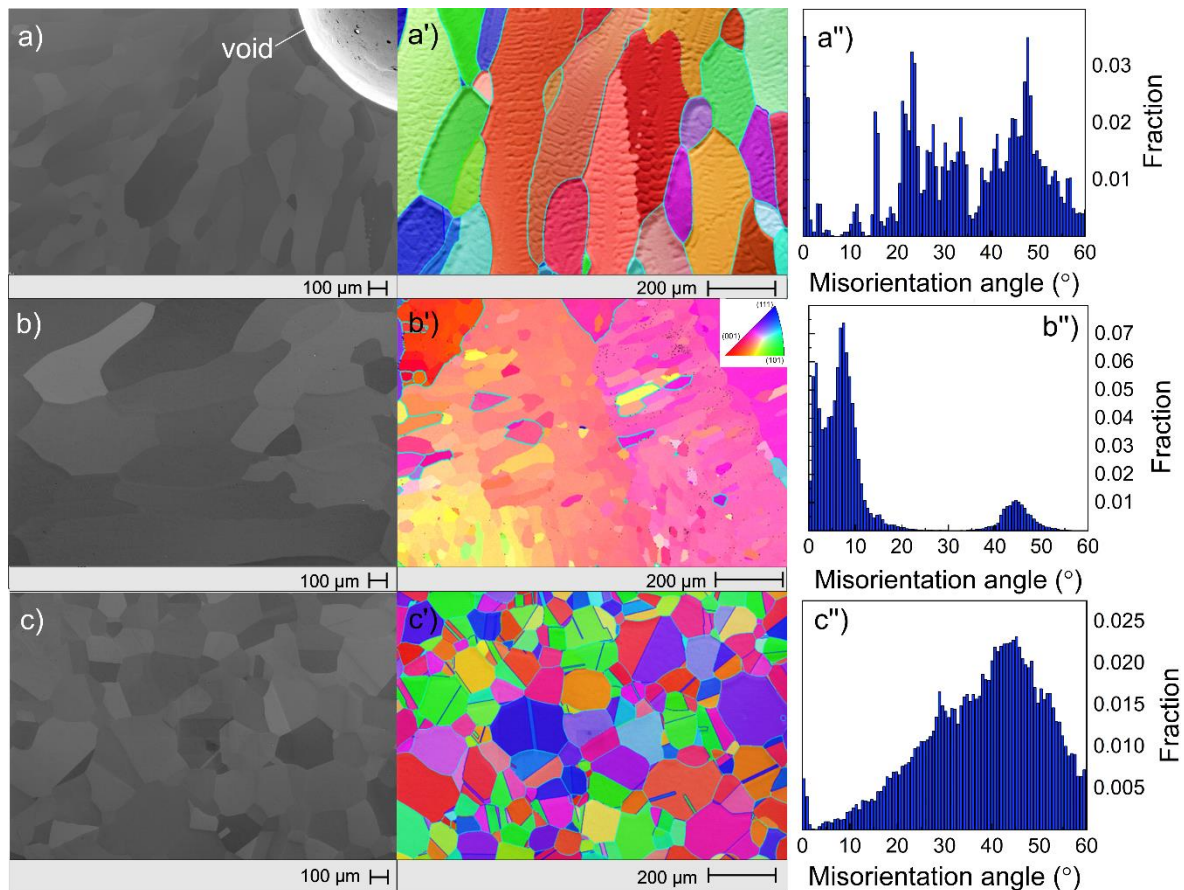


Figure 3.14. SEM images showing the microstructural evolution for the CoCrFeNi alloy solidified at different undercooling: a)  $\Delta T = 38$  K; b) a)  $\Delta T = 150$  K; c)  $\Delta T = 212$  K. Panels a', b' and c' show the EBSD color code orientation maps of the same samples. Panels a'', b'' and c'' present the distributions of the corresponding grain boundary misorientation angles.

### *Medium undercooling*

Coarse grains solidified from the surface to the center of the sample are also seen for the intermediate undercooling (Fig. 3.14b). However, in contrast to the weakly undercooled sample, distinct dendritic structures with a primary trunk and secondary arms are no longer recognizable at increased undercooling, and the large grains are decorated by numerous fine sub-grain structures (Fig. 3.14b'). The GBMA (Fig. 3.14b'') is characterized by a trimodal

distribution with a peak at about  $45^\circ$  for the boundary orientations of the coarser grains, a major peak at about  $9^\circ$ , and low-angle boundaries due to the sub-grains. It should be noticed, however, that there are few grains in the observed region.

### *Large undercooling*

For the sample solidified at the large undercooling, only fine equiaxed grains homogeneously distributed over the sample volume can be observed (Figs. 3.14c and 3.14c'). The EBSD inverse pole figure (Fig. 3.14c') shows a random orientation of the grains along with the formation of coherent annealing twins, marked by blue lines. The random grain orientation is also reflected by a wide GBMA distribution (Fig. 3.14c'') where most grain boundaries are high angle misoriented. The boundary misorientations reveal that twinned crystals consist predominantly (92%) of  $T3 \langle 111 \rangle$  oriented twins which are low energy coherent boundaries.

A similar microstructural evolution has been observed for the ternary CrFeNi and CoCrNi MEAs. The corresponding SEM and EBSD images are shown in Appendix 2 (Figs. A2.10 and A2.11).

## **3.3 Discussion**

### **3.3.1 *bcc-fcc* nucleation and growth competition**

Crystal nucleation and initial stages of crystal growth are the most notable events in crystallization. However, experimental studies of these phenomena are rather difficult due to the duration and length scale of these events. Therefore, atomic simulations have been used trying to corroborate the experimental findings. Using molecular dynamics simulation Wolde *et al.* [157] investigated the nucleation/growth competition between *bcc/fcc* phases in a Lennard-Jones system, which is known to have a stable *fcc* structure up to the melting temperature. They found that in a melt undercooled by  $\Delta T = 0.2 T_l$ , predominantly *bcc*-like precritical nuclei formed and the nuclei cores became *fcc*-like when the clusters reached their critical size. It was therefore concluded that the *fcc*-like structures nucleate inside the *bcc*-like precritical nuclei. In contrast, Swope and Anderson [158] argued that both *bcc* and *fcc* phases nucleate in an undercooled Lennard-Jones melt at the initial stage, and only *the fcc* phase grows subsequently, which can be described as a growth competition rather than a nucleation competition. In a more recent publication, using phase-field modeling Tang *et al.* [159] showed that *bcc* precursors act as substrates for medium-range atoms to attain the long-

range order and stabilize the *fcc* nuclei. Nonetheless, Tang *et al.* [159] pointed out that even though in their simulation and in that of Wolde *et al.* [157] the *bcc* phase acts as a substrate for *fcc* nucleation, the mechanisms are rather different and further studies are required to clarify them.

High-speed videos were taken during the solidification of CrFeNi, CoCrNi, and CoCrFeNi undercooled melts (Figs. 3.5b, 3.5d, and 3.5f, and corresponding video montages in Appendix 2) showed that in the case of a double recalescence the *fcc* phase always nucleates and grows from the primary *bcc* phase. Even though the time and length scales in our experiments are completely different from those in computer simulations, it is in qualitative agreement regarding the solidification sequence predicted by the modeling of Wolde *et al.* [157] and Tang *et al.* [159]. Li, Ozawa, and Kuribayashi [160] have also concluded on the determining role of nucleation in a competition of stable and metastable phases with similar crystalline structures like *fcc* and *bcc*, whereas the growth competition controls the phase selection for crystals with substantially different structures.

It has been shown for different systems that even though the driving force for solidification of the stable phase (*fcc*) is greater than that of the metastable phase (*bcc*), at  $T_n < T_{l(bcc)}$ , the phase selection in undercooled melts is governed by the solid-liquid interfacial energy [156]. Volkmann *et al.* [161] calculated the activation energies for homogenous and heterogeneous nucleation using both the classical nucleation theory [162] and the diffuse interface theory (DIT) developed by [163], for different compositions of the Fe-Cr-Ni system. Their results demonstrated that due to smaller interfacial energy between the *bcc* nucleus and the undercooled melt, there is a higher probability for the nucleation of the metastable phase beyond a critical undercooling. In a second part of the work of Volkmann *et al.* [155], it was shown that the DIT model with nucleus composition deviations could better describe the experimental results found using EML and the drop tube techniques. Koseki and Flemings [164] estimated the interfacial energies for different possible nucleation sites and showed that *the fcc* phase should preferentially nucleate on the grain boundaries of a preexisting *bcc* phase.

One peculiarity of the present study is that a double recalescence event could never be captured by the pyrometer, in contrast to the reported results for binary and ternary systems [151–153]. As already mentioned, this was due to the extremely short lifetime of the metastable *bcc* phase ( $< 2$  ms) being smaller than the time-resolution of the pyrometer. As discussed by Matson [153], the lifetime of the metastable *bcc* phase in ternary Fe-Cr-Ni alloys is strongly dependent on the composition and can last from a few microseconds for a

Ni:Cr ratio of 2.4 up to several seconds when the ratio is 0.6. In some studies of Fe-Cr-Ni alloys, the metastable *bcc* phase could even be ‘frozen’ in the microstructure [164].

As mentioned in the Introduction of this Chapter, Li *et al.* [145], Wang *et al.* [146], and Zhang *et al.* [147] reported on metastable *bcc* phase precipitates in the final microstructure of undercooled CoCrFeNi alloy processed by the glass fluxing method. Li *et al.* [16] showed the volume fraction of the metastable *bcc* phase for an undercooled sample to be 15 % after solidification. In work [145], the volume fraction of the secondary phase (*bcc*) of 16-18 % was reported to be independent of liquid undercooling for  $\Delta T$  between 50 and 300 K. Wang *et al.* [146] and Zhang *et al.* [147] suggested that the *bcc* phase was formed as a secondary phase in their studies, which is different from the findings of the present work in which the *bcc* appears as a transient primary phase in the undercooled melts. Wang *et al.* [146] claimed that segregation to interdendritic regions leads to the formation of Ni- and Cr-rich islands, which would then be susceptible, as in stainless steels, to form a *fcc* and a *bcc* phase, respectively. However, according to the solute trapping models [165,166], and experimental results [167], at large undercooling the crystallization mode is predominantly collision-controlled. The heat extraction rate from the melt is the major factor limiting the solidification velocity. At 300 K undercooling most of the primary solid forms during recalescence. Thus, a large volume fraction of the sample solidifies under conditions where segregations are partially or completely suppressed due to the fast attachment kinetics.

The calculations of the stable and metastable *x-T* diagrams for the composition section (CoCrNi)-Fe were performed using the Thermo-Calc 2020a software from Thermo-Calc AB [168] and thermodynamic databases TCHEA4 of Chen *et al.* [50], TCFE10 from Thermo-Calc AB [169], and the thermodynamic description of quinary Al-Co-Cr-Fe-Ni system from Stryzhyboroda *et al.* [170]. The stable diagram was calculated with all phases included in the databases for the Co-Cr-Fe-Ni system. The metastable diagram was calculated via rejection of the *fcc* and  $L_{12}$  phases.

The stable and metastable phase diagrams for the (CoCrNi)-Fe section calculated by V. Witusiewicz (ACCESS e.V., Aachen) using the thermodynamic descriptions of the quaternary Co-Cr-Fe-Ni system from Refs. [50,169,170] is presented in Fig. 3.15. All three databases resulted in virtually similar stable phase diagrams; the temperature of solidus for the equiatomic composition measured by DSC is slightly below the calculated liquidus line. Rejection of the *fcc* and  $L_{12}$  phases by calculation of the metastable diagrams resulted in the appearance of *bcc* phase below liquidus in all composition range of Fe. However, the calculated liquid/*bcc* equilibria for the equiatomic quaternary composition (CoCrFeNi)

deviates from the present experimental findings by about 50-70 K. Such significant differences induced us to re-optimize the ternary interaction parameters  ${}^{\circ}L^{bcc}(\text{Co,Cr,Fe})$  of the *bcc* and  ${}^{\circ}L^{fcc}(\text{Co,Cr,Fe})$  of the *fcc* phases given in the description [170].

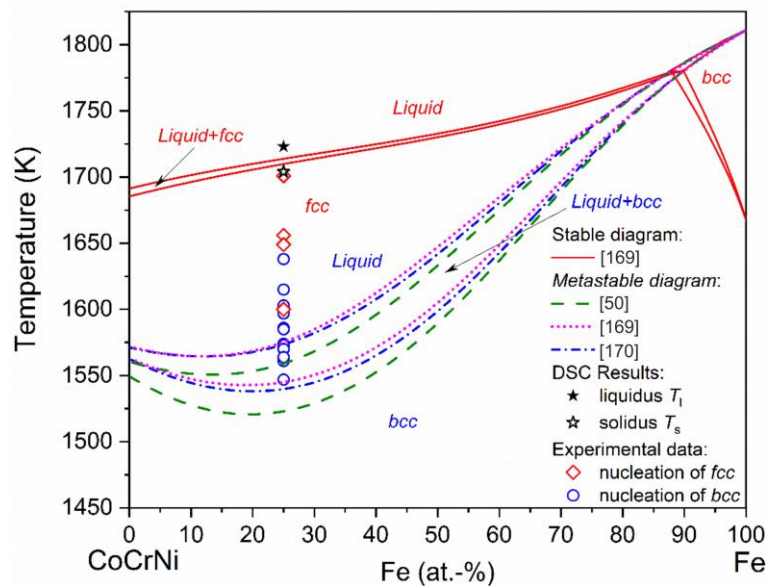


Figure 3.15. Stable and metastable equilibria for (CoCrNi)-Fe composition section calculated using available thermodynamic databases [50,169,170].

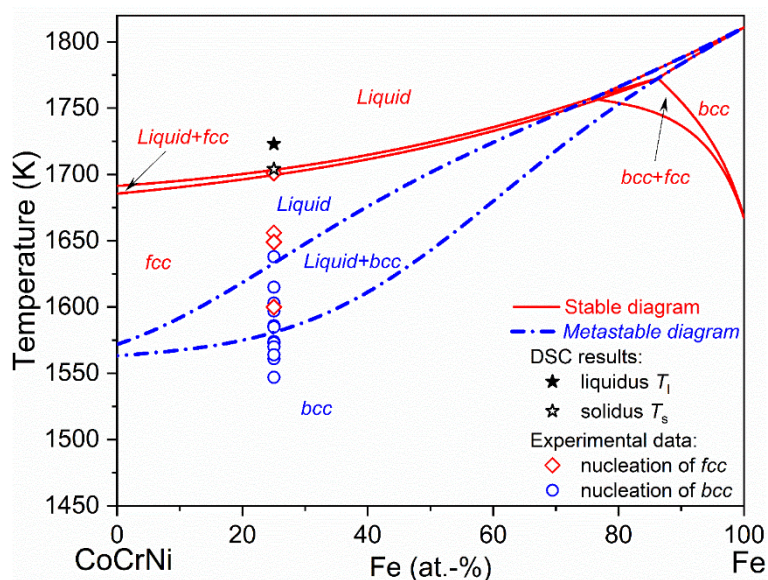


Figure 3.16. Stable and metastable equilibria for (CoCrNi)-Fe composition section calculated after re-optimization of the thermodynamic description of *fcc* and *bcc* phases from Ref. [170].

In the process of optimization, the weight for the solidus temperature measured by DSC was selected to be twice larger in comparison with the liquidus due to its better

determination as it follows from the practical guide on differential thermal analysis of metals and alloys by the National Institute of Standards and Technology [171]. The re-optimized stable and metastable phase diagrams show a very good agreement with the experimental data as illustrated in Fig. 3.16.

### 3.3.2. Crystal growth kinetics

The growth velocities of the stable *fcc* phase (Fig. 3.10) show similar dependences on the undercooling for the equiatomic CrFeNi, CoCrNi, and CoCrFeNi alloys studied in the present work as well as for Fe-(rich)-Cr-Ni alloys from Refs. [153,155]. Furthermore, practically the same  $v$ -values have been reported by Barth *et al.* [172] for the *fcc* phase in binary Fe<sub>70</sub>Ni<sub>30</sub> and Fe<sub>75</sub>Ni<sub>25</sub> electromagnetically levitated melts. The growth velocity of the *bcc* crystals (Fig. 3.11) also exhibits a similar behavior for CoCrFeNi, CrFeNi, compared with Fe-(rich)-Cr-Ni [155], and binary Fe-2Ni [156] alloys if it is considered as a function of the melt undercooling relative to the metastable liquidus temperature of the *bcc* phase and not to the alloys' melting temperature. This is reasonable, as the driving force for the *bcc* growth is determined by the undercooling  $\Delta T_{l(bcc)}$ .

The crystal growth velocity of both *fcc* and *bcc* phases increases with undercooling. At low  $\Delta T$ , sluggish crystal growth is governed mainly by diffusion of the solute elements. At higher undercooling, the driving force for crystallization increases leading to a transition from diffusion- to thermally controlled growth. Diffusionless growth with complete trapping of the solute elements is not evidenced from the  $v(\Delta T)$  dependence in Fig. 3.10. Nonetheless, taking into account a low partitioning coefficient associated with the *fcc* phase (Fig. 3.16) and its high growth rates of 10-20 m/s at  $\Delta T = 150$ -160 K (Fig. 3.10) such transition should not be excluded.

At all degrees of undercooling, the *fcc* phase grows remarkably faster than the metastable *bcc*, which agrees with previous reports [150,151,172]. It is however noteworthy that the growth velocities of both phases is principally the same in Fe-rich binary Fe-Ni [156] and ternary Fe-Ni-Cr [153,155] alloys, as well as in the equiatomic CrFeNi, CoCrNi, and CoCrFeNi alloys. This suggests that the crystal growth kinetics does not become sluggish in the medium-entropy and high-entropy alloys studied here. This finding corroborates with the diffusion studies of Vaidya *et al.* [70] who have shown that solid-state diffusion coefficients of the elements in a polycrystalline CoCrFeNi are comparable to those of binary alloys.

Recently, Zhang *et al.* [147] reported the growth velocity of the *fcc* phase as a function of melt undercooling for the quaternary CoCrFeNi alloy in comparison to the ternary CoFeNi and binary CoNi alloys. The velocity was calculated from high-speed video data, as in the present work, but the samples were undercooled using the glass fluxing technique. Interestingly, the crystallization kinetics for CoFeNi and CoNi alloys reported by Zhang *et al.* [147] is like that observed in the present study, which was the same for all alloys studied. However, the growth velocity for the *fcc* phase in the quaternary CoCrFeNi alloy from Ref. [147] is at least one order of magnitude smaller at any undercooling level. For example,  $v \approx 28$  m/s was obtained for  $\Delta T = 180$  K in the present work (Fig. 3.10), whereas  $v \approx 0.4$  m/s was reported in Ref. [147] at a comparable undercooling. Zhang *et al.* [147] suggested the addition of Cr, and not the number of elements, causes the crystallization to become sluggish. This is not the case in our findings since the  $v$  of ternary CrFeNi and CoCrNi alloys, which have a higher concentration of Cr (in at. %), are of the same order of magnitude as that of CoCrFeNi. If the processing method should have such a huge influence on the  $v$  for the quaternary CoCrFeNi alloy is an open question.

Considering the delay time for nucleation of the *fcc* phase within the preexisting metastable *bcc* phase in undercooled Fe-Cr-Ni stainless steel alloys, Matson [173] proposed a retained damage model based on the idea that the free energy of the metastable *bcc* phase increases due to the accumulation of defects (e.g., dislocations, tilt boundaries, and lattice strain) during rapid crystal growth and/or melt convection. Thus, the more crystal defects are formed in the metastable phase lattice, the larger is the driving force for nucleation of the *fcc* phase. As the growth kinetics depends on the melt undercooling, the latter (indirectly) influences the *bcc-fcc* transition. Matson *et al.* [154] have recently shown that the delay time for the *bcc-fcc* transition in Fe-Cr-Ni stainless steels was reduced by  $\sim 5$  times from some 2 to 0.4 ms if the undercooling changed from approx. 70 to 140 K. A similar decrease of  $\tau$  is observed for CrFeNi, CoCrNi, and CoCrFeNi alloys when the undercooling increases from approx. 90 to 140 K; however, it changes remarkably slower with further undercooling as can be seen in Fig. 3.12. It has also to be mentioned that the delay time for the *bcc-fcc* transition in Fe-Cr-Ni stainless steels was shown to be affected to a much larger extent by the melt convection [154], which is significant in the case of electromagnetic levitation.



### 3.3.3. Microstructural evolution

XRD and microstructure analysis of the samples solidified at different undercooling levels provided no evidence for the metastable *bcc* phase to be present in the final microstructure in any of the alloys studied (Figs. 3.13, 3.14, and Figs. A2.10 and A2.11 in Appendix 2). This confirms that the metastable *bcc* phase formed above a critical undercooling completely transforms into the stable *fcc* during solidification. As the *fcc* phase nucleates and grows in the *bcc* + liquid mushy zone, the release of the latent heat raises the temperature to  $T_{l(fcc)}$ , well above  $T_{l(bcc)}$  (see Fig. 3.7 and Fig. 3.16), promoting complete remelting of the residual metastable phase. Based on the observed lifetime of the *bcc* phase (Fig. 3.5, Fig. 3.7), a cooling rate of the order of  $10^3 \text{ K} \cdot \text{s}^{-1}$  would be required to ‘freeze-in’ this metastable phase. Under the current experimental conditions, the *bcc* phase cannot be preserved, and the final microstructure is formed by the *fcc* phase as a SPSS.

Microstructure analysis shows an evident transition from coarse columnar grains (Figs. 3.14a and 3.14b, and Fig. A2.11 in Appendix 2) to refined equiaxed grains (Fig. 3.14c and Fig. A2.11 in Appendix 2) upon increasing undercooling. The reasons for grain refinement in undercooled melts of pure metals and alloys has been a long-standing scientific debate since Walker first noticed it to occur in undercooled pure Ni (see the book of Chalmers [174]). Among different theories attempting to explain this phenomenon [175–182] most widely accepted is the fragmentation of primary dendrites taking place during recalescence or shortly after it while still in the semi-solid state [177–182]. Schwarz *et al.* [179] suggested that dendrite fragmentation proceeds by remelting driven by minimization of the solid-liquid interfacial energy. According to this model, fragmentation can occur if a characteristic time of dendritic breakup is shorter than the time required for complete solidification. The breakup time is decreasing with decreasing dendrite tip radius, which reduces to some critical value upon a certain undercooling. Simultaneously, the increase of the growth velocity and associated solute trapping results in supersaturation of the growing crystalline phase further enhancing the driving force for fragmentation. In some alloy systems, a discontinuity in the  $v(\Delta T)$  curves are found to coincide with the onset of grain refinement [66]. Although no such discontinuity could be seen for the CoCrFeNi alloy, a steep rise in the growth velocity of the *fcc* phase above  $\Delta T \sim 160 \text{ K}$  (Fig. 3.10) might indicate a critical undercooling for the spontaneous grain refinement evidenced by the microstructure (Fig. 3.14c’).

EBSD analysis (Figures 3.14a’ and 3.14c’, as well as Figs. A2.11 and A2.12 in Appendix 2) show that the samples do not have any preferential texture at low and large



undercooling. Random distribution of crystal orientations can be explained by the rotation of growing grains under the effect of electromagnetic stirring, which is always present in EML. The low-angle subgrain boundaries observed in Fig. 3.14b' support the idea of dendrite deformation [183] to occur during solidification at intermediate undercooling and might be regarded as an initial stage for dendrite fragmentation at deeper undercooling. Li *et al.* [184] performed a detailed analysis of the electromagnetic stirring effect by comparing the microstructural evolution of the Ni<sub>99</sub>B<sub>1</sub> alloy processed by EML and electrostatic levitation (ESL). While the samples processed in ESL fully developed dendrites could grow at low and medium undercooling, this was not the case for EML where equiaxed grains were formed. A second major difference was a significant texturing in the samples processed by ESL in contrast to EML which showed randomly oriented grains for large, medium, and low undercooling.

In Fig. 3.14c' and Fig. A2.11 in Appendix 2, the presence of coherent annealing twins can be noticed for many grains at large undercooling. While the occurrence of deformation twins [185] and annealing twins formed during recrystallization [93,138] is a common feature for the CoCrFeNi, CrFeNi, and CoCrNi alloys, the appearance of annealing twins during solidification of these alloys has not been reported so far, to our knowledge. However, this conforms to a study of undercooled Ni<sub>99</sub>B<sub>1</sub> melts by Li *et al.* [184], who have shown twins in the samples solidified at a high undercooling. We believe that in the case of CoCrFeNi, CrFeNi, and CoCrNi alloys the twins are formed due to the thermal stresses in the rapidly growing *fcc* phase during recalescence and are annealed upon a temperature increase due to the heat release. The former is evidenced by the fact that twins are not observed in all grains (Fig. 3.14c'). During recalescence, only some fraction of the liquid is transformed into a primary solid and therefore only these grains are prone to show twins. In contrast, the remaining liquid that is reheated up to the liquidus temperature solidifies at a slower cooling rate so that there are virtually no twins. Also, as the crystal growth is slower at smaller undercooling, no twinned crystals could be found in the samples solidified at low and medium undercooling (Figs. 3.14a' and 3.14b'). The formation of coherent low-energy twin boundaries during solidification of the CoCrFeNi and CoCrNi together with spontaneous grain refinement opens a promising landscape for grain-boundary engineering and provides a possibility to tune the mechanical properties of MEA and HEAs during solidification.

## Chapter 4: The effect of Al addition to the CoCrFeNi alloy on the non-equilibrium solidification behaviour

In this Chapter, non-equilibrium solidification behavior has been investigated when a small quantity of aluminum was added to the quaternary CoCrFeNi studied in the previous Chapter. Again, the goal was to understand phase selection, crystal growth kinetics, and microstructural evolution as a function of melt undercooling.

### 4.1 Introduction

It is well-described in the literature that the addition of aluminum to the quaternary CoCrFeNi alloy induces a transition from a single-phase *fcc* solid solution in  $(Al_x)CoCrFeNi$  with  $x = 0 - 0.4$  (molar fraction), to a dual-phase *fcc* and *bcc* microstructure for  $x = 0.5 - 0.8$ . A spinodal decomposition takes place upon cooling from higher temperatures and a *fcc* + *bcc*/B2 is stable at room temperature. For  $x \geq 0.9$  a *bcc*/B2 structure is formed [136,186]. The reason for such phase transitions is attributed to the larger atomic radius of Al compared to the transition metals which generate a volumetric strain, thus, making the more loose-packed *bcc* crystal structure favorable as the Al content is increased [62].

The transition from *fcc* to *bcc*/B2 is accompanied by remarkable changes in mechanical properties. For example, the Vickers hardness increases from  $HV\ 113 \pm 4$  for  $x = 0.25$  (molar fraction) to  $HV\ 433 \pm 22$  for  $x = 1$  [186]. The *fcc*-structured alloys have good ductility but low strength, while the *bcc*/B2 alloys have considerably higher strength but limited ductility. For instance, the equimolar AlCoCrFeNi HEA is brittle at room temperature, which is attributed to a weave-like microstructure formed due to the spinodal formation of *bcc* and B2 phases [187].

It was initially believed that the  $Al_{0.3}CoCrFeNi$  alloy would form a stable *fcc* SPSS at room temperature, but soon after several reports described that this was a non-stable configuration [188–191]. According to the  $H_{el}$  vs.  $VEC$  empirical criterion proposed by Andreoli *et al.* [19], this composition is predicted to lie just outside the *fcc* SPSS region. Shun *et al.* [189] investigated as-cast samples and the influence of different annealing temperatures on the microstructure of this alloy. SEM micrographs of the as-cast and the annealed samples at 973 K for 72 hours showed a *fcc* SPSS microstructure. However, TEM analysis revealed spherical nanosized precipitates homogeneously distributed in the matrix of the as-cast alloy, and after annealing at 973 K, nanosized platelet precipitates were identified.

Both precipitates were determined to be ordered  $L1_2$  phase. After annealing at 1173 K for 72 hours, micro-sized rod-shaped particles appeared in the  $fcc$  matrix which were indexed as ordered B2 phase.

The mechanical properties of the  $Al_{0.3}CoCrFeNi$  alloy were reported to be significantly tuned by a combination of different thermomechanical treatments, as was shown by Gwalani *et al.* [192], which makes it attractive for structural applications. A tensile yield-strength increase from 160 to 1800 MPa was described depending on precipitate type, morphology, distribution, and size. According to the authors, this is the highest yield strength increase ever reported for the same alloy without composition modification, due to only microstructure engineering.

In Chapter 3, a double recalescence was shown to occur for CrFeNi, CoCrNi, and CoCrFeNi alloys when sufficiently undercooled. Moreover, it was shown that rapid crystallization kinetics and that grain refinement occurred at large undercooling. It is the goal of this study to evaluate the effects of non-equilibrium solidification on the  $Al_{0.3}CoCrFeNi$  HEA.

## 4.2 Results and Discussion

Figure 4.1 shows a 3D (time-wavevector-intensity) plot of a  $Al_{0.3}CoCrFeNi$  sample processed in the EML facility during *in situ* XRD.

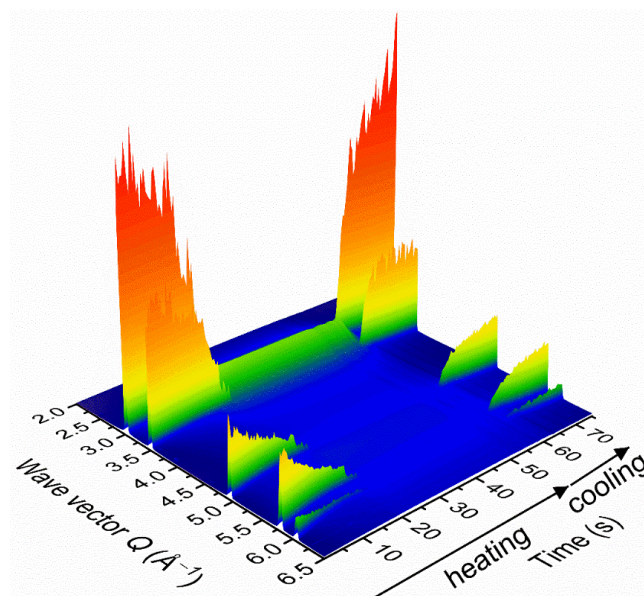


Figure 4.1. 3D plot showing XRD intensities  $I(Q)$  measured from an electromagnetically levitated  $Al_{0.3}CoCrFeNi$  sample during a heating-cooling cycle; the melt was undercooled by 77 K before crystallization, as shown in Fig. 4.2.

Figure 4.2 represents the run depicted in Fig. 4.1 but as a 2D contour plot representing the wave vector  $Q$  vs. XRD intensities. The detector sampling rate was 20 Hz. The temperature-time profile is shown in the upper panel. Temperatures started to be recorded around 600 K upon heating from room temperature. Only a diffuse halo observed at 1690 K and higher temperatures confirms that the sample is completely molten (lower panel). This point (1690 K) is defined as the liquidus temperature  $T_l$ . A peak in the temperature-time curve at 1741 K is related to a change of emissivity occurring as the melting of the samples starts. This point (1741 K) is defined as the solidus temperature  $T_s$ . The difference between  $T_s$  and  $T_l$  is  $\Delta T = 77$  K.

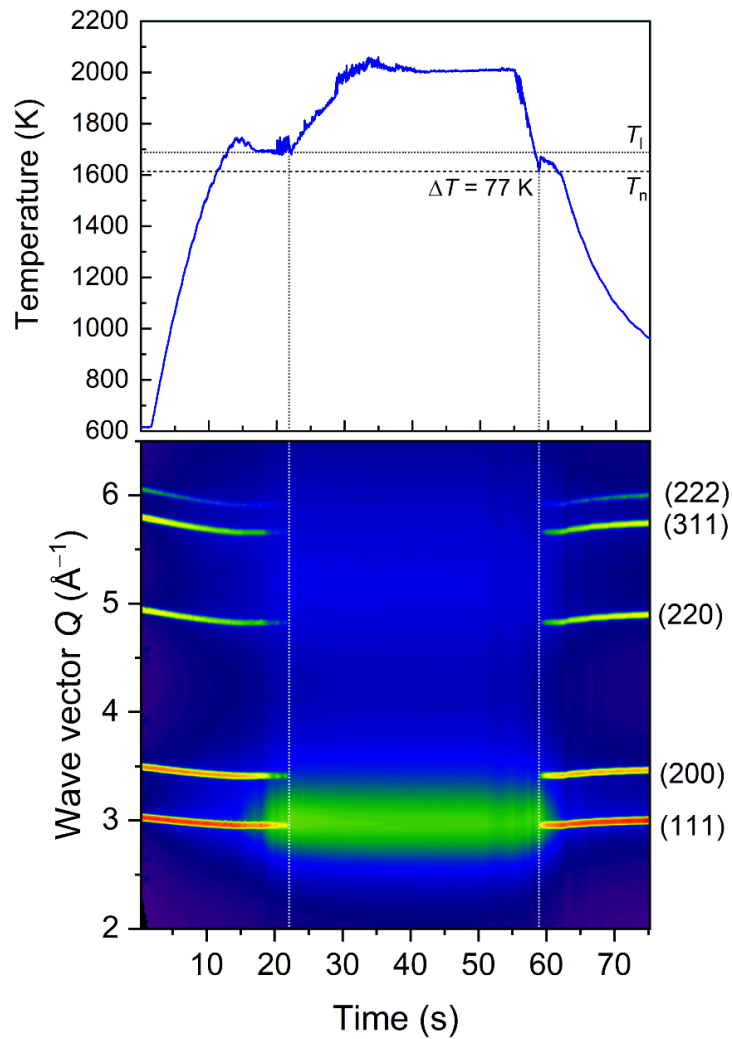


Figure 4.2. Time-temperature curve and corresponding XRD contour plot measured from a levitated  $\text{Al}_{0.3}\text{CoCrFeNi}$  samples with liquid undercooling of 77 K. The detector sampling rate was 20 Hertz.

The DSC curve plotted in Fig. 4.3 was used to determine the  $T_s$  and  $T_l$ , and these values were used to calibrate the time-temperature curve shown in Fig. 4.2. There is a narrow difference between  $T_s$  and  $T_l$  of 20 K. Besides the evident endothermic reaction

corresponding to the melting of the sample, where the solidus and liquidus were determined as 1670 and 1690 K, respectively, an exothermic peak is shown by the inset arrow at  $\sim 880$  K. This may indicate the formation of the  $L1_2$  phase upon heating of the specimen [193].

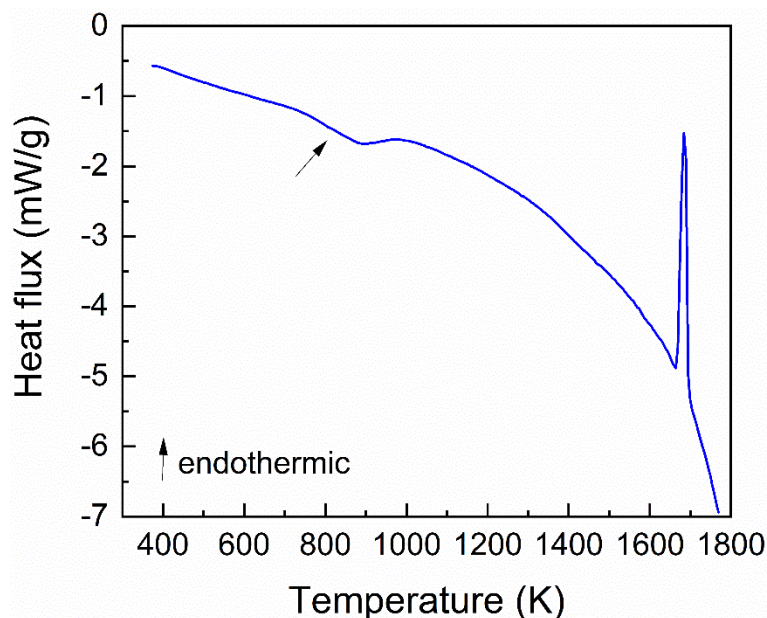


Figure 4.3. DSC scan measured on the  $Al_{0.3}CoCrNi$  alloy at a heating rate of  $20\text{ K}\cdot\text{min}^{-1}$ .

Returning to Fig. 4.2, the sample was overheated by about 300 K above  $T_l$ , maintained at this temperature for some time, and afterward cooled by reducing the power to the induction coil and by applying jet-gas cooling (He). The liquid was undercooled by 77 K below liquidus, and the nucleation temperature  $T_n$  recorded as 1613 K, followed by a recalescence with peak temperature at 1672 K. During the subsequent cooling of the sample to  $\sim 950$  K no other thermal event is observed on the  $T(t)$  plot. From the beginning to the end of the experiment only diffraction peaks of a *fcc* structure are seen (lower panel), while (100) peaks relative to a superlattice structure of the  $L1_2$  phase were never observed. This was always the case for other XRD runs performed *in situ*. It was discussed in the Introduction of this Chapter that a SPSS microstructure is a non-equilibrium state for this alloy at lower temperatures. However, the samples are heated at a rate of  $\sim 130 - 150\text{ K s}^{-1}$  in the EML experiments, and under these conditions, the precipitation of equilibrium phases can be kinetically suppressed. On the other hand, the XRD profiles measured during cooling are limited to temperatures above 900 K and the formation of the  $L1_2$  phase, for example, is predicted as a solid-state transformation at lower temperatures according to CALPHAD calculations [193]. Furthermore, the cooling rates were always  $\sim 100 - 150\text{ K s}^{-1}$  which

makes it unlikely that intermediate-temperature equilibrium phases will be formed. The structure and microstructure of the solidified samples will be addressed later.

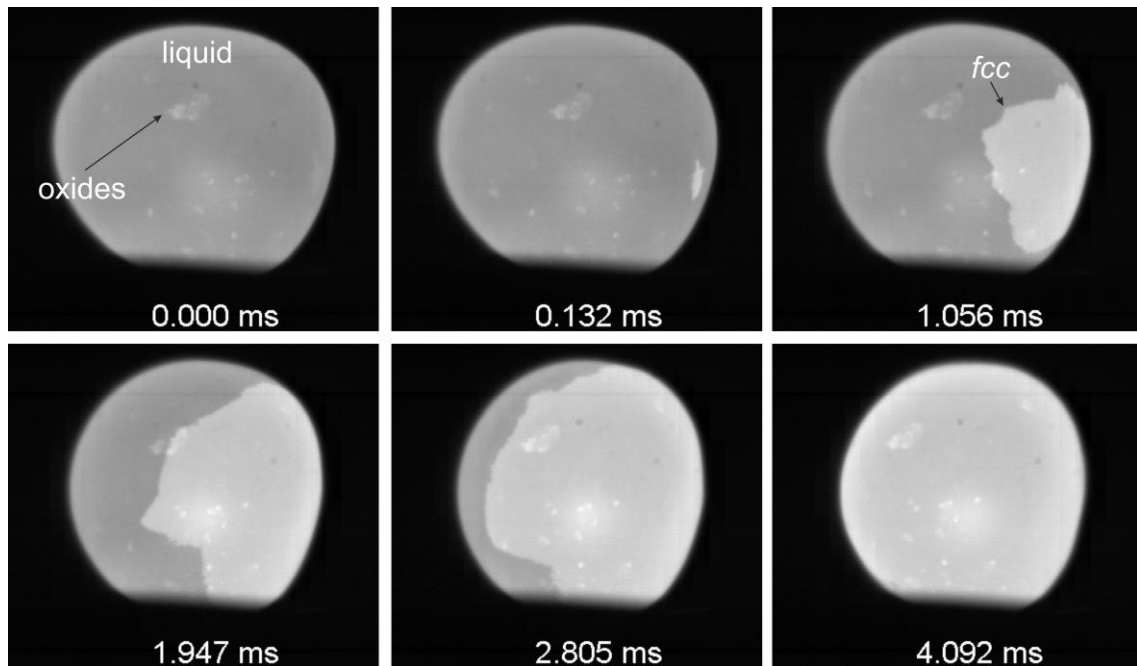


Figure 4.4. Digital images showing the crystallization of a  $\text{Al}_{0.3}\text{CoCrFeNi}$  HEA melt with a maximum  $\Delta T = 70$  K. The time scale was set to zero at a moment shortly before the crystallization onset.

The first major difference observed in the experiments with the  $\text{Al}_{0.3}\text{CoCrFeNi}$  alloy, compared to the  $\text{CoCrFeNi}$  and MEAs detailed in Chapter 3, is that the addition of Al limits the degree to which the liquid can be undercooled. While undercooling up to 215 K was described for the  $\text{CoCrFeNi}$  alloy in Chapter 3, the maximum  $\Delta T$  achieved for the five-component composition studied here was 88 K. The decrease in the ability to undercool the liquid may not be linked to the addition of Al itself but rather to heterogenous nucleation caused by the formation of oxides. The formation of oxides on the surface of the molten material was observed during casting of samples to be used in EML experiments. While an attempt was made to remove them mechanically (grinding and subsequent ultrasonic cleaning), these oxides were also present during EML processing as shown in Fig. 4.4 (brighter spots in the darker liquid in the upper left panel). This limited the studies on phase selection, crystallization kinetics, and microstructural evolution, for this alloy, to the region of low undercooling.

In Figure 4.4 the sequence of images represents the crystallization of the  $\text{Al}_{0.3}\text{CoCrFeNi}$  HEA at  $\Delta T = 70$  K. The first panel in the upper row shows the molten alloy

(darker-gray) at its maximum undercooling before crystallization. Also, oxides are observed on the surface of the droplet. The time was set to zero at this instance for convenience. From the second panel and thereafter a medium-gray phase grows continuously from the right-hand side of the image to the left until it completely overtakes the whole sample.

From all high-speed videos analyzed, where the nucleation point could be captured, only a single phase crystallizing was always observed. The *in situ* XRD experiments (Figs. 4.1 and 4.2) allow us to conclude that the crystallization occurs from liquid to a *fcc* SPSS, within the undercooling range evaluated, as illustrated in Figure 4.4. Due to limited undercooling of the  $\text{Al}_{0.3}\text{CoCrFeNi}$  samples in the present study, it is not possible to make any conclusion about a probable formation of a metastable *bcc* phase at higher undercooling.

The crystal growth kinetics of the  $\text{Al}_{0.3}\text{CoCrFeNi}$  as a function of melt undercooling is shown in Fig. 4.5. Crystal growth velocities  $v$  were determined in the same manner as in Fig. 3.9. The  $v(\Delta T)$  shows the same trend as the  $\text{CoCrFeNi}$ ,  $\text{CrFeNi}$ , and  $\text{CoCrNi}$  alloys (Fig. 3.10), and  $v$  is slow in the low undercooling range, as can be seen in Figure 4.5 and Table 4.1. In Fig. 4.5 the  $v(\Delta T)$  is also shown for the MEAs described previously in Chapter 3 and the data for the Fe-12Cr-16Ni (at. %) stainless steel from Matson *et al.* [153]. The growth velocity of the  $\text{Al}_{0.3}\text{CoCrFeNi}$  HEA is slower compared to the equiatomic ternary alloys discussed in Chapter 3, and Fe-12Cr-16Ni stainless steel at a comparable undercooling (Fig. 4.5). Nonetheless, they are in the same order of magnitude. Again, dendritic growth at low undercooling is controlled by chemical diffusion which in turn limits the growth velocity. The more sluggish crystal growth of the  $\text{Al}_{0.3}\text{CoCrFeNi}$  may be related to solute rejection at the liquid/solid interface. As was shown by Liu *et al.* [194] during directional solidification of the  $\text{Al}_{0.7}\text{CoCrFeNi}$  HEA, Al and Cr tend to strongly segregate to the interdendritic regions while Fe and Co partition to the dendrite's core.

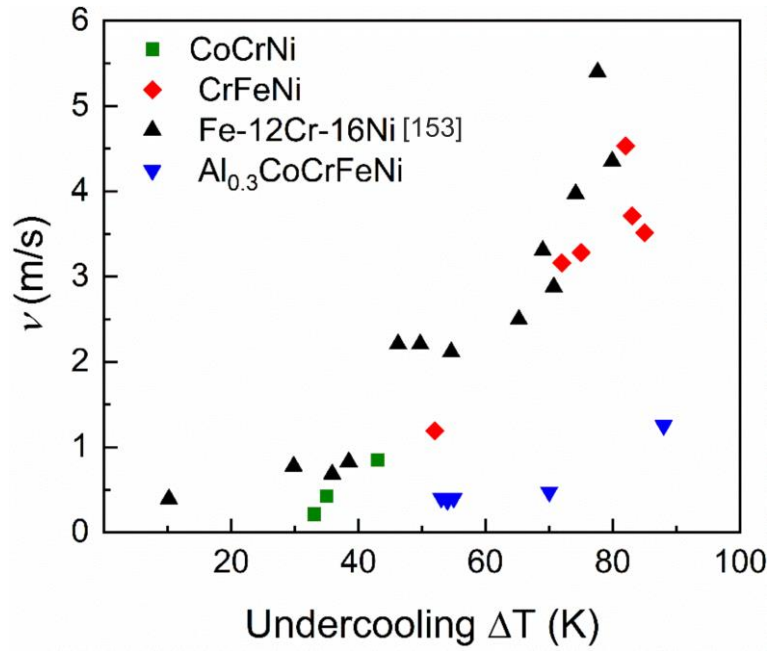


Figure 4.5. Crystal growth velocity  $v$  as a function of undercooling of the  $\text{Al}_{0.3}\text{CoCrFeNi}$  HEA. Also added to the plot are the values of  $v$  for CoCrNi and CrFeNi MEAs (Chapter 3, section 3.2.2), and Fe-12Cr-16Ni [153].

Table 4.1. Crystal growth velocity  $v$  as a function of melt undercooling for the  $\text{Al}_{0.3}\text{CoCrFeNi}$  HEA.

Undercooling $\Delta T$ (K)	Crystal growth velocity $v$ (ms)
53	0.402
54	0.374
55	0.4024
70	0.473
88	1.254

The room-temperature X-ray profiles obtained by an in-house diffractometer (see section 2.4) are presented for two samples solidified under EML processing with liquid undercooling of 30 and 70 K in Fig. 4.6. The diffractogram of the  $\Delta T = 30$  K sample (Fig. 4.6a) reveals a mixture of a disordered  $fcc$  plus ordered  $L1_2$  phases. The  $L1_2$  phase is evident from the discrete (100) superlattice peak at  $\sim 28^\circ$  which is a prohibited diffraction reflection for the face-centered cubic structure. Contrary, the sample solidified with an undercooling of 70 K (Fig. 4.6b) only shows peaks of a  $fcc$  crystal structure.



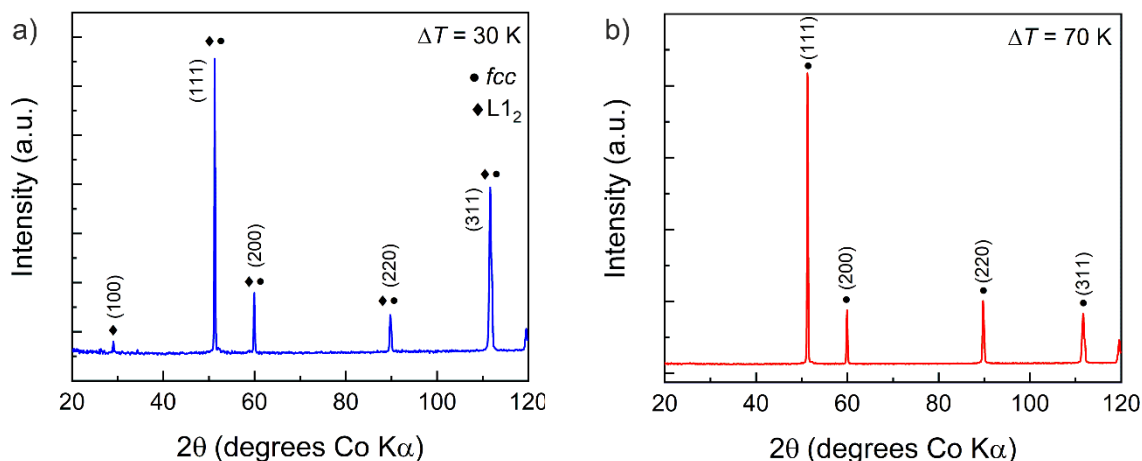


Figure 4.6. *Ex situ* X-ray diffraction patterns of solidified samples of the  $\text{Al}_{0.3}\text{CoCrFeNi}$  HEA under EML processing. a)  $\Delta T = 30$  K; b)  $\Delta T = 70$  K.

As mentioned previously, the formation of intermetallic B2 and  $L_{12}$  phases are predicted as solid-state transformations by thermodynamic calculations. The  $L_{12}$  phase is expected to precipitate at temperatures below 873 K [193]. It can also be seen from the DSC scan in Figure 4.3. Its formation is dependent on the cooling rate since it was sometimes reported [195] and other times not [189]. In this study, the cooling rate in the solid-state is virtually the same for the different undercooling, see a comparison in Fig. A3.1 in Appendix 3. However, the *in situ* measurements are limited to  $\sim 900 - 1000$  K on cooling. The formation of the  $L_{12}$  intermetallic phase shown in Fig. 4.6a should have happened after the sample was dropped into the  $\text{Al}_2\text{O}_3$  crucible and therefore it was not monitored. As discussed earlier (100) superlattice peaks were never observed on the *in situ* XRD patterns.

Figure 4.7 shows a comparison between the cross-sectioned microstructures of the  $\text{Al}_{0.3}\text{CoCrFeNi}$  alloy, processed in the EML, for two different undercooling levels,  $\Delta T = 30$  and 70 K. All images were obtained using EBSD and the experimental setup was described in section 2.4. In the left panels, the grain maps showing different grains in random colors are presented. In the central panels, the inverse pole figures are displayed and the right panels show the phase maps for the different  $\Delta T$ .

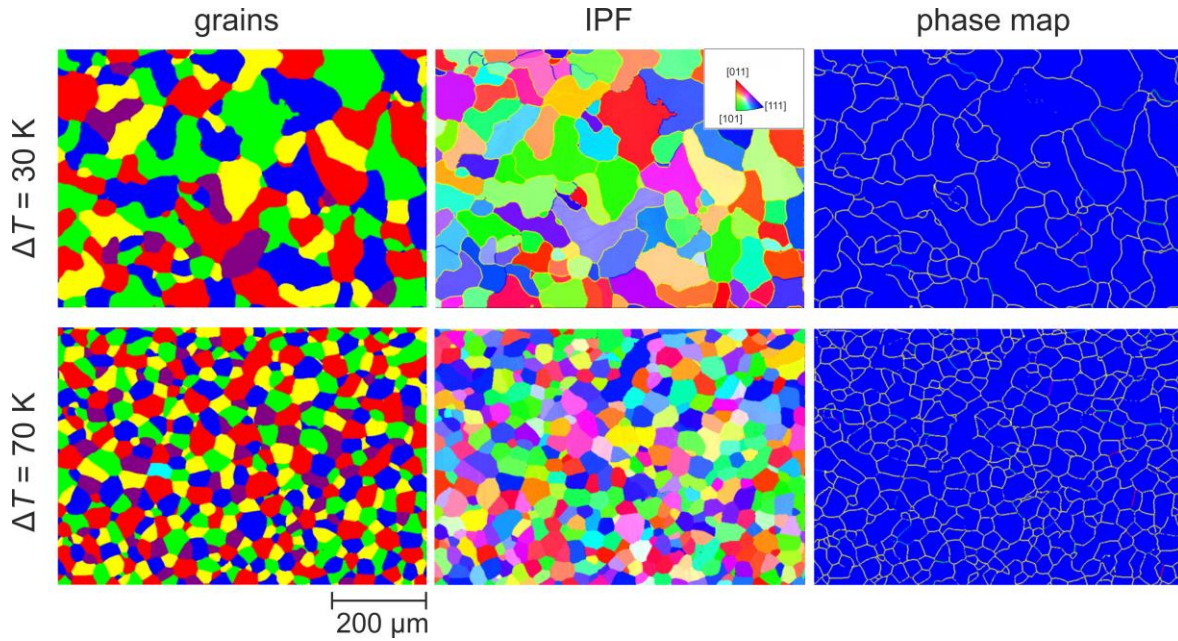


Figure 4.7. EBSD images of  $\text{Al}_{0.3}\text{CoCrFeNi}$  samples solidified during EML-processing at different undercooling. Left panels – grain maps; central panels – inverse pole figures; right panels – phase maps.

Observing the grain maps it is clear to see an intense grain refinement as the liquid undercooling increases from 30 to 70 K. At  $\Delta T = 30$  K the mostly coarse grains have an undefined shape while for  $\Delta T = 70$  K the grains have a refined equiaxed morphology. This observation is the second major difference between the alloys investigated in Chapter 3 and the  $\text{Al}_{0.3}\text{CoCrFeNi}$  alloy. For CrFeNi, CoCrNi, and CoCrFeNi alloys spontaneous grain refinement was only observed at large undercooling (see Fig. 3.14), while grain refinement is noticed at low undercooling for the five-component alloy. Furthermore, the formation of annealing twins is not seen for the equiaxed grains of  $\text{Al}_{0.3}\text{CoCrFeNi}$  at  $\Delta T = 70$  K (see the IPF), which contrasts with the grain refined microstructures shown in Figs. 3.14c' and A2.11 in Appendix 2. This evidence supports the conclusion that recrystallization did not occur in the post recalescence period for the  $\text{Al}_{0.3}\text{CoCrFeNi}$  alloy.

Spontaneous grain refinement taking place during solidification at low undercooling has been observed experimentally for other alloy systems, e.g., Ni-base superalloy [176], Ni-Cu [178,179], Ni-C [196], and Fe-Ni alloys [197]. The rationale for spontaneous grain refinement at low undercooling is explained by the same mechanism as in deeply undercooled melts; dendritic break-up and coarsening caused by remelting if the dendrite break-up time  $\Delta t_{bu}$  is less than the post recalescence time  $\Delta t_{sol}$  [178]. As mentioned in Chapter 3, the driving force for fragmentation of the primary dendrites is an attempt of the

system to minimize the solid/liquid interface area via heat and solute diffusion in the bulk phases. The break-up time as a function of melt undercooling  $\Delta t_{bu}(\Delta T)$  can be estimated as [177]:

$$\Delta t_{bu}(\Delta T) \approx \frac{3}{2} \frac{R(\Delta T)^3}{d_0 D_c} \left| \frac{m_l c_0 (1 - k_E)}{\Delta H_f / C_p} \right| \quad (\text{Eq. 4.1})$$

where  $R(\Delta T)$  is the dendrite trunk radius dependence on undercooling,  $m_l$  the equilibrium liquidus slope,  $c_0$  the nominal alloy's composition,  $k_E$  the equilibrium partition coefficient,  $\Delta H_f$  the heat of fusion,  $C_p$  the specific heat at constant pressure,  $D_c$  the solute diffusivity in the liquid, and  $d_0 (= \Gamma C_p / \Delta H_f)$  the capillarity length where  $\Gamma$  is the Gibbs-Thomson coefficient. According to Ref. [177], there is a proportionality constant between  $R(\Delta T) / R_{tip}(\Delta T) = 20$ , being  $R_{tip}$  the dendrite tip radius.

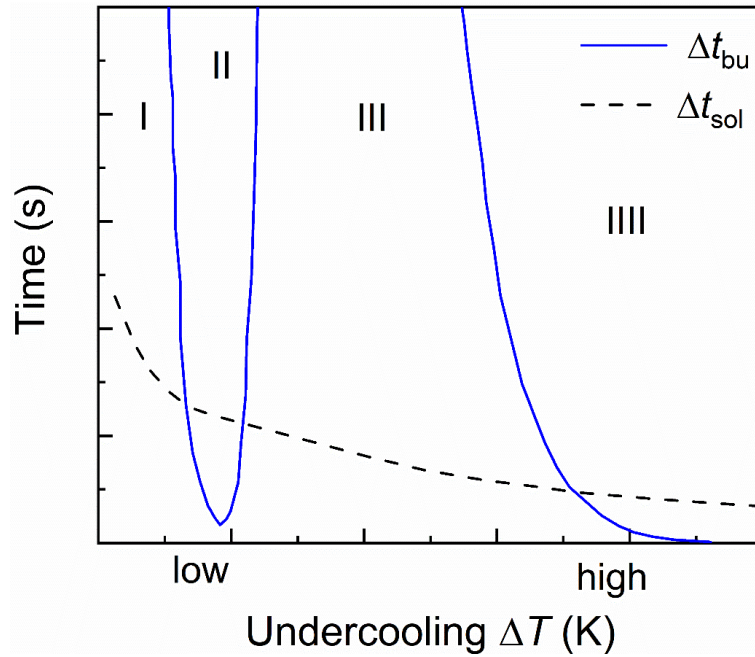


Figure 4.8. Schematic representation of dendritic break-up time  $\Delta t_{bu}$  as a function of melt undercooling according to Eq. 4.1. [177].

Equation 4.1 predicts two consecutive grain refinement regions (II and III) for alloys as a function of undercooling, one at low and another at higher  $\Delta T$ , as can be seen in Fig. 4.8. The  $\Delta t_{bu}$  decreases sharply until a minimum, rises also sharply until reaching a maximum, and then decreases continuously. The reason for a minimum and maximum in the  $\Delta t_{bu}(\Delta T)$  is justified by the dependence of the  $R_{tip}$  to melt undercooling. Since chemical

diffusion controls dendritic growth at low undercooling the tip radius decreases as the concentration gradient becomes steeper at the solid/liquid interface. This is the first region of grain refinement (region II in Fig. 4.8).

In the next stage, with increasing  $\Delta T$  and consequently increasing  $v$ , solute trapping causes the concentration gradient to become smaller which in turn increases the tip radius. At this undercooling level, columnar dendrites are observed again in the solidified samples (region III in Fig. 4.8). Beyond a critical undercooling the dendritic growth is mostly thermally controlled and the increase in thermal gradient between the solid/liquid interface causes the tip radius to decrease once more. This is the second region in  $\Delta t_{bu}(\Delta T)$  curve where grain refinement is observed (region IIII in Fig. 4.8).

The inverse pole figures (Fig. 4.7) show that in both cases there is no crystallographic texture. As discussed in Chapter 3, under the effect of electromagnetic stirring the growing dendrites can be moved and rotate in the remaining liquid. Though the preferential growth of *fcc* dendrites occurs in the  $\langle 100 \rangle$  crystallographic directions, due to the weak anisotropy of the liquid/solid surface tension, the motion and rotation of the individual dendrites lead to a non-textured microstructure [198]. Li *et al.* [184] have stated that fluid flow has a more pronounced effect at low undercooling where the growth velocity is slower and it is weakened as  $\Delta T$  increases.

The phase maps shown in Fig. 4.7, on the right-hand panels, show that in both cases only a single-phase *fcc* structure is observed. The EBSD technique cannot distinguish the difference in Kikuchi patterns from *fcc* and  $L1_2$  phases since they have similar crystal structures. This reason, added to the nanoscale size of the precipitates detailed by Ref. [189], makes it impossible to distinguish the two phases in the EBSD map of the  $\Delta T = 30$  K sample.

Figure 4.9 illustrates a dendritic structure, in three dimensions, formed during the solidification of the  $Al_{0.3}CoCrFeNi$  alloy with a melt undercooling of 30 K. As the solid reached the central part of the sphere the liquid had been consumed by crystallization and the dendrites grew into a void. After sectioning the cross-section of the sample the dendritic structure was exposed. The image was captured using the BSE detector in the SEM with 20 kV acceleration and it was artificially colored.

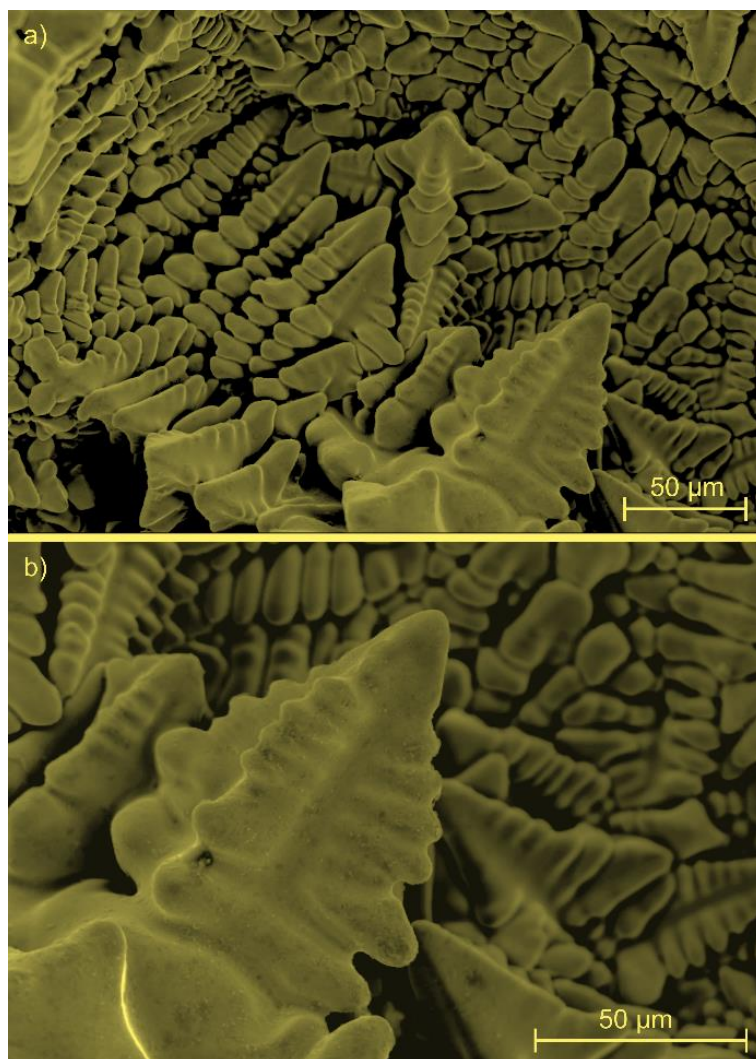


Figure 4.9. The dendritic structure of the Al<sub>0.3</sub>CoCrFeNi HEA solidified with a  $\Delta T = 30$  K.

## Chapter 5: Non-equilibrium solidification of the NbTiVZr refractory high-entropy alloy

This Chapter describes the non-equilibrium solidification experiments carried out with the refractory NbTiVZr HEA which has been described in the literature to crystallize mainly with a body-centered cubic crystal structure.

### 5.1 Introduction

The search for materials suitable for high-temperature and radiation-resistant applications gained a new perspective with the introduction of refractory high-entropy alloys (RHEAs) [102]. This design concept opened new avenues for exploring a compositional space based on the high melting temperature metallic elements of the periodic table (W, Ta, Mo, Nb, Hf, V, Zr). At the same time, it brings challenges in understanding phase formation and stability ranges, mechanical properties, and corrosion resistance under such extreme conditions. Resolving these key material properties are required to cross the bridge between scientific enthusiasm and practical applications.

The NbTiVZr equiatomic composition was proposed as a low density ( $\rho = 6.52 \text{ g cm}^{-3}$ ) RHEA [199,200], showing good compressive ductility and strong work hardening behavior at room temperature. The compression yield strength data for this alloy, at the high-temperature regime, seems to be scattered. Low yield strengths of 75 and 58 MPa at 1273 K were reported in Refs. [200] and [201], respectively. This perhaps limits its use for high-temperature applications but it does not exclude service at moderate temperatures [202]. Contrarily, Jia *et al.* [203] observed that the strength of this alloy reached a maximum of 500 MPa and then stabilized at 200 MPa during compression testing, also at 1273 K.

Senkov *et al.* [199] produced NbTiVZr samples by arc melting followed by hot isostatic pressing at 1473 K and 207 MPa for 2 hours. In sequence, the alloy was homogenized at 1473 K for 24 hours and cooled with a low rate of  $10 \text{ K min}^{-1}$ . The microstructure was composed of large grains ( $\sim 600 \text{ }\mu\text{m}$ ) with a body-centered cubic (*bcc*) crystal structure and homogeneously distributed Zr-rich regions of 20 – 30  $\mu\text{m}$  inside the grains, and sub-micron V-rich particles inside the Zr-rich regions. The crystal structure of the precipitates could not be identified with (XDR) due to their small volume fraction.

King *et al.* [202] used a high throughput computational tool, Alloy Search and Predict, to screen over one million four-component equiatomic compositions, looking for



those which would form a single-phase solid solution (SPSS) at the melting temperature and have low thermal neutron absorption cross-section. The NbTiVZr alloy was found to comply with both requirements. In their study [202], the as-cast and homogenized alloy (1473 K, 100 hours) followed by water quenching formed a *bcc* SPSS microstructure. After subsequent aging at 973 K for 100 hours, it decomposed into a *bcc* matrix and hexagonal closed-packed (*hcp*) and  $V_2Zr$  (C15-Laves) minor phases.

The formation of a *bcc* SPSS in the homogenized and quenched state in Ref. [202], and in the as-cast condition in Ref. [63] differs from the microstructure observed in Ref. [199]. The discrepancy was attributed to different cooling rates from the homogenized or liquid state [202]. As has been demonstrated for many HEAs [17,142,191,204], kinetics plays an important role in determining the final microstructures, and a metastable SPSS may be 'frozen' depending on the processing conditions.

A challenge in the study of refractory materials is that high-temperature measurements are usually difficult due to instrumentation limits. For example, determining the liquidus  $T_l$  and solidus  $T_s$  temperatures cannot be done using conventional differential scanning calorimetry. On the other hand, an electromagnetic levitation (EML) technique allows for processing and investigating even in the liquid state. This study aims at understanding phase and microstructure formation upon non-equilibrium solidification and during heating/cooling of the NbTiVZr RHEA. A better understanding of metastability, temperature-dependent phase transformations, and the role of kinetics is required for a proper choice of the processing parameters during fabrication and potential use of this material in high-temperature and/or radiation-resistant applications.

## 5.2 Results

### 5.2.1 *In situ* synchrotron X-ray diffraction

Figure 5.1a shows a temperature-time profile measured during a heating/cooling cycle, coupled with the time-resolved XRD patterns plotted as a color-contour diagram. The pyrometer was calibrated using the melting point of pure vanadium by measuring in the EML facility at the same processing conditions. Thermal analysis using a calorimeter was not possible since the NbTiVZr samples reacted with both  $Al_2O_3$  and  $ZrO_2$  crucibles. The solidus  $T_s$  and liquidus  $T_l$  temperatures for the NbTiVZr alloy were registered during 16 heating/cooling cycles carried out in the EML facility, and the average temperature and standard deviation were calculated (Table 5.1).

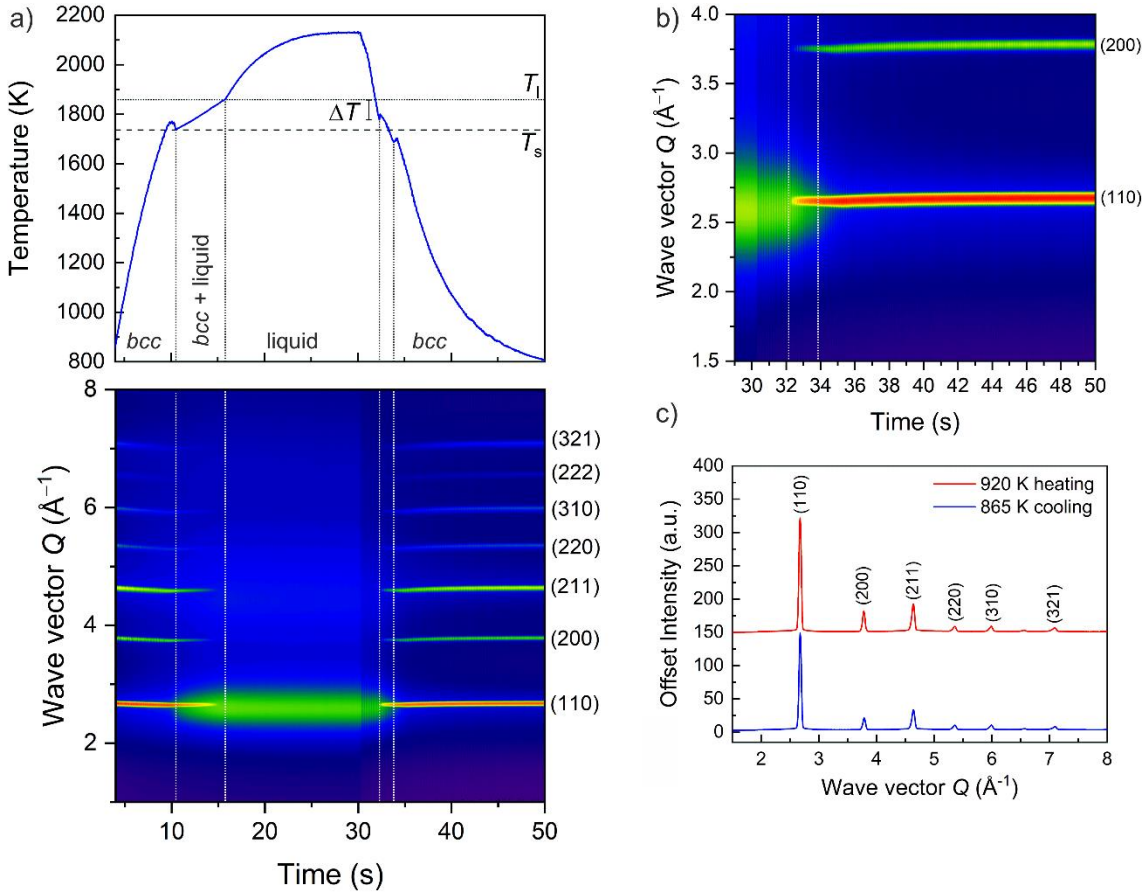


Figure 5.1. (a) Thermogram and corresponding XRD contour plot measured from an undercooled NbTiVZr alloy by  $\Delta T = 80$  K; (b) Inset XRD contour plot from Fig. 5.1a showing the crystallization event upon cooling from the liquid state; (c) comparison of XRD profiles at the initial and final stages of EML-processing.

Table 5.1. The solidus  $T_s$  and liquidus  $T_l$  temperatures of the NbTiVZr RHEA measured with a one-color pyrometer during heating in the EML facility and calculated using the ThermoCalc AB software and the TCHEA4 database (calculations by V.T. Witusiewicz).

	$T_s$ (K)	$T_l$ (K)
Experimental	$1736 \pm 12$	$1858 \pm 7$
CALPHAD	1762	1926

Lever rule thermodynamic calculations and Scheil solidification simulation were performed by V.T. Witusiewicz (ACCESS e.V., Aachen) using the Thermo-Calc 2020a software from Thermo-Calc AB [168] and the TCHEA4 database [50]. In both cases, all phases modeled in the TCHEA4 relating to the Nb-Ti-V-Zr system were entered. The values of  $T_s$  and  $T_l$  from the equilibrium thermodynamic calculations are included in Table 5.1.



In Figure 5.1a, a peak appearing at 1766 K on the thermogram, measured during heating, is due to a change of emissivity upon the onset of melting. The solidus temperature  $T_s$  is registered as 1736 K. During heating up to  $T_s$  only XRD peaks corresponding to a *bcc* crystal structure can be identified. The melting ends at 1858 K and the liquid is further overheated by approximately 300 K above  $T_l$ . During this stage, only diffuse scattering is measured, confirming that the alloy is completely molten. The liquid is then cooled by lowering the input power to the induction coil and by two jet-streams of He directed to the sample's surface by opposite sides. At 1778 K spontaneous nucleation is recorded by the pyrometer which yields a liquid undercooling of  $\Delta T = 80$  K. A peak appearing upon crystallization is related to the change of emissivity. The XRD peaks that appear following this stage correspond to a *bcc* crystal structure. Figure 5.1c shows the X-ray diffractograms for this particular cycle at two distinct temperatures; during heating at 856 K and cooling at 806 K. It is clear from the patterns that the initial and final states show the same (*bcc*) structure. A 3D XRD plot corresponding to the crystallization of the sample is shown in Fig. A4.1 in Appendix 4.

Figure 5.2a shows a temperature-time profile coupled with the time-resolved XRD patterns for a NbTiVZr sample heated up close to the liquidus temperature, but without reaching a complete melting. This is seen from the (110), (200), and (211) peaks that extend throughout the whole duration of the experiment. During heating from room temperature up to  $T_s$  only diffraction peaks that are indexed to a *bcc* structure are recognizable. In the semisolid state, between ~15 s and 75 s Bragg peaks of the *bcc* phase overlap with diffuse peaks scattered by the liquid phase, see for example the XRD pattern at 1830 K and at ~ 56 s in Figure 5.2c.

Upon the sample cooling, starting from approximately ~ 75 s, reflections of several crystalline phases are observed in the XRD patterns, see the enlarged plot in Fig. 5.2b. These peaks are indexed to two extra *bcc* phases. The onset temperature for the appearance of the *bcc*#2 is 1491 K and the onset temperature for the *bcc*#3 phase is 1281 K. A small peak on the temperature-time profile around 74 s (Fig. 5.2a) corresponds to a change of the emissivity of the alloy upon crystallization. A 3D XRD plot measured during cooling of this sample is shown in Fig. A4.2 in Appendix 4.

The samples were always weighed before and after the levitation experiments and the maximum weight loss was ~ 0.01 wt. %. This indicates that neither oxidation nor crucial compositional changes occurred.

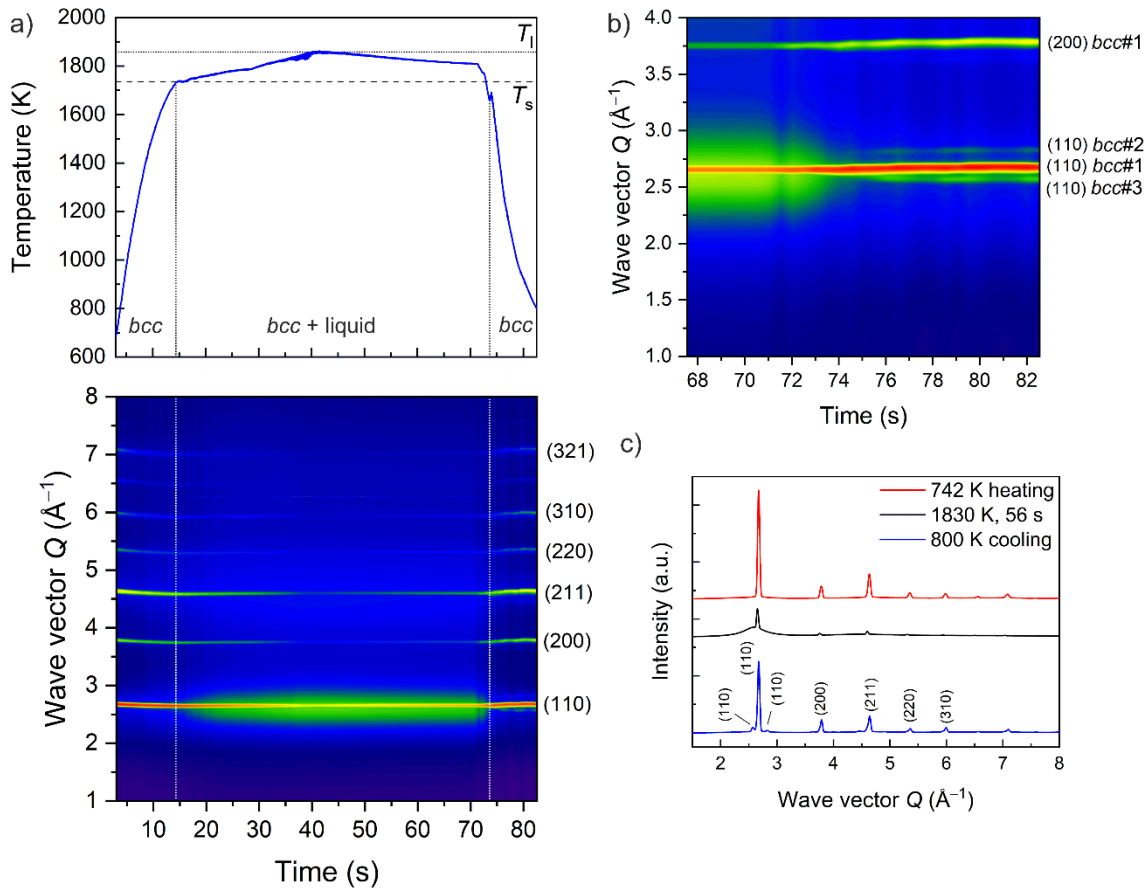


Figure 5.2. (a) Thermogram and corresponding XRD contour plot measured from a NbTiVZr alloy heated between  $T_l$  and  $T_s$  and cooled. (b) Inset XRD contour plot from Fig 5.2a showing the appearance of different diffraction peaks upon cooling. (c) comparison of XRD profiles at the initial and final stages of EML processing, and also at the semisolid state.

### 5.2.2 Room temperature synchrotron X-ray diffraction

Figure 5.3 displays the *ex situ* synchrotron XRD measurements of the samples shown in Figs. 5.1 and 5.2 after solidification. In Figure 5.3a only peaks corresponding to a *bcc* SPSS (*bcc*#1) are seen. In Fig. 5.3b besides the peaks corresponding to the primary *bcc* phase (*bcc*#1), additional (110) reflections are marked for *bcc*#2 and *bcc*#3 phases. Fig. 5.3c shows the same pattern as in Fig. 5.3b but with a reduced scale of intensity so the reflections from other crystallographic planes from *bcc*#2 and *bcc*#3 are distinguishable.

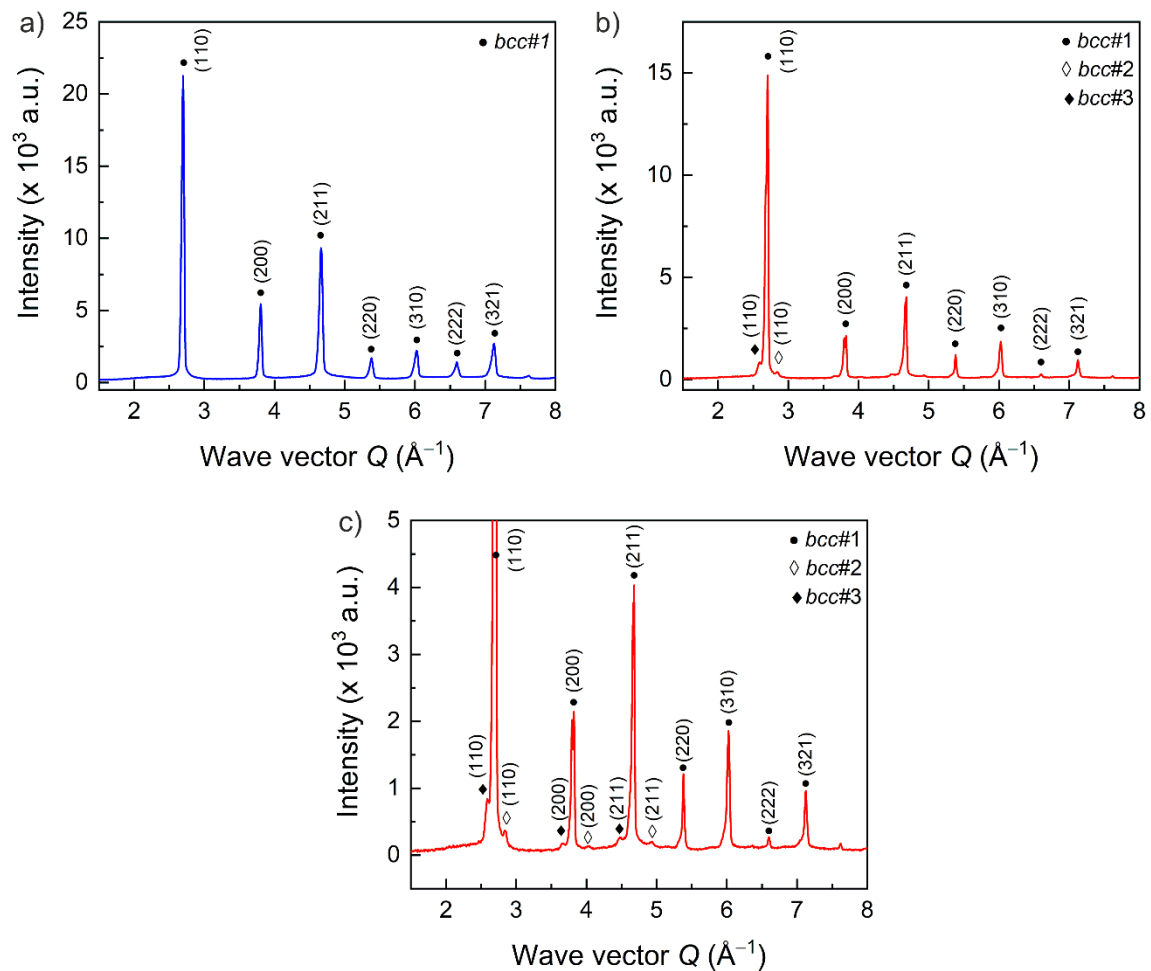


Figure 5.3. Room temperature XRD patterns measured with high-energy synchrotron radiation. a) sample solidified from the liquid state with a melt undercooling of 80 K; b) sample solidified from the semi-solid state; c) The same XRD pattern shown in Fig. 3b but with a reduced scale of Intensity to highlight different diffraction peaks from different crystallographic planes of *bcc#2* and *bcc#3* phases.

### 5.2.3 High-speed video imaging

Digital images representing the solidification of a NbTiVZr melt at a maximum undercooling of 107 K are shown in Fig. 5.4a. In the upper left panel, the melt at its maximum undercooling is seen. In the upper-middle panel, a phase can be observed (brighter contrast) growing in the liquid (darker contrast). The remaining panels show the sequence of the crystallization process. The difference in the contrast is due to the release of latent heat from the crystallizing solid. In Fig. 5.4b the variation of the images' grayscale level, measured on a 50 x 50-pixel area in the central part of a sample in the videos, is shown as a function of time during the crystallization of the liquid. The grayscale dataset is smoothed because the crystallization is slower than the rotation of the sample. This makes either the

liquid or solid phase to be within the analyzed area in a certain period. Therefore, a periodic pattern of the grayscale is observed especially once the crystallization starts. The solidification sequence is shown in Fig. A4.3 in Appendix 4.

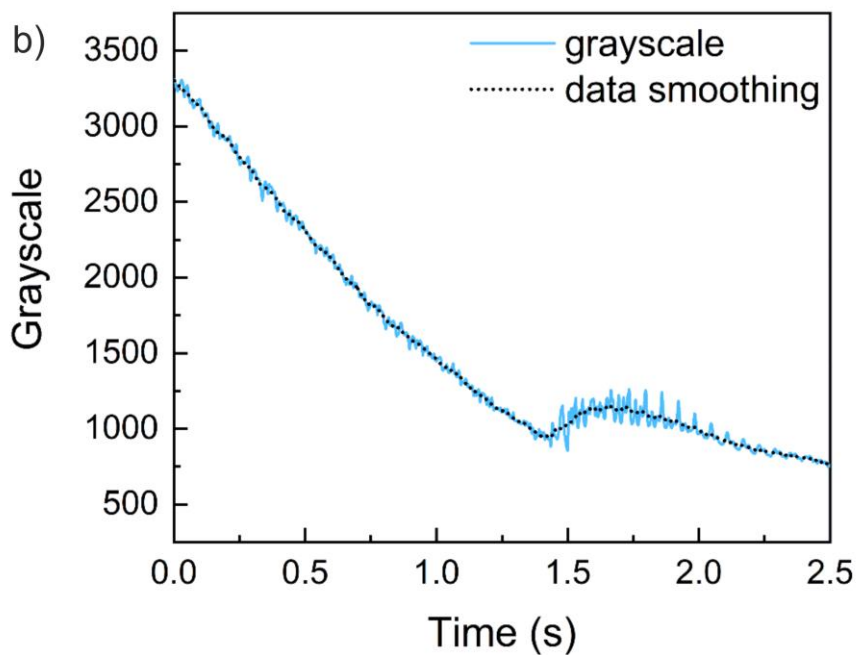
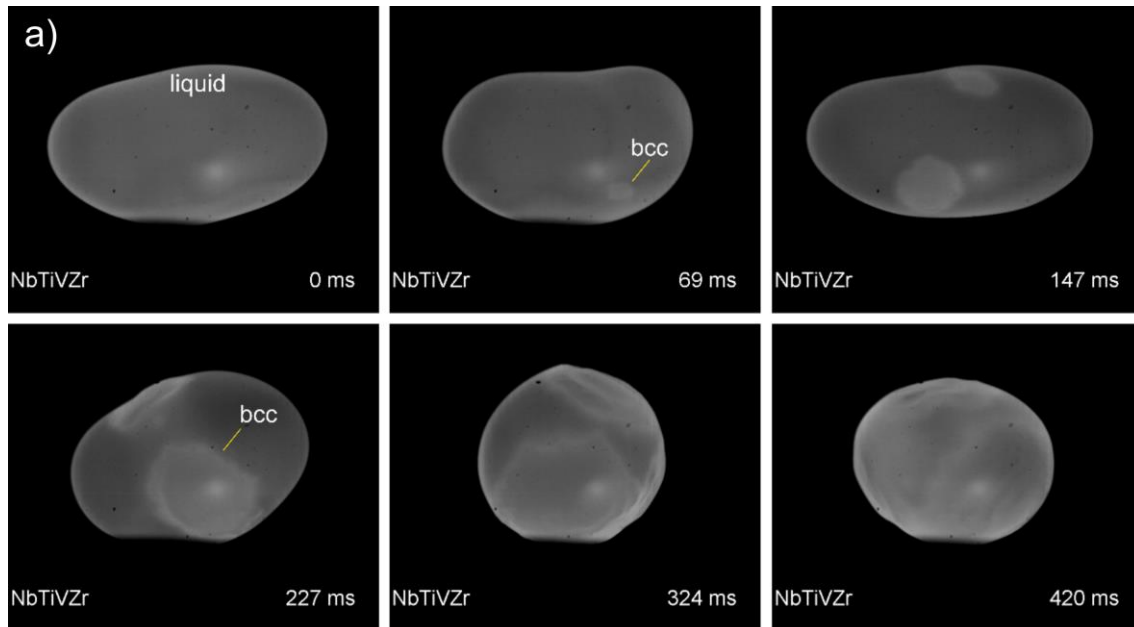


Figure 5.4. a) Digital images representing the solidification of a NbTiVZr HEA melt with a maximum undercooling of 107 K. The time scale was set to zero at a moment shortly before the crystallization onset. b) Variation of the grayscale level on a 50 x 50-pixel area as a function of time measured in the central part of the sample shown in Fig. 5.4a.

### 5.2.4 Microstructure and structure analysis

SEM micrographs recorded using the BSE detector, combined with corresponding EDX elemental maps, are displayed in Figs. 5.5a and 5.5b and 5.5c and 5.5d for the samples shown in Figs. 5.3a and 5.3b, respectively. Figure 5.5a shows a dendritic microstructure with solute rejection to interdendritic regions (brighter contrast). From the EDX elemental mappings, it is possible to observe that the dendrite cores are rich in Nb and Ti, while they are depleted of Zr and V. Despite the evident microsegregation (Fig. 5.5b), no second phase can be recognized from the SEM image (Fig. 5.5a) which is in agreement with the *in situ* (Fig. 5.1) and *ex situ* synchrotron XRD measurements in Fig. 5.3a.

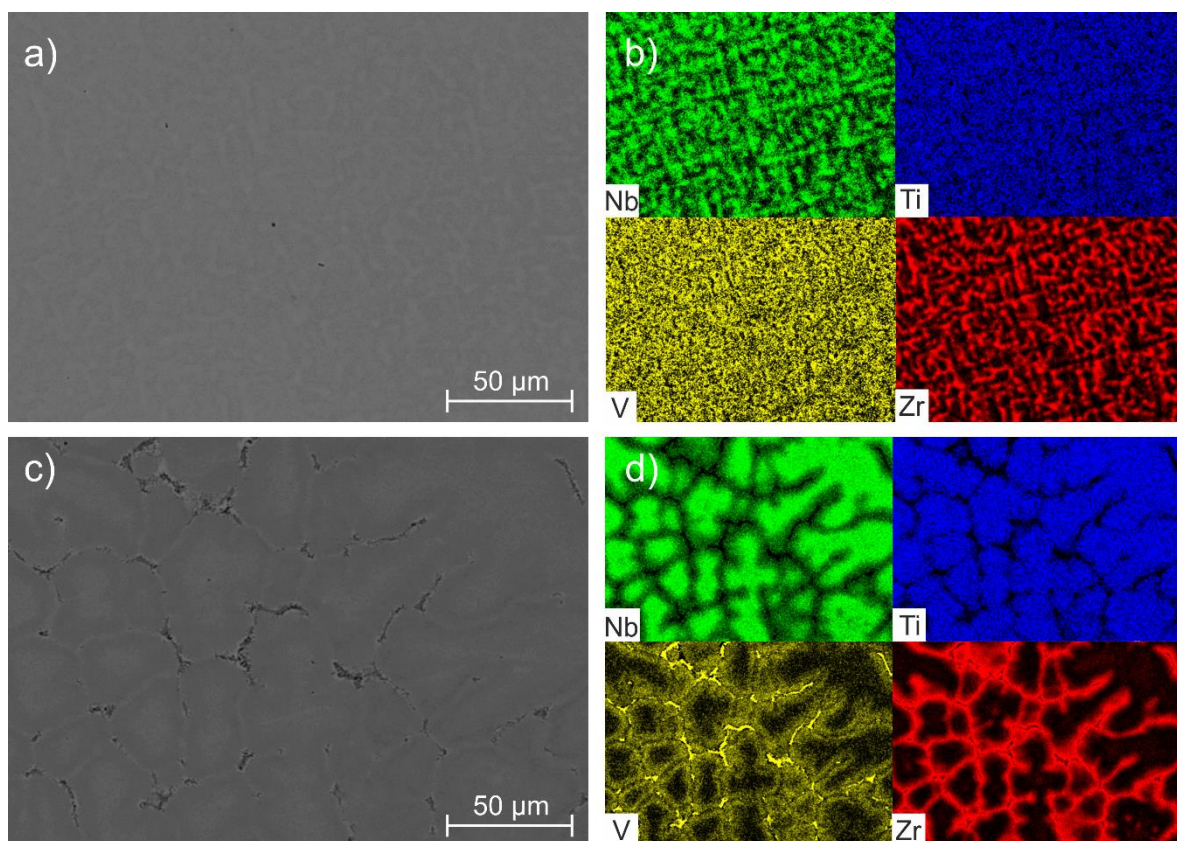


Figure 5.5. Microstructural characterization of the NbTiVZr solidified samples. a) EBS SEM image of the sample solidified with a melt undercooling of 80 K. b) EDX maps from the region shown in 5.5a. c) BSE SEM image of the sample solidified from the semisolid state. d) EDX maps from the region shown in 5.5c.

In Fig. 5c, a dendritic microstructure, which is much coarser than that shown in Fig. 5a, is observed with three different contrast regions from the SEM-BSE image: a medium-bright region corresponding to the matrix, a brighter region along the grain boundaries, and submicron-sized dark particles inside the latter. The EDX mappings show that the matrix,



*bcc*#1 in the XRD profile in Fig. 5.3b, is rich in Nb and Ti, while depleted of Zr and V. The bright regions along the grain boundaries seen in the BSE SEM image (Fig. 5.5c) are enriched with Zr and V, and the dark particles are rich with vanadium. SEM and SEM-EDX images with higher magnification are shown in Fig. A4.4 in Appendix 4. The crystal structure of the precipitates was further investigated using TEM by R.G. Mendes (IFW Dresden and Utrecht University).

Figure 5.6a shows a SEM-BSE image of the dendritic microstructure of a sample solidified with a melt undercooling of 80 K, as illustrated in Fig. 5.5a. The red line marks the area from which a FIB-SEM cross-section for further TEM investigations was prepared. A low magnification TEM image of the prepared cross-section is shown in Figure 5.6b. Multiple SAED measurements were acquired to confirm the presence of a single *bcc* phase. Typical electron diffractograms for different regions of the sample are shown in Figure 5.6c and Figure 5.6d. The diffraction pattern was indexed as a *bcc* phase with a lattice parameter of 0.330 nm corresponding to the lattice parameter determined from the synchrotron XRD at room temperature (Fig. 5.3a).

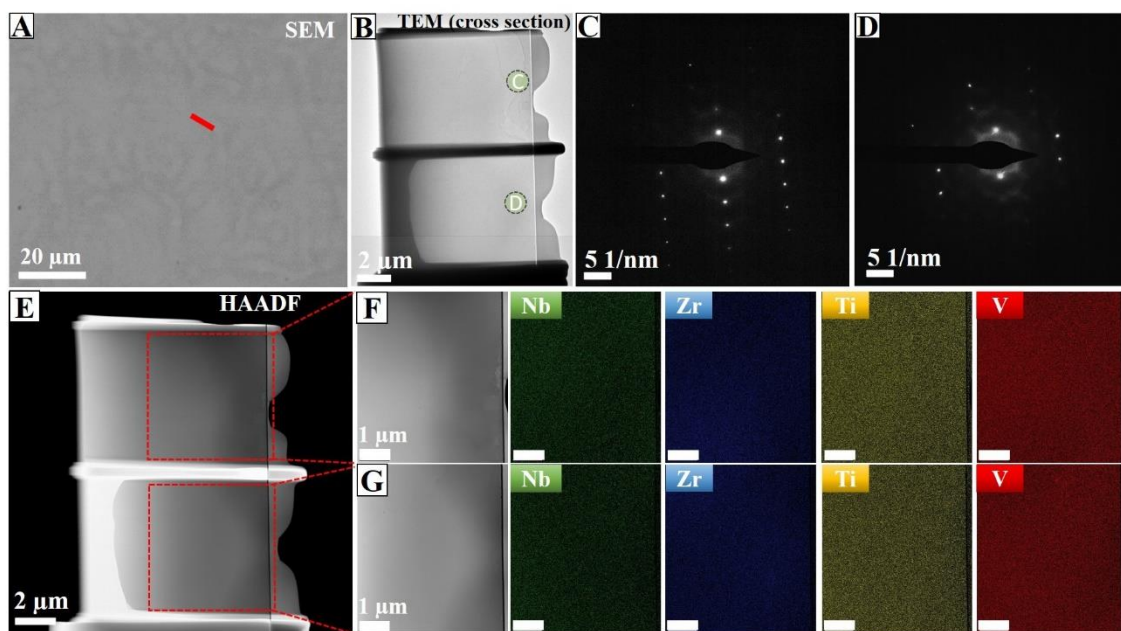


Figure 5.6. a) BSE SEM image showing the dendritic microstructure and the red line corresponding to the area where the TEM cross-section was prepared. b) shows a TEM image of the specimen cross-section. Panels c) and d) show the SAED pattern for two different regions of the cross-section. e) HAADF image of the cross-section and the corresponding EDX elemental mapping for the different regions shown in panels f) and g).

Figure 5.6e shows images of the cross-sectional specimens collected with a high-angle annular dark-field (HAADF) detector with the TEM operating in the scanning mode (STEM). STEM is a variation of TEM that uses a focused electron beam that is scanned over a thin specimen. STEM-HAADF imaging allows the differentiation between different atomic elements due to differences in atomic mass as in this imaging mode, the intensity scales with approximately the atomic number squared ( $I \sim Z^2$ ). STEM also makes it possible to probe the local chemical composition of the specimen using the EDX detector. STEM-EDX mappings of different regions of the sample (Figure 5.6f and Figure 5.6g) show the homogeneous nature of the sample. A thorough investigation of the cross-section was conducted with high-resolution images and multiple regions for SAED were acquired and presented in Appendix 4 (Figs. A4.5 and A4.6).

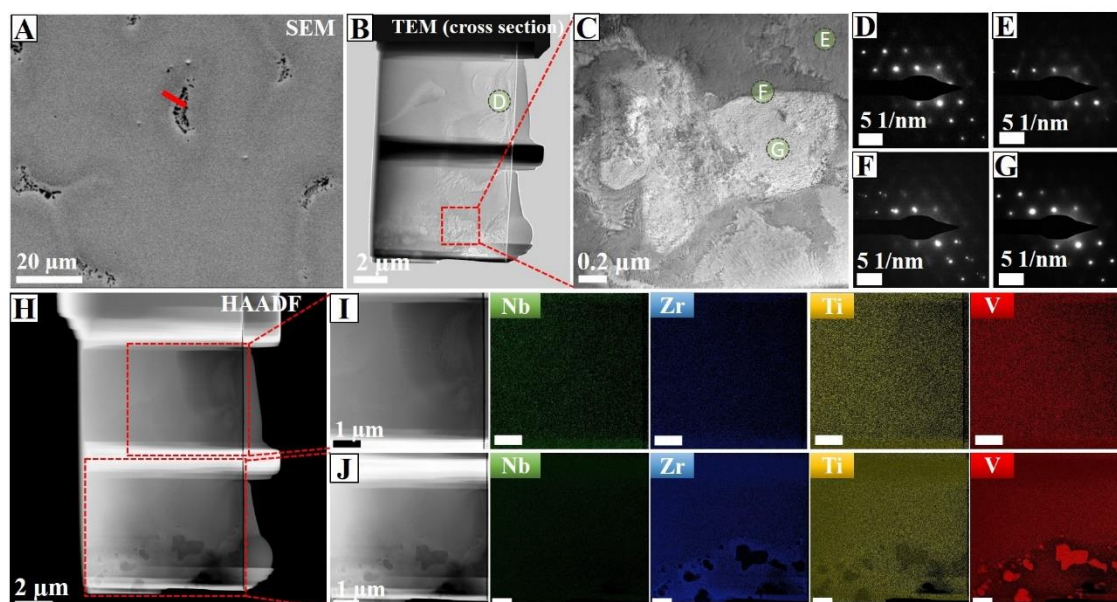


Figure 5.7. a) SEM image showing the different contrast corresponding to different phases. The dark contrast corresponds to the V-rich region (lattice constant: 0.312 nm), the brighter contrast corresponds to the Zr-rich region (lattice constant: 0.344 nm), and the medium-bright contrast corresponds to the matrix (lattice constant: 0.330 nm). The red line depicts the area from which a cross-section of the specimen was prepared; b) TEM image showing the cross-section of the specimen; c) High-magnification TEM showing the region with all phases coexisting. Panels d-g are SAED patterns for the matrix, the interface between V-rich and Zr-rich regions, and the V-rich region, respectively. HAADF image of the cross-section is shown in panel h. The local elemental mapping for the different regions shown in panels i and j. The elemental mapping of panel i (matrix) is homogeneous, whereas the one from panel j shows clearly the different chemical compositions.

Figure 5.7 shows images of a sample processed from the semisolid state, as illustrated in the XRD pattern in Fig. 5.3b. The SEM-EBS image is shown in Fig. 5.7a. To investigate in detail these three regions, a cross-section indicated by the red line in Fig. 5.7a has been studied by TEM. Low magnification and high magnification TEM images depicting the different regions of interest are shown in Fig. 5.7b and Fig. 5.7c, respectively. Figure 5.7d and Figure 5.7e show electron diffraction patterns corresponding to the matrix (lattice constant: 0.330 nm). A thorough study of the matrix was also conducted in this case with a high-resolution image and multiple SAED patterns and is presented in Appendix 4 (Fig. A4.7).

Figure 5.7f shows a diffraction pattern on the interface between the Zr-rich region (lattice constant: 0.344 nm) and the V-rich region (lattice constant: 0.312 nm), where it is possible to distinguish two different diffraction points due to the slightly different lattice parameters. Figure 5.7g presents the diffraction pattern of the V-rich particles (lattice constant: 0.312 nm). All patterns were indexed corresponding to the (100) zone axis of a *bcc* crystal structure, showing that all grains and interfaces are aligned in the same *bcc* superstructure. The TEM-EDX elemental mapping of the different regions depicted in the HAADF image (Fig. 5.7h) shows that Nb, Zr, Ti, and V are homogeneously distributed in the matrix (Figure 5.7i), whereas Figure 5.7j clearly shows the V-rich and Zr-rich regions at the grain-boundary. This is in agreement with the EDX maps obtained with SEM (Fig. 5.5d). High-resolution images of all phases are presented in Appendix 4 (Fig. A4.8) while the elemental mapping images of higher magnifications are presented in Fig. A4.9 in Appendix 4.

## 5.3 Discussion

### 5.3.1 Phase formation upon solidification

To the best of the author's knowledge, no experimental values of  $T_s$  and  $T_l$  have been reported in the literature for this RHEA. This is supposedly due to the reactivity of this alloy with the crucible materials during DTA experiments at high temperature, as that observed in the present study. The solidus temperature  $T_s = 1736 \pm 12$  K (Fig. 5.1 and Table 5.1), as determined using the pyrometer in the EML device, is in good agreement (only 26 K lower) with the value predicted for equilibrium conditions by CALPHAD, as shown in Fig. 5.8 and Table 5.1. The liquidus temperature  $T_l = 1858 \pm 7$  K is 68 K lower than that predicted by CALPHAD (Fig. 5.8 and Table 5.1). Usually  $T_s$  is much less dependent on heating rates and



sample sizes than  $T_l$  [205]. Considering the mean value of  $T_s$  and the standard deviation in Table 5.1, one can see a very good agreement with CALPHAD prediction. On the other hand,  $T_l$  should be much more dependent on the heating rate and sample mass [205], but even so, the values are in reasonable agreement.

The crystallization of a *bcc#1* SPSS, which can be seen when the liquid was undercooled by 80 K in Fig. 5.1, agrees with previous studies where it was observed during quenching from the liquid state [63] or homogenized state [202]. Indeed, from equilibrium thermodynamic calculations (Fig. 5.8) one may observe a wide stability range of the primary *bcc#1* phase formed below  $T_l$ . For equilibrium conditions the formation of a second *bcc#2* phase is predicted by CALPHAD via a spinodal decomposition, starting at 1041 K, see Fig. 5.8.

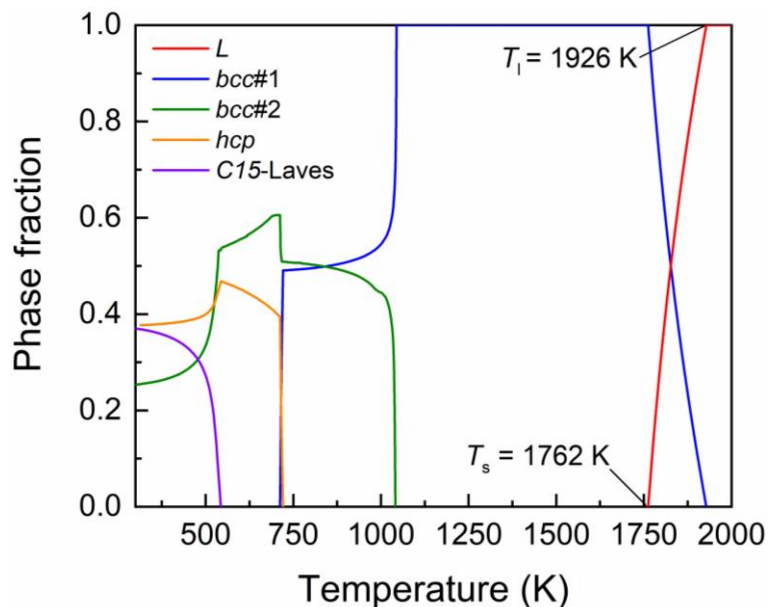


Figure 5.8. Phase fraction as a function of temperature for equilibrium solidification predicted using the ThermoCalc AB software and the TCHEA4 database.

Yurchenko *et al.* [206] had observed a splitting of the (110) *bcc* peak for as-cast and homogenized (1473 K, 24 hours) NbTiVZr samples, which could indicate the formation of two *bcc* phases either during casting, homogenization, or subsequent cooling. From the microstructural analysis, a small fraction of a second phase was observed at the grain boundaries. Nonetheless, the authors stated that the reason for the peak splitting should be further studied. The *in situ* XRD peaks shown in Figure 5.1 do not show splitting and the microstructural and structural analysis (Figs. 5.1a, 5.3a, 5.5a, and 5.6) further confirm its

homogenous nature despite that microsegregation of Zr and V is observed in the interdendritic regions (Fig. 5.5b). Based on this evidence it is safe to conclude that the only transformation that occurred was from the liquid into a *bcc#1* SPPS when the melt was undercooled by 80 K (Fig. 5.1).

In Fig. 5.2 the *in situ* XRD patterns revealed the formation of different phases as the sample was cooled from the semisolid state. Postmortem analysis of the samples disclosed the formation of two additional *bcc* phases at the grain boundaries (Figs. 5.3b, 5.5c, and 5.7). From the onset temperatures of the *bcc#2* and *bcc#3* (Fig. 5.2b), which are 245 and 455 K below  $T_s$ , one could naturally conclude that they occurred as solid-state transformations. However, during non-equilibrium solidification constitutional undercooling may lead to an overall change in the composition of the remaining liquid. The interdendritic liquid then solidifies at a different  $T_s$  than the nominal alloy's composition. Furthermore, the pyrometer only measures a small surface area on the north pole of the droplet. It cannot distinguish temperature gradients over the sample and it does not probe local temperatures. The formation of *bcc#2* and *bcc#3* phases (Fig. 5.2) occurred during the final stage of solidification with crystallization of the interdendritic liquid. This is evident from the solidified microstructures shown in Figs. 5.5c and 5.5d. While the sample was cooled between  $T_l$  and  $T_s$  solute partitioning from the primary dendrites (*bcc#1*) to the interdendritic regions created the compositional conditions for their formation.

Non-equilibrium solidification of the NbTiVZr alloy calculated using the Scheil-Gulliver model is shown in Fig. 5.9. The solidification proceeds between  $T_l = 1926$  K, which is the same as for the equilibrium conditions, and a eutectic temperature  $T_e \approx 1491$  K at what the fraction of the liquid phase decreases to about 1 %. The temperature dependences for the compositions of the liquid and the solid phases are shown in Fig. 5.10. The Scheil-Gulliver simulation suggests that cores of the *bcc#1* dendrites formed in earlier stage of solidification are enriched with Nb and Ti (Fig. 5.10 b, T above  $\sim 1770$  K). Upon cooling, both V and Zr continuously segregate into the interdendritic liquid (Fig. 10a) and start to dominate in the peripheral areas of the dendrites (Fig. 10b, T below  $\sim 1735$  K). Below 1492 K, the interdendritic liquid solidifies into the V-rich *bcc#2* and a Zr-rich *bcc#3* phases via eutectic reaction which completely finishes at 1491 K. These results agree with the element distribution maps presented in Fig. 5.5d and in Fig. A4.4 in Appendix 4. Also, such solidification path conforms with the in-situ XRD measurement upon solidification of the NbTiVZr alloy from the semisolid state (Fig. 5.2). In that case, the (110) reflection of a V-rich phase was observed to appear at 1491 K. The (110) peak of a Zr-rich phase was noticed

at a lower temperature (1281 K). The discrepancy on the formation of the metastable bcc phases between the Scheil-Gulliver calculation and in-situ XRD measurements could be explained either by some deviation of the real and simulated solidification paths or by somewhat imperfect modelling of the TCHEA4 database, or by experimental uncertainty. Indeed, the molar fraction of the bcc #2 and bcc #3 phases is very small and they can be noticed on XRD patterns only when they reach a detectable quantity at the X-ray beam position.

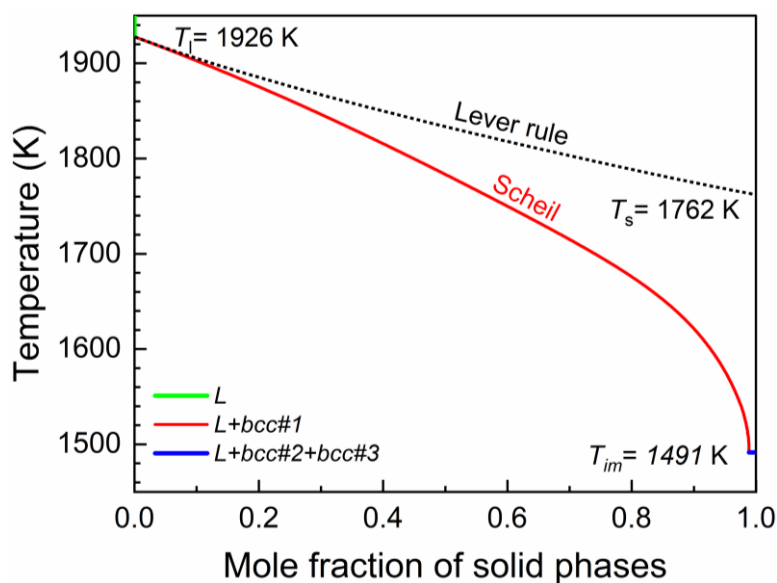


Figure 5.9. The temperature dependence of the fraction of solid phases during solidification of the NbTiVZr alloy under the equilibrium (Lever rule) and non-equilibrium (Scheil) conditions simulated with the ThermoCalc AB software using the TCHEA4 database.

The *ex situ* XRD patterns (Figs. 5.3a and 5.3b) confirm that in both cases the phases formed at high temperature, as shown from the *in situ* XRD patterns in Figs. 5.1 and 5.2, and are preserved at room temperature. The formation of equilibrium *hcp* and C15-Laves phases which are predicted by CALPHAD (see Fig. 5.8) and have been experimentally observed after long-time annealing, at lower temperatures [202,206], were kinetically suppressed due to the fast cooling rate ( $\sim 100 \text{ K s}^{-1}$ ) in the solid-state.

The sequence of images in Fig. 5.4a reveals that multiple grains nucleate and grow in the undercooled melt simultaneously and that they collide as solidification progresses. It is obvious from the plot of the gray value versus time (Fig. 5.4b) that only one recalescence (quasi-adiabatic release of heat upon crystallization) occurs. Thus, considering the *in situ*

XRD showed in Fig. 5.1, the crystallizing solid corresponds to dendrites of a single *bcc*#1 phase.

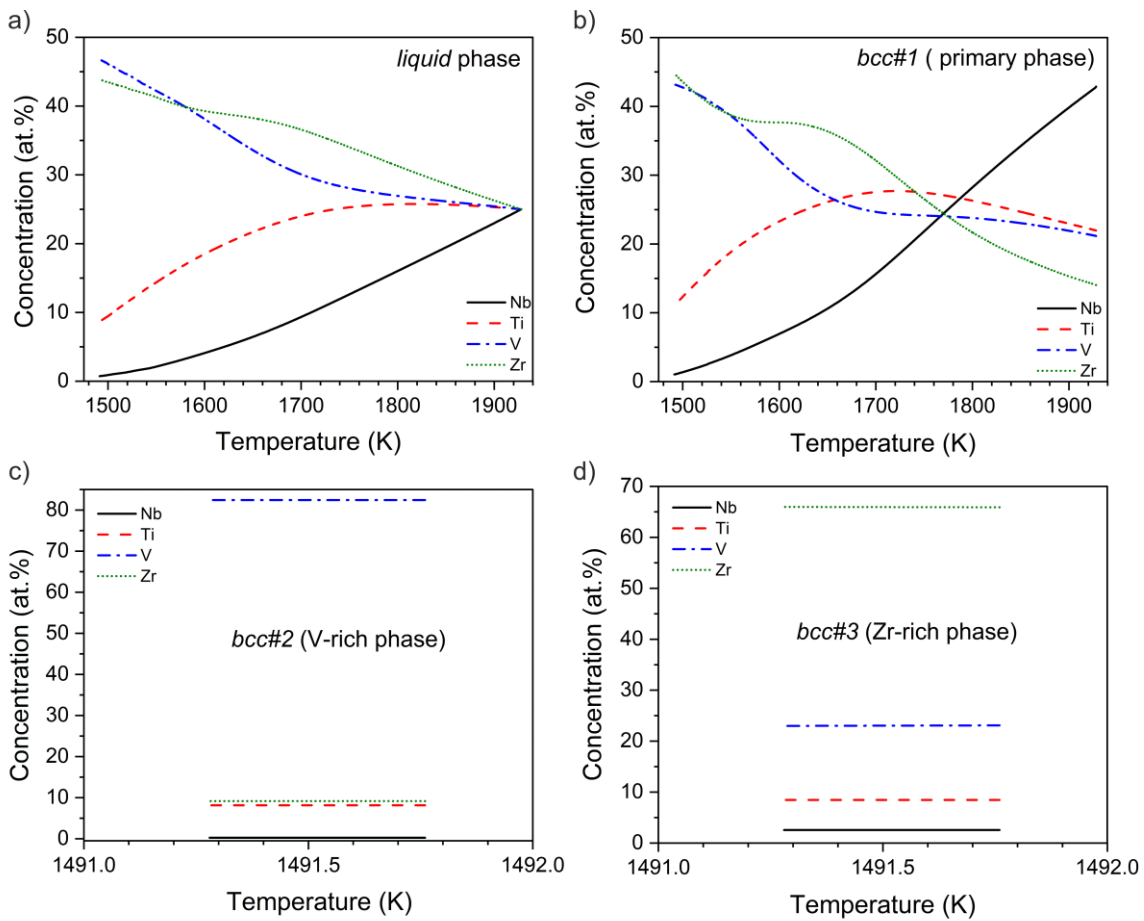


Fig. 5.10. Composition of the liquid and solid phases predicted by Scheil-Gulliver solidification simulation of NbTiVZr.

### 5.3.2 Crystal growth kinetics

The crystal growth kinetics  $v$  of the NbTiVZr RHEA is exceptionally sluggish, see Table 5.2, when compared to the *fcc*-structured medium- and HEAs measured by the same technique by Andreoli et al. [130]. The  $v$  of *fcc* phase, at  $\Delta T = 100$  K, for CrFeNi, CoCrNi, and CoCrFeNi equiatomic alloys were in the range of 5-10 m/s, while for the *bcc* phase in NbTiVZr it is estimated to be in the range of 0.015 – 0.017 m/s, which is two orders of magnitude slower. For the NbTiVZr RHEA  $\Delta T = 100$  K represents an undercooling of 0.05  $T_l$ . The  $v$  is sluggish in this undercooling level because it should mostly be diffusion-controlled as evidenced by the microstructure (see Figs. 5.5a and 5.5b). Wang *et al.* [207], who also used high-speed imaging during electrostatic levitation, reported that the  $v$  of the *bcc* phase for the NbMoTaWZr RHEA was 0.23 and 0.98 m/s for  $\Delta T = 82$  and 355 K,

respectively, but that  $v$  reached a maximum of 13.5 m/s at  $\Delta T = 640$  K. In this study such high undercooling levels were not achieved, however, at comparable  $\Delta T$  (82 in Ref. [207], 77 K in this study) the  $v$  of the NbTiVZr alloy is one order of magnitude slower than the NbMoTaWZr RHEA.

Table 5.2. Crystal growth velocity  $v$  as a function of melt undercooling upon crystallization of the NbTiVZr RHEA.

Undercooling $\Delta T$ (K)	Crystal growth velocity $v$ (m/s)
77	$\sim 0.009$
101	$\sim 0.015$
107	$\sim 0.017$
112	$\sim 0.019$
145	$\sim 0.037$

### 5.3.3 Structural and microstructural features

At very low undercooling, which must be the case when the melt was slowly cooled from the semisolid state (Fig. 5.2), constitutional undercooling is dominant. At this level of undercooling the dendrite tip is capable of coarsening which can lead to coarser microstructures. This is observed when comparing the dendritic structures shown in Figs. 5.5a and 5.5c. Crystal growth velocity should be very limited which also contributes to coarsening of the microstructure. Unfortunately, the visualization of the solidification when samples are processed in this manner cannot be done because of the extremely weak contrast between the liquid and the crystalline phase, due to a small release of latent heat. Under these conditions solute rejection occurring at the solid/liquid interface has had sufficient time to result in partitioning which is evident from the interdendritic regions in Figs. 5.5c and 5.5d. Contrarily, the microstructure of the sample solidified under an undercooling of 80 K revealed a much finer dendritic structure and less severe microsegregation (Figs. 5.5a and 5.5b). At moderate undercooling (e.g., 80 K) the decrease of dendrite tip and faster crystal growth kinetics may lead to smaller dendrites (Fig. 5.5a).

The X-ray diffraction pattern shown in Fig. 5.3b and the TEM analysis (Fig. 5.7) confirmed the presence of three distinct *bcc* solid solution phases when the sample was slowly cooled from the semisolid state. The appearance of three different *bcc* phases in the NbTiVZr RHEA was reported after compression deformation at 1273 K by Senkov *et al.* [201]. Before testing, the samples were cast, hot isostatically pressed at 1473 K and 207 MPa

for 2 h, and then annealed at 1473 K for 24 h and revealed a SPSS *bcc* structure. The lattice constant of the *bcc*#1 was 0.332 nm before testing, and after compression, it was 0.332, 0.345, and 0.324 nm for the three *bcc* phases, respectively. Three distinct *bcc* phases were also reported for the NbTiVZr alloy in Ref. [200] after compression tests at 1273 K. The lattice constants determined in the present work are, respectively, 0.330, 0.312, and 0.344 nm, for *bcc*#1, *bcc*#2, and *bcc*#3 as determined from the room temperature synchrotron XRD patterns plotted in Figs. 5.3a, 5.3b, and 5.3c.

The ternary phase diagrams of Ti-V-Zr and Nb-V-Zr ternary systems show a miscibility gap extending over a wide compositional range due to the separation of the primary *bcc* phase into two composition sets, one being rich and one being poor in Zr [208]. It is reasonable to assume that these miscibility gaps are responsible for the decomposition occurring in the quaternary system. Senkov *et al.* [200] had suggested the appearance of the three *bcc* phases at temperatures below 1673 K. The present experimental work provides evidence for the formation of three *bcc* phases in the NbTiVZr RHEA under non-equilibrium solidification conditions.

## Chapter 6: Solid-state thermophysical properties of CrFeNi, CoCrNi, and CoCrFeNi medium- and high-entropy alloys

The goal of this study was to investigate, using conventional laboratory techniques, such as dilatometry and DSC, the solid-state thermophysical properties of the CoCrFeNi HEA, and two medium-entropy alloys (MEAs) which are suballoys to the latter: CrFeNi and CoCrNi.

### 6.1 Introduction

Understanding the solid-state thermophysical properties of metals and alloys is crucial for applications. Detailed knowledge of thermophysical behavior is imperative to design efficient systems and predict thermal stresses that may reduce a component's service life [209].

There has been extensive work on the thermophysical properties of Ni-Cr binary and ternary alloys over the last 70 years. For example, in 1951 German scientist Hans Thomas observed abnormal changes to the electrical resistivity, following heat treatments at low temperatures, for a series of electrical-resistance alloys, including Ni-Cr, with no apparent phase transformations nor magnetic transitions [210]. In his publication, the phenomenon was described as the "*Komplex Zustand*", which translates to English as the 'complex state', and it is known today as the K-state transition. Later, it has been demonstrated that this intriguing event not only affects the electrical resistivity but also other thermophysical properties such as thermal expansion [211], heat capacity [212], thermal conductivity [209], and mechanical properties [213] of some alloys containing at least one transition metal as the solvent element.

Different reasons have been proposed for the occurrence of the K-state transition such as; (1) formation of Guinier-Preston zones [214]; (2) atomic long-range order (LRO) [213,215], which was reported for long-time annealing of alloys near the stoichiometric composition of intermetallic phases; (3) chemical short-range order (CSRO) [216,217]; and (4) changes in electronic configuration due to local lattice distortions [218]. Up to this date, the physical reasons for the occurrence of the K-state transition are still not completely understood.

According to Marucco and Nath [213], ordering, be it short-range or long-range, will have the following effects on crystal structure: (i) lattice parameter contraction which leads to dimensional instability; (ii) thermal and electrical characteristics variations; and (iii)

changes in mechanical properties due to pile-ups of dislocation dipoles. An order-disorder transformation should be evident in the thermal expansion coefficient due to a lattice constant change, and in the heat capacity measurements as the result of the change in enthalpy during the transformation [209].

## 6.2 Results

The methods used to measure the thermophysical properties of the medium- and high-entropy alloys studied here were described in Chapter 2. The relative expansion dependence curves to temperature of CrFeNi, CoCrFeNi, and CoCrFeNi alloys are shown in Fig. 6.1. The coefficient of linear thermal expansion  $\alpha$  of the three alloys, obtained by dilatometry, is shown as a function of temperature in Fig. 6.2a. The  $\alpha$  represents the first derivative of the relative expansion curves shown in Fig. 6.1. At the low-temperature range (below 800 K) CoCrNi shows a slightly lower  $\alpha$  than CrFeNi and CoCrFeNi compositions. In the high-temperature limit (above 900 K) all three alloys seem to have remarkably similar  $\alpha$ . The values of  $\alpha$  extracted from the dilatometry curves are, respectively, 22.27, 22.77, and 22.04 ( $10^{-6} \text{ K}^{-1}$ ) for CrFeNi, CoCrNi, and CoCrFeNi at 1260 K, the highest experimental temperature.

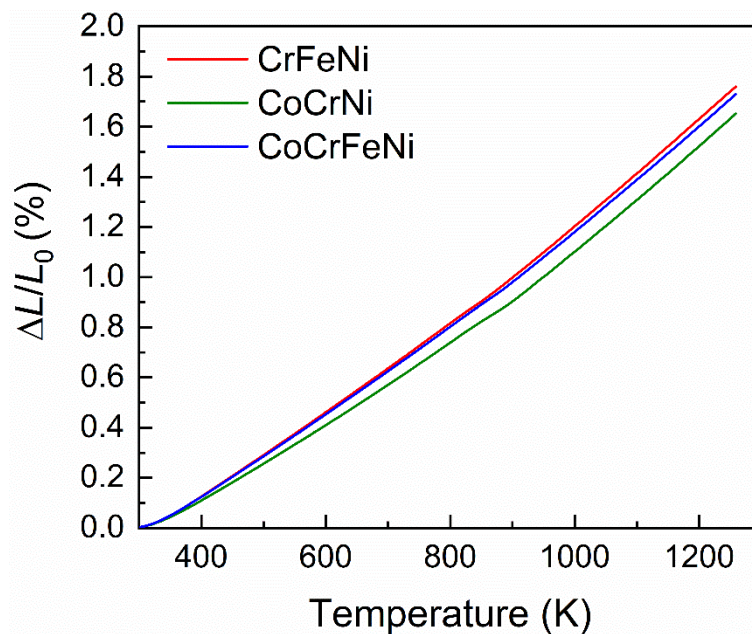


Figure 6.1. Relative elongation ( $\Delta L/L_0$ ) measured during heating ( $10 \text{ K} \cdot \text{min}^{-1}$ ) in the dilatometer.

A discontinuity on the temperature-dependent  $\alpha$  is seen for all three alloys in the temperature range of 750 – 950 K (Fig. 6.2a). Figure 6.2b shows the  $\alpha$  of the CoCrFeNi alloy measured during the first and second heating. As can be observed, in the first heating a



minimum occurs at  $\sim 860$  K followed by an increment in the thermal expansion coefficient with increasing temperature. In the second heating cycle, however, there is no minimum on the  $\alpha(T)$  curve. Instead, a sudden increase in  $\alpha$  occurs at the same temperature range where the minimum in the first heating exists.

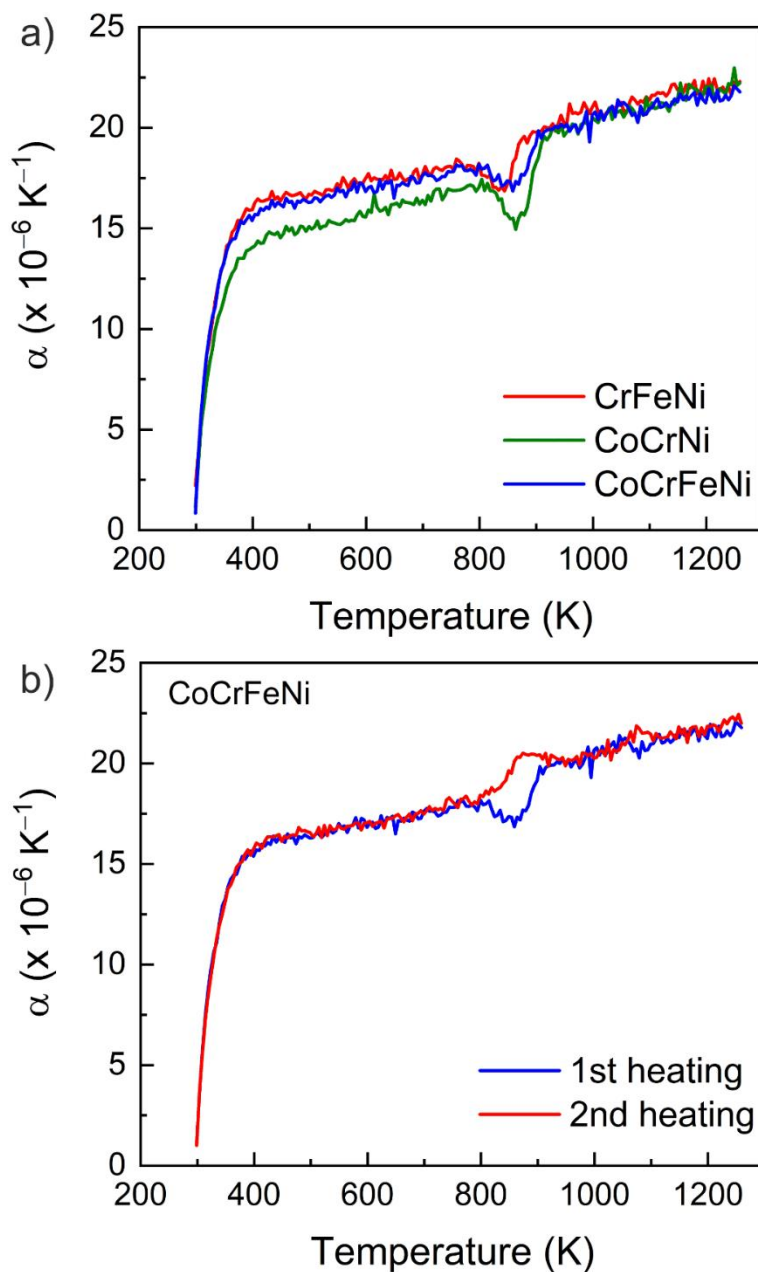


Figure 6.2. (a) The thermal expansion coefficient  $\alpha$  of CrFeNi, CoCrNi, and CoCrFeNi alloys measured during heating ( $10 \text{ K} \cdot \text{min}^{-1}$ ); (b)  $\alpha$  of the CoCrFeNi alloy measured during the first and second heating.

In Fig. 6.3 the temperature-dependent magnetic moment of the three alloys is presented. No magnetic transition is observed in the temperature range of 293 to 1073 K. The Curie temperatures  $T_c$ , obtained from the temperature-dependent magnetic moment curves are, respectively, 23 and 134 K, for CrFeNi and CoCrFeNi. It was not possible to determine the  $T_c$  of the CoCrNi alloy since it is below the low limit of 10 K in the experimental setup. Literature reports the value of 7 K [219].

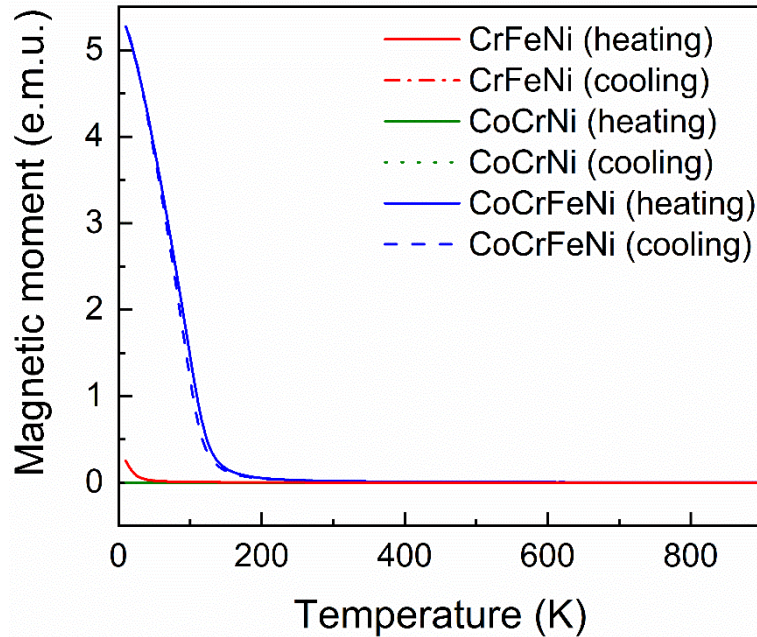


Figure 6.3. The temperature-dependent magnetic moment during heating-cooling cycles ( $5 \text{ K} \cdot \text{min}^{-1}$ ) of CrFeNi, CoCrNi, and CoCrFeNi equiatomic alloys.

The heat capacity  $C_p$  of CrFeNi, CoCrNi, and CoCrFeNi alloys as a function of temperature (400-1000 K) is shown in Figure 6.4. Again, in the first heating, all three alloys show minima in the  $C_p(T)$  curves, in the temperature range of 730 – 950 K, followed by a steep increase in the heat capacity upon further heating. The heating-cooling cycles were repeated twice to eliminate the effect of exothermal reactions due to non-equilibrium cooling during casting. One may note that during the second heating all alloys show a steep increase in  $C_p$  in the same temperature range as the first heating, however, no minima occur.

In Fig. 6.5 the XRD profiles of the as-cast and annealed (973 K for 24 hours) samples of CrFeNi, CoCrNi, and CoCrFeNi alloys are displayed. It is observed that in both conditions only Bragg peaks corresponding to a *fcc* structure are distinguishable, for all alloys. The

changes of peak intensity ratio, particularly large for the CoCrNi alloy, indicate texture changes upon annealing.

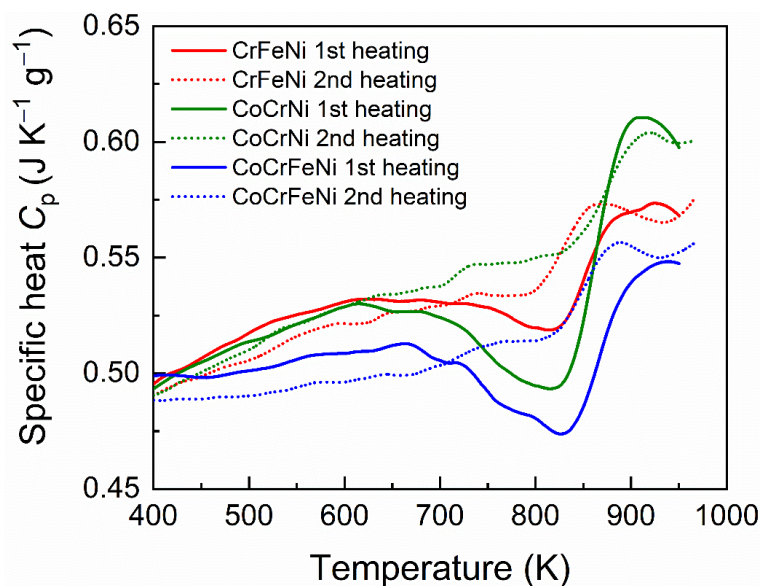


Figure 6.4. The heat capacity  $C_p$  of CrFeNi, CoCrNi, and CoCrFeNi alloys measured during the first and second heating cycles. The heating rate was  $10 \text{ K} \cdot \text{min}^{-1}$ .

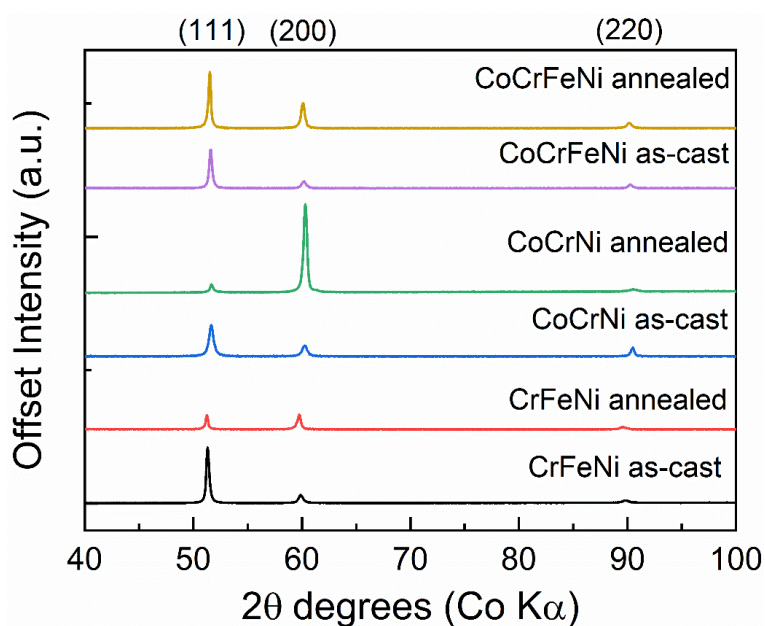


Figure 6.5. X-ray diffraction patterns of CrFeNi, CoCrNi, and CoCrFeNi alloys in the as-cast and annealed states.

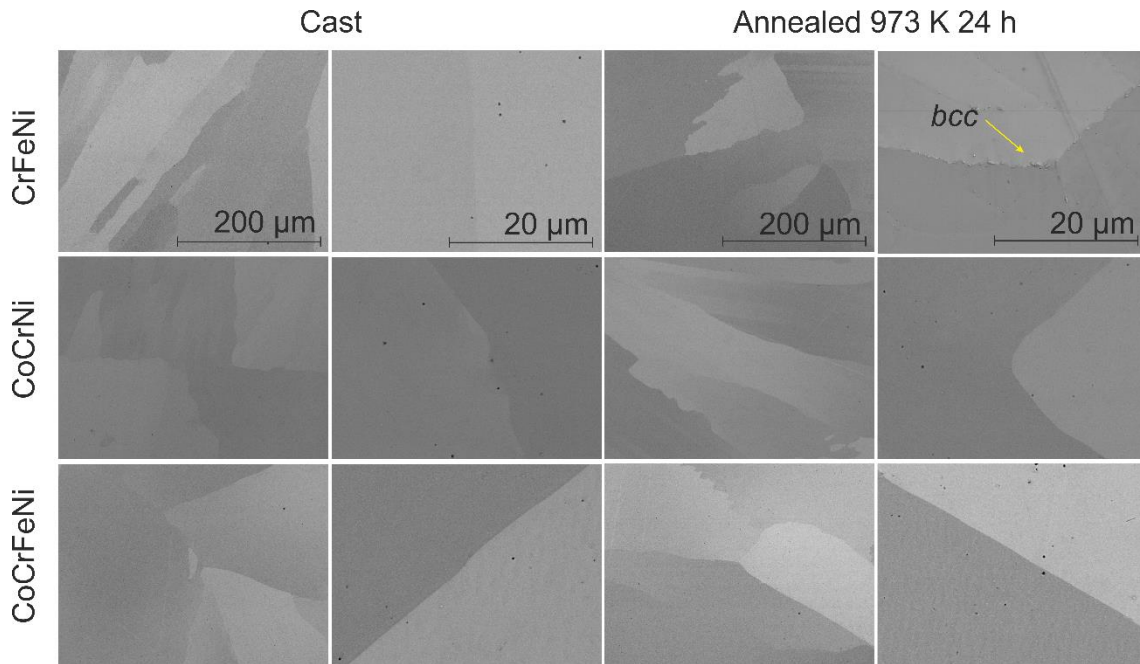


Figure 6.6. The microstructures of CrFeNi, CoCrNi, and CoCrFeNi alloys for two different magnifications; in the as-cast state (two first columns) and the annealed state (two last columns).

To investigate a possible influence of annealing on the microstructural/phase transformations resulting from annealing of the alloys during the thermophysical measurements, samples of the alloys were thermally treated for 24 hours at 973 K as described in section 2.9. The microstructures of CrFeNi, CoCrNi, and CoCrFeNi alloys are shown in Fig. 6.6 for the two different states; as-cast and annealed. The CoCrNi and CoCrFeNi microstructures reveal a SPSS in both conditions. In contrast to the XRD profile shown in Fig. 6.5, the SEM analysis of CrFeNi alloy reveals precipitates of a minor second phase at the grain boundaries (last column, first row) after the annealing treatment. As mentioned in section 3.1, Laplanche *et al.* [144] had noticed the formation of precipitates at the grain boundaries of the CrFeNi alloy after thermomechanical processing and annealing. Based on XRD and EBSD data they determined that the precipitates had the *bcc* structure. Precipitation of a *bcc* phase is predicted by CALPHAD calculations below 1273 K for the CrFeNi alloy [93].

## 6.3 Discussion

### 6.3.1 Thermophysical properties

The  $\alpha$  of CrFeNi, CoCrNi, and CoCrFeNi alloys (Fig. 6.2a) show an exponential temperature dependence in the temperature range of 293 to 1203 K. This is a similar trend

to that reported for austenitic steels by van Bohemen [220]. The thermal expansion coefficient of CrFeNi, CoCrNi, and CoCrFeNi alloys has been measured previously. For example, Laplanche *et al.* [144] determined the  $\alpha(T)$  for all three alloys investigated in this study, while in another study Laplanche *et al.* [221] determined the  $\alpha(T)$  for a single-crystal CoCrNi alloy. However, in both cases, their measurements were limited to 700 K. A comparison between  $\alpha$  at 700 K, obtained in this work and Refs. [144,221], is shown in Table 6.1. One may note that for the polycrystalline CoCrNi and CoCrFeNi alloys reported in Ref. [144] there is a very good agreement to the values described here. For the CrFeNi alloy, however, there is a slight disagreement, and the reasons are unknown at this moment.

Table 6.1. Comparison of the thermal expansion coefficient  $\alpha$  between this study and those reported in the literature.

Alloy	$\alpha$ at 700 K ( $10^{-6}$ K $^{-1}$ )		
	Ref. [221]	Ref. [144]	This work
CrFeNi	--	16.6	17.8
CoCrNi	--	16.4	16.5
CoCrNi (sc)	16.0	--	--
CoCrFeNi	--	17.3	17.4

sc = single-crystal

Anomalies in the thermal expansion coefficients are seen for the three alloys between 750 and 950 K (Fig. 6.2a). Chou *et al.* [54] had observed the same anomaly for a homogenized CoCrFeNi alloy, during dilatometry measurements, in the temperature range of 293 to 1073 K also at a heating rate of 10 K  $\cdot$  min $^{-1}$ . They attributed this to an Invar-type thermal expansion anomaly that occurs at the Curie temperature. However, from Fig. 6.3 one can see that in the temperature range of 300 – 1000 K no magnetic transition is observed for this alloy. Therefore, a transition from a paramagnetic to a ferromagnetic state is excluded as the possible cause for the anomalies in the  $\alpha(T)$  curves.

Lattice vibrations play a major contributing role in the thermal expansion of crystalline materials. It is usually very responsive to composition, planar atomic density, electron configuration, magnetic state, and interatomic interactions [222]. Recrystallization has previously been reported to cause a similar anomaly in  $\alpha(T)$  of low-carbon steels [222] at the same temperature range as those observed in Fig. 6.2. However, the alloys were previously hot rolled and further cold-rolled, thus, a driving force for recrystallization was

present. This is not the case in this study where the samples were in the as-cast state. The only effect that should be expected is normal grain growth. However, grain growth does not necessarily cause anomalies in  $\alpha(T)$  since it would, in general, be observed for other alloys. Regarding the valley which is seen in the first heating cycle (Fig. 6.2b), a possible explanation for its occurrence is the annihilation of vacancies and defects from non-equilibrium solidification (as-cast samples), as it was never observed on the second heating. The fact that an increment in  $\alpha$  is still seen on the second heating cycle indicates that the transitions are reversible.

As magnetic transitions, first-order phase transformations (for CoCrNi and CoCrFeNi alloys), and recrystallization and texture formation are discarded as the probable causes for the observed eccentric curves in  $\alpha(T)$ , the S-shaped anomalies may be caused by chemical atomic ordering involving the diffusion-controlled redistribution of atoms during heating of the sample. The anomalies observed in Fig. 6.2 are similar to those which have been reported previously for Ni-Cr alloys in Ref. [209] and were attributed to a chemical short-range order transition.

The same peculiar behavior is also observed in the  $C_p(T)$  curves (Fig. 6.4). As the samples were heated and cooled for two consecutive cycles it becomes evident that the phenomenon is reversible. Kim *et al.* [215] used thermal analysis to investigate order-disorder reactions in a Ni-Cr alloy (alloy 600) for a series of different mechanical- and heat-treated samples. They observed S-shaped curves, like those seen in Fig. 6.4, with exothermic and endothermic reactions in the temperature range of 330 to 873 K. The reaction temperatures were shown to be dependent on the thermomechanical treatment and that cold rolling could lower the reaction temperature. Based on the analysis of the activation energies they concluded about the existence of a substitutional diffusion process that leads to a short-range order-disorder transformation.

Jin *et al.* [223] also observed the same endothermic reactions in the  $C_p(T)$  curves, for a series of Cr-containing alloys going from binary to HEAs, at the same temperature ranges as those observed in this study. Neutron diffraction patterns at room- and high-temperature revealed no sign of superlattice peaks and the *fcc* SPSS structure was confirmed. Based on the observed evidence and literature reports they attributed the transitions in  $C_p(T)$  to the K-state effect caused by chemical short-range order/disorder reaction. In their study [223], they have also estimated the temperature dependence of  $\alpha$ , for the CoCrNi and CoCrFeNi alloys, based on the data of lattice expansion derived from neutron diffraction

patterns as a function of temperature (300 – 1273 K). The results agree with those in Fig. 6.2 in that the  $\alpha$  of CoCrNi, in the low-temperature range, is lower than CoCrFeNi and in the high-temperature range they are equivalent. Interestingly,  $\alpha$  increased monotonically and no minima or sharp slope increase were observed during the whole measurement.

The K-state effect on the  $C_p(T)$  of the CoCrNi equiatomic composition has been theoretically studied by Pei *et al.* [59] using the Wang–Landau Monte Carlo method and simulated annealing algorithms to understand the reasons for a peak around 900 K. There were discrepancies in the peak position temperatures of 80-180 K for the theoretical specific heat curve and the experimental one. The authors argued that when the vibrational and electronic entropies are ignored in the calculations the difference between the total entropies of the ordered and disordered phases is underestimated, which results in an overestimation of the transition temperature. By calculating the short-range order parameters, the atomic ordering transition was revealed. According to the authors, reordering of Cr–Ni, and Cr–Co pairs occurs, whilst Co–Ni nearest neighbors do not change strongly.

Already several studies have claimed to observe CSRO experimentally in MEAs and HEAs, including CoCrNi alloy. These studies will be addressed in the next section.

### 6.3.2 Short-range order in medium- and high-entropy alloys

The experimental determination of CSRO in metallic alloys is by no means a trivial task. X-ray diffraction evidence of CSRO is rather difficult to be determined, especially for alloys containing Cr, Fe, and Ni simultaneously, due to the similarity of the atomic scattering factors [224]. To overcome this difficulty, Cenedese *et al.* [225] employed thermal neutron diffuse scattering on three single-crystal specimens (heat-treated at 773 K for 10 hours) with identical chemical but a different isotopic composition of a  $\text{Fe}_{0.56}\text{Cr}_{0.21}\text{Ni}_{0.23}$  stainless steel alloy. This enabled them to distinguish a local CSRO between Ni and Cr atoms.

Zhang *et al.* [58] used X-ray and neutron total scattering and extended X-ray absorption fine structure (EXAFS) techniques to investigate the local atomic arrangements of the CoCrNi alloy, in single-crystals and single-phase polycrystalline samples. By analyzing the pair distribution functions, extracted from the neutron and X-ray experiments, they found that no obvious lattice distortion was present. Furthermore, by fitting the experimental EXAFS function, using a disordered *fcc* cluster with 55 atoms built based on the Warren-Cowley parameter calculation, they revealed that Cr is favorably bonded with Ni and Co and results in CSRO. As a result, CoCrNi alloy, despite does not show any long-range chemical order, cannot be considered a truly disordered system.

Applying energy-filtered TEM, Zhang *et al.* [61] compared the diffraction patterns and dark field images measured from the CoCrNi samples water-quenched from 1200 °C and samples further annealed at 1000 °C for 120 hours, and subsequently furnace cooled. The diffraction patterns of the annealed sample showed obvious streaks along with the [111] directions between *fcc* Bragg spots, and the dark field images from this region revealed nanoscale domains. Neither of these features were observed in the water-quenched sample. This was interpreted by the authors as structural CSRO.

Recently, Fantin *et al.* [226] used EXAFS, measured at the K-edges of the transition metals and Al, for a single-phase *fcc* (homogenized above the dual-phase temperature)  $\text{Al}_8\text{Co}_{17}\text{Cr}_{17}\text{Cu}_8\text{Fe}_{17}\text{Ni}_{33}$  (at. %) HEA. The SPSS state was confirmed by different methods at different length scales (ranging from optical microscopy to atom-probe tomography). They could determine that Cu has a preferential affinity to Al atoms ( $\sim 2.7$  Al atoms), followed by Ni ( $\sim 2.2$  Al atoms), Fe and Co ( $\sim 1.5$  Al atoms), and Cr ( $\sim 0.9$  Al atoms), while Al-Al first neighbors were virtually not detected. This indicates that some degree of CSRO occurs in this HEA. Furthermore, the local lattice distortion was quantified as  $\sim 0.03$  Å considering the 1<sup>st</sup> atomic shells of each element which is much inferior to that predicted if the atomic radii are considered.

CSRO seems to be more common in medium- and high-entropy alloys than originally assumed based on the entropic effect. Experimental proof that a short-range order-disorder transition occurs in CrFeNi, CoCrNi, and CoCrFeNi alloys requires further complex experiments which are beyond the scope of this study. Some ideas about possible experimental setups that may reveal the nature of the anomalies observed in  $\alpha(T)$  and  $C_p(T)$  will be addressed in Chapter 8: Outlook.



## Chapter 7: Summary

### 7.1 Empirical rule of phase formation of complex concentrated alloys

The analysis of an extensive database containing 235 complex concentrated alloys (Appendix 1) carried out in the present work reveals clear trends in predicting the phase stability and formation by simple empirical criteria which can be summarized as follows.

The elastic-strain-energy  $\Delta H_{el}$  parameter shows three distinct regions for complex concentrated alloys: (i) the single-phase solid-solution alloys with *fcc* crystal structure precipitate predominantly in the range of  $\Delta H_{el} \leq 6.05 \text{ kJ mol}^{-1}$ ; (ii) The range of  $6.05 < \Delta H_{el} \leq 22 \text{ kJ mol}^{-1}$  contains most of the *bcc* SPSS alloys, and other types of complex concentrated alloys (e.g. ss + IMs, IMs, or duplex alloys); and the region (iii) for  $\Delta H_{el} > 22 \text{ kJ mol}^{-1}$ , where all bulk metallic glasses and  $\sim 56\%$  of the single-phase intermetallics can be found.

The  $\Delta H_{el}$  vs. *VEC* criterion (Fig. 1.3) is a straightforward guideline that can be used to predict single-phase solid-solution formation in complex concentrated alloys. The criterion shows an improved ability to predict single-phase solid-solution alloys from intermetallic-forming alloys, especially for the alloys that precipitate the  $\mu$  phase, when it is compared with the different approaches already used in literature.

The vanadium-containing complex concentrated alloys forming the  $\sigma$  phase are by far the most common IM phase to overlap within the SPSS-predicted regions in the literature. The alloys that are prone to form the  $\sigma$  phase and contain V are difficult to predict by using the empirical methods because of their near-zero enthalpy of mixing, low atomic-size mismatch, and low elastic-strain energy. Further investigation should be carried out to establish reliable models.

The simplified  $\Delta H_{el}$  parameter improves the quality to predict single-phase solid-solution microstructures compared to the well-established  $\delta$  parameter. The  $\Delta H_{el}$  parameter, together with those previously reported in the literature, can be used in the design of new complex concentrated alloys.

### 7.2 Non-equilibrium solidification of medium- and high-entropy alloys

Electromagnetic levitation was used to containerlessly process and undercool samples of the equiatomic CoCrFeNi, CrFeNi, and CoCrNi alloys. The non-equilibrium solidification was monitored *in situ* using pyrometry, high-speed video, and high-energy synchrotron X-ray diffraction. All three compositions showed a double recalescence with

the primary formation of a transient metastable *bcc* phase if the liquid was sufficiently undercooled.

The *in situ* XRD and high-speed video recording showed that all three compositions form a *fcc* single-phase solid solution directly from the melt at a low undercooling. However, at a sufficiently large undercooling, crystallization occurred with the primary formation of a transient metastable *bcc* phase, as revealed by the high-speed videos. In this case, the nucleation of the *fcc* phase always happened within growing *bcc* dendrites, confirming this to be the preferential nucleation site for the *fcc* phase. The delay time, a time interval between the nucleation of the *bcc* and *fcc* phases showed an inverse relation to the melt undercooling, explained by the accumulation of defects in the growing *bcc* dendrites as the undercooling was increased.

The growth velocities of the *fcc* and *bcc* phases in CoCrFeNi, CrFeNi, and CoCrNi alloys agreed well with those reported for Fe-Ni alloys and Fe-(rich)-Cr-Ni alloys. The growth kinetics do not change with the increasing number of elements in these systems and are not sluggish.

The microstructural evolution for the three alloys is as follows: at low undercooling, fully developed dendrites of no specific texture were formed; as the undercooling was increased to 100-150 K, columnar grains developed sub-grain structures; beyond a critical undercooling,  $\Delta T \sim 160$  K for CoCrFeNi, the microstructure evolved to considerably refined, randomly oriented equiaxed grains, with multiple T3  $\langle 111 \rangle$  twins.

The *in situ* non-equilibrium solidification study of the Al<sub>0.3</sub>CoCrFeNi HEA could reveal significant differences compared to the equiatomic CoCrFeNi, CrFeNi, and CoCrNi alloys. The first major difference observed was that the ability of the liquid to be undercooled is diminished. This fact may be linked to the formation of stable oxides on the surface of the alloy which acts as heterogeneous nucleation sites.

The crystal growth kinetics, evaluated in the low undercooling range, shows that growth velocity  $v(\Delta T)$  for the five-component alloy is lower at comparable undercooling. Nonetheless, they were in the same order of magnitude.

Spontaneous grain refinement with the formation of equiaxed grains was observed at low undercooling ( $\Delta T = 70$  K) for the Al<sub>0.3</sub>CoCrFeNi HEA, while for the MEAs and the CoCrFeNi HEA grain refined microstructures were only observed under a deep undercooling regime. The equiaxed grains do not form twins which can be interpreted as that no recrystallization occurred following recalescence. The natural grain refinement occurring at low undercooling is associated with the dendritic break-up and remelting of dendrites as the

system attempts to minimize the solid/liquid interface area via heat and solute diffusion in the bulk phases.

The initial state and solidification kinetics play a central role in the high-temperature phase formation of the NbTiVZr RHEA. While a *bcc* single-phase microstructure was formed when the liquid was undercooled over 80 K, solidification from the semisolid state between  $T_l$  and  $T_s$  lead to the development of a multi-phase microstructure. In the first case, as the driving force for crystallization is proportional to the liquid undercooling, a non-equilibrium solidification is established with (relatively) higher crystal growth rates which were evident from the fine solidified microstructure. In the latter case, with negligible undercooling, a coarse dendritic microstructure was formed with intense microsegregation of vanadium and zirconium into the interdendritic regions and appearance of two additional *bcc* phases at the grain boundaries. The solute microsegregation and formation of the *bcc*#2 and *bcc*#3 phases could be explained by Scheil-Gulliver solidification that was simulated by the CALPHAD approach using the TCHEA4 database. The discrepancy on the onset temperature for the formation of the *bcc*#3 phase between CALPHAD prediction and experiment can be explained either by deviation of the real and simulated solidification paths, or somewhat imperfect modelling of the TCHEA4 database or experimental uncertainty. The growth velocity of the primary *bcc* phase in the NbTiVZr alloy is found to be about one order of magnitude smaller than that of the NbMoTaWZr alloy at a similar undercooling reported in the literature.

### 7.3 Thermophysical properties of the medium- and high-entropy alloys

The temperature-dependent thermal expansion coefficient  $\alpha$  and constant pressure heat capacity  $C_p$  were measured using dilatometry and differential scanning calorimetry for the CrFeNi, CoCrNi, and CoCrFeNi alloys. All alloys showed an anomalous behavior, in both  $\alpha$  and  $C_p$ , in the temperature range of 730 – 950 K. Temperature-dependent magnetic moment measurements showed that a magnetic transition is not responsible for the observed phenomenon, as the Curie temperature of these alloys is below room temperature.

While CoCrNi and CoCrFeNi are single-phase solid solutions in both as-cast state and after annealing at 973 K for 24 hours, eliminating first-order phase transformations as a possible cause, the CrFeNi showed micron-scale *bcc* precipitates at the grain boundaries. Recrystallization and texture can also be disregarded as the reasons for the S-shaped curves since no driven force for recrystallization is present. Based on literature reports of Ni-Cr,

stainless-steels, and HEAs, it is believed that the abrupt changes in the slope of  $\alpha$  and  $C_p$  may be caused by a diffusional local chemical ordering during *in situ* measurements. Nonetheless, the exact nature and the driving force for the transitions require further theoretical and experimental investigations.

## Chapter 8: Outlook

The non-equilibrium solidification studies of medium- and high-entropy alloys in the present work opened several new questions. Concerning the results obtained in Chapter 3, the formation of a transient primary *bcc* phase in CoCrFeNi and ternary suballoys at the initial stages of crystallization leads to two main questions: (1) what is the chemical composition of the primary phase? Does it have the same composition as the liquid, being the only difference to the stable phase (*fcc*) the crystallographic arrangement of its constituents? Or it nucleates as a completely different composition with the rejection of solute to the liquid? (2) Is it possible to ‘freeze-in’ the metastable phase, thus, making it possible to study its characteristics?

Being able to conserve the primary *bcc* in the solidified microstructures would provide the answers to questions 1 and 2. An alternative is to use different containerless solidification methods to achieve this goal. One option is to perform studies using the drop tube technique. Another option is to perform studies in an electrostatic levitation (ESL) device. As discussed in Chapter 3, because in ESL the samples are free from magnetic stirring the delay time  $\tau$  between the nucleation of the metastable and the stable phases, in some studies, has been shown to increase by 5-fold. Furthermore, it would be thought-provoking to compare crystal growth velocities and microstructure formation under ESL conditions to the results described in this work.

It would also be interesting to vary the amount of each element in these compositions and investigate the influence in phase selection, delay time, crystal growth kinetics, and the resulting microstructures using EML. This would allow for a deeper understanding of the influence of specific elements in the non-equilibrium solidification behavior in these systems. Not only that, but also it would be of scientific importance to describe these features for different classes of medium- and high-entropy alloys. Since the compositional space of HEAs is so vast, it is imperative to select alloys that have a clear potential for industrial applications.

Regarding the study on the thermophysical properties of CoCrFeNi, CrFeNi, and CoCrNi alloys the major question that arose is to understand the nature of the anomalies revealed in the dilatometry, and specific heat capacity curves. It was initially planned for January 2021 to conduct Extended X-Ray Absorption Fine Structure (EXAFS) experiments in the European Synchrotron Radiation Facility (Grenoble) in collaboration with Dr. Andrea

Fantin (TU Berlin/ Helmholtz-Zentrum Berlin). Unfortunately, due to the restrictions imposed by the COVID-19 pandemic, the beamtime was rescheduled for late May 2021. It is expected that EXAFS analysis may shed light on the nearest atomic neighbors of the CoCrFeNi alloy in two different conditions: (i) homogenized at 1473 K for 24 hours and, (ii) annealed for 24 hours at 973 K (just above the peak temperature of the anomaly). It is known that the absorption edges of Co, Cr, Fe, and Ni are relatively close which makes the determination rather difficult. So, at this moment it is just speculation, and only after the analysis of the results, it will be possible to conclude. Another possible experimental tool for understanding the different atomic-level structures of CoCrFeNi and its suballoys, in the homogenized and annealed states, would be neutron diffraction studies using isotopic substitution of elements.

## Appendix 1

Table A1. Compositions, crystal structures, phase constitutions, atomic-size mismatches  $\delta$ , enthalpies of mixing  $\Delta H_{mix}$ , valence electron concentrations  $VEC$ , and the elastic-strain energies  $\Delta H_{el}$  of 235 high-entropy alloys.  $VEC$ ,  $\delta$ ,  $\Delta H_{mix}$  is taken from Refs. [27, 34] and calculated  $\Delta H_{el}$ .

Composition	Structure	Phases	Ref.	$\delta$ %	$\Delta H_{mix}$ kJ mol <sup>-1</sup>	$VEC$	$\Delta H_{el}$ kJ mol <sup>-1</sup>
Al <sub>0.25</sub> CoCrCu <sub>0.75</sub> FeNi	<i>fcc</i>	<i>fcc</i> SPSS	[227]	3.1	-0.7	8.4	1.82
Al <sub>0.25</sub> CoCrCu <sub>0.75</sub> FeNiTi <sub>0.5</sub>	<i>fcc</i>	<i>fcc</i> SPSS	[228]	5.1	-7.3	8	6.89
Al <sub>0.25</sub> CoCrFeMoNi	<i>fcc</i> + <i>fcc</i>	2ss	[36]	3.7	-7.1	7.8	7.39
Al <sub>0.25</sub> CoCrFeNi	<i>fcc</i>	<i>fcc</i> SPSS	[54]	3.3	-6.8	7.9	1.91
Al <sub>0.25</sub> NbTaTiV	<i>bcc</i>	<i>bcc</i> SS	[229]	3.5	-4.8	4.6	7.34
Al <sub>0.2</sub> CrCuFe	<i>fcc</i> + <i>bcc</i>	2ss	[24]	2.9	7.7	8	2.36
Al <sub>0.2</sub> CrCuFeNi <sub>2</sub>	<i>fcc</i>	<i>fcc</i> SPSS	[24]	2.8	0.1	8.8	1.53
Al <sub>0.375</sub> CoCrFeNi	<i>fcc</i>	<i>fcc</i> SPSS	[54]	3.9	-8	7.8	2.76
Al <sub>0.3</sub> CoCrCuFeNi	<i>fcc</i>	<i>fcc</i> SPSS	[4]	3.2	0.2	8.5	2.05
Al <sub>0.3</sub> CoCrFeMo <sub>0.1</sub> Ni	<i>fcc</i>	<i>fcc</i> SPSS	[36]	3.8	-7.3	7.8	3.04
Al <sub>0.3</sub> CoCrFeNi	<i>fcc</i> + L1 <sub>2</sub>	ss + IM	[36]	3.6	-7.3	7.9	2.26
Al <sub>0.3</sub> CoCrFeNiTi <sub>0.1</sub>	<i>fcc</i>	<i>fcc</i> SPSS	[36]	4.1	-8.9	7.8	3.60
Al <sub>0.3</sub> CrCuFeMnNi	<i>fcc</i> + <i>bcc</i>	2ss	[230]	3.1	-0.3	8.1	4.35
Al <sub>0.3</sub> CrFe <sub>1.5</sub> MnNi <sub>0.5</sub>	<i>bcc</i> + <i>fcc</i> + B2	2ss + IM	[41]	3.3	-5.5	7.2	5.41
Al <sub>0.4</sub> CrCuFeNi <sub>2</sub>	<i>fcc</i>	<i>fcc</i> SPSS	[24]	3.6	-1.7	8.6	2.60
Al <sub>0.5</sub> CoCrCu <sub>0.5</sub> FeNi	<i>fcc</i>	<i>fcc</i> SPSS	[227]	4.1	-4.6	8	3.28
Al <sub>0.5</sub> CoCrCuFeNiTi	<i>fcc</i> + <i>bcc</i> + $\sigma$	2ss + IM	[231]	6.1	-11.6	7.6	10.97
Al <sub>0.5</sub> CoCrCuFeNiTi <sub>0.2</sub>	<i>fcc</i>	<i>fcc</i> SPSS	[231]	4.6	-4.1	8.1	4.96
Al <sub>0.5</sub> CoCrCuFeNiTi <sub>0.4</sub>	<i>fcc</i> + <i>bcc</i>	2ss	[231]	5.1	-6.4	8	6.68
Al <sub>0.5</sub> CoCrCuFeNiTi <sub>0.6</sub>	<i>fcc</i> + <i>bcc</i>	2ss	[231]	5.5	-8.4	7.9	8.25
Al <sub>0.5</sub> CoCrCuFeNiTi <sub>0.8</sub>	<i>fcc</i> + <i>bcc</i> + $\sigma$	2ss + IM	[231]	5.8	-10.1	7.7	9.67
Al <sub>0.5</sub> CoCrCuFeNiTi <sub>1.2</sub>	<i>fcc</i> + <i>bcc</i> + $\sigma$	2ss + IM	[231]	6.3	-12.9	7.5	12.15
Al <sub>0.5</sub> CoCrCuFeNiV	<i>fcc</i> + <i>bcc</i> + $\sigma$	2ss + IM	[38]	4	-5.3	7.8	3.57
Al <sub>0.5</sub> CoCrCuFeNiV <sub>0.2</sub>	<i>fcc</i>	<i>fcc</i> SPSS	[38]	3.9	-2.5	8.2	3.20
Al <sub>0.5</sub> CoCrCuFeNiV <sub>0.4</sub>	<i>fcc</i> + <i>bcc</i>	2ss	[38]	3.9	-3.3	8.1	3.32
Al <sub>0.5</sub> CoCrCuFeNiV <sub>0.6</sub>	<i>fcc</i> + <i>bcc</i> + $\sigma$	2ss + IM	[38]	3.9	-4.1	8	3.42
Al <sub>0.5</sub> CoCrCuFeNiV <sub>0.8</sub>	<i>fcc</i> + <i>bcc</i> + $\sigma$	2ss + IM	[38]	4	-4.7	7.9	3.50
Al <sub>0.5</sub> CoCrCuFeNiV <sub>1.2</sub>	<i>fcc</i> + <i>bcc</i>	2ss	[38]	4	-5.7	7.7	3.54
Al <sub>0.5</sub> CoCrCuFeNiV <sub>1.4</sub>	<i>fcc</i> + <i>bcc</i>	2ss	[38]	4	-6.1	7.6	3.66
Al <sub>0.5</sub> CoCrCuFeNiV <sub>1.6</sub>	<i>fcc</i> + <i>bcc</i>	2ss	[38]	4	-6.5	7.5	3.68
Al <sub>0.5</sub> CoCrCuFeNiV <sub>1.8</sub>	<i>fcc</i> + <i>bcc</i>	2ss	[38]	3.9	-6.8	7.5	3.72
Al <sub>0.5</sub> CoCrCuFeNiV <sub>2</sub>	<i>fcc</i> + <i>bcc</i>	2ss	[38]	3.9	-7.1	7.4	3.73
Al <sub>0.5</sub> CoCrFeNi	<i>fcc</i> + <i>bcc</i>	2ss	[54]	4.3	-9.1	7.7	3.54

Al <sub>0.5</sub> CoCrFeNiTi	fcc + bcc + L	2ss + IM	[109]	6.5	-19.6	7	13.02
Al <sub>0.5</sub> CrCuFeMnNi	fcc + bcc	2ss	[230]	3.8	-1.9	7.9	5.14
Al <sub>0.5</sub> CrFe <sub>1.5</sub> MnNi <sub>0.5</sub>	bcc + fcc + B2	2ss + IM	[41]	4	-7.3	7	6.36
Al <sub>0.5</sub> NbTaTiV	bcc	bcc SS	[229]	3.4	-8.4	4.6	6.99
Al <sub>0.6</sub> CrCuFeNi <sub>2</sub>	fcc	fcc SS	[24]	4.2	-3.3	8.4	3.53
Al <sub>0.75</sub> CoCrCu <sub>0.25</sub> FeNi	fcc + bcc	2ss	[227]	4.8	-8.5	7.6	4.73
Al <sub>0.75</sub> CoCrCu <sub>0.25</sub> FeNiTi <sub>0.5</sub>	bcc + bcc	2ss	[228]	5.9	-14.4	7.3	9.40
Al <sub>0.75</sub> CoCrFeNi	fcc + bcc	2ss	[54]	4.9	-10.9	7.4	4.95
Al <sub>0.875</sub> CoCrFeNi	fcc + bcc	ss + IM	[54]	5.1	-11.7	7.3	5.58
Al <sub>0.8</sub> CoCrCuFeNi	fcc + bcc	2ss	[4]	4.5	-3.6	8	4.41
Al <sub>0.8</sub> CrCu <sub>1.5</sub> FeMnNi	fcc + bcc	2ss	[230]	4.3	-1.7	7.9	4.91
Al <sub>0.8</sub> CrCuFe <sub>1.5</sub> MnNi	fcc + bcc	2ss	[230]	4.3	-3.3	7.7	5.91
Al <sub>0.8</sub> CrCuFeMn <sub>1.5</sub> Ni	fcc + bcc	2ss	[230]	4.3	-4.2	7.6	6.39
Al <sub>0.8</sub> CrCuFeMnNi	fcc + bcc	2ss	[230]	4.4	-4	7.7	6.19
Al <sub>0.8</sub> CrCuFeNi <sub>2</sub>	fcc	fcc SS	[24]	4.6	-4.6	8.2	4.45
Al <sub>1.25</sub> CoCrFeNi	bcc	bcc SS	[54]	5.6	-13.4	7	7.24
Al <sub>1.2</sub> CrCuFe	fcc + bcc	2ss	[24]	5.3	-0.5	6.8	8.20
Al <sub>1.2</sub> CrCuFeNi <sub>2</sub>	fcc + bcc	2ss	[24]	5.2	-6.8	7.8	6.00
Al <sub>1.3</sub> CoCrCuFeNi	fcc + bcc	2ss	[4]	5.2	-6.2	7.6	6.28
Al <sub>1.3</sub> CoCrFeNi	bcc + B2	ss + IM	[186]	5.7	-13.7	7	7.44
Al <sub>1.5</sub> CoCrCu <sub>0.5</sub> FeNi	fcc + bcc	2ss	[232]	5.6	-10.1	7.2	7.50
Al <sub>1.5</sub> CoCrCuFeNi	fcc + bcc	2ss	[4]	5.4	-7.1	7.5	6.92
Al <sub>1.5</sub> CoCrFeNi	bcc	bcc SS	[54]	5.8	-14.3	6.8	8.17
Al <sub>1.6</sub> CoCrCuFeNi	fcc + fcc + B2	2ss + IM	[231]	5.5	-7.8	7.4	7.22
Al <sub>1.75</sub> CoCrFeNi	bcc + B2	ss + IM	[186]	5.9	-14.9	6.6	8.99
Al <sub>1.8</sub> CoCrCuFeNi	fcc + bcc	2ss	[4]	5.6	-8.1	7.3	7.78
Al <sub>10</sub> Cu <sub>15</sub> Nb <sub>5</sub> Ni <sub>13</sub> Zr <sub>57</sub> <sup>a</sup>	amorphous	BMG	[233]	10	-33.9	5.8	50.56
Al <sub>10</sub> Cu <sub>15</sub> Ni <sub>10</sub> Zr <sub>65</sub> <sup>a</sup>	amorphous	BMG	[234]	9.7	-33.9	5.5	51.43
Al <sub>10</sub> Cu <sub>20</sub> Ni <sub>12</sub> Ti <sub>5</sub> Zr <sub>53</sub> <sup>a</sup>	amorphous	BMG	[234]	10.3	-34.1	6	49.87
Al <sub>10</sub> Cu <sub>20</sub> Ni <sub>8</sub> Ti <sub>5</sub> Zr <sub>57</sub> <sup>a</sup>	amorphous	BMG	[28]	9.8	-31.5	5.8	48.14
Al <sub>2.3</sub> CoCrCuFeNi	fcc + bcc + B2	2ss + IM	[4]	5.9	-9.4	7	8.99
Al <sub>2.5</sub> CoCrCuFeNi	fcc + bcc + B2	2ss + IM	[4]	6	-9.8	6.9	9.38
Al <sub>2.5</sub> CoCrFeNi	bcc	bcc ss	[235]	6.2	-16.1	6.2	10.90
Al <sub>2.8</sub> CoCrCuFeNi	bcc	bcc ss	[236]	6	-10.3	6.7	9.96
Al <sub>2</sub> CoCrCu <sub>0.5</sub> FeNi	fcc + bcc	2ss	[237]	5.9	-11.6	6.8	8.95
Al <sub>2</sub> CoCrFeNi	bcc	bcc ss	[54]	6.1	-15.4	6.5	9.71
Al <sub>3.25</sub> CoCrCuFeNi	fcc + bcc + B2	2ss + IM	[231]	6.1	-10.8	6.5	10.68
Al <sub>3</sub> CoCrFeNi	bcc	bcc ss	[235]	6.3	-16.4	6	11.81
Al <sub>7.5</sub> Cu <sub>17.5</sub> Ni <sub>10</sub> Zr <sub>65</sub> <sup>a</sup>	amorphous	BMG	[234]	10	-32.2	5.8	53.12
Al <sub>7</sub> Cu <sub>46</sub> Y <sub>5</sub> Zr <sub>42</sub> <sup>a</sup>	amorphous	BMG	[238]	12.5	-24.9	7.1	46.99



$\text{Al}_8\text{Cu}_{12}\text{Ni}_{14}\text{Zr}_{66}^a$	amorphous	BMG	[234]	9.9	-35.4	5.6	55.15
$\text{Al}_8\text{Cu}_7\text{Ni}_{19}\text{Zr}_{66}^a$	amorphous	BMG	[234]	10.1	-39.3	5.5	58.12
$\text{Al}_9\text{Cu}_{16}\text{Ni}_9\text{Zr}_{66}^a$	amorphous	BMG	[234]	9.7	-32.4	5.6	51.23
$\text{AlCo}_{0.5}\text{CrCu}_{0.5}\text{FeNi}$	<i>fcc + bcc</i>	2ss	[232]	5.2	-7.9	7.4	6.18
$\text{AlCo}_{0.5}\text{CrCuFeNi}$	<i>fcc + bcc</i>	2ss	[239]	5	-4.5	7.7	5.64
$\text{AlCo}_{0.5}\text{CrFeMo}_{0.5}$	<i>bcc + \sigma</i>	ss + IM	[240]	5.5	-9.7	6.1	10.45
$\text{AlCo}_{0.5}\text{CrFeMo}_{0.5}\text{Ni}$	<i>bcc + \sigma</i>	ss + IM	[240]	5.6	-11.7	6.9	8.92
$\text{AlCo}_{1.5}\text{CrCu}_{0.5}\text{FeNi}$	<i>fcc + bcc</i>	2ss	[232]	5	-7.8	7.7	5.20
$\text{AlCo}_{1.5}\text{CrFeMo}_{0.5}$	<i>bcc + \sigma</i>	ss + IM	[240]	5.5	-10.4	6.7	8.79
$\text{AlCo}_{1.5}\text{CrFeMo}_{0.5}\text{Ni}$	<i>bcc + \sigma</i>	ss + IM	[240]	5.4	-11.1	7.3	7.63
$\text{AlCo}_{1.5}\text{CrFeNiTi}_{0.5}$	<i>fcc + bcc</i>	2ss	[241]	6	-17.2	7.1	9.80
$\text{AlCo}_2\text{CrCu}_{0.5}\text{FeNi}$	<i>fcc + bcc</i>	2ss	[232]	4.8	-7.7	7.8	4.81
$\text{AlCo}_2\text{CrFeMo}_{0.5}$	<i>fcc + bcc + \sigma</i>	2ss + IM	[240]	5.4	-10.4	6.9	8.12
$\text{AlCo}_2\text{CrFeMo}_{0.5}\text{Ni}$	<i>fcc + bcc + \sigma</i>	2ss + IM	[240]	5.3	-10.7	7.4	7.10
$\text{AlCo}_2\text{CrFeNiTi}_{0.5}$	<i>fcc + bcc</i>	2ss	[241]	5.9	-16.4	7.2	9.09
$\text{AlCo}_{3.5}\text{CrCu}_{0.5}\text{FeNi}$	<i>fcc + bcc</i>	2ss	[232]	4.5	-7	8	4.50
$\text{AlCo}_3\text{CrCu}_{0.5}\text{FeNi}$	<i>fcc + bcc</i>	2ss	[232]	4.6	-7.3	7.9	4.19
$\text{AlCo}_3\text{CrFeNiTi}_{0.5}$	<i>fcc + bcc</i>	2ss	[241]	5.7	-15	7.5	7.94
$\text{AlCoCr}_{0.5}\text{Cu}_{0.5}\text{FeNi}$	<i>fcc + bcc</i>	2ss	[232]	5.3	-8.3	7.7	6.17
$\text{AlCoCr}_{0.5}\text{CuFeNi}$	<i>fcc + bcc</i>	2ss	[239]	5.1	-5	8	5.64
$\text{AlCoCr}_{0.5}\text{FeMo}_{0.5}\text{Ni}$	<i>bcc + \sigma</i>	ss + IM	[242]	5.7	-12.1	7.2	8.91
$\text{AlCoCr}_{1.5}\text{Cu}_{0.5}\text{FeNi}$	<i>fcc + bcc</i>	2ss	[232]	4.9	-7.6	7.4	5.21
$\text{AlCoCr}_{1.5}\text{FeMo}_{0.5}\text{Ni}$	<i>bcc + \sigma</i>	ss + IM	[242]	5.3	-10.8	7	7.63
$\text{AlCoCr}_2\text{Cu}_{0.5}\text{FeNi}$	<i>fcc + bcc</i>	2ss	[232]	4.7	-7.2	7.3	4.82
$\text{AlCoCr}_2\text{FeMo}_{0.5}\text{Ni}$	<i>bcc + \sigma</i>	ss + IM	[242]	5.1	-10.3	6.9	7.12
$\text{AlCoCrCu}_{0.25}\text{FeNi}$	<i>bcc</i>	bcc ss	[22]	5.2	-9.9	7.4	5.90
$\text{AlCoCrCu}_{0.25}\text{FeNiTi}_{0.5}$	<i>bcc + bcc</i>	2ss	[243]	6	-15.5	7.1	10.15
$\text{AlCoCrCu}_{0.5}\text{Fe}$	<i>fcc + bcc</i>	2ss	[232]	5.2	-6.1	7	6.74
$\text{AlCoCrCu}_{0.5}\text{Fe}_{0.5}\text{Ni}$	<i>fcc + bcc</i>	2ss	[232]	5.3	-8.9	7.5	6.09
$\text{AlCoCrCu}_{0.5}\text{Fe}_{1.5}\text{Ni}$	<i>fcc + bcc</i>	2ss	[232]	4.9	-7.1	7.6	5.80
$\text{AlCoCrCu}_{0.5}\text{Fe}_2\text{Ni}$	<i>fcc + bcc</i>	2ss	[232]	4.7	-6.5	7.6	4.92
$\text{AlCoCrCu}_{0.5}\text{FeNi}$	<i>bcc</i>	bcc ss	[239]	5.1	-7.9	7.5	5.65
$\text{AlCoCrCu}_{0.5}\text{FeNi}_{0.5}$	<i>fcc + bcc</i>	2ss	[232]	5.1	-7.3	7.3	6.15
$\text{AlCoCrCu}_{0.5}\text{FeNi}_{1.5}$	<i>fcc + bcc</i>	2ss	[232]	5	-8.3	7.8	5.22
$\text{AlCoCrCu}_{0.5}\text{FeNi}_2$	<i>fcc + bcc</i>	2ss	[232]	4.9	-8.4	7.9	4.36
$\text{AlCoCrCu}_{0.5}\text{FeNi}_{2.5}$	<i>fcc + bcc</i>	2ss	[232]	4.8	-8.4	8.1	4.53
$\text{AlCoCrCu}_{0.5}\text{FeNi}_3$	<i>fcc + bcc</i>	2ss	[232]	4.7	-8.4	8.2	4.25
$\text{AlCoCrCu}_{0.5}\text{FeNiTi}_{0.5}$	<i>bcc + bcc</i>	2ss	[243]	5.9	-13.4	7.2	9.72
$\text{AlCoCrCu}_{0.5}\text{Ni}$	<i>bcc</i>	bcc ss	[244]	5.5	-10.2	7.4	6.59
$\text{AlCoCrCuFe}_{0.5}\text{Ni}$	<i>fcc + bcc</i>	2ss	[239]	5.1	-5.6	7.8	5.56

AlCoCrCuFeMoNiTiVZr	<i>fcc + bcc</i>	2ss	[245]	8.1	-17.2	6.6	21.07
AlCoCrCuFeNi <sub>0.5</sub>	<i>fcc + bcc</i>	2ss	[239]	4.9	-3.9	7.6	5.61
AlCoCrCuFeNiTi	<i>bcc + fcc + bcc</i>	3ss	[246]	6.3	-13.8	7.3	11.95
AlCoCrCuFeNiTiV	<i>fcc + bcc</i>	2ss	[244]	5.9	-13.9	7	10.74
AlCoCrCuFeNiV	<i>fcc + bcc</i>	2ss	[246]	4.7	-7.8	7.4	5.21
AlCoCrCuNi	<i>fcc + bcc</i>	2ss	[55]	5.3	-6.6	7.8	5.94
AlCoCrCuNiTi	B2 + <i>fcc + σ</i>	ss + IM	[247]	6.6	-16.7	7.2	13.15
AlCoCrCuNiTiY	AlNi <sub>2</sub> Ti + Cu <sub>2</sub> Y	IM	[247]	15.2	-19.3	6.6	30.26
AlCoCrCuNiTiY <sub>0.5</sub>	AlNi <sub>2</sub> Ti + Cu <sub>2</sub> Y	IM	[247]	12.6	-18.3	6.8	22.26
AlCoCrCuNiTiY <sub>0.8</sub>	AlNi <sub>2</sub> Ti + Cu <sub>2</sub> Y	IM	[247]	14.3	-19	6.7	27.17
AlCoCrFe <sub>0.6</sub> Mo <sub>0.5</sub> Ni	<i>bcc + σ</i>	ss + IM	[40]	5.6	-12.3	7	8.75
AlCoCrFe <sub>1.5</sub> Mo <sub>0.5</sub> Ni	<i>bcc + σ</i>	ss + IM	[40]	5.3	-10.5	7.2	7.73
AlCoCrFe <sub>2</sub> Mo <sub>0.5</sub> Ni	<i>bcc + σ</i>	ss + IM	[40]	5.2	-9.7	7.2	7.27
AlCoCrFeMo <sub>0.1</sub> Ni	<i>bcc</i>	<i>bcc</i> ss	[248]	5.3	-12.1	7.2	6.66
AlCoCrFeMo <sub>0.2</sub> Ni	<i>bcc + σ</i>	ss + IM	[248]	5.4	-12	7.2	7.12
AlCoCrFeMo <sub>0.3</sub> Ni	<i>bcc + σ</i>	ss + IM	[248]	5.4	-11.8	7.1	7.52
AlCoCrFeMo <sub>0.4</sub> Ni	<i>bcc + σ</i>	ss + IM	[248]	5.5	-11.6	7.1	7.89
AlCoCrFeMo <sub>0.5</sub>	<i>bcc + σ</i>	ss + IM	[240]	5.5	-10.3	6.4	9.56
AlCoCrFeMo <sub>0.5</sub> Ni	<i>bcc + σ</i>	ss + IM	[40]	5.5	-11.4	7.1	8.23
AlCoCrFeMo <sub>0.5</sub> Ni <sub>0.5</sub>	<i>bcc + σ</i>	ss + IM	[249]	5.5	-11.1	6.8	8.86
AlCoCrFeMo <sub>0.5</sub> Ni <sub>1.5</sub>	<i>fcc + bcc + σ</i>	2ss + IM	[249]	5.4	-11.5	7.3	7.67
AlCoCrFeMo <sub>0.5</sub> Ni <sub>2</sub>	<i>fcc + bcc + σ</i>	2ss + IM	[249]	5.4	-11.5	7.5	7.17
AlCoCrFeNb <sub>0.1</sub> Ni	<i>bcc</i>	<i>bcc</i> ss	[250]	5.5	-13.3	7.2	7.26
AlCoCrFeNb <sub>0.25</sub> Ni	<i>bcc + bcc + L</i>	ss + IM	[250]	5.8	-14.7	7.1	8.77
AlCoCrFeNb <sub>0.5</sub> Ni	<i>fcc + bcc + L</i>	ss + IM	[250]	6.2	-16.5	7	10.95
AlCoCrFeNi	<i>fcc + B2</i>	ss + IM	[186]	5.3	-12.3	7.2	6.17
AlCoCrFeNiTi	<i>bcc + bcc</i>	2ss	[251]	6.6	-21.6	6.7	14.00
AlCoCrFeNiTi <sub>0.5</sub>	<i>bcc + bcc</i>	2ss	[241]	6.2	-17.9	6.9	10.62
AlCoCrFeNiTi <sub>1.5</sub>	<i>fcc + bcc + L</i>	2ss + IM	[251]	6.9	-23.9	6.5	16.54
AlCoCrFeNiTiVZr	amorphous	BMG	[234]	8.7	-26.8	6.1	25.06
AlCoCu <sub>0.33</sub> FeNi	<i>fcc + fcc + B2</i>	2ss + IM	[44]	5.5	-9.2	7.9	7.06
AlCoCu <sub>0.5</sub> FeNi	<i>fcc + bcc</i>	2ss	[232]	5.6	-8.7	7.9	6.80
AlCoCuNi	<i>fcc + bcc</i>	2ss	[55]	5.8	-8	8.3	7.13
AlCoFeMo <sub>0.5</sub> Ni	<i>bcc + σ</i>	ss + IM	[242]	6	-12.7	7.3	9.71
AlCr <sub>0.5</sub> CuFeNiTi	<i>fcc + bcc</i>	2ss	[252]	6.5	-15.4	7.1	14.40
AlCr <sub>1.5</sub> CuFeNiTi	<i>fcc + bcc</i>	2ss	[252]	6.2	-12.3	6.9	12.69
AlCr <sub>2</sub> CuFeNiTi	<i>fcc + bcc</i>	2ss	[252]	6	-11.1	6.9	11.96
AlCr <sub>3</sub> CuFeNiTi	<i>fcc + bcc</i>	2ss	[252]	5.8	-9.3	6.8	10.73
AlCrCu <sub>0.5</sub> FeNi	<i>fcc + bcc</i>	2ss	[232]	5.3	-7.7	7.2	6.82
AlCrCuFeMnNi	<i>bcc</i>	<i>bcc</i> ss	[230]	4.8	-5.1	7.5	6.80

AlCrCuFeNi <sub>2</sub>	<i>fcc</i>	<i>fcc</i> ss	[24]	4.9	-5.8	8	5.26
AlCrCuFeNiTi	<i>fcc</i> + <i>bcc</i>	2ss	[252]	6.4	-13.7	7	13.51
AlCrFeNi <sub>0.75</sub>	<i>bcc</i> + B2	ss + IM	[44]	5.6	-13.2	6.5	8.11
AlCrMoTaTiZr	amorphous	BMG	[253]	6.6	-16.1	4.7	22.89
AlCrTaTiZr	amorphous	BMG	[254]	7.1	-20	4.4	27.16
AlFeNiTiVZr	amorphous	BMG	[234]	8.7	-31.3	5.7	29.75
AlNbTaTiV	<i>bcc</i>	<i>bcc</i> ss	[229]	3.2	-13.4	4.4	6.37
AlTiVYZr	compound	IM	[22]	12.3	-14.9	3.8	33.31
Co <sub>1.5</sub> CrFeNi <sub>1.5</sub> Ti <sub>0.5</sub>	<i>fcc</i>	<i>fcc</i> ss	[43]	4.6	-10.7	8.1	5.54
CoCrCu <sub>0.5</sub> FeNi	<i>fcc</i>	<i>fcc</i> ss	[255]	1.2	0.5	8.6	0.22
CoCrCu <sub>0.75</sub> FeNi	<i>fcc</i> + <i>fcc</i>	2ss	[231]	1.2	2.2	8.7	0.28
CoCrCuFeMn	<i>fcc</i> + <i>bcc</i>	2ss	[16]	0.9	4.2	8.2	2.92
CoCrCuFeMnNi	<i>fcc</i>	<i>fcc</i> ss	[2]	1.1	1.4	8.5	2.57
CoCrCuFeNi	<i>fcc</i>	<i>fcc</i> ss	[42]	1.2	3.2	8.8	0.34
CoCrCuFeNiTi	<i>fcc</i> + <i>L</i>	ss + IM	[42]	5.7	-8.4	8	9.73
CoCrCuFeNiTi <sub>0.5</sub>	<i>fcc</i>	<i>fcc</i> ss	[42]	4.5	-3.7	8.4	5.61
CoCrCuFeNiTi <sub>0.8</sub>	<i>fcc</i> + <i>L</i>	ss + IM	[42]	5.3	-6.8	8.1	8.20
CoCrCuFeNiTi <sub>2</sub>	compound	IM	[22]	6.7	-14	7.4	15.48
CoCrCuFeNiTiVZr	amorphous	BMG	[234]	8.8	-16.8	7.1	22.60
CoCrFeMnNbNi	compound	IM	[2]	5.9	-12	7.5	11.75
CoCrFeMnNi	<i>fcc</i>	<i>fcc</i> ss	[2]	1.1	-4.2	8	2.98
CoCrFeMnNiTi	compound	IM	[2]	5.8	-13.4	7.3	11.35
CoCrFeMo <sub>0.3</sub> Ni	<i>fcc</i>	<i>fcc</i> ss	[36]	3	-4.2	8.1	2.58
CoCrFeMo <sub>0.5</sub> Ni	<i>fcc</i> + $\sigma$	ss + IM	[39]	3.5	-4.3	8	4.00
CoCrFeMo <sub>0.85</sub> Ni	<i>fcc</i> + $\sigma$ + $\mu$	ss + IM	[39]	4.2	-4.6	7.9	5.86
CoCrFeMoNiTiVZr	amorphous	BMG	[234]	8.6	-18.8	6.5	24.08
CoCrFeNbNi	<i>fcc</i> + C14	ss + IM	[34]	5.7	-14.9	8.8	12.44
CoCrFeNi	<i>fcc</i>	<i>fcc</i> ss	[255]	1.2	-3.8	8.3	0.03
CoCrFeNiTa	<i>bcc</i> + C14	ss + IM	[34]	5.7	-14.4	8.8	14.48
CoCrFeNiTi	$\chi$ + C14 + $\eta$	IM	[34]	6.2	-16.3	7.4	11.69
CoCrFeNiTi <sub>0.3</sub>	<i>fcc</i>	<i>fcc</i> SS	[256]	4.1	-8.9	8	4.30
CoCrFeNiTi <sub>0.5</sub>	<i>fcc</i> + <i>L</i> + $\sigma$ + <i>R</i>	ss + IM	[256]	5	-11.6	7.8	6.74
CoCrFeNiV	<i>fcc</i> + $\sigma$	ss + IM	[34]	2.2	-9	8.8	1.74
CoCrFeNiW	<i>fcc</i> + $\mu$	ss + IM	[34]	3.8	-2.9	7.8	8.80
CoCrFeNiY	<i>bcc</i> + <i>Y</i> + <i>YNi</i> + <i>Y</i> <sub>2</sub>	ss + IM	[34]	16.4	-9.3	7.2	28.54
CoCrFeNiZr	<i>bcc</i> + C15	ss + IM	[34]	10.8	-22.7	7.4	26.43
CoCrMnNiV	<i>fcc</i> + $\sigma$	ss + IM	[16]	2.8	-9.1	7.4	3.68
CoCuFeNi	<i>fcc</i> + <i>fcc</i>	2ss	[44]	1.1	4.7	9.5	0.42
CoCuFeNiTiVZr	amorphous	BMG	[234]	9.2	-20.2	7.3	25.10
CoCuFeNiV	<i>fcc</i>	<i>fcc</i> SS	[22]	2.8	-2.2	8.6	1.78

CoFeMnMoNi	fcc + $\mu$	ss + IM	[16]	4.4	-4	8	7.74
CoFeMnNiV	fcc + $\sigma$	ss + IM	[16]	2.8	-9	7.8	3.93
CoFeMoNiTiVZr	amorphous	BMG	[234]	8.8	-21.8	6.6	26.15
Cr <sub>2</sub> Cu <sub>2</sub> Fe <sub>2</sub> MnNi <sub>2</sub>	<i>fcc</i> + <i>bcc</i>	2ss	[257]	1.1	3.6	8.6	1.95
Cr <sub>2</sub> Cu <sub>2</sub> FeMn <sub>2</sub> Ni <sub>2</sub>	<i>fcc</i> + <i>bcc</i>	2ss	[257]	1.1	2.4	8.4	3.14
Cr <sub>2</sub> CuFe <sub>2</sub> Mn <sub>2</sub> Ni <sub>2</sub>	<i>fcc</i> + <i>bcc</i>	2ss	[257]	1	0.1	8.1	3.30
Cr <sub>2</sub> CuFe <sub>2</sub> MnNi	<i>fcc</i> + <i>bcc</i>	2ss	[257]	0.9	2.6	8	2.35
CrCu <sub>0.7</sub> FeNi	<i>fcc</i> + <i>bcc</i>	2ss	[258]	1.2	3	8.6	0.35
CrCu <sub>2</sub> Fe <sub>2</sub> Mn <sub>2</sub> Ni	<i>fcc</i> + <i>bcc</i>	2ss	[257]	0.9	4.7	8.5	3.24
CrCu <sub>2</sub> Fe <sub>2</sub> MnNi <sub>2</sub>	<i>fcc</i>	<i>fcc</i> SPSS	[257]	1.1	3.9	8.9	2.16
CrCuFeMn <sub>2</sub> Ni <sub>2</sub>	<i>fcc</i>	<i>fcc</i> SPSS	[257]	1.1	-0.5	8.4	3.88
CrCuFeMnNi	<i>fcc</i> + <i>bcc</i>	2ss	[235]	1	2.7	8.4	3.00
CrCuFeMoNi	<i>fcc</i> + <i>bcc</i>	2ss	[235]	4.1	4.6	8.2	6.17
CrCuFeNiZr	<i>bcc</i> + IM	ss + IM	[235]	10	-14.4	7.8	26.04
CrCuMnNi	<i>fcc</i> + <i>bcc</i>	2ss	[259]	1.1	1.8	8.5	3.26
CrFeMnNiTi	<i>bcc</i> + L	ss + IM	[2]	6	-13.3	7	13.14
CrNbTiVZr	<i>bcc</i> + IM	ss + IM	[199]	7.7	-4.6	4.8	28.98
CrNbTiZr	<i>bcc</i> + IM	ss + IM	[199]	7.8	-5	4.8	33.64
Cu <sub>47</sub> Ni <sub>8</sub> Ti <sub>34</sub> Zr <sub>11</sub> <sup>a</sup>	amorphous	BMG	[233]	8.6	-15.4	7.8	24.19
Cu <sub>60</sub> Hf <sub>10</sub> Ti <sub>10</sub> Zr <sub>20</sub> <sup>a</sup>	amorphous	BMG	[234]	10.3	-17.3	8.2	34.51
CuFeHfTiZr	IM	IM	[260]	9.8	-15.8	6.2	47.77
CuFeNiTiVZr	amorphous	BMG	[234]	9.2	-18.8	7	27.95
CuHfNiTiZr	amorphous	BMG	[260]	10.3	-27.4	6.6	46.69
CuNbNiTiZr	amorphous	BMG	[261]	9.4	-21.3	6.8	33.03
FeMoNiTiVZr	amorphous	BMG	[234]	8.6	-19.8	6.2	28.02
HfNbTaTiZr	<i>bcc</i>	<i>bcc</i> SPSS	[103]	4.1	2.7	4.4	11.13
MoNbTaVW	<i>bcc</i>	<i>bcc</i> SPSS	[95]	3.2	-4.6	5.4	5.31
MoNbTaW	<i>bcc</i>	<i>bcc</i> SPSS	[95]	2.2	-6.5	5.5	3.59
MoNbTiV <sub>0.25</sub> Zr	<i>bcc</i>	<i>bcc</i> SPSS	[262]	5.3	-2.6	4.8	16.29
MoNbTiV <sub>0.5</sub> Zr	<i>bcc</i>	<i>bcc</i> SPSS	[262]	5.6	-2.7	4.8	17.00
MoNbTiV <sub>0.75</sub> Zr	<i>bcc</i>	<i>bcc</i> SPSS	[262]	5.8	-2.7	4.8	17.43
MoNbTiV <sub>1.5</sub> Zr	<i>bcc</i>	<i>bcc</i> SPSS	[262]	6.1	-2.7	4.8	17.70
MoNbTiV <sub>2</sub> Zr	<i>bcc</i>	<i>bcc</i> SPSS	[262]	6.1	-2.7	4.8	17.42
MoNbTiV <sub>3</sub> Zr	<i>bcc</i>	<i>bcc</i> SPSS	[262]	6.2	-2.5	4.9	16.43
MoNbTiVZr	<i>bcc</i>	<i>bcc</i> SPSS	[262]	5.9	-2.7	4.8	17.66
MoNbTiZr	<i>bcc</i>	<i>bcc</i> SPSS	[262]	5	-2.5	4.8	15.19
NbTaTiV	<i>bcc</i>	<i>bcc</i> SPSS	[229]	3.6	-0.3	4.8	7.74
NbTiV <sub>2</sub> Zr	<i>bcc</i> + <i>bcc</i> + <i>bcc</i>	3ss	[199]	6.6	-1.3	4.6	20.58
NbTiVZr	<i>bcc</i>	<i>bcc</i> SPSS	[199]	6.2	-0.3	4.5	20.08

## Appendix 2

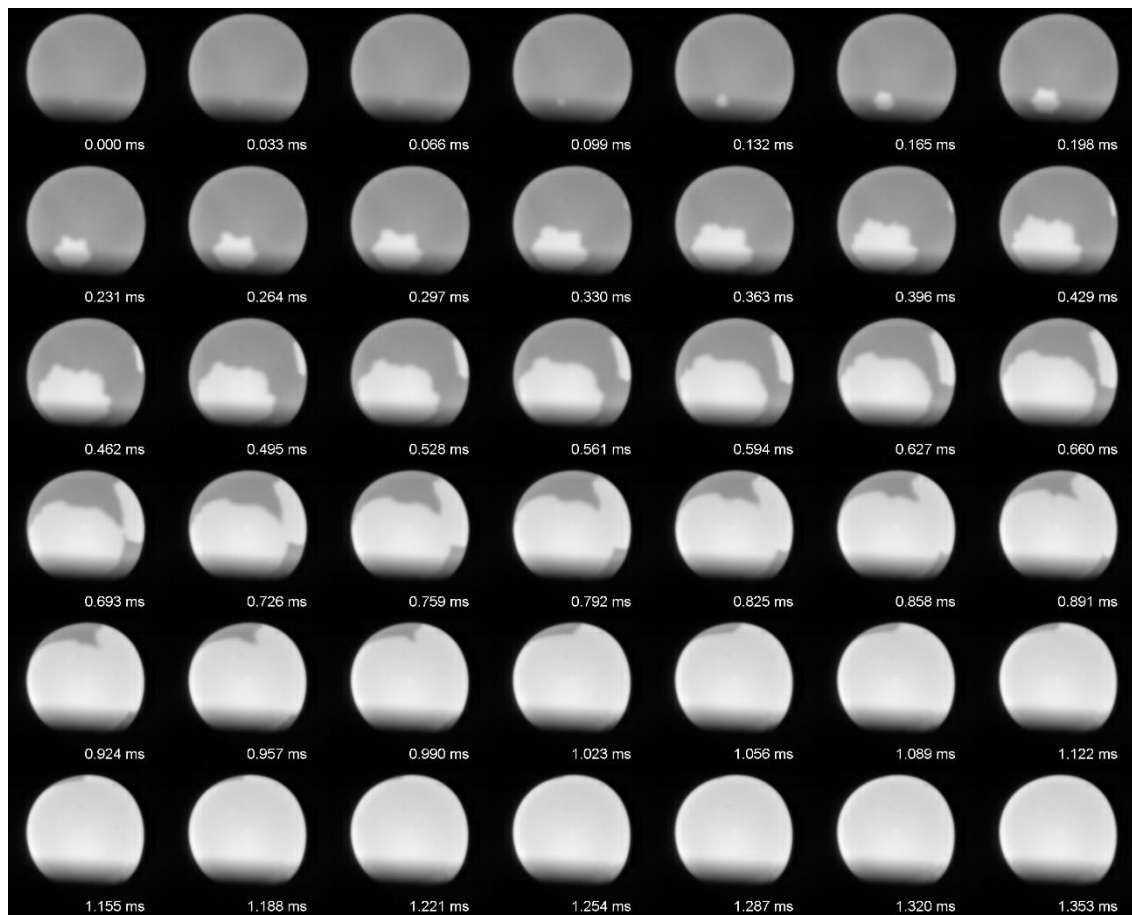


Figure A2.1. Video montage sequence of CrFeNi undercooled by 70 K before solidification. The time is set to zero just before the crystallization event.

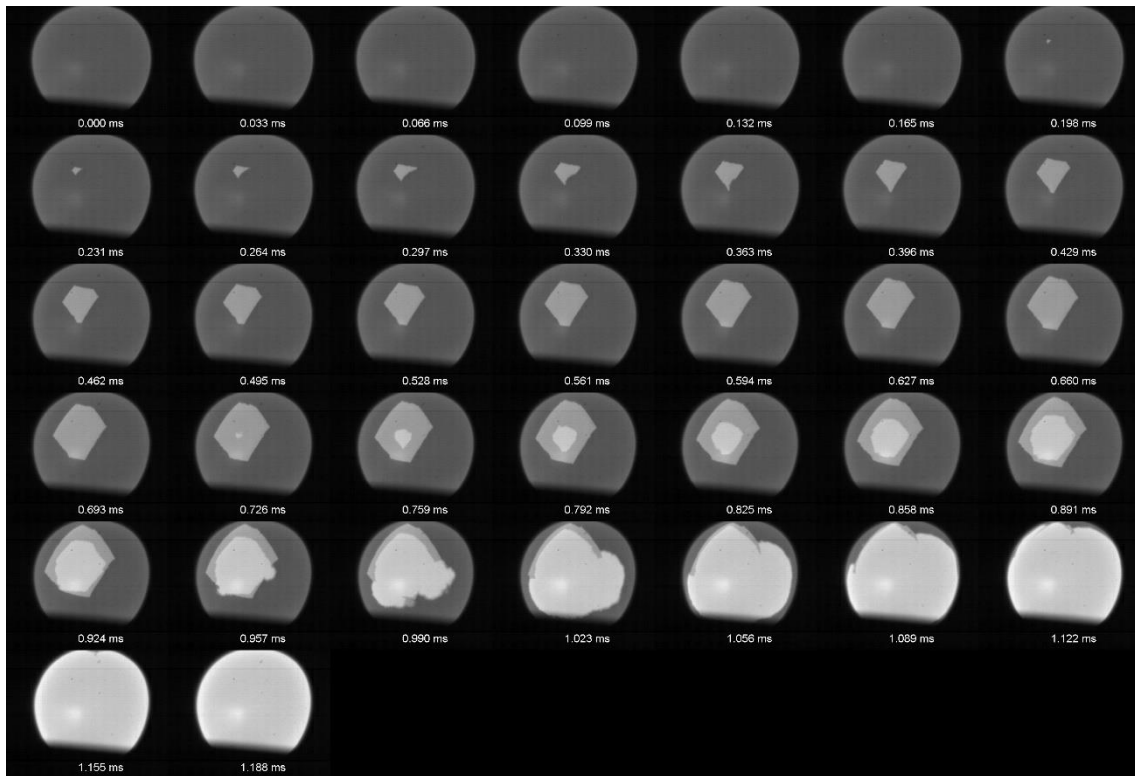


Figure A2.2. Video montage sequence of CrFeNi undercooled by 138 K before solidification. The time is set to zero just before the crystallization event.

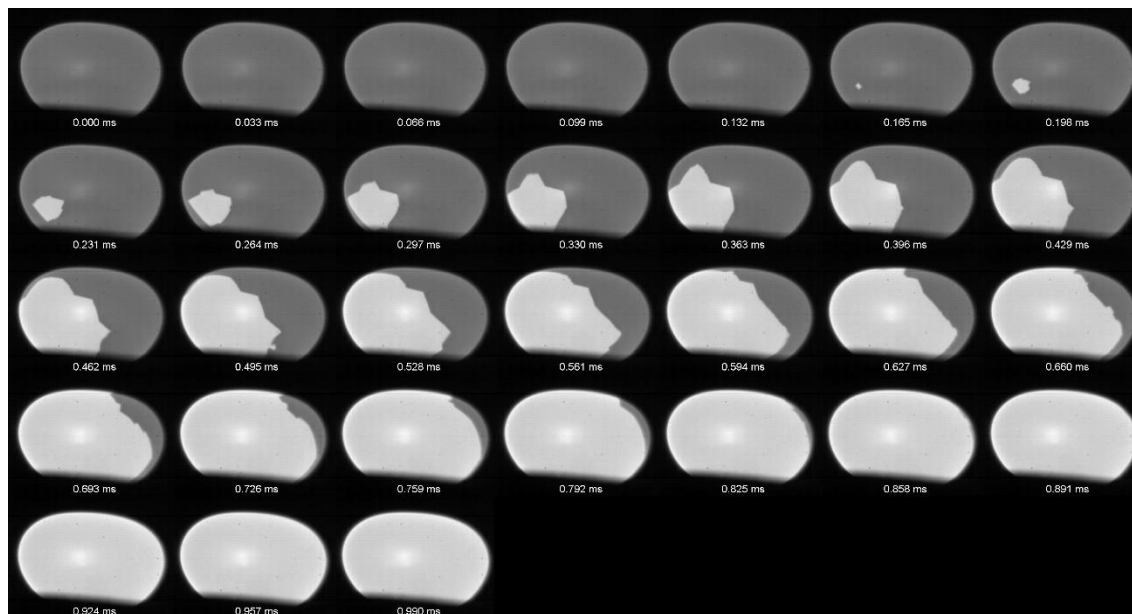


Figure A2.3. Video montage sequence of CoCrFeNi undercooled by 120 K before solidification. The time is set to zero just before the crystallization event.

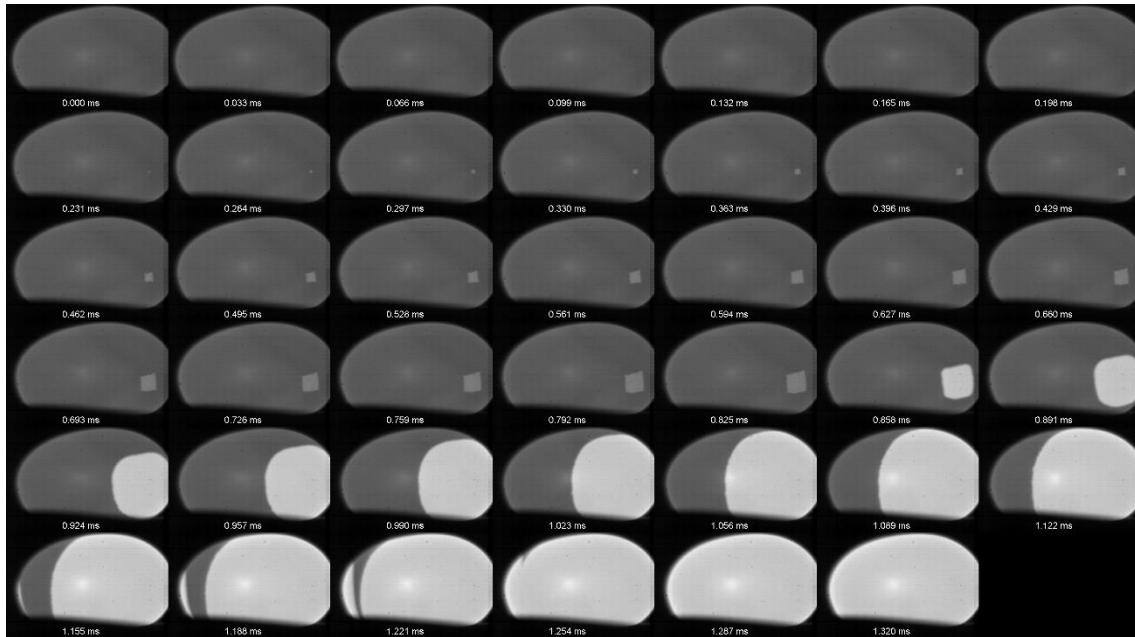


Figure A2.4. Video montage sequence of CoCrFeNi undercooled by 150 K before solidification. The time is set to zero just before the crystallization event.



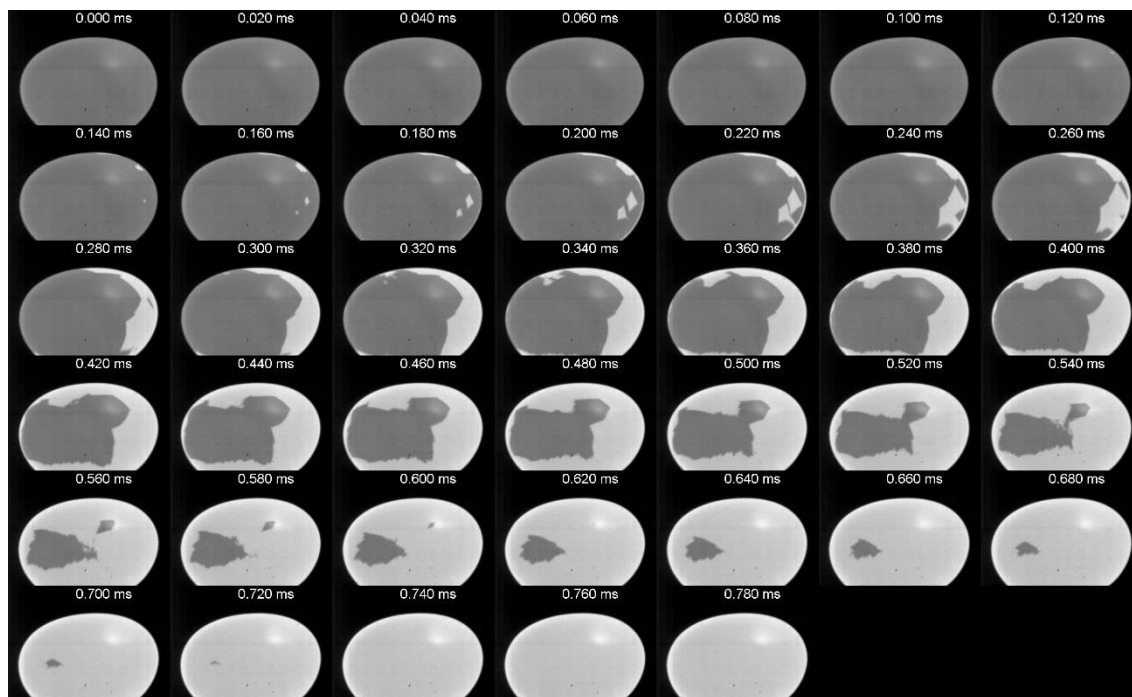


Figure A2.5. Video montage sequence of CoCrNi undercooled by 84 K before solidification. The time is set to zero just before the crystallization event.

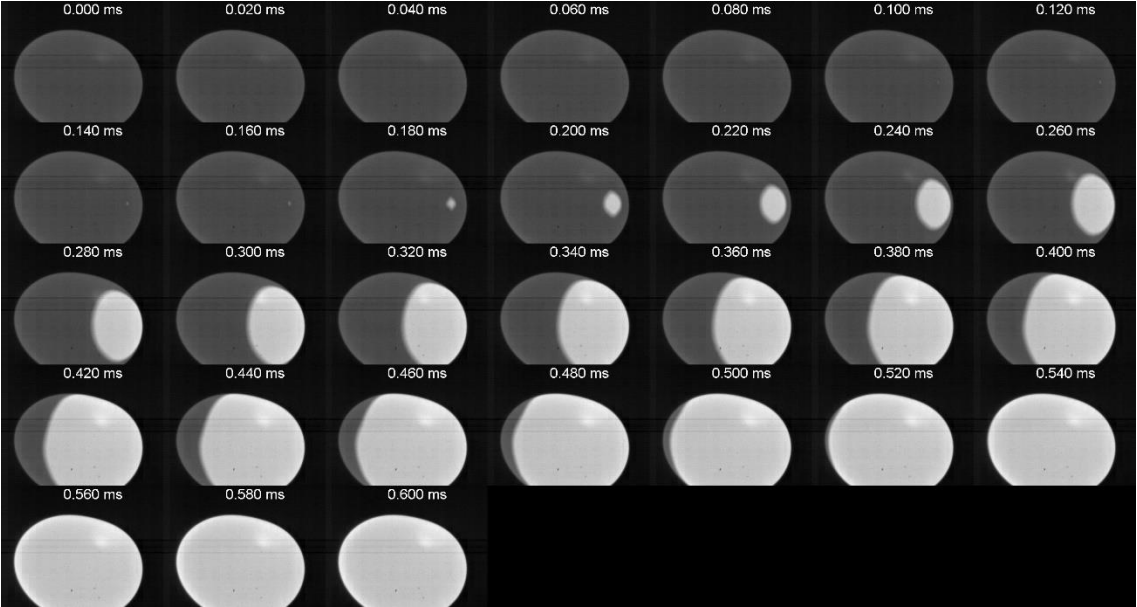


Figure A2.6. Video montage sequence of CoCrNi undercooled by 155 K before solidification. The time is set to zero just before the crystallization event.

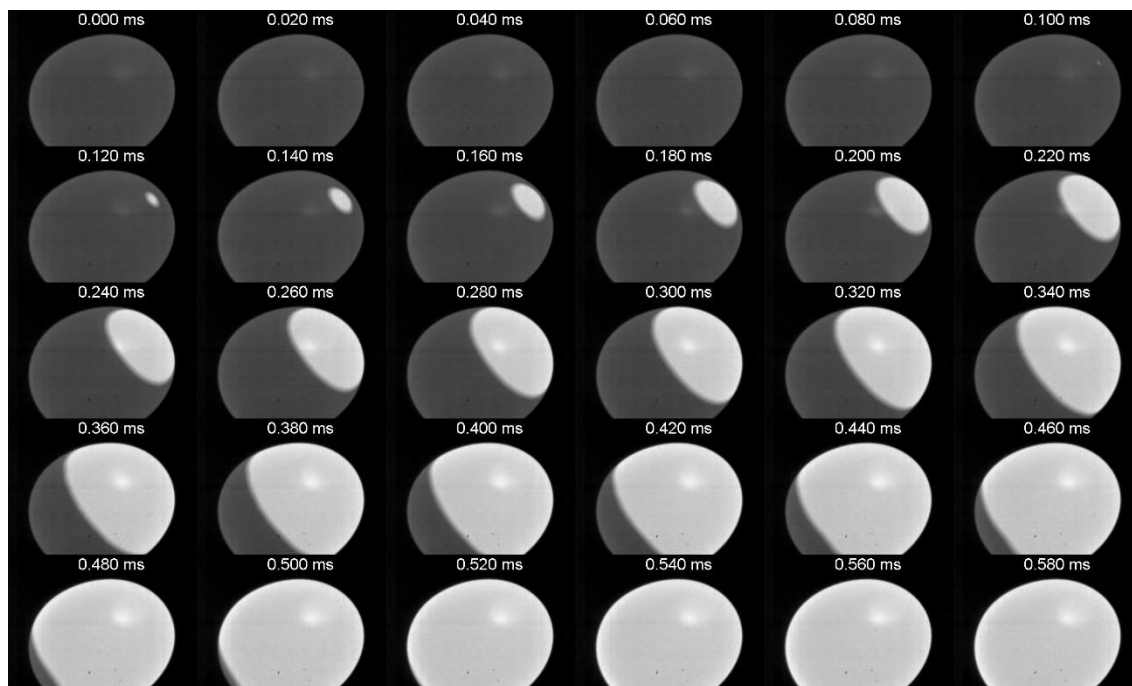


Figure A2.7. Video montage sequence of CoCrNi undercooled by 160 K before solidification. The time is set to zero just before the crystallization event.

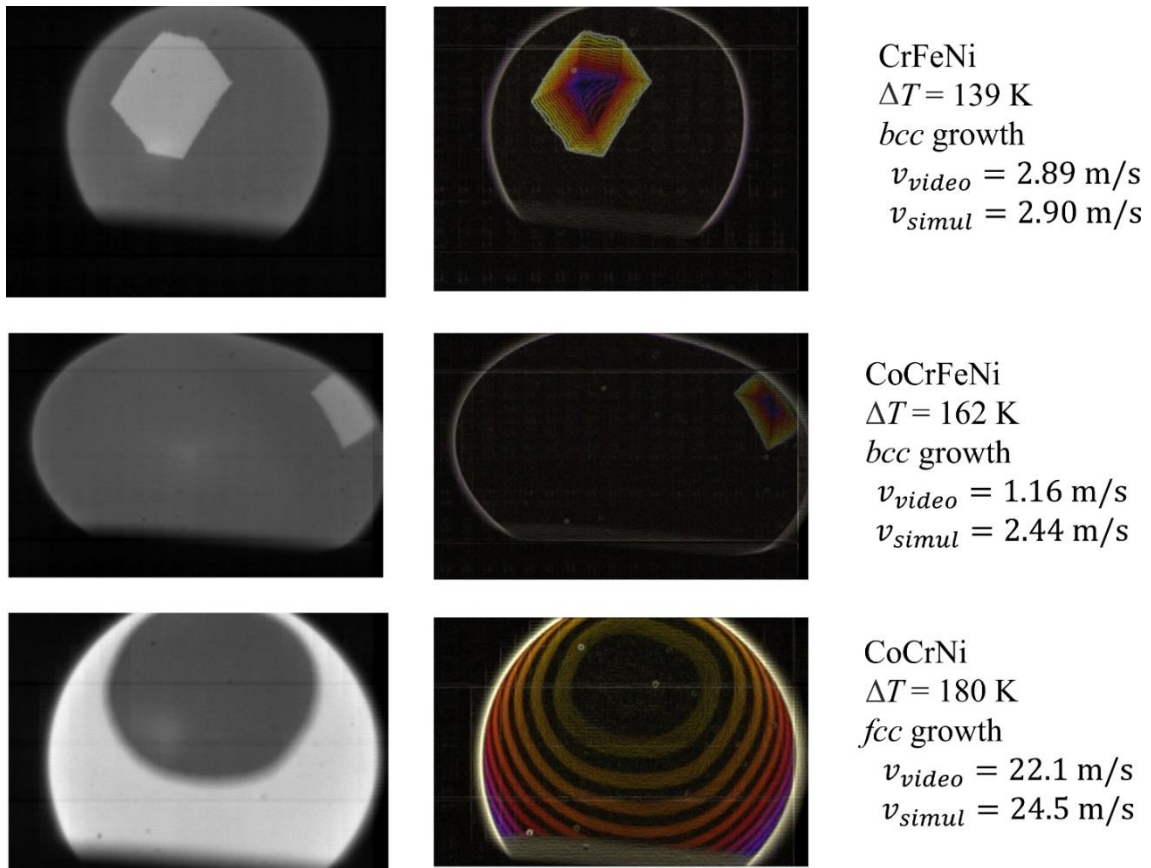


Figure A2.8. *Left panels* – snapshots of the *bcc* and *fcc* crystals growing in the undercooled melts; *right panels* – line contours of the crystals shown on the left panels showing their evolution with time: a) *bcc* phase in CrFeNi melt at  $\Delta T = 139$  K; b) *fcc* phase in CoCrNi melt at  $\Delta T = 180$  K; c) *bcc* phase in CoCrFeNi at  $\Delta T = 162$  K.  $v_{video}$  – crystal growth velocity calculated directly from the recalescence front travel distance;  $v_{simul}$  – dendrite tip velocity obtained from simulations as shown in Fig. A2.9.

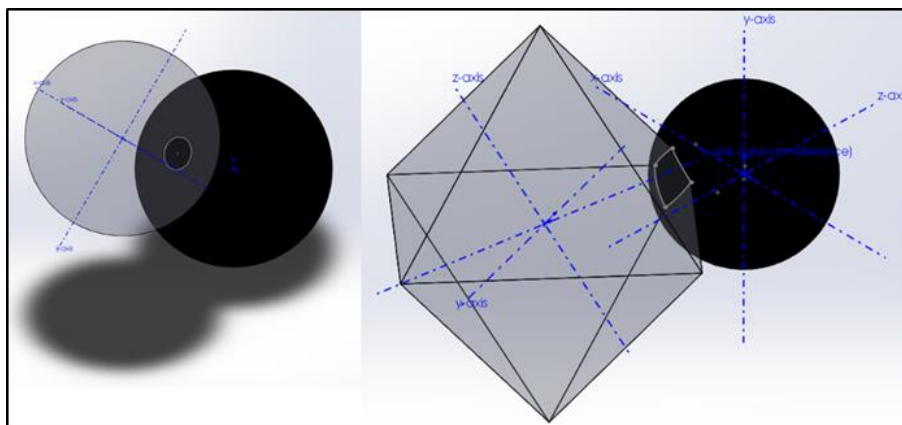


Figure A2.9. The simulation of semi-solid dendrite growth in electromagnetically levitated samples performed by Y. Yang (University of Alberta, Canada): Isometric view of a) sphere simulating the *fcc* dendrite growing in CoCrNi; b) octahedron simulating the *bcc* dendrite growing in CrFeNi; *black spheres* – molten alloys. The model dendrites have been moved and rotated until the surface intersection curve fitted the desired contours in the reference images when viewed from the front. This way, a series of intersection curves were created and projected onto a 2-dimensional sketch in the front plane.



Figure A2.10. Backscattered electrons SEM images showing the microstructure of CrFeNi alloy in the as-cast state (a), solidified at the melt undercooling  $\Delta T = 38$  K (b) and  $\Delta T = 93$  K (c).

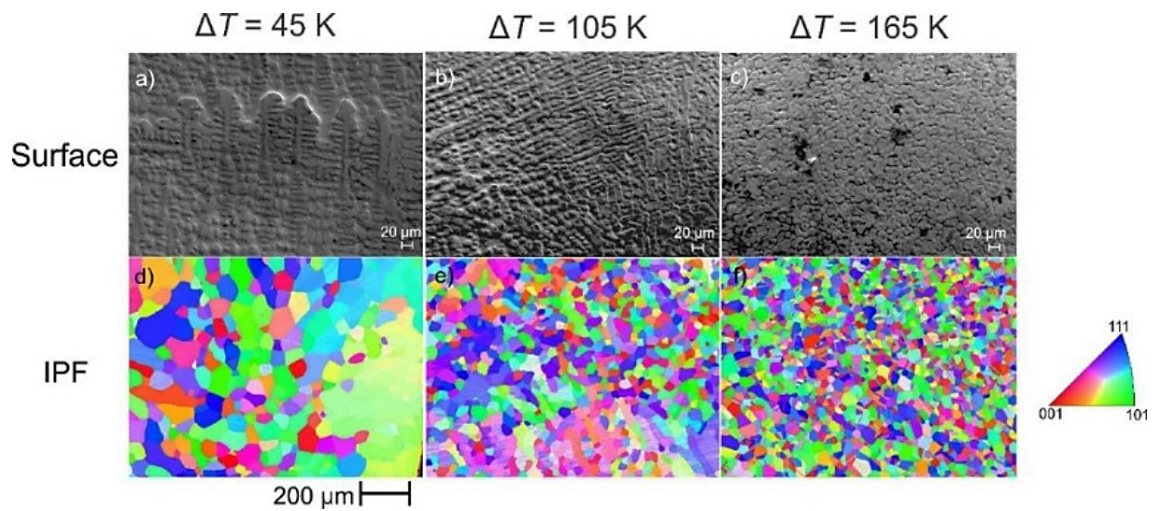


Figure A2.11. a) – c) Secondary electron SEM images taken from the surface of CoCrNi alloy solidified at a different level of the melt undercooling in the EML facility. d) – f) Inverse pole figures (IPF) measured from the cross-sections of the same samples.

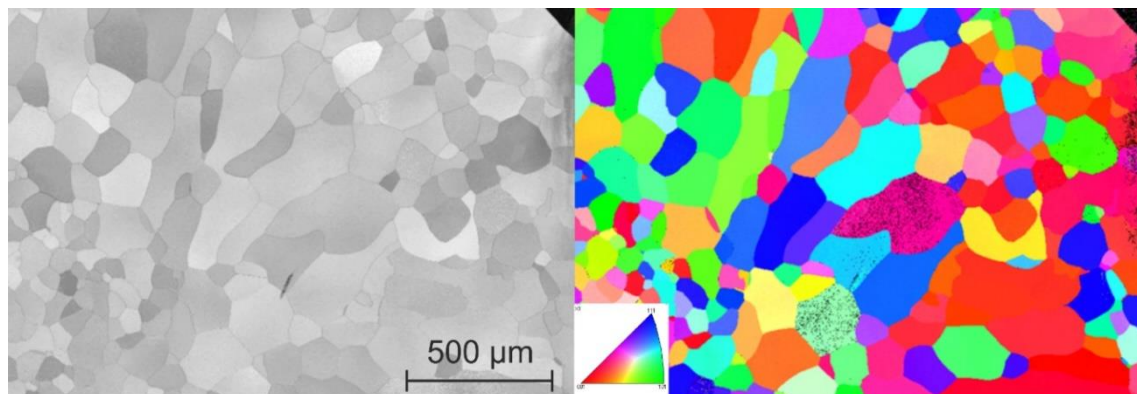


Figure A2.12. *Left panel* – EBSD pattern quality for a CoCrFeNi sample solidified with low undercooling ( $\Delta T = 50 \text{ K}$ ). *Right panel* – Inverse pole figure showing the random distribution of grain orientations.

## Appendix 3

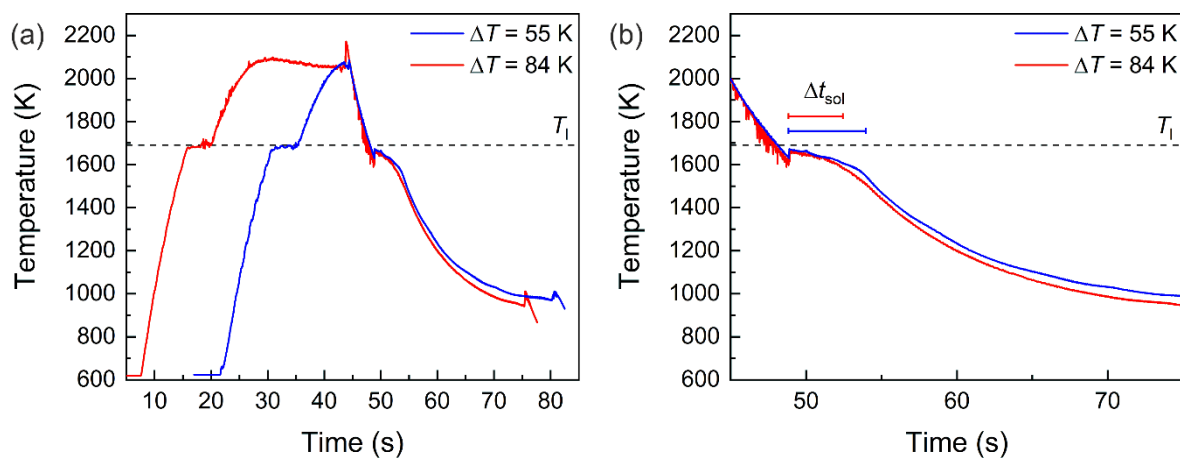


Figure. A3.1. (a) Comparison of the cooling rate after recalcescence for two samples of the  $\text{Al}_{0.3}\text{CoCrFeNi}$ ,  $\Delta T = 55$  and 84 K. b) Inset of the cooling curve seen in a showing the different post-recalcescence solidification times for the different undercooling.



## Appendix 4

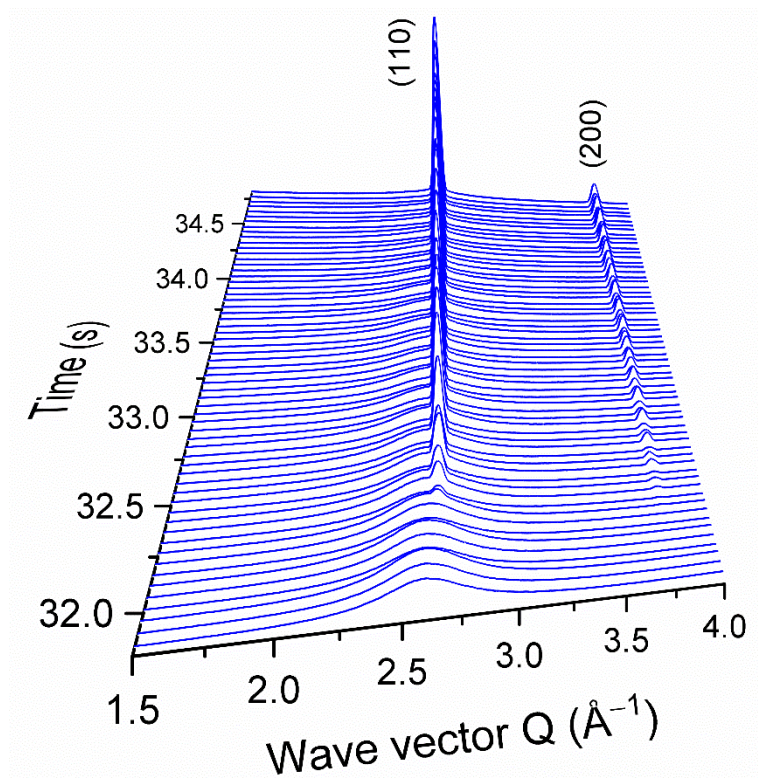


Figure A4.1. 3D XRD plot during crystallization of the sample shown in Fig. 5.1.



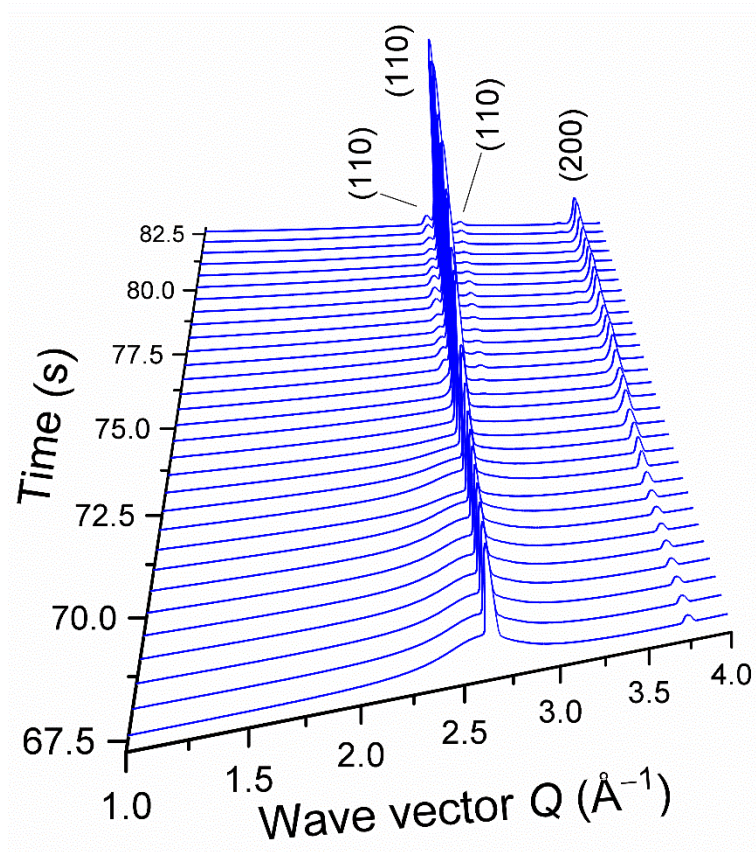


Figure A4.2. 3D XRD plot during cooling of the sample shown in Fig. 5.2 evidencing the peaks that appear around 75 s.

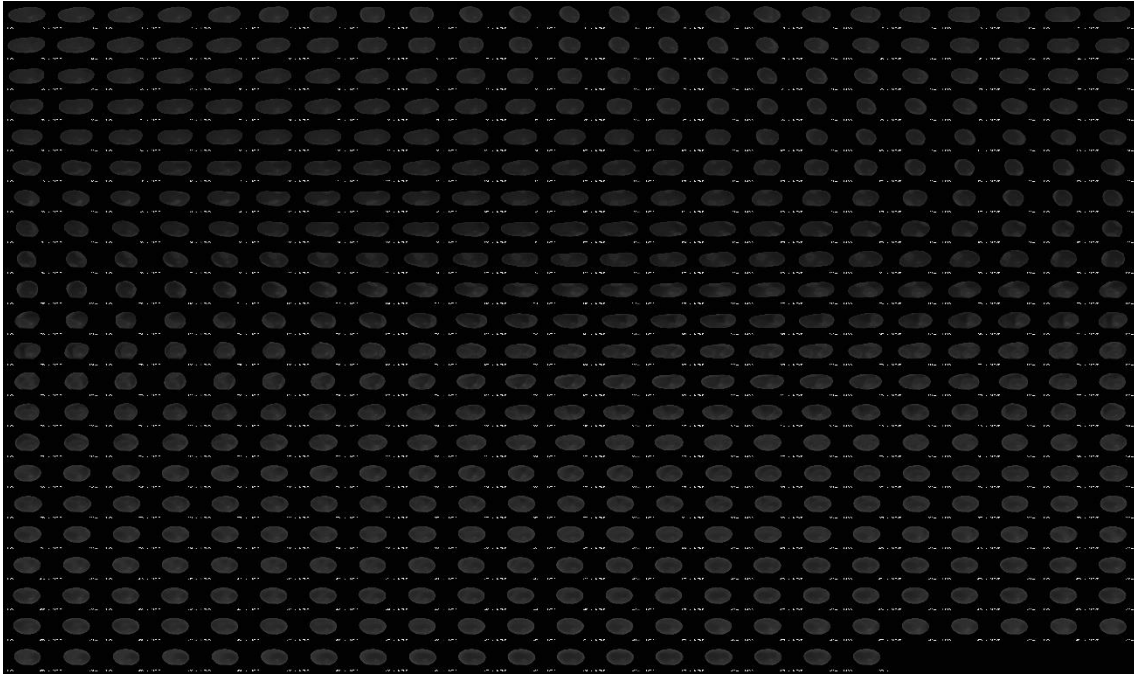


Figure A4.3. Video montage sequence of the NbTiVZr refractory high-entropy alloy undercooled by 107 K before solidification. The time is set to zero just before the crystallization event.

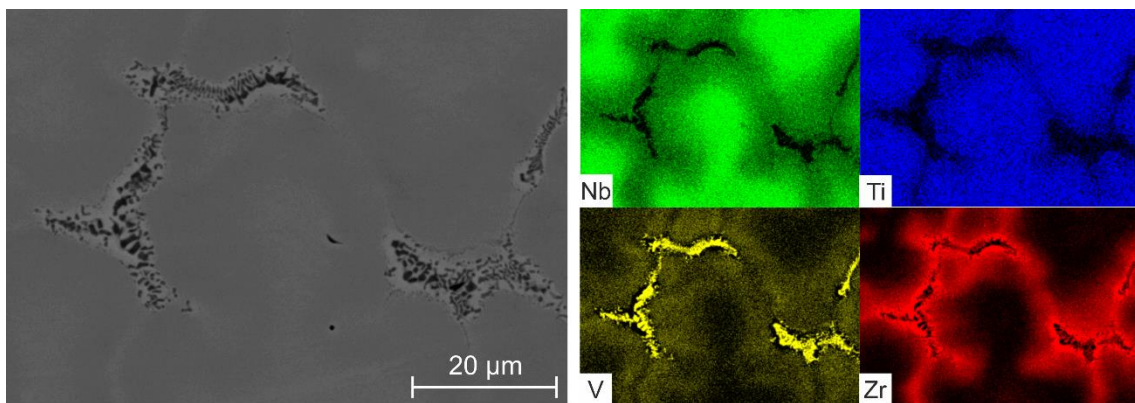


Figure A4.4. Higher EBS SEM magnification of the sample shown in Fig. 5.5c.

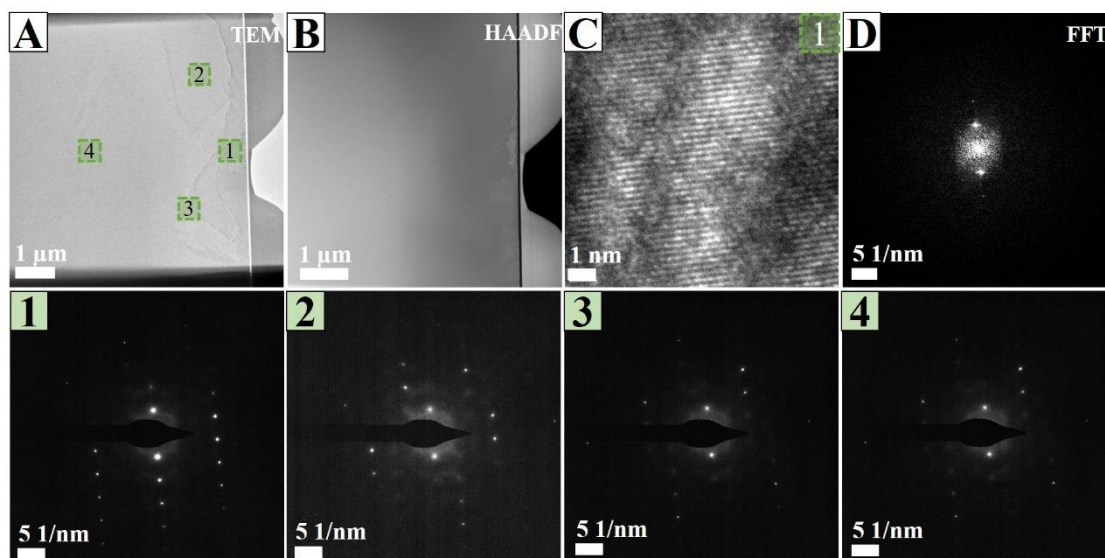


Figure A4.5 a) TEM image showing the cross-section of the matrix. The numbered green regions correspond to the points where the SAED patterns were collected and presented in the bottom numbered row. b) HAADF image of the same region presented in panel a). c) High-resolution TEM image of region 1 and its fast Fourier transform (FFT) shown in panel d). TEM images here and in the next figures were obtained by R.G. Mendes (IFW-Dresden and the University of Utrecht).

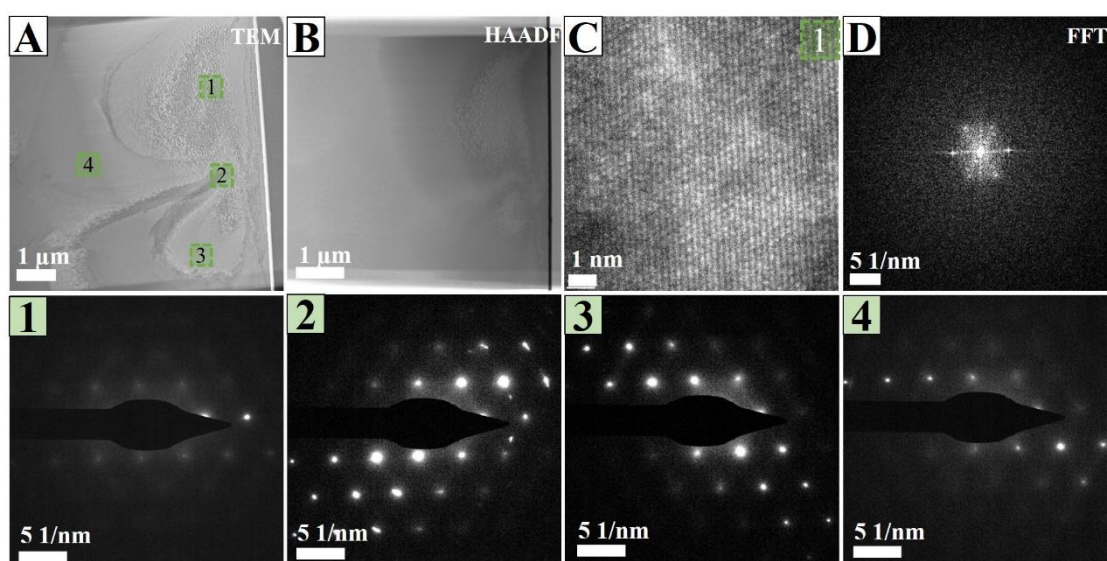


Figure A4.6. a) TEM image showing the cross-section of the matrix. The numbered green regions correspond to the points where the SAED patterns were collected and presented in the bottom numbered row. b) HAADF image of the same region presented in panel a). c) High-resolution TEM image of region 1 and its fast Fourier transform (FFT) shown in panel d).



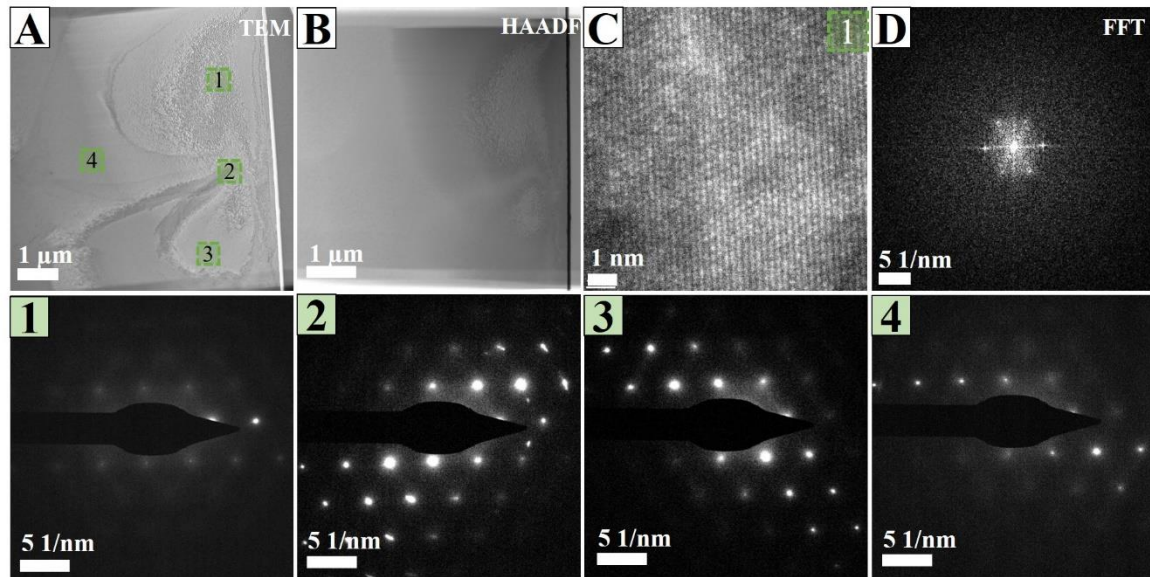


Figure A4.7. a) TEM image showing the cross-section of the matrix. The numbered green regions correspond to the points where the SAED patterns were collected and presented in the bottom numbered row. b) HAADF image of the same region presented in panel a). c) High-resolution TEM image of region 1 and its fast Fourier transform (FFT) shown in panel d).

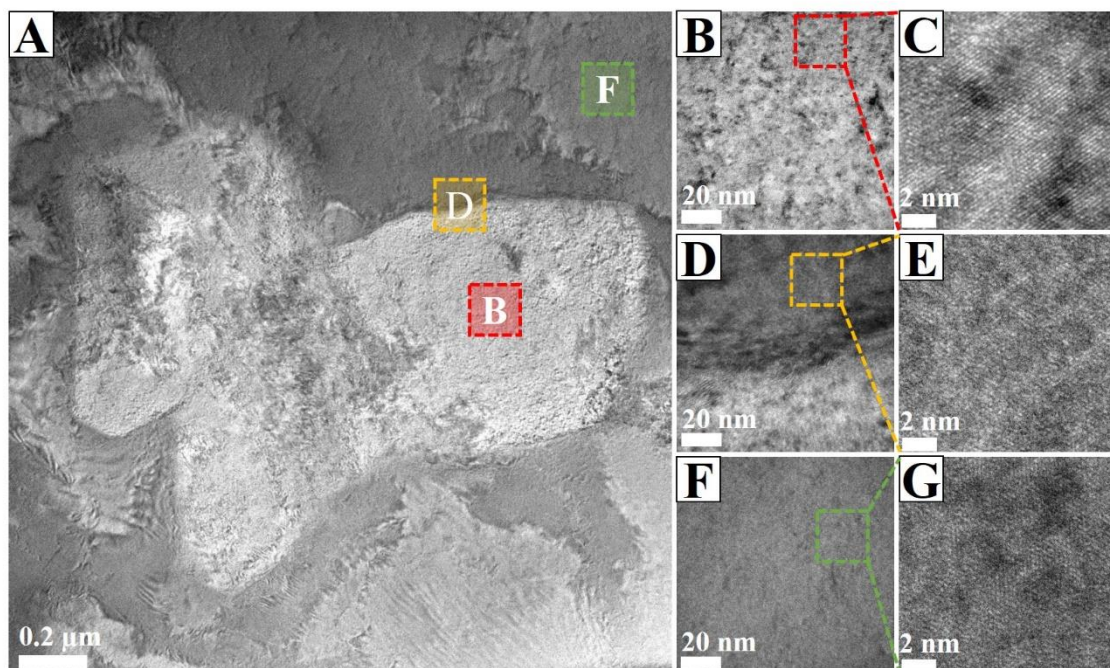


Figure A4.8. a) TEM image showing the three coexisting bcc phases: b) V-rich region, d) interface between V-rich and Zr-rich regions, and f) matrix. Panels c, e, and g correspond to high-magnification TEM images of the V-rich, Zr-rich, and matrix regions, respectively.

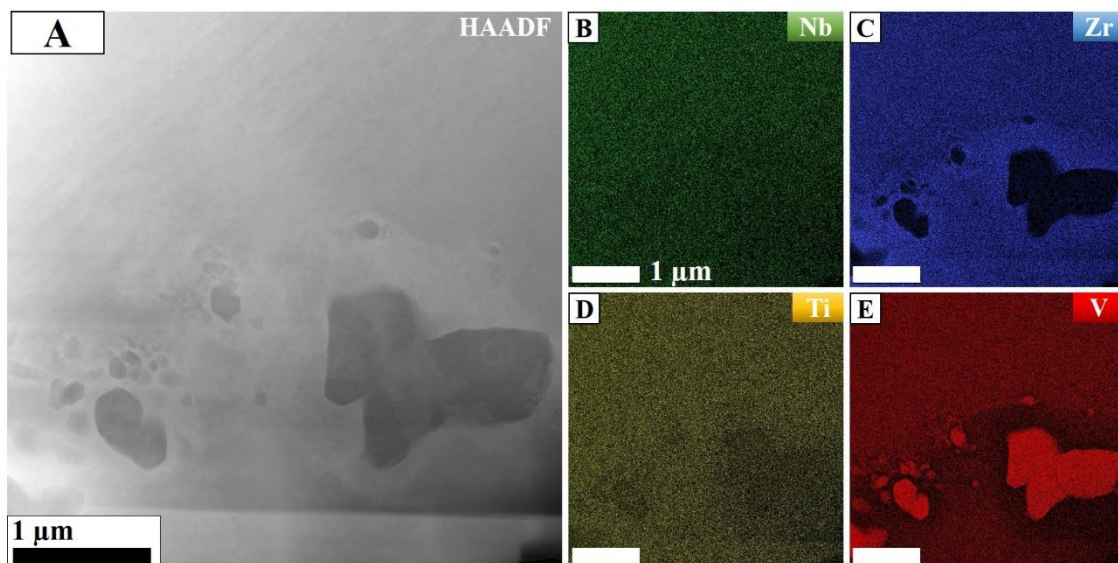


Figure A4.9. a) High-magnification HAADF image showing the V-rich regions in dark contrast. b, c, d, and e show the EDX elemental mapping for Nb, Zr, Ti, and V, respectively.

## References

- [1] M.C. Gao, P.K. Liaw, J.W. Yeh, Y. Zhang, *High-entropy alloys: Fundamentals and applications*, Springer International Publishing, Cham, 2016. doi:10.1007/978-3-319-27013-5.
- [2] B. Cantor, I.T.H. Chang, P. Knight, A.J.B. Vincent, Microstructural development in equiatomic multicomponent alloys, *Mater. Sci. Eng. A.* 375–377 (2004) 213–218. doi:10.1016/j.msea.2003.10.257.
- [3] P.-K. Huang, J.-W. Yeh, T.-T. Shun, S.-K. Chen, Multi-Principal-Element Alloys with Improved Oxidation and Wear Resistance for Thermal Spray Coating, *Adv. Eng. Mater.* 6 (2004) 74–78. doi:10.1002/adem.200300507.
- [4] J.-W. Yeh, S.-K. Chen, S.-J. Lin, J.-Y. Gan, T.-S. Chin, T.-T. Shun, C.-H. Tsau, S.-Y. Chang, Nanostructured High-Entropy Alloys with Multiple Principal Elements: Novel Alloy Design Concepts and Outcomes, *Adv. Eng. Mater.* 6 (2004) 299–303. doi:10.1002/adem.200300567.
- [5] W. Lu, C.H. Liebscher, G. Dehm, D. Raabe, Z. Li, Bidirectional Transformation Enables Hierarchical Nanolaminate Dual-Phase High-Entropy Alloys, *Adv. Mater.* 30 (2018) 1804727. doi:10.1002/adma.201804727.
- [6] Z. Li, K.G. Pradeep, Y. Deng, D. Raabe, C.C. Tasan, Metastable high-entropy dual-phase alloys overcome the strength-ductility trade-off, *Nature.* 534 (2016) 227–230. doi:10.1038/nature17981.
- [7] M.C. Gao, D.B. Miracle, D. Maurice, X. Yan, Y. Zhang, J.A. Hawk, High-entropy functional materials, *J. Mater. Res.* 33 (2018) 3138–3155. doi:10.1557/jmr.2018.323.
- [8] D.B. Miracle, O.N. Senkov, A critical review of high entropy alloys and related concepts, *Acta Mater.* 122 (2017) 448–511. doi:10.1016/j.actamat.2016.08.081.
- [9] E.P. George, D. Raabe, R.O. Ritchie, High-entropy alloys, *Nat. Rev. Mater.* 15 (2019) 761–767. doi:10.1038/s41578-019-0121-4.
- [10] D. Herlach, Non-Equilibrium Solidification of Undercooled Metallic Melts, *Metals (Basel).* 4 (2014) 196–234. doi:10.3390/met4020196.
- [11] S. Jeon, M. Kolbe, V. Kaban, G. String, A. Cleaver, I. Kaban, O. Shuleshova, J. Gao, D.M. Matson, Metastable solidification pathways of undercooled eutectic CoSi–CoSi<sub>2</sub> alloys, *Acta Mater.* 176 (2019) 43–52.

- doi:10.1016/j.actamat.2019.06.048.
- [12] S. Wang, Atomic Structure Modeling of Multi-Principal-Element Alloys by the Principle of Maximum Entropy, *Entropy*. 15 (2013) 5536–5548.  
doi:10.3390/e15125536.
- [13] E.S. Machlin, *An Introduction to Aspects of Thermodynamics and Kinetics Relevant to Materials Science*, Elsevier, 2007. doi:10.1016/B978-0-08-046615-6.X5016-4.
- [14] J.-W. Yeh, Alloy design strategies and future trends in high-entropy alloys, *JOM*. 65 (2013) 1759–1771. doi:10.1007/s11837-013-0761-6.
- [15] F. Zhang, C. Zhang, S.L. Chen, J. Zhu, W.S. Cao, U.R. Kattner, An understanding of high entropy alloys from phase diagram calculations, *Calphad*. 45 (2014) 1–10. doi:10.1016/j.calphad.2013.10.006.
- [16] F. Otto, Y. Yang, H. Bei, E.P. George, Relative effects of enthalpy and entropy on the phase stability of equiatomic high-entropy alloys, *Acta Mater*. 61 (2013) 2628–2638. doi:10.1016/j.actamat.2013.01.042.
- [17] E.J. Pickering, R. Muñoz-Moreno, H.J. Stone, N.G. Jones, Precipitation in the equiatomic high-entropy alloy CrMnFeCoNi, *Scr. Mater*. 113 (2016) 106–109. doi:10.1016/j.scriptamat.2015.10.025.
- [18] S.A. Kube, J. Schroers, Metastability in high entropy alloys, *Scr. Mater*. 186 (2020) 392–400. doi:10.1016/j.scriptamat.2020.05.049.
- [19] A.F. Andreoli, J. Orava, P.K. Liaw, H. Weber, M.F. de Oliveira, K. Nielsch, I. Kaban, The elastic-strain energy criterion of phase formation for complex concentrated alloys, *Materialia*. 5 (2019) 100222. doi:10.1016/j.mtla.2019.100222.
- [20] O.N. Senkov, D.B. Miracle, A new thermodynamic parameter to predict formation of solid solution or intermetallic phases in high entropy alloys, *J. Alloys Compd*. 658 (2016) 603–607. doi:10.1016/j.jallcom.2015.10.279.
- [21] Y. Zhang, Y.J. Zhou, Solid Solution Formation Criteria for High Entropy Alloys, *Mater. Sci. Forum*. 561–565 (2007) 1337–1339.  
doi:10.4028/www.scientific.net/MSF.561-565.1337.
- [22] Y. Zhang, Y.J. Zhou, J.P. Lin, G.L. Chen, P.K. Liaw, Solid-Solution Phase Formation Rules for Multi-component Alloys, *Adv. Eng. Mater*. 10 (2008) 534–538. doi:10.1002/adem.200700240.
- [23] A. Takeuchi, A. Inoue, Mixing enthalpy of liquid phase calculated by miedema's scheme and approximated with sub-regular solution model for assessing forming

- ability of amorphous and glassy alloys, *Intermetallics*. 18 (2010) 1779–1789.  
doi:10.1016/j.intermet.2010.06.003.
- [24] S. Guo, C. Ng, J. Lu, C.T. Liu, Effect of valence electron concentration on stability of fcc or bcc phase in high entropy alloys, *J. Appl. Phys.* 109 (2011) 103505.  
doi:10.1063/1.3587228.
- [25] J.M. López, J.A. Alonso, The Atomic Size-Mismatch Contribution to the Enthalpy of Formation of Concentrated Substitutional Metallic Solid Solutions, *Phys. Status Solidi*. 85 (1984) 423–428. doi:10.1002/pssa.2210850211.
- [26] D.A. Porter, K.E. Easterling, M.Y. Sherif, *Phase transformations in metals and alloys*, third edition, 2009.
- [27] I. Toda-Caraballo, P.E.J. Rivera-Díaz-del-Castillo, A criterion for the formation of high entropy alloys based on lattice distortion, *Intermetallics*. 71 (2016) 76–87.  
doi:10.1016/j.intermet.2015.12.011.
- [28] X. Yang, Y. Zhang, Prediction of high-entropy stabilized solid-solution in multi-component alloys, *Mater. Chem. Phys.* 132 (2012) 233–238.  
doi:10.1016/j.matchemphys.2011.11.021.
- [29] M.G. Poletti, L. Battezzati, Electronic and thermodynamic criteria for the occurrence of high entropy alloys in metallic systems, *Acta Mater.* 75 (2014) 297–306. doi:10.1016/j.actamat.2014.04.033.
- [30] S. Fang, X. Xiao, L. Xia, W. Li, Y. Dong, Relationship between the widths of supercooled liquid regions and bond parameters of Mg-based bulk metallic glasses, *J. Non. Cryst. Solids*. 321 (2003) 120–125. doi:10.1016/S0022-3093(03)00155-8.
- [31] Y.F. Ye, C.T. Liu, Y. Yang, A geometric model for intrinsic residual strain and phase stability in high entropy alloys, *Acta Mater.* 94 (2015) 152–161.  
doi:10.1016/j.actamat.2015.04.051.
- [32] A.B. Melnick, V.K. Soolshenko, Thermodynamic design of high-entropy refractory alloys, *J. Alloys Compd.* 694 (2017) 223–227. doi:10.1016/j.jallcom.2016.09.189.
- [33] The Photographic Periodic Table of the Elements, (n.d.).  
<http://periodictable.com/index.html>.
- [34] M.-H.H. Tsai, J.-H.H. Li, A.-C.C. Fan, P.-H.H. Tsai, Incorrect predictions of simple solid solution high entropy alloys: Cause and possible solution, *Scr. Mater.* 127 (2017) 6–9. doi:10.1016/j.scriptamat.2016.08.024.
- [35] J.-M. Joubert, Crystal chemistry and Calphad modeling of the  $\sigma$  phase, *Prog. Mater. Sci.* 53 (2008) 528–583. doi:10.1016/j.pmatsci.2007.04.001.



- [36] T.-T. Shun, C.-H. Hung, C.-F. Lee, Formation of ordered/disordered nanoparticles in FCC high entropy alloys, *J. Alloys Compd.* 493 (2010) 105–109. doi:10.1016/j.jallcom.2009.12.071.
- [37] M.-H. Tsai, K.-Y. Tsai, C.-W. Tsai, C. Lee, C.-C. Juan, J.-W. Yeh, Criterion for Sigma Phase Formation in Cr- and V-Containing High-Entropy Alloys, *Mater. Res. Lett.* 1 (2013) 207–212. doi:10.1080/21663831.2013.831382.
- [38] M.-R. Chen, S.-J. Lin, J.-W. Yeh, M.-H. Chuang, S.-K. Chen, Y.-S. Huang, Effect of vanadium addition on the microstructure, hardness, and wear resistance of Al<sub>0.5</sub>CoCrCuFeNi high-entropy alloy, *Metall. Mater. Trans. A.* 37 (2006) 1363–1369. doi:10.1007/s11661-006-0081-3.
- [39] T.-T. Shun, L.-Y. Chang, M.-H. Shiu, Microstructure and mechanical properties of multiprincipal component CoCrFeNiMo<sub>x</sub> alloys, *Mater. Charact.* 70 (2012) 63–67. doi:10.1016/j.matchar.2012.05.005.
- [40] C.-Y. Hsu, T.-S. Sheu, J.-W. Yeh, S.-K. Chen, Effect of iron content on wear behavior of AlCoCrFexMo<sub>0.5</sub>Ni high-entropy alloys, *Wear.* 268 (2010) 653–659. doi:10.1016/j.wear.2009.10.013.
- [41] K.-C. Hsieh, C.-F. Yu, W.-T. Hsieh, W.-R. Chiang, J.S. Ku, J.-H. Lai, C.-P. Tu, C.C. Yang, The microstructure and phase equilibrium of new high performance high-entropy alloys, *J. Alloys Compd.* 483 (2009) 209–212. doi:10.1016/j.jallcom.2008.08.118.
- [42] X.F. Wang, Y. Zhang, Y. Qiao, G.L. Chen, Novel microstructure and properties of multicomponent CoCrCuFeNiTi<sub>x</sub> alloys, *Intermetallics.* 15 (2007) 357–362. doi:10.1016/j.intermet.2006.08.005.
- [43] Y.L. Chou, J.W. Yeh, H.C. Shih, The effect of molybdenum on the corrosion behaviour of the high-entropy alloys Co<sub>1.5</sub>CrFeNi<sub>1.5</sub>Ti<sub>0.5</sub>Mo<sub>x</sub> in aqueous environments, *Corros. Sci.* 52 (2010) 2571–2581. doi:10.1016/j.corsci.2010.04.004.
- [44] A.K. Singh, A. Subramaniam, On the formation of disordered solid solutions in multi-component alloys, *J. Alloys Compd.* 587 (2014) 113–119. doi:10.1016/j.jallcom.2013.10.133.
- [45] Z. Wang, Y. Huang, Y. Yang, J. Wang, C.T.T. Liu, Atomic-size effect and solid solubility of multicomponent alloys, *Scr. Mater.* 94 (2015) 28–31. doi:10.1016/j.scriptamat.2014.09.010.
- [46] A.K. Singh, N. Kumar, A. Dwivedi, A. Subramaniam, A geometrical parameter for the formation of disordered solid solutions in multi-component alloys,

- Intermetallics. 53 (2014) 112–119. doi:10.1016/j.intermet.2014.04.019.
- [47] Y.F. Ye, Q. Wang, J. Lu, C.T. Liu, Y. Yang, Design of high entropy alloys: A single-parameter thermodynamic rule, *Scr. Mater.* 104 (2015) 53–55. doi:10.1016/j.scriptamat.2015.03.023.
- [48] S. Guo, Q. Hu, C. Ng, C.T. Liu, More than entropy in high-entropy alloys: Forming solid solutions or amorphous phase, *Intermetallics*. 41 (2013) 96–103. doi:10.1016/j.intermet.2013.05.002.
- [49] A.S. Wilson, Formation and effect of topologically close-packed phases in nickel-base superalloys, *Mater. Sci. Technol. (United Kingdom)*. 33 (2017) 1108–1118. doi:10.1080/02670836.2016.1187335.
- [50] H.-L. Chen, H. Mao, Q. Chen, Database development and Calphad calculations for high entropy alloys: Challenges, strategies, and tips, *Mater. Chem. Phys.* 210 (2018) 279–290. doi:10.1016/j.matchemphys.2017.07.082.
- [51] S. Gorsse, O. Senkov, About the Reliability of CALPHAD Predictions in Multicomponent Systems, *Entropy*. 20 (2018) 899. doi:10.3390/e20120899.
- [52] G. Bracq, M. Laurent-Brocq, L. Perrière, R. Pirès, J.-M. Joubert, I. Guillot, The fcc solid solution stability in the Co-Cr-Fe-Mn-Ni multi-component system, *Acta Mater.* 128 (2017) 327–336. doi:10.1016/j.actamat.2017.02.017.
- [53] J.-W. Yeh, Recent progress in high-entropy alloys, *Ann. Chim. Sci. Des Matériaux*. 31 (2006) 633–648. doi:10.3166/acsm.31.633-648.
- [54] H.-P. Chou, Y.-S. Chang, S.-K. Chen, J.-W. Yeh, Microstructure, thermophysical and electrical properties in  $Al_xCoCrFeNi$  ( $0 \leq x \leq 2$ ) high-entropy alloys, *Mater. Sci. Eng. B*. 163 (2009) 184–189. doi:10.1016/j.mseb.2009.05.024.
- [55] J.-W. Yeh, S.-Y. Chang, Y.-D. Hong, S.-K. Chen, S.-J. Lin, Anomalous decrease in X-ray diffraction intensities of Cu–Ni–Al–Co–Cr–Fe–Si alloy systems with multi-principal elements, *Mater. Chem. Phys.* 103 (2007) 41–46. doi:10.1016/j.matchemphys.2007.01.003.
- [56] L.R.R. Owen, E.J.J. Pickering, H.Y.Y. Playford, H.J.J. Stone, M.G.G. Tucker, N.G.G. Jones, An assessment of the lattice strain in the CrMnFeCoNi high-entropy alloy, *Acta Mater.* 122 (2017) 11–18. doi:10.1016/j.actamat.2016.09.032.
- [57] Y. Tong, K. Jin, H. Bei, J.Y.P. Ko, D.C. Pagan, Y. Zhang, F.X. Zhang, Local lattice distortion in NiCoCr, FeCoNiCr and FeCoNiCrMn concentrated alloys investigated by synchrotron X-ray diffraction, *Mater. Des.* 155 (2018) 1–7. doi:10.1016/j.matdes.2018.05.056.

- [58] F.X. Zhang, S. Zhao, K. Jin, H. Xue, G. Velisa, H. Bei, R. Huang, J.Y.P.P. Ko, D.C. Pagan, J.C. Neufeind, W.J. Weber, Y. Zhang, Local Structure and Short-Range Order in a NiCoCr Solid Solution Alloy, *Phys. Rev. Lett.* 118 (2017) 1–6. doi:10.1103/PhysRevLett.118.205501.
- [59] Z. Pei, R. Li, M.C. Gao, G.M. Stocks, Statistics of the NiCoCr medium-entropy alloy: Novel aspects of an old puzzle, *Npj Comput. Mater.* 6 (2020) 122. doi:10.1038/s41524-020-00389-1.
- [60] B. Yin, S. Yoshida, N. Tsuji, W.A. Curtin, Yield strength and misfit volumes of NiCoCr and implications for short-range-order, *Nat. Commun.* 11 (2020) 2507. doi:10.1038/s41467-020-16083-1.
- [61] R. Zhang, S. Zhao, J. Ding, Y. Chong, T. Jia, C. Ophus, M. Asta, R.O. Ritchie, A.M. Minor, Short-range order and its impact on the CrCoNi medium-entropy alloy, *Nature.* 581 (2020) 283–287. doi:10.1038/s41586-020-2275-z.
- [62] S.A. Kube, S. Sohn, D. Uhl, A. Datye, A. Mehta, J. Schroers, Phase selection motifs in High Entropy Alloys revealed through combinatorial methods: Large atomic size difference favors BCC over FCC, *Acta Mater.* 166 (2019) 677–686. doi:10.1016/j.actamat.2019.01.023.
- [63] Y. Tong, S. Zhao, H. Bei, T. Egami, Y. Zhang, F. Zhang, Severe local lattice distortion in Zr- and/or Hf-containing refractory multi-principal element alloys, *Acta Mater.* 183 (2020) 172–181. doi:10.1016/j.actamat.2019.11.026.
- [64] K.-Y. Tsai, M.-H. Tsai, J.-W. Yeh, Sluggish diffusion in Co–Cr–Fe–Mn–Ni high-entropy alloys, *Acta Mater.* 61 (2013) 4887–4897. doi:10.1016/j.actamat.2013.04.058.
- [65] J. Dąbrowa, M. Danielewski, State-of-the-Art Diffusion Studies in the High Entropy Alloys, *Metals (Basel)*. 10 (2020) 347. doi:10.3390/met10030347.
- [66] S. V. Divinski, A. V. Pokoev, N. Esakkiraja, A. Paul, A Mystery of “Sluggish Diffusion” in High-Entropy Alloys: The Truth or a Myth?, *Diffus. Found.* 17 (2018) 69–104. doi:10.4028/www.scientific.net/DF.17.69.
- [67] A. Paul, Comments on “Sluggish diffusion in Co–Cr–Fe–Mn–Ni high-entropy alloys” by K.Y. Tsai, M.H. Tsai and J.W. Yeh, *Acta Materialia* 61 (2013) 4887–4897, *Scr. Mater.* 135 (2017) 153–157. doi:10.1016/j.scriptamat.2017.03.026.
- [68] D. Gaertner, J. Kottke, G. Wilde, S. V. Divinski, Y. Chumlyakov, Tracer diffusion in single crystalline CoCrFeNi and CoCrFeMnNi high entropy alloys, *J. Mater. Res.* 33 (2018) 3184–3191. doi:10.1557/jmr.2018.162.

- [69] J. Kottke, D. Utt, M. Laurent-Brocq, A. Fareed, D. Gaertner, L. Perrière, Ł. Rogal, A. Stukowski, K. Albe, S. V. Divinski, G. Wilde, Experimental and theoretical study of tracer diffusion in a series of (CoCrFeMn) $_{100-x}$ Ni $_x$  alloys, *Acta Mater.* 194 (2020) 236–248. doi:10.1016/j.actamat.2020.05.037.
- [70] M. Vaidya, K.G. Pradeep, B.S. Murty, G. Wilde, S.V. Divinski, Bulk tracer diffusion in CoCrFeNi and CoCrFeMnNi high entropy alloys, *Acta Mater.* 146 (2018) 211–224. doi:10.1016/j.actamat.2017.12.052.
- [71] S. Gorsse, D.B. Miracle, O.N. Senkov, Mapping the world of complex concentrated alloys, *Acta Mater.* 135 (2017) 177–187. doi:10.1016/j.actamat.2017.06.027.
- [72] M. Kang, K. Lim, J. Won, K. Lee, Y. Na, Al-Ti-Containing Lightweight High-Entropy Alloys for Intermediate Temperature Applications, *Entropy.* 20 (2018) 355. doi:10.3390/e20050355.
- [73] K.M. Youssef, A.J. Zaddach, C. Niu, D.L. Irving, C.C. Koch, A Novel Low-Density, High-Hardness, High-entropy Alloy with Close-packed Single-phase Nanocrystalline Structures, *Mater. Res. Lett.* 3 (2015) 95–99. doi:10.1080/21663831.2014.985855.
- [74] R. Feng, M. Gao, C. Lee, M. Mathes, T. Zuo, S. Chen, J. Hawk, Y. Zhang, P. Liaw, Design of Light-Weight High-Entropy Alloys, *Entropy.* 18 (2016) 333. doi:10.3390/e18090333.
- [75] R. Li, J.C. Gao, K. Fan, Study to Microstructure and Mechanical Properties of Mg Containing High Entropy Alloys, *Mater. Sci. Forum.* 650 (2010) 265–271. doi:10.4028/www.scientific.net/MSF.650.265.
- [76] Y.L. Chen, C.W. Tsai, C.C. Juan, M.H. Chuang, J.W. Yeh, T.S. Chin, S.K. Chen, Amorphization of equimolar alloys with HCP elements during mechanical alloying, *J. Alloys Compd.* 506 (2010) 210–215. doi:10.1016/j.jallcom.2010.06.179.
- [77] I. Basu, J.T.M. De Hosson, Strengthening mechanisms in high entropy alloys: Fundamental issues, *Scr. Mater.* 187 (2020) 148–156. doi:10.1016/j.scriptamat.2020.06.019.
- [78] M. Koyama, Twinning-Induced Plasticity (TWIP) Steel, in: *Ref. Modul. Mater. Sci. Mater. Eng.*, Elsevier, 2020: pp. 1–12. doi:10.1016/B978-0-12-819726-4.00067-3.
- [79] L. Remy, A. Pineau, Twinning and strain-induced F.C.C.  $\rightarrow$  H.C.P. transformation in the Fe-Mn-Cr-C system, *Mater. Sci. Eng.* 28 (1977) 99–107. doi:10.1016/0025-5416(77)90093-3.
- [80] D. Wei, X. Li, J. Jiang, W. Heng, Y. Koizumi, W.-M. Choi, B.-J. Lee, H.S. Kim, H.

- Kato, A. Chiba, Novel Co-rich high performance twinning-induced plasticity (TWIP) and transformation-induced plasticity (TRIP) high-entropy alloys, *Scr. Mater.* 165 (2019) 39–43. doi:10.1016/j.scriptamat.2019.02.018.
- [81] Z. Li, K.G. Pradeep, Y. Deng, D. Raabe, C.C. Tasan, Metastable high-entropy dual-phase alloys overcome the strength–ductility trade-off, *Nature*. 534 (2016) 227–230. doi:10.1038/nature17981.
- [82] J. Su, D. Raabe, Z. Li, Hierarchical microstructure design to tune the mechanical behavior of an interstitial TRIP-TWIP high-entropy alloy, *Acta Mater.* 163 (2019) 40–54. doi:10.1016/j.actamat.2018.10.017.
- [83] Y. Deng, C.C. Tasan, K.G. Pradeep, H. Springer, A. Kostka, D. Raabe, Design of a twinning-induced plasticity high entropy alloy, *Acta Mater.* 94 (2015) 124–133. doi:10.1016/j.actamat.2015.04.014.
- [84] D. Liang, C. Zhao, W. Zhu, P. Wei, F. Jiang, Y. Zhang, Q. Sun, F. Ren, Overcoming the strength-ductility trade-off via the formation of nanoscale Cr-rich precipitates in an ultrafine-grained FCC CrFeNi medium entropy alloy matrix, *Mater. Sci. Eng. A.* 762 (2019) 138107. doi:10.1016/j.msea.2019.138107.
- [85] S.W.W. Wu, G. Wang, Y.D.D. Jia, J. Yi, Q.J.J. Zhai, C.T.T. Liu, B.A.A. Sun, H.J.J. Chu, J. Shen, P.K.K. Liaw, T.Y.Y. Zhang, Q. Wang, Y.D.D. Jia, J. Yi, Q.J.J. Zhai, J.B. Liu, B.A.A. Sun, H.J.J. Chu, J. Shen, P.K.K. Liaw, C.T.T. Liu, T.Y.Y. Zhang, Enhancement of strength-ductility trade-off in a high-entropy alloy through a heterogeneous structure, *Acta Mater.* 165 (2019) 444–458. doi:10.1016/j.actamat.2018.12.012.
- [86] T. Lu, T. He, P. Zhao, K. Sun, A.F. Andreoli, H. Chen, W. Chen, Z. Fu, S. Scudino, Fine tuning in-synch the mechanical and magnetic properties of FeCoNiAl<sub>0.25</sub>Mn<sub>0.25</sub> high-entropy alloy through cold rolling and annealing treatment, *J. Mater. Process. Technol.* 289 (2021) 116945. doi:10.1016/j.jmatprotec.2020.116945.
- [87] C. Zhang, C. Zhu, T. Harrington, K. Vecchio, Design of non-equiatomic high entropy alloys with heterogeneous lamella structure towards strength-ductility synergy, *Scr. Mater.* 154 (2018) 78–82. doi:10.1016/j.scriptamat.2018.05.020.
- [88] S.R. Reddy, S. Yoshida, U. Sunkari, A. Lozinko, J. Joseph, R. Saha, D. Fabijanic, S. Guo, P.P. Bhattacharjee, N. Tsuji, Engineering heterogeneous microstructure by severe warm-rolling for enhancing strength-ductility synergy in eutectic high entropy alloys, *Mater. Sci. Eng. A.* 764 (2019) 138226. doi:10.1016/j.msea.2019.138226.

- [89] B. Gludovatz, A. Hohenwarter, D. Catoor, E.H. Chang, E.P. George, R.O. Ritchie, A fracture-resistant high-entropy alloy for cryogenic applications, *Science* (80-. ). 345 (2014) 1153–1158. doi:10.1126/science.1254581.
- [90] R.O. Ritchie, The conflicts between strength and toughness, *Nat. Mater.* 10 (2011) 817–822. doi:10.1038/nmat3115.
- [91] Z. Wu, H. Bei, G.M. Pharr, E.P. George, Temperature dependence of the mechanical properties of equiatomic solid solution alloys with face-centered cubic crystal structures, *Acta Mater.* 81 (2014) 428–441. doi:10.1016/j.actamat.2014.08.026.
- [92] B. Gludovatz, A. Hohenwarter, K.V.S. Thurston, H. Bei, Z. Wu, E.P. George, R.O. Ritchie, Exceptional damage-tolerance of a medium-entropy alloy CrCoNi at cryogenic temperatures, *Nat. Commun.* 7 (2016) 10602. doi:10.1038/ncomms10602.
- [93] M. Schneider, G. Laplanche, Effects of temperature on mechanical properties and deformation mechanisms of the equiatomic CrFeNi medium-entropy alloy, *Acta Mater.* 204 (2021) 116470. doi:10.1016/j.actamat.2020.11.012.
- [94] J. Chen, X. Zhou, W. Wang, B. Liu, Y. Lv, W. Yang, D. Xu, Y. Liu, A review on fundamental of high entropy alloys with promising high-temperature properties, *J. Alloys Compd.* 760 (2018) 15–30. doi:10.1016/j.jallcom.2018.05.067.
- [95] O.N. Senkov, G.B. Wilks, D.B. Miracle, C.P. Chuang, P.K. Liaw, Refractory high-entropy alloys, *Intermetallics.* 18 (2010) 1758–1765. doi:10.1016/j.intermet.2010.05.014.
- [96] O.N. Senkov, G.B. Wilks, J.M. Scott, D.B. Miracle, Mechanical properties of Nb<sub>25</sub>Mo<sub>25</sub>Ta<sub>25</sub>W<sub>25</sub> and V<sub>20</sub>Nb<sub>20</sub>Mo<sub>20</sub>Ta<sub>20</sub>W<sub>20</sub> refractory high entropy alloys, *Intermetallics.* 19 (2011) 698–706. doi:10.1016/j.intermet.2011.01.004.
- [97] O.N. Senkov, D.B. Miracle, K.J. Chaput, J.P. Couzinie, Development and exploration of refractory high entropy alloys - A review, *J. Mater. Res.* 33 (2018) 3092–3128. doi:10.1557/jmr.2018.153.
- [98] O.N. Senkov, S.V. Senkova, C. Woodward, Effect of aluminum on the microstructure and properties of two refractory high-entropy alloys, *Acta Mater.* 68 (2014) 214–228. doi:10.1016/j.actamat.2014.01.029.
- [99] V. Soni, B. Gwalani, T. Alam, S. Dasari, Y. Zheng, O.N. Senkov, D. Miracle, R. Banerjee, Phase inversion in a two-phase, BCC+B2, refractory high entropy alloy, *Acta Mater.* 185 (2020) 89–97. doi:10.1016/j.actamat.2019.12.004.
- [100] O.N. Senkov, J.K. Jensen, A.L. Pilchak, D.B. Miracle, H.L. Fraser, Compositional

- variation effects on the microstructure and properties of a refractory high-entropy superalloy  $\text{AlMo}_{0.5}\text{NbTa}_{0.5}\text{TiZr}$ , *Mater. Des.* 139 (2018) 498–511.  
doi:10.1016/j.matdes.2017.11.033.
- [101] D.B. Miracle, M.-H.H. Tsai, O.N. Senkov, V. Soni, R. Banerjee, Refractory high entropy superalloys (RSAs), *Scr. Mater.* 187 (2020) 445–452.  
doi:10.1016/j.scriptamat.2020.06.048.
- [102] O.N. Senkov, D.B. Miracle, K.J. Chaput, J.-P. Couzinie, Development and exploration of refractory high entropy alloys—A review, *J. Mater. Res.* 33 (2018) 1–37. doi:10.1557/jmr.2018.153.
- [103] O.N. Senkov, J.M. Scott, S.V. Senkova, D.B. Miracle, C.F. Woodward, Microstructure and room temperature properties of a high-entropy TaNbHfZrTi alloy, *J. Alloys Compd.* 509 (2011) 6043–6048. doi:10.1016/j.jallcom.2011.02.171.
- [104] V. Soni, O.N. Senkov, B. Gwalani, D.B. Miracle, R. Banerjee, Microstructural Design for Improving Ductility of An Initially Brittle Refractory High Entropy Alloy, *Sci. Rep.* 8 (2018) 8816. doi:10.1038/s41598-018-27144-3.
- [105] X. Fu, C.A. Schuh, E.A. Olivetti, Materials selection considerations for high entropy alloys, *Scr. Mater.* 138 (2017) 145–150. doi:10.1016/j.scriptamat.2017.03.014.
- [106] X. Yan, Y. Zhang, Functional properties and promising applications of high entropy alloys, *Scr. Mater.* 187 (2020) 188–193. doi:10.1016/j.scriptamat.2020.06.017.
- [107] T. Zuo, M.C. Gao, L. Ouyang, X. Yang, Y. Cheng, R. Feng, S. Chen, P.K. Liaw, J.A. Hawk, Y. Zhang, Tailoring magnetic behavior of  $\text{CoFeMnNiX}$  ( $X = \text{Al, Cr, Ga, and Sn}$ ) high entropy alloys by metal doping, *Acta Mater.* 130 (2017) 10–18.  
doi:10.1016/j.actamat.2017.03.013.
- [108] Z. Rao, B. Dutta, F. Körmann, W. Lu, X. Zhou, C. Liu, A.K. Silva, U. Wiedwald, M. Spasova, M. Farle, D. Ponge, B. Gault, J. Neugebauer, D. Raabe, Z. Li, Beyond Solid Solution High-Entropy Alloys: Tailoring Magnetic Properties via Spinodal Decomposition, *Adv. Funct. Mater.* 31 (2021) 2007668.  
doi:10.1002/adfm.202007668.
- [109] K. Zhang, Z. Fu, Effects of annealing treatment on phase composition and microstructure of  $\text{CoCrFeNiTiAl}_x$  high-entropy alloys, *Intermetallics.* 22 (2012) 24–32. doi:10.1016/j.intermet.2011.10.010.
- [110] J.M. Anirudha Karati, and B.S.M. Soumyaranajan Mishra, Functional Properties of High Entropy Alloys, in: T. S. Srivatsan and Manoj Gupta (Ed.), *High Entropy Alloy. Innov. Adv. Appl.*, First edit, CRC Press, Boca Raton, 2002: p. 733.

- [111] L. Xue, L. Shao, Q. Luo, B. Shen, Gd<sub>25</sub>RE<sub>25</sub>Co<sub>25</sub>Al<sub>25</sub> (RE = Tb, Dy and Ho) high-entropy glassy alloys with distinct spin-glass behavior and good magnetocaloric effect, *J. Alloys Compd.* 790 (2019) 633–639. doi:10.1016/j.jallcom.2019.03.210.
- [112] J. Li, L. Xue, W. Yang, C. Yuan, J. Huo, B. Shen, Distinct spin glass behavior and excellent magnetocaloric effect in Er<sub>20</sub>Dy<sub>20</sub>Co<sub>20</sub>Al<sub>20</sub>RE<sub>20</sub> (RE = Gd, Tb and Tm) high-entropy bulk metallic glasses, *Intermetallics*. 96 (2018) 90–93. doi:10.1016/j.intermet.2018.03.002.
- [113] J. Huo, L. Huo, J. Li, H. Men, X. Wang, A. Inoue, C. Chang, J.-Q. Wang, R.-W. Li, High-entropy bulk metallic glasses as promising magnetic refrigerants, *J. Appl. Phys.* 117 (2015) 073902. doi:10.1063/1.4908286.
- [114] J. Huo, L. Huo, H. Men, X. Wang, A. Inoue, J. Wang, C. Chang, R.-W. Li, The magnetocaloric effect of Gd-Tb-Dy-Al-M (M = Fe, Co and Ni) high-entropy bulk metallic glasses, *Intermetallics*. 58 (2015) 31–35. doi:10.1016/j.intermet.2014.11.004.
- [115] W. Sheng, J.-Q. Wang, G. Wang, J. Huo, X. Wang, R.-W. Li, Amorphous microwires of high entropy alloys with large magnetocaloric effect, *Intermetallics*. 96 (2018) 79–83. doi:10.1016/j.intermet.2018.02.015.
- [116] Y. Yuan, Y. Wu, X. Tong, H. Zhang, H. Wang, X.J. Liu, L. Ma, H.L. Suo, Z.P. Lu, Rare-earth high-entropy alloys with giant magnetocaloric effect, *Acta Mater.* 125 (2017) 481–489. doi:10.1016/j.actamat.2016.12.021.
- [117] J. Huo, J.-Q. Wang, W.-H. Wang, Denary high entropy metallic glass with large magnetocaloric effect, *J. Alloys Compd.* 776 (2019) 202–206. doi:10.1016/j.jallcom.2018.10.328.
- [118] S.-M. Na, P.K. Lambert, H. Kim, J. Paglione, N.J. Jones, Thermomagnetic properties and magnetocaloric effect of FeCoNiCrAl-type high-entropy alloys, *AIP Adv.* 9 (2019) 035010. doi:10.1063/1.5079394.
- [119] A. Perrin, M. Sorescu, M.-T. Burton, D.E. Laughlin, M. McHenry, The Role of Compositional Tuning of the Distributed Exchange on Magnetocaloric Properties of High-Entropy Alloys, *JOM*. 69 (2017) 2125–2129. doi:10.1007/s11837-017-2523-3.
- [120] M. Kurniawan, A. Perrin, P. Xu, V. Keylin, M. McHenry, Curie Temperature Engineering in High Entropy Alloys for Magnetocaloric Applications, *IEEE Magn. Lett.* 7 (2016) 1–5. doi:10.1109/LMAG.2016.2592462.
- [121] Y.-F. Kao, S.-K. Chen, J.-H. Sheu, J.-T. Lin, W.-E. Lin, J.-W. Yeh, S.-J. Lin, T.-H.



- Liou, C.-W. Wang, Hydrogen storage properties of multi-principal-component CoFeMnTi<sub>x</sub>VyZr<sub>z</sub> alloys, *Int. J. Hydrogen Energy*. 35 (2010) 9046–9059.  
doi:10.1016/j.ijhydene.2010.06.012.
- [122] K.-H. Young, J. Nei, C. Wan, R. Denys, V. Yartys, Comparison of C14- and C15-Predominated AB<sub>2</sub> Metal Hydride Alloys for Electrochemical Applications, *Batteries*. 3 (2017) 22. doi:10.3390/batteries3030022.
- [123] R.B. Strozi, D.R. Leiva, G. Zepon, W.J. Botta, J. Huot, Effects of the Chromium Content in (TiVNb)<sub>100-x</sub>Cr<sub>x</sub> Body-Centered Cubic High Entropy Alloys Designed for Hydrogen Storage Applications, *Energies*. 14 (2021) 3068.  
doi:10.3390/en14113068.
- [124] C. Zlotea, M.A. Sow, G. Ek, J.-P. Couzinié, L. Perrière, I. Guillot, J. Bourgon, K.T. Møller, T.R. Jensen, E. Akiba, M. Sahlberg, Hydrogen sorption in TiZrNbHfTa high entropy alloy, *J. Alloys Compd.* 775 (2019) 667–674.  
doi:10.1016/j.jallcom.2018.10.108.
- [125] H. Jiang, R.I. Gomez-Abal, P. Rinke, M. Scheffler, Electronic band structure of zirconia and hafnia polymorphs from the GW perspective, *Phys. Rev. B*. 81 (2010) 085119. doi:10.1103/PhysRevB.81.085119.
- [126] O. Muck, Method of and devices for melting materials, in particular conductive materials, by means of induced electric currents, Patent number: 422004, 1923.
- [127] E.C. Okress, D.M. Wroughton, G. Comenetz, P.H. Brace, J.C.R. Kelly, Electromagnetic Levitation of Solid and Molten Metals, *J. Appl. Phys.* 23 (1952) 545–552. doi:10.1063/1.1702249.
- [128] D.M. Herlach, D.M. Matson, *Solidification of Containerless Undercooled Melts*, Wiley-VCH Verlag GmbH & Co. KGaA, Weinheim, Germany, 2012.  
doi:10.1002/9783527647903.
- [129] P. R. Rony, *The Electromagnetic Levitation of Metals*, Berkeley, 1964.  
[https://digital.library.unt.edu/ark:/67531/metadc865504/m2/1/high\\_res\\_d/4035813.pdf](https://digital.library.unt.edu/ark:/67531/metadc865504/m2/1/high_res_d/4035813.pdf).
- [130] A.F. Andreoli, O. Shuleshova, V.T. Witusiewicz, Y. Wu, Y. Yang, O. Ivashko, A.-C. Dippel, M. v. Zimmermann, K. Nielsch, I. Kaban, In situ study of non-equilibrium solidification of CoCrFeNi high-entropy alloy and CrFeNi and CoCrNi ternary suballoys, *Acta Mater.* 212 (2021) 116880.  
doi:10.1016/j.actamat.2021.116880.
- [131] A.P. Hammersley, S.O. Svensson, M. Hanfland, A.N. Fitch, D. Hausermann, D.

- Häusermann, Two-dimensional detector software: From real detector to idealised image or two-theta scan, *High Press. Res.* 14 (1996) 235–248.  
doi:10.1080/08957959608201408.
- [132] T. Degen, M. Sadki, E. Bron, U. König, G. Nénert, The high score suite, in: *Powder Diffr.*, 2014. doi:10.1017/S0885715614000840.
- [133] T.J.B. Holland, S.A.T. Redfern, UNITCELL: A nonlinear least-squares program for cell-parameter refinement implementing regression and deletion diagnostics, *J. Appl. Crystallogr.* (1997). doi:10.1107/S0021889896011673.
- [134] J. Thomas, T. Gemming, ELDISCA C# — a new version of the program for identifying electron diffraction patterns, in: W.T. Luysberg M., Tillmann K. (Ed.), *EMC 2008 14th Eur. Microsc. Congr.* 1–5 Sept. 2008, Aachen, Ger., Springer Berlin Heidelberg, Berlin, Heidelberg, 2008: pp. 231–232. doi:10.1007/978-3-540-85156-1\_116.
- [135] ASTM E 1269-11, Standard Test Method for Determining Specific Heat Capacity by Differential Scanning Calorimetry, *Am. Soc. Test. Mater.* (2011).
- [136] W.-L.W.-R. Wang, W.-L.W.-R. Wang, S.-C. Wang, Y.-C. Tsai, C.-H. Lai, J.-W. Yeh, Effects of Al addition on the microstructure and mechanical property of  $\text{Al}_x\text{CoCrFeNi}$  high-entropy alloys, *Intermetallics*. 26 (2012) 44–51.  
doi:10.1016/j.intermet.2012.03.005.
- [137] M.S. Lucas, G.B. Wilks, L. Mauger, J.A. Muñoz, O.N. Senkov, E. Michel, J. Horwath, S.L. Semiatin, M.B. Stone, D.L. Abernathy, E. Karapetrova, Absence of long-range chemical ordering in equimolar  $\text{FeCoCrNi}$ , *Appl. Phys. Lett.* 100 (2012) 251907. doi:10.1063/1.4730327.
- [138] Z. Wu, H. Bei, F. Otto, G.M.M. Pharr, E.P.P. George, Recovery, recrystallization, grain growth and phase stability of a family of FCC-structured multi-component equiatomic solid solution alloys, *Intermetallics*. 46 (2014) 131–140.  
doi:10.1016/j.intermet.2013.10.024.
- [139] Y. Brif, M. Thomas, I. Todd, The use of high-entropy alloys in additive manufacturing, *Scr. Mater.* 99 (2015) 93–96. doi:10.1016/j.scriptamat.2014.11.037.
- [140] W. Huo, F. Fang, X. Liu, S. Tan, Z. Xie, J. Jiang, Remarkable strain-rate sensitivity of nanotwinned  $\text{CoCrFeNi}$  alloys, *Appl. Phys. Lett.* 114 (2019) 101904.  
doi:10.1063/1.5088921.
- [141] U. Dahlborg, J. Cornide, M. Calvo-Dahlborg, T.C. Hansen, A. Fitch, Z. Leong, S. Chambreland, R. Goodall, Structure of some  $\text{CoCrFeNi}$  and  $\text{CoCrFeNiPd}$

- multicomponent HEA alloys by diffraction techniques, *J. Alloys Compd.* 681 (2016) 330–341. doi:10.1016/j.jallcom.2016.04.248.
- [142] F. He, Z. Wang, Q. Wu, J. Li, J. Wang, C.T.T. Liu, Phase separation of metastable CoCrFeNi high entropy alloy at intermediate temperatures, *Scr. Mater.* 126 (2017) 15–19. doi:10.1016/j.scriptamat.2016.08.008.
- [143] K.A. Christofidou, E.J. Pickering, P. Orsatti, P.M. Mignanelli, T.J.A. Slater, H.J. Stone, N.G. Jones, On the influence of Mn on the phase stability of the CrMn<sub>x</sub>FeCoNi high entropy alloys, *Intermetallics*. 92 (2018) 84–92. doi:10.1016/j.intermet.2017.09.011.
- [144] G. Laplanche, P. Gadaud, C. Bärsch, K. Demtröder, C. Reinhart, J. Schreuer, E.P. George, Elastic moduli and thermal expansion coefficients of medium-entropy subsystems of the CrMnFeCoNi high-entropy alloy, *J. Alloys Compd.* 746 (2018) 244–255. doi:10.1016/j.jallcom.2018.02.251.
- [145] J. Li, W. Jia, J. Wang, H. Kou, D. Zhang, E. Beaugnon, Enhanced mechanical properties of a CoCrFeNi high entropy alloy by supercooling method, *Mater. Des.* 95 (2016) 183–187. doi:10.1016/j.matdes.2016.01.112.
- [146] J. Wang, T. Guo, J. Li, W. Jia, H. Kou, Microstructure and mechanical properties of non-equilibrium solidified CoCrFeNi high entropy alloy, *Mater. Chem. Phys.* 210 (2018) 192–196. doi:10.1016/j.matchemphys.2017.06.037.
- [147] J. Zhang, X. Li, Y. Zhang, F. Zhang, H. Wu, X. zong Wang, Q. Zhou, H. Wang, Sluggish dendrite growth in an undercooled high entropy alloy, *Intermetallics*. 119 (2020) 106714. doi:10.1016/j.intermet.2020.106714.
- [148] S. Wang, X.F. Yao, Y.Q. Su, Y.J. Ma, High temperature image correction in DIC measurement due to thermal radiation, *Meas. Sci. Technol.* 26 (2015) 095006. doi:10.1088/0957-0233/26/9/095006.
- [149] J. Schindelin, I. Arganda-Carreras, E. Frise, V. Kaynig, M. Longair, T. Pietzsch, S. Preibisch, C. Rueden, S. Saalfeld, B. Schmid, J.-Y. Tinevez, D.J. White, V. Hartenstein, K. Eliceiri, P. Tomancak, A. Cardona, Fiji: an open-source platform for biological-image analysis, *Nat. Methods*. 9 (2012) 676–682. doi:10.1038/nmeth.2019.
- [150] J.E. Rodriguez, C. Kreischer, T. Volkmann, D.M. Matson, Solidification velocity of undercooled Fe-Co alloys, *Acta Mater.* 122 (2017) 431–437. doi:10.1016/j.actamat.2016.09.047.
- [151] R. Hermann, W. Löser, H.G. Lindenkreuz, W. Yang-Bitterlich, C. Michel, A.

- Diefenbach, S. Schneider, W. Dreier, Metastable phase formation in undercooled Fe-Co melts under terrestrial and parabolic flight conditions, *Microgravity Sci. Technol.* 19 (2007) 5–10. doi:10.1007/BF02870982.
- [152] T. Koseki, M.C. Flemings, Solidification of undercooled Fe-Cr-Ni alloys: Part I. Thermal behavior, *Metall. Mater. Trans. A.* 26 (1995) 2991–2999. doi:10.1007/BF02669655.
- [153] D.M. Matson, Growth Competition During Double Recalescence in Fe-Cr-Ni Alloys, *MRS Proc.* 551 (1998) 227–234. doi:10.1557/proc-551-227.
- [154] D.M. Matson, X. Xiao, J.E. Rodriguez, J. Lee, R.W. Hyers, O. Shuleshova, I. Kaban, S. Schneider, C. Karrasch, S. Burggraff, R. Wunderlich, H.-J.J. Fecht, Use of Thermophysical Properties to Select and Control Convection During Rapid Solidification of Steel Alloys Using Electromagnetic Levitation on the Space Station, *Jom.* 69 (2017) 1311–1318. doi:10.1007/s11837-017-2396-5.
- [155] T. Volkman, W. Löser, D.M. Herlach, W. Löser, Nucleation and phase selection in undercooled Fe-Cr-Ni melts: Part II. Containerless solidification experiments, *Metall. Mater. Trans. A Phys. Metall. Mater. Sci.* 28 (1997) 461–469. doi:10.1007/s11661-997-0147-x.
- [156] K. Eckler, F. Gärtner, H. Assadi, A.F.F. Norman, A.L.L. Greer, D.M.M. Herlach, Phase selection, growth, and interface kinetics in undercooled Fe-Ni melt droplets, *Mater. Sci. Eng. A.* 226–228 (1997) 410–414. doi:10.1016/S0921-5093(96)10654-7.
- [157] P.R. ten Wolde, M.J. Ruiz-Montero, D. Frenkel, Numerical Evidence for bcc Ordering at the Surface of a Critical fcc Nucleus, *Phys. Rev. Lett.* 75 (1995) 2714–2717. doi:10.1103/PhysRevLett.75.2714.
- [158] W.C. Swope, H.C. Andersen,  $10^6$ -particle molecular-dynamics study of homogeneous nucleation of crystals in a supercooled atomic liquid -particle molecular-dynamics study of homogeneous nucleation of crystals in a supercooled atomic liquid, *Phys. Rev. B.* 41 (1990) 7042–7054. doi:10.1103/PhysRevB.41.7042.
- [159] S. Tang, J.C. Wang, B. Svendsen, D. Raabe, Competitive bcc and fcc crystal nucleation from non-equilibrium liquids studied by phase-field crystal simulation, *Acta Mater.* 139 (2017) 196–204. doi:10.1016/j.actamat.2017.08.015.
- [160] M. Li, S. Ozawa, K. Kuribayashi, On determining the phase-selection principle in solidification from undercooled melts - Competitive nucleation or competitive growth?, *Philos. Mag. Lett.* 84 (2004) 483–493. doi:10.1080/0950083042000271090.

- [161] T. Volkman, W. Löser, D.M. Herlach, W. Löser, Nucleation and phase selection in undercooled Fe-Cr-Ni melts: Part I. Theoretical analysis of nucleation behavior, *Metall. Mater. Trans. A*. 28 (1997) 453–460. doi:10.1007/s11661-997-0146-y.
- [162] D. Turnbull, Formation of Crystal Nuclei in Liquid Metals, *J. Appl. Phys.* 21 (1950) 1022–1028. doi:10.1063/1.1699435.
- [163] L. Gránásy, Diffuse interface theory of nucleation, *J. Non. Cryst. Solids*. 162 (1993) 301–303. doi:10.1016/0022-3093(93)91250-7.
- [164] T. Koseki, M.C. Flemings, Solidification of undercooled Fe-Cr-Ni alloys: Part II. Microstructural evolution, *Metall. Mater. Trans. A Phys. Metall. Mater. Sci.* 27 (1996) 3226–3240. doi:10.1007/BF02663873.
- [165] M.J. Aziz, Model for solute redistribution during rapid solidification, *J. Appl. Phys.* 53 (1982) 1158–1168. doi:10.1063/1.329867.
- [166] S.L. Sobolev, Local non-equilibrium diffusion model for solute trapping during rapid solidification, *Acta Mater.* 60 (2012) 2711–2718. doi:10.1016/j.actamat.2012.01.036.
- [167] K. Eckler, R.F. Cochrane, D.M. Herlach, B. Feuerbacher, M. Jurisch, Evidence for a transition from diffusion-controlled to thermally controlled solidification in metallic alloys, *Phys. Rev. B*. 45 (1992) 5019–5022. doi:10.1103/PhysRevB.45.5019.
- [168] Thermo-Calc AB Software, (2020). <https://thermocalc.com/>.
- [169] Steel and Fe-Alloys Database, (2020). <https://thermocalc.com/products/databases/steel-and-fe-alloys/>.
- [170] O. Stryzhyboroda, V.T. Witusiewicz, S. Gein, D. Röhrens, U. Hecht, Phase Equilibria in the Al–Co–Cr–Fe–Ni High Entropy Alloy System: Thermodynamic Description and Experimental Study, *Front. Mater.* 7 (2020). doi:10.3389/fmats.2020.00270.
- [171] W.J. Boettinger, U.R. Kattner, K.-W. Moon, J.H. Perepezko, DTA and heat-flux dsc measurements of alloy melting and freezing, in: J.-C. Zhao (Ed.), *Methods Phase Diagr. Determ.*, Elsevier, 2007: pp. 151–221. doi:10.1016/B978-008044629-5/50005-7.
- [172] M. Barth, K. Eckler, D.M.M. Herlach, H. Alexander, Rapid crystal growth in undercooled FeNi melts, *Mater. Sci. Eng. A*. 133 (1991) 790–794. doi:10.1016/0921-5093(91)90187-R.
- [173] D.M. Matson, Retained free energy as a driving force for phase transformation during rapid solidification of stainless steel alloys in microgravity, *Npj*

- Microgravity. 4 (2018) 22. doi:10.1038/s41526-018-0056-x.
- [174] B. Chalmers, Principles of Solidification, in: Appl. Solid State Phys., 1970. doi:10.1007/978-1-4684-1854-5\_5.
- [175] G. Horvay, The tension field created by a spherical nucleus freezing into its less dense undercooled melt, Int. J. Heat Mass Transf. (1965). doi:10.1016/0017-9310(65)90110-9.
- [176] L. Feng, Y. Gencang, G. Xuefeng, Research of grain refinement in undercooled DD3 single crystal superalloy, Mater. Sci. Eng. A. 311 (2001) 54–63. doi:10.1016/S0921-5093(01)00932-7.
- [177] D.M. Herlach, K. Eckler, A. Karma, M. Schwarz, Grain refinement through fragmentation of dendrites in undercooled melts, Mater. Sci. Eng. A. 304–306 (2001) 20–25. doi:10.1016/S0921-5093(00)01553-7.
- [178] A.M. Mullis, R.F. Cochrane, Spontaneous grain refinement in alloy systems at low undercooling, Mater. Sci. Eng. A. 304–306 (2001) 267–271. doi:10.1016/S0921-5093(00)01521-5.
- [179] M. Schwarz, A. Karma, K. Eckler, D.M. Herlach, Physical Mechanism of Grain Refinement in Solidification of Undercooled Melts, Phys. Rev. Lett. 73 (1994) 1380–1383. doi:10.1103/PhysRevLett.73.1380.
- [180] H. Wang, F. Liu, Y. Tan, Modeling grain refinement for undercooled single-phase solid-solution alloys, Acta Mater. 59 (2011) 4787–4797. doi:10.1016/j.actamat.2011.04.021.
- [181] S.A.A. Moir, K. Eckler, D.M.M. Herlach, Evolution of microstructures resulting from dendrite growth in undercooled Fe–Cr–Ni melts, Acta Mater. 46 (1998) 4029–4036. doi:10.1016/S1359-6454(98)00057-3.
- [182] A.M. Mullis, E.G. Castle, R.F. Cochrane, The origins of spontaneous grain refinement in deeply undercooled metallic melts, IOP Conf. Ser. Mater. Sci. Eng. 117 (2016) 155–167. doi:10.1088/1757-899X/117/1/012054.
- [183] R. Rahimi, H. Biermann, O. Volkova, J. Mola, On the origin of subgrain boundaries during conventional solidification of austenitic stainless steels, IOP Conf. Ser. Mater. Sci. Eng. 373 (2018) 012005. doi:10.1088/1757-899X/373/1/012005.
- [184] M. Li, T. Ishikawa, K. Nagashio, K. Kuribayashi, S. Yoda, A comparative EBSD study of microstructure and microtexture formation from undercooled Ni<sub>99</sub>B<sub>1</sub> melts solidified on an electrostatic levitator and an electromagnetic levitator, Acta Mater. 54 (2006) 3791–3799. doi:10.1016/j.actamat.2006.04.010.

- [185] W. Wu, M. Song, S. Ni, J. Wang, Y. Liu, B. Liu, X. Liao, Dual mechanisms of grain refinement in a FeCoCrNi high-entropy alloy processed by high-pressure torsion, *Sci. Rep.* 7 (2017) 46720. doi:10.1038/srep46720.
- [186] Y.-F. Kao, T.-J. Chen, S.-K. Chen, J.-W. Yeh, Microstructure and mechanical property of as-cast, -homogenized, and -deformed  $Al_xCoCrFeNi$  ( $0 \leq x \leq 2$ ) high-entropy alloys, *J. Alloys Compd.* 488 (2009) 57–64. doi:10.1016/j.jallcom.2009.08.090.
- [187] Y. Ma, B. Jiang, C. Li, Q. Wang, C. Dong, P. Liaw, F. Xu, L. Sun, The BCC/B2 Morphologies in  $Al_xNiCoFeCr$  High-Entropy Alloys, *Metals (Basel)*. 7 (2017) 57. doi:10.3390/met7020057.
- [188] X. Wang, W. Zhou, P. Liu, S. Song, K.M. Reddy, Atomic scale structural characterization of B2 phase precipitated along FCC twin boundary in a CoCrFeNiAl<sub>0.3</sub> high entropy alloy, *Scr. Mater.* 162 (2019) 161–165. doi:10.1016/j.scriptamat.2018.11.016.
- [189] T.T. Shun, Y.C. Du, Microstructure and tensile behaviors of FCC Al<sub>0.3</sub>CoCrFeNi high entropy alloy, *J. Alloys Compd.* 479 (2009) 157–160. doi:10.1016/j.jallcom.2008.12.088.
- [190] S. Gangireddy, B. Gwalani, K. Liu, R. Banerjee, R.S. Mishra, Microstructures with extraordinary dynamic work hardening and strain rate sensitivity in Al<sub>0.3</sub>CoCrFeNi high entropy alloy, *Mater. Sci. Eng. A.* 734 (2018) 42–50. doi:10.1016/j.msea.2018.07.088.
- [191] Q. Tang, Y. Huang, H. Cheng, X. Liao, T.G. Langdon, P. Dai, The effect of grain size on the annealing-induced phase transformation in an Al<sub>0.3</sub>CoCrFeNi high entropy alloy, *Mater. Des.* 105 (2016) 381–385. doi:10.1016/j.matdes.2016.05.079.
- [192] S. Gangireddy, B. Gwalani, V. Soni, R. Banerjee, R.S. Mishra, Contrasting mechanical behavior in precipitation hardenable  $Al_xCoCrFeNi$  high entropy alloy microstructures: Single phase FCC vs. dual phase FCC-BCC, *Mater. Sci. Eng. A.* 739 (2019) 158–166. doi:10.1016/j.msea.2018.10.021.
- [193] E.A. Anber, A.C. Lang, E.A. Lass, P.K. Suri, J.L. Hart, D.S. D’Antuono, H. Diao, R. Feng, R. Doherty, P.K. Liaw, M.L. Taheri, Insight into the kinetic stabilization of Al<sub>0.3</sub>CoCrFeNi high-entropy alloys, *Materialia*. 14 (2020) 100872. doi:10.1016/j.mtla.2020.100872.
- [194] G. Liu, L. Liu, X. Liu, Z. Wang, Z. Han, G. Zhang, A. Kostka, Microstructure and mechanical properties of Al<sub>0.7</sub>CoCrFeNi high-entropy-alloy prepared by directional

- solidification, *Intermetallics*. 93 (2018) 93–100. doi:10.1016/j.intermet.2017.11.019.
- [195] L. Ma, Z. Gao, S. Hu, Z. Zeng, J. Xu, J. Wang, Effect of cooling rate on microstructure and mechanical properties of Al<sub>0.3</sub>CoCrFeNi high-entropy alloy, *Mater. Res. Express*. 6 (2019) 056540. doi:10.1088/2053-1591/ab0597.
- [196] K. Eckler, A.F. Norman, F. Gärtner, A.L. Greer, D.M. Herlach, Microstructures of dilute Ni C alloys obtained from undercooled droplets, *J. Cryst. Growth*. 173 (1997) 528–540. doi:10.1016/S0022-0248(96)01066-4.
- [197] Y.Z. Chen, F. Liu, G.C. Yang, N. Liu, C.L. Yang, H. Xie, Y.H. Zhou, Grain refinement of Fe<sub>75</sub>Ni<sub>25</sub> alloys at low undercooling, *Mater. Charact.* 59 (2008) 412–416. doi:10.1016/j.matchar.2007.02.009.
- [198] S. LI, H. WANG, F. LIU, Microstructure and microtexture evolution of undercooled Ni-15%Cu alloy, *Trans. Nonferrous Met. Soc. China*. 23 (2013) 3265–3270. doi:10.1016/S1003-6326(13)62862-9.
- [199] O.N. Senkov, S.V. Senkova, C. Woodward, D.B. Miracle, Low-density, refractory multi-principal element alloys of the Cr–Nb–Ti–V–Zr system: Microstructure and phase analysis, *Acta Mater.* 61 (2013) 1545–1557. doi:10.1016/j.actamat.2012.11.032.
- [200] O.N. Senkov, S. Rao, K.J. Chaput, C. Woodward, Compositional effect on microstructure and properties of NbTiZr-based complex concentrated alloys, *Acta Mater.* 151 (2018) 201–215. doi:10.1016/j.actamat.2018.03.065.
- [201] O.N. Senkov, S. V. Senkova, D.B. Miracle, C. Woodward, Mechanical properties of low-density, refractory multi-principal element alloys of the Cr-Nb-Ti-V-Zr system, *Mater. Sci. Eng. A*. 565 (2013) 51–62. doi:10.1016/j.msea.2012.12.018.
- [202] D.J.M. King, S.T.Y. Cheung, S.A. Humphry-Baker, C. Parkin, A. Couet, M.B. Cortie, G.R. Lumpkin, S.C. Middleburgh, A.J. Knowles, High temperature, low neutron cross-section high-entropy alloys in the Nb-Ti-V-Zr system, *Acta Mater.* 166 (2019) 435–446. doi:10.1016/j.actamat.2019.01.006.
- [203] Y. Jia, L. Zhang, P. Li, X. Ma, L. Xu, S. Wu, Y. Jia, G. Wang, Microstructure and Mechanical Properties of Nb–Ti–V–Zr Refractory Medium-Entropy Alloys, *Front. Mater.* 7 (2020) 1–11. doi:10.3389/fmats.2020.00172.
- [204] G. Laplanche, S. Berglund, C. Reinhart, A. Kostka, F. Fox, E.P. George, Phase stability and kinetics of  $\sigma$ -phase precipitation in CrMnFeCoNi high-entropy alloys, *Acta Mater.* 161 (2018) 338–351. doi:10.1016/j.actamat.2018.09.040.
- [205] M. Žaludová, B. Smetana, S. Zlá, J. Dobrovská, K. Gryc, K. Michalek, R. Dudek,



- Study of DTA method experimental conditions and of their influence on obtained data of metallic systems, *Met. 2012 - Conf. Proceedings, 21st Int. Conf. Metall. Mater.* (2012) 640–645.
- [206] N. Yurchenko, N. Stepanov, M. Tikhonovsky, G. Salishchev, Phase Evolution of the  $Al_xNbTiVZr$  ( $x = 0; 0.5; 1; 1.5$ ) High Entropy Alloys, *Metals (Basel)*. 6 (2016) 298. doi:10.3390/met6120298.
- [207] W.L. Wang, L. Hu, S.J. Yang, A. Wang, L. Wang, B. Wei, Liquid Supercoolability and Synthesis Kinetics of Quinary Refractory High-entropy Alloy, *Sci. Rep.* 6 (2016) 1–7. doi:10.1038/srep37191.
- [208] M. Gasik, H. Yu, Phase Equilibria and Thermal Behaviour of Biomedical Ti-Nb-Zr Alloy, *17th Plansee Semin.* 1 (2009) RM 29/1-RM 29/7.
- [209] B.H. Rabin, W.D. Swank, R.N. Wright, Thermophysical properties of Alloy 617 from 25°C to 1000°C, *Nucl. Eng. Des.* 262 (2013) 72–80. doi:10.1016/j.nucengdes.2013.03.048.
- [210] H. Thomas, *Über Widerstandslegierungen*, *Zeitschrift für Phys.* 232 (1951) 219–232.
- [211] R.G. Davies, An X-ray and dilatometric study of order and the “K-state” in iron-aluminum alloys, *J. Phys. Chem. Solids.* 24 (1963) 985–992. doi:10.1016/0022-3697(63)90002-7.
- [212] W. Bendick, H.H. Ettwig, W. Pepperhoff, Anomalies in specific heat and thermal expansion of FCC iron alloys, *J. Phys. F Met. Phys.* 8 (1978) 2525–2534. doi:10.1088/0305-4608/8/12/012.
- [213] A. Marucco, B. Nath, Effects of ordering on the properties of Ni-Cr alloys, *J. Mater. Sci.* 23 (1988) 2107–2114. doi:10.1007/BF01115776.
- [214] E. Starke, V. Gerold, A. Guy, An investigation of the k-effect in Nickel-Aluminum alloys, *Acta Metall.* 13 (1965) 957–964. doi:10.1016/0001-6160(65)90003-9.
- [215] S. Kim, I.H. Kuk, J.S. Kim, Order–disorder reaction in Alloy 600, *Mater. Sci. Eng. A.* 279 (2000) 142–148. doi:10.1016/S0921-5093(99)00640-1.
- [216] E.E. Stansbury, C.R. Brooks, T.L. Arledge, Specific-Heat Anomalies in Solid Solutions of Chromium and Molybdenum in Nickel: Evidence for Short-Range Order, *J. Inst. Met.* (1966).
- [217] R.J. Taunt, B. Ralph, Ordering and the K-effect in  $Ni_2Cr$ , *Phys. Status Solidi.* 29 (1975) 431–442. doi:10.1002/pssa.2210290211.
- [218] H. Logie, J. Jackson, J. Anderson, F.R. Nabarro, Effect of plastic deformation on

- resistivity of gold-palladium alloys, *Acta Metall.* 9 (1961) 707–713.  
doi:10.1016/0001-6160(61)90100-6.
- [219] H. Ge, H. Song, J. Shen, F. Tian, Effect of alloying on the thermal-elastic properties of 3d high-entropy alloys, *Mater. Chem. Phys.* 210 (2018) 320–326.  
doi:10.1016/j.matchemphys.2017.10.046.
- [220] S.M.C. van Bohemen, The nonlinear lattice expansion of iron alloys in the range 100–1600K, *Scr. Mater.* 69 (2013) 315–318. doi:10.1016/j.scriptamat.2013.05.009.
- [221] G. Laplanche, M. Schneider, F. Scholz, J. Frenzel, G. Eggeler, J. Schreuer, Processing of a single-crystalline CrCoNi medium-entropy alloy and evolution of its thermal expansion and elastic stiffness coefficients with temperature, *Scr. Mater.* 177 (2020) 44–48. doi:10.1016/j.scriptamat.2019.09.020.
- [222] T. De Cock, C. Capdevila, F.G. Caballero, C.G. de Andrés, Interpretation of a dilatometric anomaly previous to the ferrite-to-austenite transformation in a low carbon steel, *Scr. Mater.* 54 (2006) 949–954. doi:10.1016/j.scriptamat.2005.10.052.
- [223] K. Jin, S. Mu, K. An, W.D. Porter, G.D. Samolyuk, G.M. Stocks, H. Bei, Thermophysical properties of Ni-containing single-phase concentrated solid solution alloys, *Mater. Des.* 117 (2017) 185–192. doi:10.1016/j.matdes.2016.12.079.
- [224] A.Z. Menshikov, C. Dimitrov, A.E. Teplykh, Local Atomic Redistribution Under Irradiation in  $\gamma$ -NiFeCr Alloys, *J. Phys. III.* 7 (1997) 1899–1908.  
doi:10.1051/jp3:1997231.
- [225] P. Cenedese, F. Bley, S. Lefebvre, Diffuse scattering in disordered ternary alloys: neutron measurements of local order in a stainless steel  $\text{Fe}_{0.56}\text{Cr}_{0.21}\text{Ni}_{0.23}$ , *Acta Crystallogr. Sect. A Found. Crystallogr.* 40 (1984) 228–240.  
doi:10.1107/S0108767384000489.
- [226] A. Fantin, G.O. Lepore, A.M. Manzoni, S. Kasatkov, T. Scherb, T. Huthwelker, F. d’Acapito, G. Schumacher, Short-range chemical order and local lattice distortion in a compositionally complex alloy, *Acta Mater.* 193 (2020) 329–337.  
doi:10.1016/j.actamat.2020.04.034.
- [227] Y.J. Zhou, Y. Zhang, F.J. Wang, G.L. Chen, Phase transformation induced by lattice distortion in multiprincipal component  $\text{CoCrFeNiCu}_x\text{Al}_{1-x}$  solid-solution alloys, *Appl. Phys. Lett.* 92 (2008) 241917. doi:10.1063/1.2938690.
- [228] F.J. Wang, Y. Zhang, G.L. Chen, Atomic packing efficiency and phase transition in a high entropy alloy, *J. Alloys Compd.* 478 (2009) 321–324.  
doi:10.1016/j.jallcom.2008.11.059.

- [229] X. Yang, Y. Zhang, P.K. Liaw, Microstructure and Compressive Properties of NbTiVTaAl<sub>x</sub> High Entropy Alloys, *Procedia Eng.* 36 (2012) 292–298. doi:10.1016/j.proeng.2012.03.043.
- [230] H.-Y. Chen, C.-W. Tsai, C.-C. Tung, J.-W. Yeh, T.-T. Shun, C.-C. Yang, S.-K. Chen, Effect of the substitution of Co by Mn in Al-Cr-Cu-Fe-Co-Ni high-entropy alloys, *Ann. Chim. Sci. Des Matériaux.* 31 (2006) 685–698. doi:10.3166/acsm.31.685-698.
- [231] C.-J. Tong, Y.-L. Chen, J.-W. Yeh, S.-J. Lin, S.-K. Chen, T.-T. Shun, C.-H. Tsau, S.-Y. Chang, Microstructure characterization of Al<sub>x</sub>CoCrCuFeNi high-entropy alloy system with multiprincipal elements, *Metall. Mater. Trans. A.* 36 (2005) 881–893. doi:10.1007/s11661-005-0283-0.
- [232] G.-Y. Ke, G.-Y. Chen, T. Hsu, J.-W. Yeh, FCC and BCC equivalents in as-cast solid solutions of Al<sub>x</sub>Co<sub>y</sub>Cr<sub>z</sub>Cu<sub>0.5</sub>Fe<sub>v</sub>Ni<sub>w</sub> high-entropy alloys, *Ann. Chim. Sci. Des Matériaux.* 31 (2006) 669–684. doi:10.3166/acsm.31.669-684.
- [233] S. GUO, C.T. LIU, Phase stability in high entropy alloys: Formation of solid-solution phase or amorphous phase, *Prog. Nat. Sci. Mater. Int.* 21 (2011) 433–446. doi:10.1016/S1002-0071(12)60080-X.
- [234] M. Miller, P. Liaw, *Bulk Metallic Glasses An Overview*, 2008.
- [235] C. Li, J.C. Li, M. Zhao, Q. Jiang, Effect of alloying elements on microstructure and properties of multiprincipal elements high-entropy alloys, *J. Alloys Compd.* 475 (2009) 752–757. doi:10.1016/j.jallcom.2008.07.124.
- [236] T.-K. Chen, M.-S. Wong, T.-T. Shun, J.-W. Yeh, Nanostructured nitride films of multi-element high-entropy alloys by reactive DC sputtering, *Surf. Coatings Technol.* 200 (2005) 1361–1365. doi:10.1016/j.surfcoat.2005.08.081.
- [237] C.-Y. Hsu, J. Yeh, S. Chen, T.-T. Shun, Wear resistance and high-temperature compression strength of Fcc CuCoNiCrAl<sub>0.5</sub>Fe alloy with boron addition, *Metall. Mater. Trans. A.* 35 (2004) 1465–1469. doi:10.1007/s11661-004-0254-x.
- [238] Y. Li, S.J. Poon, G.J. Shiflet, J. Xu, D.H. Kim, J.F. Löffler, Formation of bulk metallic glasses and their composites, *MRS Bull.* 32 (2007) 624–628. doi:10.1557/mrs2007.123.
- [239] C.-C. Tung, J.-W. Yeh, T. Shun, S.-K. Chen, Y.-S. Huang, H.-C. Chen, On the elemental effect of AlCoCrCuFeNi high-entropy alloy system, *Mater. Lett.* 61 (2007) 1–5. doi:10.1016/j.matlet.2006.03.140.
- [240] C.-Y. Hsu, W.-R. Wang, W.-Y. Tang, S.-K. Chen, J.-W. Yeh, Microstructure and

- mechanical properties of new  $\text{AlCo}_x\text{CrFeMo}_{0.5}\text{Ni}$  high-entropy alloys, *Adv. Eng. Mater.* 12 (2010) 44–49. doi:10.1002/adem.200900171.
- [241] F.J. Wang, Y. Zhang, Effect of Co addition on crystal structure and mechanical properties of  $\text{Ti}_{0.5}\text{CrFeNiAlCo}$  high entropy alloy, *Mater. Sci. Eng. A.* 496 (2008) 214–216. doi:10.1016/j.msea.2008.05.020.
- [242] C.-Y. Hsu, C.-C. Juan, W.-R. Wang, T.-S. Sheu, J.-W. Yeh, S.-K. Chen, On the superior hot hardness and softening resistance of  $\text{AlCoCr}_x\text{FeMo}_{0.5}\text{Ni}$  high-entropy alloys, *Mater. Sci. Eng. A.* 528 (2011) 3581–3588. doi:10.1016/j.msea.2011.01.072.
- [243] Y.J. Zhou, Y. Zhang, F.J. Wang, Y.L. Wang, G.L. Chen, Effect of Cu addition on the microstructure and mechanical properties of  $\text{AlCoCrFeNiTi}_{0.5}$  solid-solution alloy, *J. Alloys Compd.* 466 (2008) 201–204. doi:10.1016/j.jallcom.2007.11.110.
- [244] J.-W. Yeh, S.-J. Lin, T.-S. Chin, J.-Y. Gan, S.-K. Chen, T.-T. Shun, C.-H. Tsau, S.-Y. Chou, Formation of simple crystal structures in Cu-Co-Ni-Cr-Al-Fe-Ti-V alloys with multiprincipal metallic elements, *Metall. Mater. Trans. A.* 35 (2004) 2533–2536. doi:10.1007/s11661-006-0234-4.
- [245] C.W. Chang, Microstructure and Properties of As-Cast 10-Component Nanostructured  $\text{AlCoCrCuFeMoNiTiVZr}$  High-Entropy Alloy, National Tsing Hua University, 2004.
- [246] B.S. Li, Y.P. Wang, M.X. Ren, C. Yang, H.Z. Fu, Effects of Mn, Ti and V on the microstructure and properties of  $\text{AlCrFeCoNiCu}$  high entropy alloy, *Mater. Sci. Eng. A.* 498 (2008) 482–486. doi:10.1016/j.msea.2008.08.025.
- [247] Z. Hu, Y. Zhan, G. Zhang, J. She, C. Li, Effect of rare earth Y addition on the microstructure and mechanical properties of high entropy  $\text{AlCoCrCuNiTi}$  alloys, *Mater. Des.* 31 (2010) 1599–1602. doi:10.1016/j.matdes.2009.09.016.
- [248] J.M. Zhu, H.M. Fu, H.F. Zhang, A.M. Wang, H. Li, Z.Q. Hu, Microstructures and compressive properties of multicomponent  $\text{AlCoCrFeNiMo}_x$  alloys, *Mater. Sci. Eng. A.* 527 (2010) 6975–6979. doi:10.1016/j.msea.2010.07.028.
- [249] C.-C. Juan, C.-Y. Hsu, C.-W. Tsai, W.-R. Wang, T.-S. Sheu, J.-W. Yeh, S.-K. Chen, On microstructure and mechanical performance of  $\text{AlCoCrFeMo}_{0.5}\text{Ni}_x$  high-entropy alloys, *Intermetallics.* 32 (2013) 401–407. doi:10.1016/j.intermet.2012.09.008.
- [250] S.G. Ma, Y. Zhang, Effect of Nb addition on the microstructure and properties of  $\text{AlCoCrFeNi}$  high-entropy alloy, *Mater. Sci. Eng. A.* 532 (2012) 480–486. doi:10.1016/j.msea.2011.10.110.
- [251] Y.J. Zhou, Y. Zhang, Y.L. Wang, G.L. Chen, Solid solution alloys of

- AlCoCrFeNiTi<sub>x</sub> with excellent room-temperature mechanical properties, *Appl. Phys. Lett.* 90 (2007) 181904. doi:10.1063/1.2734517.
- [252] M. Chen, Y. Liu, Y. Li, X. Chen, Microstructure and mechanical properties of AlTiFeNiCuCr<sub>x</sub> high-entropy alloy with multi-principal elements, *Acta Metall. Sin.* 43 (2007) 1020–1024.
- [253] K.-H. Cheng, C.-H. Lai, S.-J. Lin, J.-W. Yeh, Structural and mechanical properties of multi-element (AlCrMoTaTiZr)N<sub>x</sub> coatings by reactive magnetron sputtering, *Thin Solid Films.* 519 (2011) 3185–3190. doi:10.1016/j.tsf.2010.11.034.
- [254] C.-H. Lai, S.-J. Lin, J.-W. Yeh, A. Davison, Effect of substrate bias on the structure and properties of multi-element (AlCrTaTiZr)N coatings, *J. Phys. D. Appl. Phys.* 39 (2006) 4628–4633. doi:10.1088/0022-3727/39/21/019.
- [255] Y.-J. Hsu, W.-C. Chiang, J.-K. Wu, Corrosion behavior of FeCoNiCrCu<sub>x</sub> high-entropy alloys in 3.5% sodium chloride solution, *Mater. Chem. Phys.* 92 (2005) 112–117. doi:10.1016/j.matchemphys.2005.01.001.
- [256] T.-T. Shun, L.-Y. Chang, M.-H. Shiu, Microstructures and mechanical properties of multiprincipal component CoCrFeNiTi<sub>x</sub> alloys, *Mater. Sci. Eng. A.* 556 (2012) 170–174. doi:10.1016/j.msea.2012.06.075.
- [257] B. Ren, Z.X. Liu, D.M. Li, L. Shi, B. Cai, M.X. Wang, Effect of elemental interaction on microstructure of CuCrFeNiMn high entropy alloy system, *J. Alloys Compd.* 493 (2010) 148–153. doi:10.1016/j.jallcom.2009.12.183.
- [258] A.K. Singh, A. Subramaniam, Thermodynamic rationalization of the microstructures of CrFeNi & CuCrFeNi alloys, *Adv. Mater. Res.* 585 (2012) 3–7. doi:10.4028/www.scientific.net/AMR.585.3.
- [259] A. Durga, K.C. Hari Kumar, B.S. Murty, Phase formation in equiatomic high entropy alloys: CALPHAD approach and experimental studies, *Trans. Indian Inst. Met.* 65 (2012) 375–380. doi:10.1007/s12666-012-0138-5.
- [260] L. Ma, L. Wang, T. Zhang, A. Inoue, Bulk Glass Formation of Ti-Zr-Hf-Cu-M (M=Fe, Co, Ni) Alloys, *Mater. Trans.* 43 (2002) 277–280. doi:10.2320/matertrans.43.277.
- [261] A. Cunliffe, J. Plummer, I. Figueroa, I. Todd, Glass formation in a high entropy alloy system by design, *Intermetallics.* 23 (2012) 204–207. doi:10.1016/j.intermet.2011.12.006.
- [262] Y. Zhang, X. Yang, P.K. Liaw, Alloy design and properties optimization of high-entropy alloys, *JOM.* 64 (2012) 830–838. doi:10.1007/s11837-012-0366-5.

## Acknowledgments

I am deeply grateful to my wife Marina and my son Benício for accepting the challenge to move to a foreign country and standing by my side, be it in the good or the bad moments. You have always supported and encouraged me and given me the strength to complete my thesis. Love!

I am thankful to my supervisor, Prof. Dr. Kornelius Nielsch, for allowing me to endeavor my doctoral study at the Technical University of Dresden. I am sincerely appreciative to my supervisor, Dr. Ivan Kaban, for providing guidance and feedback throughout this project at the Leibniz Institute for Solid State and Materials Research Dresden, IFW-Dresden.

I would like to acknowledge present and former colleagues of the research group 'Solidification and Complex Structures'. Dr. Norbert Mattern, the first person I contacted at IFW-Dresden. Dr. Jiri Orava for the fruitful discussions about metastable alloys. Dr. Yuhao Wu for sharing his experience and knowledge on non-equilibrium solidification and EML processing. Dr. Olga Shuleshova for support with the EML facility and data analysis. Mrs. Birgit Optiz and Dr. Lars Giebler for assistance with XRD. Dr. Hans Weber, Dr. Ju Wang, and Xialiang Han for discussions and pleasant time spent together.

I would like to express my sincere gratitude to the scientific, technical, and administrative staff at IFW-Dresden that have assisted me to conclude my work. Mrs. Birgit Bartusch for always being helpful with DSC and dilatometry measurements. Mrs. Dina Bieberstein for preparing the TEM samples. Dr. Rafael G. Mendes for the TEM analysis. Dr. Torsten Mix and Dr. Thomas G. Woodcock for measuring the magnetic properties. Mrs. Nicole Geißler and Mrs. Romy Keller for the help provided in different situations. Dr. Alex Funk for sharing his skills on how to operate the Micro-CT. Mr. Sven Donath for training and assistance in the casting lab. The staff at the mechanic's workshop for cutting the samples. Dr. Stefan Pilz, Dr. Holger Schwab, and Dr. Kai Neufeld for support with SEM and EBSD. Dr. Josephine Zeisig for the helping hand with microindentation tests. Mr. Bernhard Gebel for heat treatment of the samples. Mrs. Andrea Voß and Mrs. Heike Bußkamp for chemical analysis. And finally, Mrs. Brit Präbller-Wüstling for her assistance. Your help is valued!

I acknowledge the external collaborators as well. Dr. Victor T. Witusiewicz (ACCESS e.V., Aachen) for thermodynamic calculations presented in the thesis. Mr. Yanzhao Yang (University of Alberta, Canada) for the stereographic projection modeling of crystal growth.

I would also like to thank the present and former colleagues and friends of the Institute for Complex Materials that have contributed to my stay in Germany being pleasant. Dr. Omar Salman, Dr. Kang Sun, Dr. Tiwen Lu, Dr. Nazim Babacan, Tianbing He, Dr. Murillo Romero da Silva, Zichao Li, Dr. Rodolfo Batalha, Antonious Permana, Renan Almeida, Dr. Junhee Han, Dr. Konrad Kosiba, Dr. Pei Wang, Dr. Sergio Scudino, Dr. Simon Pauly, and Otto Martin.

Parts of this research were carried out at the light source PETRA III, beamline P21.1 at DESY, a member of the Helmholtz Association (HGF). I acknowledge Dr. Ann-Christin Dippel, Dr. Oleg Ivashko, Dr. Martin v. Zimmermann, Mr. Olof Gutowski, and Mr. Philipp Glaeveccke for support at beamline P21.1.

I acknowledge the Brazilian Federal Agency for Support and Evaluation of Graduate Education CAPES for the financial aid in form of a scholarship (grant number: 88887.161381/2017-00, 2017) in the frame of CAPES/DAAD/CNPq International Cooperation Program.

## List of publications

1. **A.F. Andreoli**, J. Orava, P.K. Liaw, H. Weber, M.F. de Oliveira, K. Nielsch, I. Kaban, The elastic-strain energy criterion of phase formation for complex concentrated alloys, *Materialia*. 5 (2019) 100222.
2. T. Lu, T. He, P. Zhao, K. Sun, **A.F. Andreoli**, H. Chen, W. Chen, Z. Fu, S. Scudino, Fine tuning in-sync the mechanical and magnetic properties of FeCoNiAl<sub>0.25</sub>Mn<sub>0.25</sub> high-entropy alloy through cold rolling and annealing treatment, *Journal of Materials Processing Technology*, 289 (2021) 116945.
3. **A.F. Andreoli**, O. Shuleshova, V.T. Witusiewicz, Y. Wu, Y. Yang, O. Ivashko, A.-C. Dippel, M. v. Zimmermann, K. Nielsch, I. Kaban, In situ study of non-equilibrium solidification of CoCrFeNi high-entropy alloy and CrFeNi and CoCrNi ternary suballoys, *Acta Materialia*, 212 (2021) 116880.
4. **A.F. Andreoli**, R.G. Mendes, O. Shuleshova, V.T. Witusiewicz, M.A.v. Huis, I. Kaban, Non-equilibrium solidification of the NbTiVZr refractory high-entropy alloy, *Acta Materialia* 221 (2021) 1174416.

### Contribution statement:

1. **A.F. Andreoli**: Conceptualization, Investigation, Formal analysis, Visualization, Writing - Original Draft, Review & Editing, Funding acquisition.
2. **A.F. Andreoli**: Formal analysis, Writing - Review & Editing.
3. **A.F. Andreoli**: Conceptualization, Investigation, Formal analysis, Visualization, Writing - Original Draft, Review & Editing, Funding acquisition.
4. **A.F. Andreoli**: Conceptualization, Investigation, Formal analysis, Visualization, Writing - Original Draft, Review & Editing, Funding acquisition.



## Erklärung

Hiermit versichere ich, dass ich die vorliegende Arbeit mit dem Titel "*Non-equilibrium solidification of high-entropy alloys monitored in situ by X-ray diffraction and high-speed video*" ohne unzulässige Hilfe Dritter und ohne Benutzung anderer als der angegebenen Hilfsmittel angefertigt habe; die aus fremden Quellen direkt oder indirekt übernommenen Gedanken sind als solche kenntlich gemacht. Bei der Auswahl und Auswertung des Materials sowie bei der Herstellung des Manuskripts habe ich Unterstützungsleistungen von folgenden Personen erhalten: Prof. Dr. Kornelius Nielsch und Dr. Ivan Kaban. Weitere Personen waren an der geistigen Herstellung der vorliegenden Arbeit nicht beteiligt. Insbesondere habe ich nicht die Hilfe eines kommerziellen Promotionsberaters in Anspruch genommen. Dritte haben von mir keine geldwerten Leistungen für Arbeiten erhalten, die in Zusammenhang mit dem Inhalt der vorgelegten Dissertation stehen. Die Arbeit wurde bisher weder im Inland noch im Ausland in gleicher oder ähnlicher Form einer anderen Prüfungsbehörde vorgelegt und ist auch noch nicht veröffentlicht worden. Dissertation wurde am Leibniz Institut für Festkörper und Werkstoffforschung Dresden (IFW Dresden) unter der wissenschaftlichen Betreuung von Prof. Dr. Kornelius Nielsch (TU Dresden, Institut für Werkstoffwissenschaft und IFW Dresden, Institut für Metallische Werkstoffe) und Dr. Ivan Kaban (IFW Dresden, Institut für Komplexe Materialien) angefertigt. Die Promotionsordnung der Fakultät Maschinenwesen der TU Dresden vom 22.03.2018 erkenne ich an.

.....

Angelo Fernandes Andreoli

Dresden, 18.01.2022